Surface Enhanced Raman Probes for Targeted Melanoma Detection

KATHLEEN MARIA BOWES

BOWES, KATHLEEN MARIA (2021) Surface Enhanced Raman Probes for Targeted Melanoma Detection. Doctoral thesis, Durham University.

Durham
University

Surface Enhanced Raman Spectroscopy Probes for Targeted Melanoma Detection

Kathleen M. Bowes

Declaration

The work described herein was undertaken at the Department of Chemistry, Durham University, between October 2017 and January 2021. All of the work is my own, except where specifically stated otherwise. No part has previously been submitted for a degree at this or any other university.

Statement of Copyright

Abstract

Melanoma is the deadliest form of skin cancer, and rates of melanoma in the UK appear to be rising. Despite this increase, current diagnostic methods remain slow, invasive and speculative. In this work, surface enhanced Raman spectroscopy (SERS) is proposed as an alternative diagnostic method, with the potential to provide rapid, point-of-care testing for early-stage melanoma skin cancer.

Gold nanostars decorated with red and near infrared-absorbing dyes were designed and synthesised as probes for surface enhanced resonance Raman spectroscopy (SERRS). Various dyes were evaluated as potential reporter molecules; methylene blue was chosen for the final probe structure due to its clear SERS signals and superior stability when bound to the nanostar surface. The probe was coated with a protective silica layer and functionalised with a peptide for the selective targeting of melanoma, before testing with various mammalian cell lines.

The results show that human melanoma cells dosed with the SERS probe retained SERS signals after rinsing with water, whereas the probe appeared to ‘rinse out’ of other cell lines, giving significantly diminished SERS signals. Confocal and fluorescence microscopy images also show the adhesion of the probe to human melanoma cells.

Following the success of this method, alternative reporter molecules were investigated. Namely, the use of molecular wires as potential Raman reporters was explored, as it was theorised that the conductive properties of these molecules could augment the SERS effect. The wires were synthesised and adhered to the surface of gold nanostars, in order to evaluate the effect of wire length on SERS intensity. The SERS spectra of the molecular wire-functionalised gold nanostars did not display improved signal intensity compared to gold nanostars functionalised with shorter molecules. These experiments were largely hindered due to instability of the wire-functionalised gold nanostars in solution, and so to fully rule out the possibility of molecular wire augmented SERS, work would need to be done to find a wire-functionalised substrate less prone to aggregation.

The observations herein demonstrate that a selective probe for the detection of melanoma, based on methylene blue decorated gold nanostars, was successfully created. While the preliminary results of this study indicate that the SERS method is a viable approach for melanoma detection, further optimisation of the probe is required for clinical applications. In particular, strategies to improve the SERS signal intensity are discussed.

Acknowledgements

First and foremost, I would like to thank Robert Pal for being the most supportive supervisor I could ask for, and for supplying endless encouragement, guidance, and snacks. I would also like to thank Andrew Beeby and Neil Sim for their help and advice, and Karl Coleman for the generous use of his Raman spectrometer when Andy's tragically died. Thank you as well to David Parker for use of his lab space.

For making boring days in the lab more interesting, thank you to Ed, Lewis, Andrei, Niamh, Tom, Dom, Jack and Patrycja. Thanks also to the fourth years; Bhavini, Sam, Charlie and Yulia (especially Yulia).

Thank you to my parents for helping me get this far.

And finally, I would like to thank Daniel for being there through all the highs and lows, and for believing in me when I thought I could not do it.

Abbreviations

APTMS	(3-Aminopropyl)trimethoxysilane
ASAP	Atmospheric solids analysis probe
AuNP	Gold nanoparticle
AuNS	Gold nanostar
CCD	Charge coupled device
CFU	Colony-forming unit
CTAB	Cetyl trimethylammonium bromide
CV	Cresyl violet
DAPI	4′,6-Diamidino-2-phenylindole
DCC	Dicyclohexylmethanediimine
DCM	Dichloromethane
DMAP	4-Dimethylaminopyridine
DMF	Dimethylformamide
DNS	Dansyl
EDX	Energy-dispersive X-ray spectroscopy
EF	Enhancement factor
ELISA	Enzyme-linked immunosorbent assay
EM	Electromagnetic
EPR	Enhanced permeation and retention
FDA	Food and drug administration
GPCR	G-protein coupled receptor
HGN	Hollow gold nanoparticle
LFIEF	Local field intensity enhancement factor
LSCM	Laser scanning confocal microscopy
LSP	Localised surface plasmon
LWD	Long working distance
MALDI-TOF MS	Matrix-assisted laser desorption ionization-time of flight mass spectrometry
MB	Methylene blue
MC1R	Melanocortin 1 receptor
MEF	Metal enhanced fluorescence

MNP	Magnetic nanoparticle
MSHR	Melanocyte-stimulating hormone receptor
NIR	Near infrared
NMR	Nuclear magnetic resonance
NNE	Number needed to excise
NPD-MSH	[Nleu^4-D-Phe^7] alpha-melanocyte stimulating hormone
OPE	Oligophenylene ethynylene
OPT	Oligo(phenylene triazole)
PEG	Polyethylene glycol
pNTP	p-Nitrothiophenol
PSP	Propagating surface plasmon
PVA	Polyvinyl alcohol
PVP	Polyvinylpyrrolidone
REF	Radiation enhancement factor
SAM	Self-assembled monolayer
SCC	Squamous cell carcinoma
SERRS	Surface enhanced resonance Raman spectroscopy
SERS	Surface enhanced Raman spectroscopy
SM	Single molecule
SPECT/CT	Single-photon emission computed tomography/computerised tomography
SPM	Scanning probe microscopy
SPR	Surface plasmon resonance
TBAT	Tetrabutylammonium difluorotriphenylsilicate
TEM	Transmission electron microscopy
TEOS	Tetraethyl orthosilicate
TERS	Tip enhanced Raman spectroscopy
TIR	Total internal reflection
UV-Vis	Ultraviolet-visible
WHO	World health organisation
α-MSH	Alpha-melanocyte stimulating hormone
λ_{max}	Wavelength of maximum absorption
@SiO$_2$	Silica coating

Contents

Introduction

Cutaneous melanoma is the fastest-rising form of cancer in the UK in the past 30 years, and mortality rates continue to increase.[1] However, current diagnostic tests for melanoma involve skin biopsy, which is a slow and invasive method.[2] Surface enhanced Raman spectroscopy (SERS) could potentially provide an alternative diagnostic technique to identify melanoma. SERS is based on exploiting the effect of plasmonic metal surfaces to enhance the signal from Raman scattering, which is otherwise weak.[3] Small concentrations of molecules and indeed even single molecules can be detected with great accuracy using SERS.[4] Since its initial discovery in 1974,[5] SERS has become an increasingly popular analytical method, widely utilised in a variety of applications such as the detection of pesticides and explosives.[6,7] The ability of SERS to detect small amounts of analyte in a non-invasive way makes the method an attractive possibility for use in early stage diagnostics, including in the detection of melanoma.[8] However, the use of SERS in medical applications remains limited at present, and a number of factors must be taken into account when designing a SERS probe for the purpose of medical diagnosis. In the following chapter, the concept of SERS and its potential uses in medical diagnostics are explored, and current methods for the diagnosis of melanoma are evaluated in comparison to SERS.

1.1 Raman Spectroscopy

When incident light interacts with a particle, the majority of photons are scattered elastically, neither gaining nor losing energy. [9] Elastic scattering can fall into one of two categories; Rayleigh scattering, in which the particle is smaller than the wavelength of incident light (approximately one tenth of the wavelength), or Mie scattering, in which the particle is larger than the wavelength of incident light.[10] .

Raman scattering describes the small proportion of photons scattered inelastically, occurring for approximately one in every 10^6-10^8 photons.[9,11] These photons either lose (Stokes scattering) or gain (anti-Stokes scattering) energy as a result of their interaction with the material. Raman scattering occurs when the electric field of the incident light polarises the electron cloud about the molecule (Figure 1.1), exciting it to a virtual state (Figure 1.2). Virtual states are not 'real' states of the molecule, but created when the molecule becomes polarised, although they can be thought of as a superposition of real states.

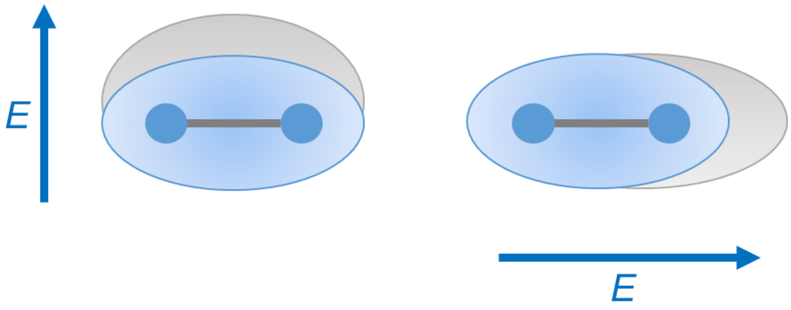

Figure 1.1: Polarisation of a molecule induced by an electric field.

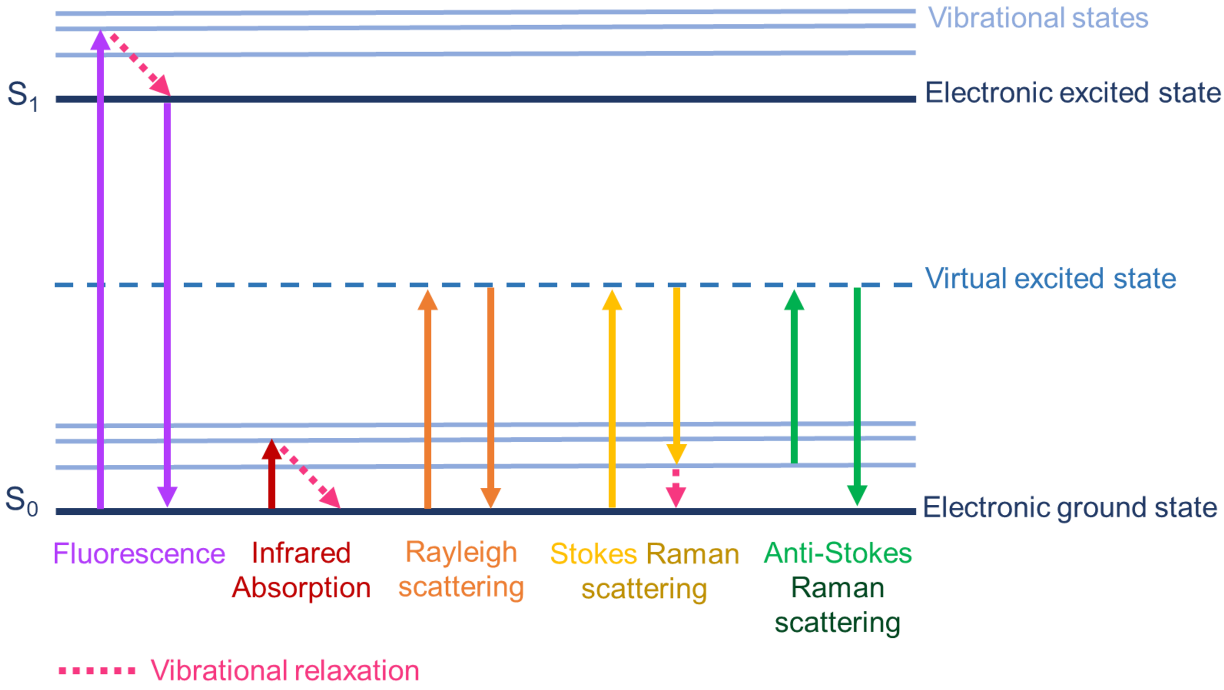

Figure 1.2: Jablonski diagram showing Raman and Rayleigh scattering, with other photochemical processes for comparison.

Raman scattering therefore depends on a change in polarizability of the molecule; this is the basic selection rule of Raman spectroscopy. This is in contrast to infrared spectroscopy, which is dependent on the dipole moment of the molecule; a change in the dipole moment results in the molecule being excited to a higher vibrational energy level. On a basic level, these selection rules mean that symmetrical molecules will give more intense Raman scattering, whereas asymmetrical molecules are more suited to IR spectroscopy. Examples of these selection rules applied to the bond vibrations of CO_2 are given in Figure 1.3. [9,11,12]

Type of bond vibration	Change in polarizability	Change in dipole moment
Symmetric stretching 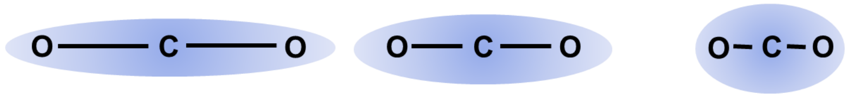	Yes Raman active	No IR inactive
Bending 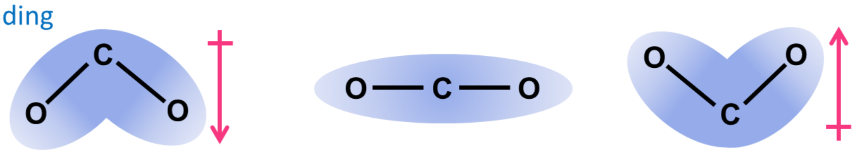	No Raman inactive	Yes IR active
Asymmetric stretching 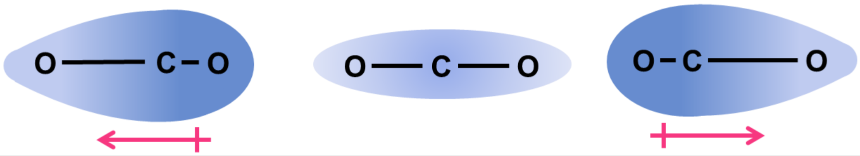	No Raman inactive	Yes IR active

Figure 1.3: Bond vibrations of CO_2, demonstrating selection rules for this molecule. Arrows indicate the net dipole moment of the molecule (if non-zero).

1.2 Surface plasmons and the SERS effect

Despite being discovered in 1928,[13] Raman spectroscopy did not take off as a characterisation technique until much later in the century, partially due to advancement in instrumentation, and also due to the discovery of the surface enhanced Raman effect in 1974,[5] which allowed the relatively small signals of Raman spectroscopy to become greatly enhanced. This enhancement effect, first observed on silver electrodes, can be attributed to surface plasmons present on metal surfaces.[5,14]

Surface plasmons (SPs) can be described as a wave of oscillating electrons induced by incident light. SPs can be sorted into two types: propagating surface plasmons (PSPs) and localised surface plasmons (LSPs).[15] PSPs are induced by incident light on a metal surface under total internal reflection (TIR) conditions, and propagate parallel to a metal surface, at the interface between the metal and dielectric material. LSPs occur in metal colloidal suspensions and as the name suggests, do not propagate but are confined to a space which is similar in length or smaller than the excitation wavelength: they are confined to a nanoparticle. LSPs are induced by incident light, causing the oscillation of electrons in the conduction band. Both these types of SP are shown in Figure 1.4, though the SERS effect is primarily affected by LSPs.

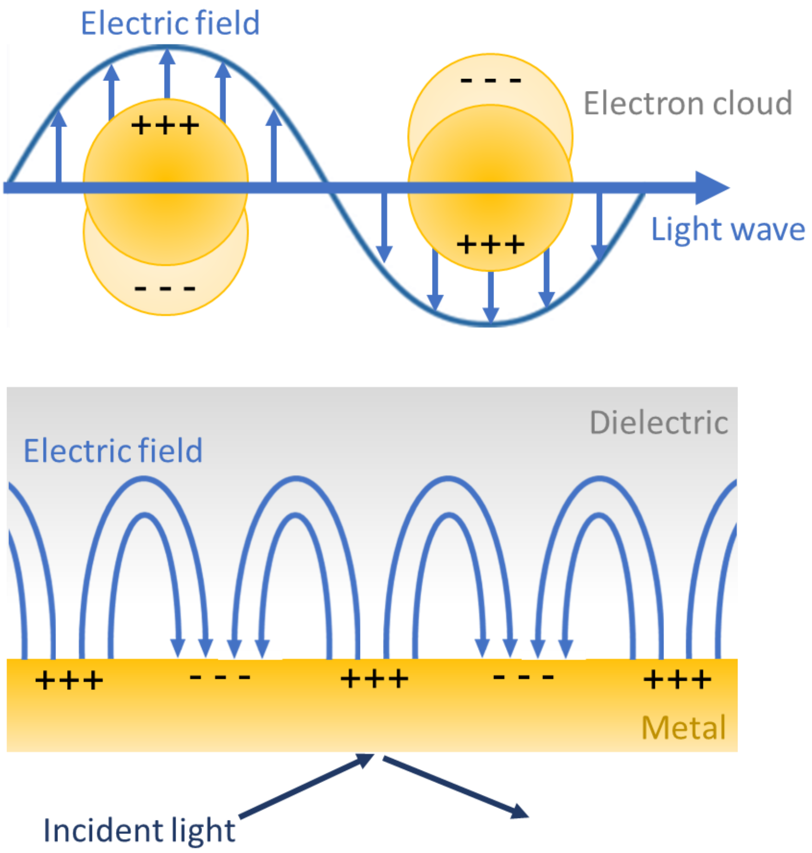

Figure 1.4: Schematic diagram of LSPs in metal nanoparticles (top) and PSPs along a metal-dielectric interface under TIR conditions (bottom).

Metal surfaces are able to efficiently enhance signals in Raman spectroscopy, in a technique known as surface enhanced Raman spectroscopy (SERS). There are two known mechanisms by which this enhancement occurs: electromagnetic enhancement, and charge transfer.[16] Since the Raman effect depends on the induced dipole of the molecule μ, which relates to the electric field E and polarizability of the molecule α (equation 1.1), these mechanisms are concerned with the effect of the metal surface on α and E, respectively.

$$\mu = \alpha E \qquad \textit{(eq. 1.1)}$$

The electromagnetic enhancement theory focuses on the effect of the metal on E, and can be understood by considering LSPs.[17,18] Incident light induces LSPs, which have an associated electric field as shown in Figure 1.3. This LSP field couples with the electric field of the incident light E_0, creating a greater, localised field at the metal surface E_{Loc}. Molecules at the metal surface which experience this increased electric field have a greater induced dipole, hence more intense Raman scattering. The local field intensity enhancement factor (LFIEF) is defined in equation 1.2.

$$LFIEF = \frac{|E_{Loc}|^2}{|E_0|^2} \qquad \textit{(eq.1.2)}$$

In addition, the LSP field couples with the electric field of the Raman scattered radiation E_R, further increasing intensity, since the intensity of light is proportional to the square of its electric field.[16–18] This relationship is shown in equation 1.3 where I is intensity, ε_0 is the permittivity of free space, c is the speed of light and E is electric field strength. The radiation enhancement factor is defined in equation 1.4.[19]

$$I = \frac{c\varepsilon_0 E^2}{2} \qquad \textit{(eq. 1.3)}$$

$$REF = \frac{|E_R|^2}{|E_0|^2} \qquad \textit{(eq. 1.4)}$$

The overall SERS enhancement factor EF is often defined as being the product of these two enhancement factors (equation 1.5).[17] However, it is often assumed that $LFIEF \approx REF$, simplifying the expression (equation 1.6). For this reason, SERS is said to enhance Raman signals by an approximate factor of E^4.

$$EF = \frac{|E_{Loc}|^2}{|E_0|^2}\frac{|E_R|^2}{|E_0|^2} \qquad \textit{(eq. 1.5)}$$

$$EF = \frac{|E_{Loc}|^4}{|E_0|^4} \qquad \textit{(eq. 1.6)}$$

SERS is often only observed experimentally when a metal surface has nanoscale features or ‘nanoscale roughness’.[12] When confined by crevices, such as the meeting point of two particles, LSPs can interact to form areas of highly localised, intense electromagnetic fields. These points areas are known as ‘hotspots’;[20] where E_{loc} and hence the overall SERS enhancement can be particularly large.

The charge transfer mechanism considers the effect of the metal on α, the polarizability of the molecule.[16–18] This mechanism only applies when a molecule is chemically bonded to the surface, and is not observed in physisorbed molecules. The simplest explanation of this mechanism is that the bound molecule forms a charge transfer complex with the metal, which has greater polarizability than the unbound molecule, and hence exhibits more intense Raman scattering. The charge transfer enhancement is thought to have a relatively small contribution to overall signal enhancement, and only ever occurs alongside the electromagnetic mechanism. The EM mechanism on the other hand can occur independently and is thought to give the largest contribution to the SERS effect.

1.3 Related SERS techniques

The SERS effect can be enhanced further when using appropriate substrates and techniques. A common example is the Surface enhanced resonance Raman effect, in which the excitation wavelength is matched with the absorption profile of the Raman reporter to yield greater signal enhancement. By using specially selected substrates, SERS is capable of detecting single molecules, and reproducible enough to allow accurate quantitative analysis. These methods are discussed in the following sections.

1.3.1 Surface Enhanced Resonance Raman

Surface enhanced resonance Raman (SERRS) was first reported by Stacy *et al.* in 1983 when recording the Raman spectrum of tris(bipyridine)ruthenium(II) chloride on a roughened silver electrode. It remains a popular technique due to the significantly improved enhancement factors produced.[21] For example, the SERRS enhancement factor of rhodamine 6G is approximately between 10^7 and 10^8 times greater than the SERS enhancement factor of pyridine.[16] Examples of Raman reporter molecules selected to utilise the SERRS effect are given in Section 1.5.1.

SERRS is a technique in which the excitation wavelength used in the Raman experiment is closely matched to an electronic excitation of a molecule being examined, resulting in enhanced Raman signals.[11,16,22,23] Exciting a molecule to a higher electronic state can result in some structural changes; if these changes result in increased polarizability, then Raman scattering will logically increase also. This enhancement can be explained by the Kramer Heisenberg Dirac (KHD) equation for polarizability (equation 1.7). Due to the size of this equation, terms are summarised in Table 1.1, for clarity.

$$\left(\alpha_{\rho\sigma}\right)_{GF} = \sum_{I}\left(\frac{\langle F|r_\rho|I\rangle\langle I|r_\sigma|G\rangle}{\omega_{GI}-\omega_L-i\Gamma_I}+\frac{\langle I|r_\rho|G\rangle\langle F|r_\sigma|I\rangle}{\omega_{IF}+\omega_L-i\Gamma_I}\right) \qquad \textit{(eq. 1.7)}$$

Term	Definition
α	Molecular polarizability
ρ	Incident polarisation direction
σ	Scattered polarisation direction
Σ	Sum over all molecular vibronic states
G	Ground vibronic state
I	Vibronic state of the excited state
F	Final ground vibronic state
L	Exciting light
Γ	Lifetime
ω	Frequency
r	Dipole operator

Table 1.1: Terms associated with the KHD equation

The numerator describes the mixing of the excited and ground states I, G and F, representing the ‘virtual’ state (Figure 1.2). The resonance Raman effect can be best understood by considering the denominator. Resonance Raman conditions are met when the energy difference between the ground and excited states is equal to the energy of the exciting light, i.e. when $\omega_{GI} = \omega_L$; this reduces the denominator of the first term to $i\Gamma_I$. Because frequencies are added in the second term, this denominator is large, hence the second term does not contribute significantly and can be ignored. The excited state involved in Raman scattering is virtual, and therefore unstable and extremely short lived, hence $i\Gamma_l$ is small. Therefore, because the denominator of the first term is small, polarizability overall is large, giving increased Raman scattering.[11]

1.3.2 Single molecule detection

Perhaps the greatest appeal of SERS is the ability to detect small concentrations of analyte down to a single molecule, making it an attractive technique for fields such as medical diagnostics.[24] Single molecule (SM) SERS was first observed in 1997 by Kneipp *et al.* and Nie *et al.*, who recorded SM SERS spectra of commercially available dyes crystal violet and rhodamine 6G (Figure 1.5).[4,25] Silver nanoparticles were used as SERS substrates, with aggregation of the particles creating hotspots required for intense SERS enhancement. The experimental set-up involved the preparation of low-concentration solutions, such that the area sampled by the Raman microscope contained approximately one dye molecule.

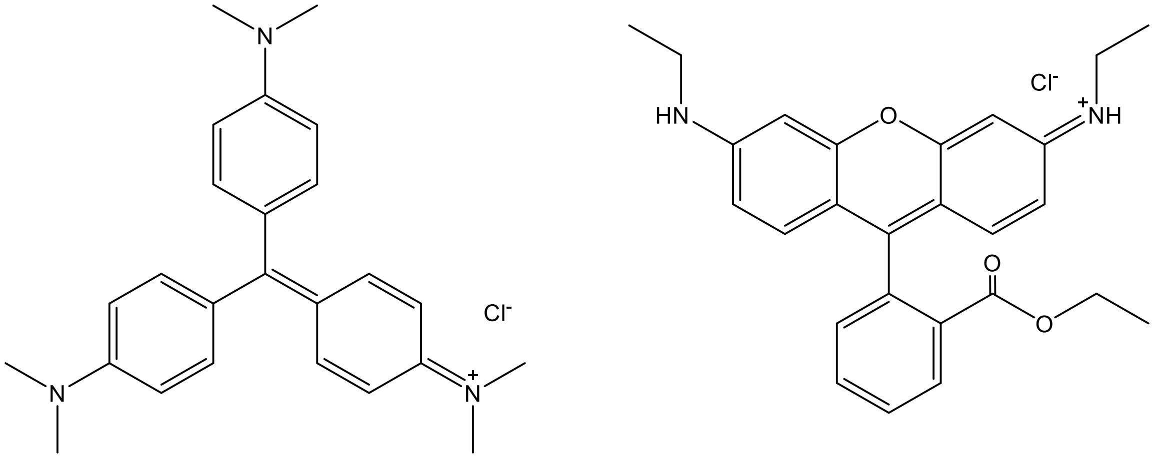

Figure 1.5: Structures of crystal violet (left) and rhodamine 6G (right).

SM SERS has proved to be an attractive technique for the study of catalytic activity, as the metal surface can act as both a SERS substrate and catalyst.[26] For instance, SM SERS has been used to investigate the plasmon catalysed dimerization of p-nitrothiophenol (Figure 1.6) to form 4,4'-dimercaptoazobenzene.[27] Zhang *et al.* controlled the amount of p-nitrothiophenol (*p*NTP) on the substrate down to the single molecule level to determine the effects of concentration on the reaction, and to determine if a reaction of the lone *p*NMP molecule would occur in the presence of the plasmonic metal surface, without other *p*NMT molecules to facilitate dimerization. Results showed that when isolated on a gold surface, the single *p*NMT molecule will undergo plasmon catalysed dissociation of the nitro group to form thiophenol, a reaction which could not have been identified or observed without SM SERS.

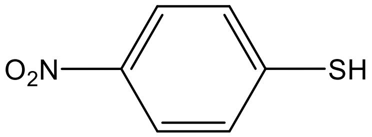

Figure 6: Structure of p-nitrothiophenol

SM SERS has also proven useful for monitoring electrochemical reactions of single molecules at electrode surfaces.[28] The first instance of this was in 2010, when the oxidation of Nile blue (Figure 1.7) adsorbed on a silver electrode was observed at the single-molecule level, using silver nanoparticles deposited on the electrode surface as a SERS substrate.[29] As the field of molecular electronics expands, SM SERS has become valuable for studying the electrochemical properties of single molecules.

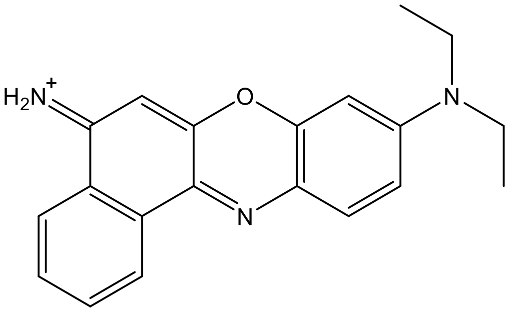

Figure 1.7: Structure of Nile blue.

Although SM SERS opens up new possibilities for SERS, there is a major flaw in the technique; uncertainty over the number of molecules bound to the substrate makes it difficult to determine whether the SERS spectrum truly shows single molecules, or several.[30] In addition, the aggregation of the substrate can produce non-homogenous aggregate clusters, lowering reproducibility. In recent years, progress has been made to improve these uncertainties; for example, the use of Langmuir-Blodgett films to control the amount of analyte bound to the SERS substrate.[24] Another technique which provides single-molecule SERS with greater accuracy is tip enhanced Raman spectroscopy (TERS). TERS is a technique combining Raman spectroscopy with scanning probe microscopy (SPM) techniques, such as atomic force microscopy.[26] In this method, the tip of the cantilever used for the SPM experiment doubles as a SERS substrate, as shown in Figure 1.8. This usually involves either coating the tip with silver or gold, or modifying the tip with a nanoparticle.[31] Because the only SERS substrate present is the single tip, and the molecules in the immediate vicinity of the tip can be identified using SPM, it is possible to confirm whether Raman spectra arise from a single molecule or several molecules.[32] This technique was first observed by Stöckle *et al.* to acquire SM TERS spectra of the dye brilliant cresyl blue.[33]

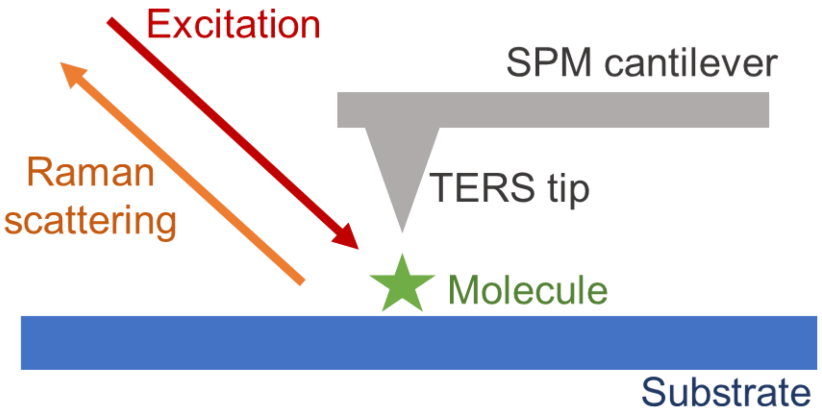

Figure 1.8: Typical TERS experimental setup.

Like standard SM SERS, SM TERS has also proven useful in monitoring electrochemical reactions.[26] In addition, TERS method has been successfully deployed to analyse the structures of biological samples, such biomembranes and DNA.[34,35] One notable example is the use of TERS to examine protein fibrils.[36] Amyloid fibrils are protein aggregates associated with neurological conditions such as Alzheimer's disease and Parkinson's disease. Fibrils such as these can be formed by insulin; these insulin fibrils are observed in conditions such as type II diabetes. Despite their important role in various diseases, the exact surface structure of these fibrils was until recently unknown. Using TERS, Kurouski *et al.* were able to determine that the outer surfaces of insulin fibrils are comprised mainly of α-helices and unordered protein structures, contrary to the previous belief that the surface was predominantly made up of β-sheets; a significant breakthrough for research into neurodegenerative and insulin-pertaining diseases.

1.3.3 Quantitative SERS analysis

Research has been moving towards using SERS as a quantitative method. Although SERS is a highly sensitive technique capable of detecting single molecules, quantitative analysis of samples remains challenging. This is mainly because SERS is inherently a localised technique, enhancing Raman scattering of molecules in close vicinity to hotspots; it is therefore difficult to analyse and quantify the sample as a whole. [37] Another issue is the uniformity of the SERS substrate, as signal enhancement can vary greatly if the substrate is not homogenous.[38] In some cases, these problems can be circumvented with use of an internal standard. Known quantities of the standard, usually a molecule or nanostructure such as a carbon nanotube, are embedded in the substrate, and SERS signals of these standards are used to normalise signals from the analyte.[38,39]

Another way to create uniformity is to create a SERS film with a homogenous structure across the entire surface area of the substrate.[40] On such example is the use of gold nanoparticle coated polystyrene beads, immobilised on quartz. These substrates, fabricated by Péron *et al.*, are capable of quantitatively detecting polycyclic aromatic hydrocarbons at concentrations as low as 1 ppm. However, the uncertainty of this detection system was shown to be around 30 %, highlighting the major drawback of SERS as a quantitative technique: reproducibility. This poor reproducibility was likely caused by the irregular clusters of gold nanoparticles which formed on the surface of the polystyrene beads. Therefore, in order to obtain good, reproducible quantitative SERS results, work must be done to fabricate more uniform substrates.

Some promising quantitative SERS results have been obtained using similar, more uniform substrates. [41] The gold 'film over nanoparticle' substrates fabricated by Peksa *et al.*, consist of a monolayer of polystyrene nanoparticles deposited on a silicon substrate and sputter coated with a 20 nm layer of gold. This substate was used to quantitatively measure amounts of the potentially harmful food colourant azorubine in soft drinks. By this method, amounts of azorubine as low as 0.5 mg dm^{-3} were detectable with good reproducibility within minutes, requiring no modification of the surface or treatment of the samples. This exemplifies of the rapid quantitative analysis SERS is capable of when an appropriate substrate is implemented.

1.4 Intrinsic SERS Probes

Non-selective SERS probes, known as intrinsic probes (Figure 1.9), are the simplest form of SERS substrate.[42] The design of an intrinsic probe can be broken into three main components: metal, shape, and size. A summary of these three components is given in the following sections.

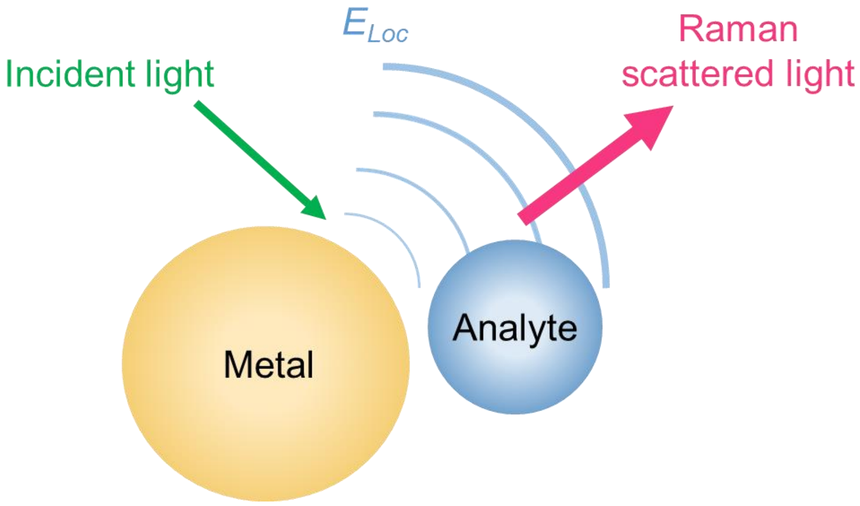

Figure 1.9: An intrinsic SERS probe.

1.4.1 Metal

Metals which support surface plasmons are alkali metals (Li, Na, K) and noble metals (Cu, Ag and Au).[43] The surface plasmon wave is a phenomenon involving delocalised electrons of the metal surface,[44] therefore, the ability of these metals to support SPs arises from their valence electron configurations.[45] The alkali and noble metals each have an unpaired s electron, which is easily delocalised.[44] These free electrons within the metal structure can, under the correct conditions, form plasmon waves, as described previously (Section 1.2).

Of the noble or 'coinage' metals, silver displays the greatest enhancement factors, followed by gold, with copper giving the lowest SERS enhancement. [46] The differing enhancement effects of these metals can be explained by considering equation 1.8, which describes the polarizability of a metal sphere with radius R, where ω_p is the plasmon resonance frequency, $\varepsilon_b(\omega)$ is the wavelength-dependent inter-band transition contribution to the dielectric function, and γ is the electron scattering rate.

$$\alpha = \frac{R^3(\varepsilon_b\omega^2 - \omega_p^2) + i\omega\gamma\varepsilon_b}{[(\varepsilon_b + 3)\omega^2 - \omega_p^2] + i\omega\gamma(\varepsilon_b + 3)} \qquad (eq.1.\ 8)$$

Large polarizability and hence strong SERS enhancement occurs in metals where $\varepsilon_b(\omega)$ and γ are small, at the desired excitation wavelength (ω). This occurs in silver, gold, copper and lithium. Silver has the largest $\varepsilon_b(\omega)$ over most excitation wavelengths, resulting in a large SERS contribution, while $\varepsilon_b(\omega)$ for copper is relatively small over the same range, giving it weaker SERS enhancement.[47] At around 600 nm, the SERS enhancement of gold is comparable to silver, as is lithium.

Alkali metals are considered by most to be less suitable for SERS applications, due to their high reactivity in air.[48] Coinage metals on the other hand are stable, give good SERS enhancement, and can be easily functionalised; thiols have a high affinity for gold, silver and copper surfaces, forming self-assembled monolayers which can be used to alter the properties of the surface to suit its purpose.[49,50]

Silver substrates have been shown experimentally to give greater SERS enhancement than gold; for example, when recording the SERS spectra of crystal violet and adenine, Kneipp *et al.* report enhancement factors approximately 100 times greater using silver nanoparticles than those obtained using gold nanoparticles.[51] Due to the toxicity of silver nanoparticles, gold SERS nanoparticles are considered more useful for biological sensing applications.[52] Gold substrates are also chemically inert,[53] allowing their use in a range of systems without affecting the signal by chemically interacting with the analyte, although the mode of binding of the analyte to the gold surface may affect the signal enhancement. Gold nanoparticles are also more stable, as they are less readily oxidised.[8] Copper substrates are generally less popular due to their poor enhancement factors compared to silver and gold.[54] They are also less stable than gold nanoparticles due to oxidation.[50]

1.4.2 Shape

A library of metal nanostructures have been developed over the years with a variety of shapes, sizes and metals for use in surface enhanced Raman spectroscopy.[8] SERS was first observed on roughened silver electrodes.[14] It was initially thought that the roughness caused increased Raman signal due to a higher surface area and therefore increased analyte concentration. However, it was later discovered that the surface roughness provided the nanoscale surface features required for surface plasmon waves to occur.[55] Following the discovery of SERS on silver electrodes, the SERS spectrum of pyridine on a silver island film was recorded by Chen *et al.*, which became a prevalent SERS substrate.[56] A silver island film consists of a layer of silver several nanometres thick, characterised by a network of nanoscale channels running through the silver, giving the appearance of islands, shown schematically in Figure 1.10. These gaps between silver islands allow hotspot formation.

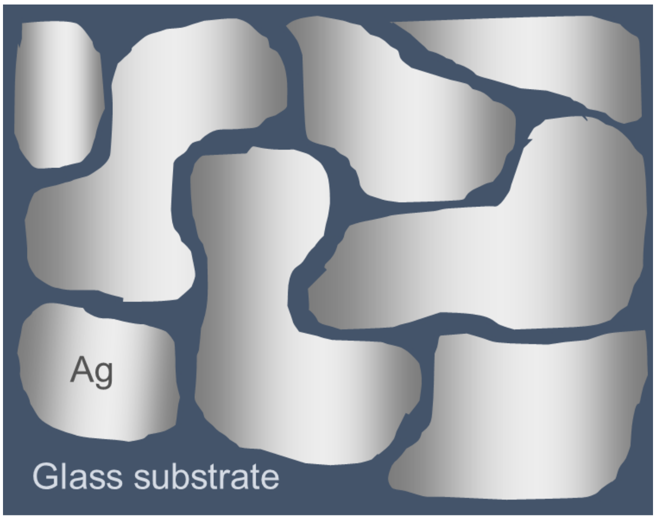

Figure 1.10: Schematic diagram of a silver island film

Presently, metal nanospheres are the most common SERS substrate due to their ease of synthesis and tunability, allowing the researcher to tailor the size of the particle to their needs (Section 1.4.3). It has been suggested that in a spherical particle, the parallel component of the plasmon wave is essentially delocalised in all directions, resulting in a more concentrated electric field.[16,57,58] However, monodisperse spherical nanoparticles do not generally produce significant SERS signal without adding an aggregating agent.[8] On aggregation, hot spots are created at the points where the particles touch in the aggregate clusters.

Hollow-shell nanoparticles are another popular shape for SERS applications.[59,60] Based on the core-shell nanoparticles first synthesised by Oldenburg *et al.* in 1998, which consisted of a gold coating or 'shell' on the surface of a silica nanoparticle, these hollow structures are fabricated by coating a template with metal, and subsequently removing the template.[59] The first hollow shells were constructed in 2005 by Liang *et al.*, using cobalt nanoparticles as a template.[61] On addition of chloroauric acid to the cobalt nanoparticle solution, Au (III) is reduced to Au (0), forming a gold coating on the cobalt nanoparticles. Simultaneously, the Co (0) of the nanoparticles is oxidised to Co (II). The result is a hollow gold sphere.[32] In more recent years, hollow shells have been synthesised from gold-on-silica core-shell particles, where the silica core is removed by chemical etching.[63,64] These methods have been elaborated to produce more exotic shapes, such as multiple-shell nanoparticles or 'nano-matryoshkas', hollow nanocubes, and nanorattles (Figure 1.11).[65–67] Hollow shells of particular interest due to their tunability.

The SPR resonance of a hollow shell is dependent on its inner diameter and shell thickness; both these factors are highly controllable, by synthesising a template of desired diameter, and by controlling the amount of coating material added in the shell formation step.[63] Hollow-shell nanoparticles also give better SERS enhancement than solid nanoparticles, which is thought to be due to coupling of the plasmon fields of the two gold surfaces: the inner surface, and the outer surface.[68]

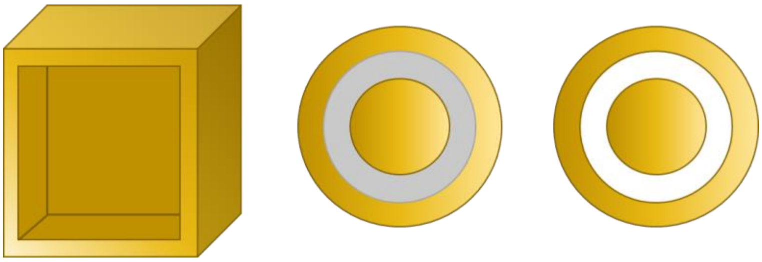

Figure 1.11: Depiction of a hollow gold nanocube, a multiple-shell gold-silica-gold nanoparticle, and a gold nanorattle.

Another common shape used for SERS applications are rod-type particles (Figure 1.12), synthesised from spherical particles by the seed growth technique.[69] The increased signal enhancement often observed for these particles, as opposed to spherical particles, is attributed to a 'lightning rod effect'. This effect is observed in nanorods and other structures with atomic scale protrusions such as an edge or point on the surface. Indeed, it can be observed in any shape with vertices, such as nanotriangles and nanocubes. The curvature of these features produces a change in electric potential, therefore giving a large electrical field in the proximity of the protrusion.[70]

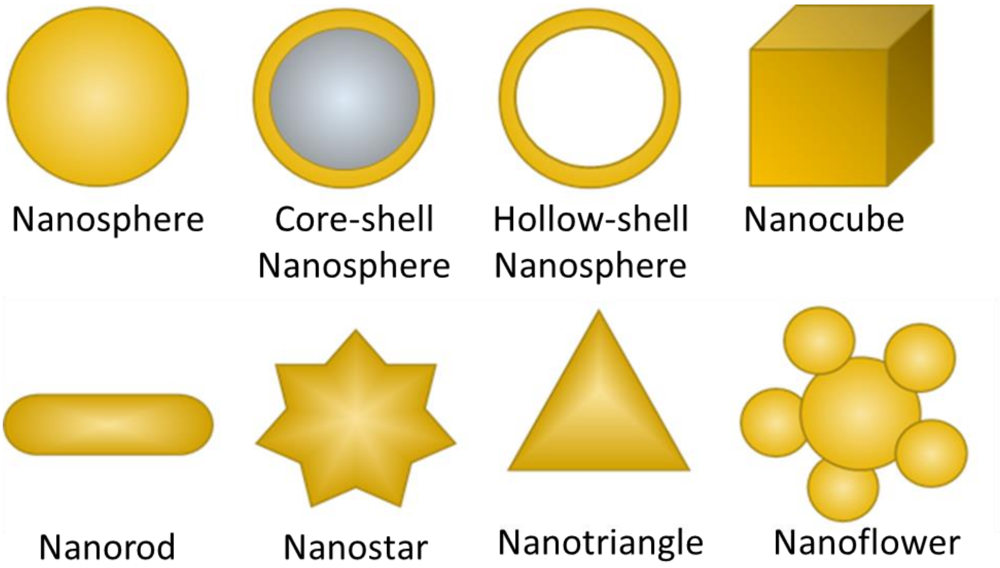

Figure 1.12: Summary of some common metal nanoshapes for SERS applications.[8]

Nanorods have the additional benefit of having two plasmon resonance bands corresponding to the short and long axes. The latter resonance is tuneable in the range of 800-1200 nm. This region is often used in SERS experiments on biological material, as there is little fluorescence, or absorbance from water and chromophores, allowing for deep light penetration into tissue and low background noise (Figure 1.13). Tuning the plasmon resonance of the SERS substrate to match the incident laser wavelength can enhance the SERS signal by utilising the surface enhanced resonant Raman spectroscopy (SERRS) effect (Section 1.3). [69,71,72] Nanorods are therefore ideal for biological SERS applications due to their tunability for absorption in the infra-red region.

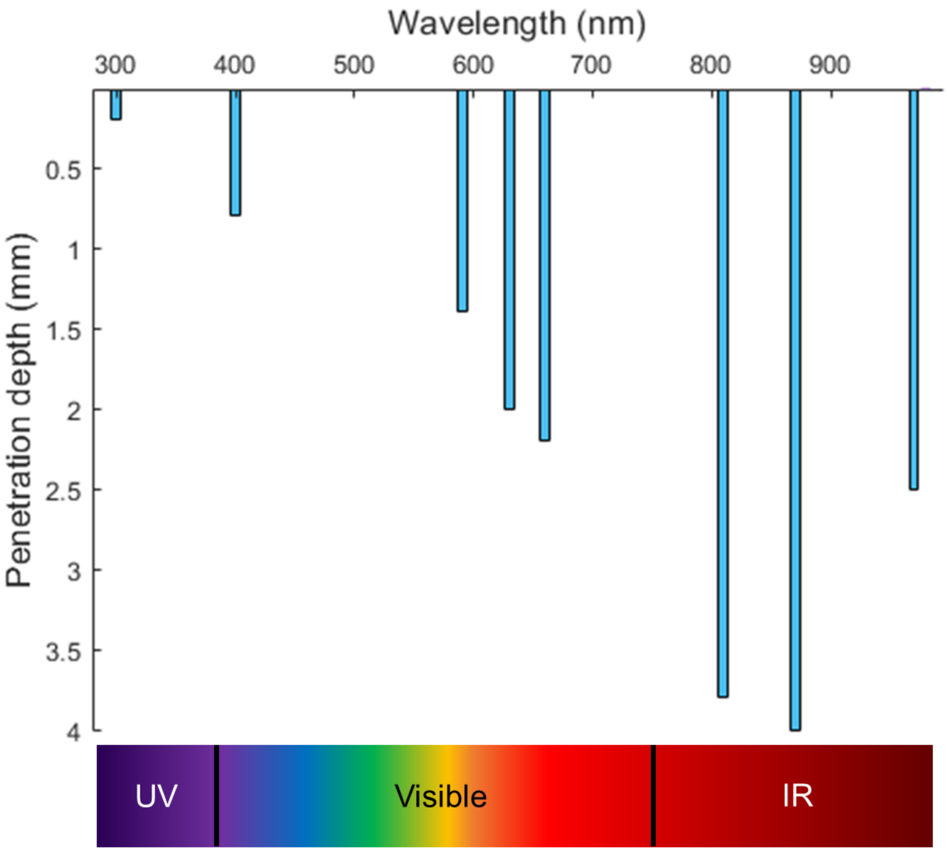

Figure 1.13: Approximate penetration depth of light into skin (data from Barolet et al.).[73]

Nanostars (Figure 1.12) are becoming increasingly prevalent, due to the many points on the structure giving a large lightening rod factor, which is tuneable by controlling the number of points of the nanostar.[74] As a general rule, nanoshapes containing more points have a much larger signal enhancing factor; for example, Tian *et al.* have shown that gold nanostars give better signal enhancement than nanotriangles, which themselves give slightly better enhancement than nanospheres.[71] However, research by Yuan *et al*. suggests that there may be an optimal number of points, after which signal enhancement begins to decrease due to interference between many hotspots.[75] Like nanorods, gold nanostars are also synthesised by the seed growth technique, as are many other nanostructures such as prisms and dodecahedra. This is a simple technique in which gold nanospheres, synthesised by citrate reduction, can be built upon with the aid of a shaping agent. This type of synthesis is shown in Chapter 2.

In addition to these more common shapes, a large array of colloids with more intricate geometry can be found in literature. For example, vapour phase deposition can also be used for complex shapes such as nanopyraminds and nanocresents, although this is less trivial synthesis.[8]

1.4.3 Size

The size of the nanoparticle can have a drastic effect on the Raman signal enhancement.[45] It is understood that larger particles give a greater SERS effect, due to the increased amount of delocalised electrons available which, when excited, produce a stronger electromagnetic field. Tian *et al.* found that silica coated nanoparticles with a 120 nm gold core enhanced Raman signals 24 times more than those with a core diameter of 55 nm.[76] This is also possibly due to the plasmon resonance of the 120 nm particles more closely matching the excitation wavelength of 633 nm.[71] However, particles with a diameter significantly larger than the excitation wavelength often show poor signal enhancement. At this size, higher order non radiative modes (multipolar plasmons) are excited more preferentially than dipolar plasmons, decreasing Raman signal enhancement.[47,77,78] The diameter of the nanoparticle also impacts its uptake into the cell; although this is dependent on many other factors such as surface coatings, Chithrani *et al*. have found that of gold nanoparticles up to 100 nm in diameter, 50 nm particles have the highest uptake efficiency into mammalian cells, so for biological applications it could be argued that nanoparticles around this size are the most useful.[79] Gold nanoparticles above 5 nm are generally regarded as having the same chemical properties as bulk gold, and are therefore considered safe for use in biological systems, provided the stabilising agent is not harmful.[80]

1.5 Extrinsic probes

A common technique for the detection of biological materials is the use of extrinsic probes (Figure 1.14).[81] Unlike intrinsic probes, which rely on the Raman scattering of the analyte itself, this technique involves the use of a Raman reporter molecule; a molecule with a large Raman cross section immobilised on the metal surface. This layer is often coated with a dielectric layer such as a polymer to trap the reporter in place, followed by a final outer coating of selective capture molecules to bind the analyte, such as antibodies in the case of biological systems. The principle of extrinsic Raman is that when the probe is bound to the analyte, the Raman spectrum of the reporter is visible. Extrinsic SERS is not only highly selective, but allows the detection of biological systems which would otherwise have many interferents and give complex, difficult to interpret spectra.

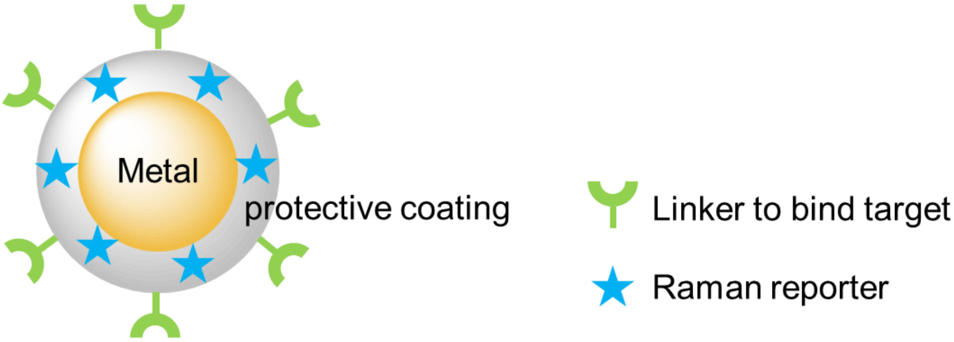

Figure 1.14: Structure of an extrinsic SERS probe.

1.5.1 Raman Reporters

In order to immobilise the reporter on the substrate surface, the chosen molecule will often have an anchoring group; a functional group with a strong affinity for the metal surface.[82] Figure 1.15 shows a number of common anchoring groups used to bind molecules to gold surfaces; these groups may also be used for silver substrates due to the similar surface chemistry of the two metals.[83]

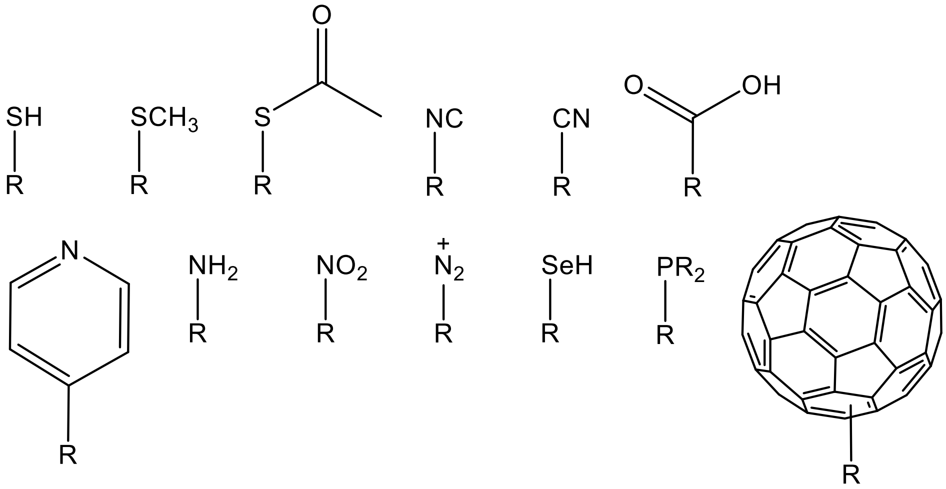

Figure 1.15: Common anchoring groups for gold surface chemistry. [84]

Arguably the most popular anchoring group for use with gold substrates is the thiol group. Thiols spontaneously form self-assembled monolayers (SAMs) in the presence of gold (0).[84] These ordered monolayers form via the generation of an RS• (thiyl) radical. In the case of other sulphur containing anchoring groups such as thioacetate, the mechanism is similar (the acetate group is spontaneously cleaved in the presence of gold to yield the thiyl radical) although this occurs more slowly than in thiols.[85] The strong affinity of the thiol group for gold can be rationalised by hard and soft acid and base (HSAB) theory; bulk metals are considered soft acids, and are therefore likely to form strong bonds with soft bases such as thiolates.[86] The tendency of thiols to form such strong S-Au bonds spontaneously makes them the standard for gold surface chemistry, and this group is found in many simple Raman reporter molecules.

Amines are less common anchoring groups due to their poorer aurophilicity, though these compounds are still known to form self-assembled monolayers on gold surfaces.[87] The N-Au interaction can be characterised as a weak covalent bond.[88] Carboxylic acids are also know to form self-assembled monolayers on gold; unlike amines and thiols, these bidentate anchoring groups adsorb to the surface via both oxygen atoms when the acid is deprotonated.[84] In some cases carboxylic acids have been shown to exhibit better ordering on the substrate surface than thiols, although their binding strength is weaker.[89]

The anchoring group can also be removed during the monolayer formation process to yield a direct Au-C bond.[84] This is the case for diazonium salts, which are typically bound to the metal surface by electrochemical grafting.[90] In this technique, the diazonium group is electrochemically reduced to an aryl radical, which then reacts with the gold surface to form an Au-C covalent bond. Although this is a less facile method than the SAM formation of thiols, it is an attractive option due to the strong bond formation, as Au-C bonds have been shown to be around 0.4 eV stronger than Au-S bonds formed by analogous thiol molecules.

Many SERS systems in the literature utilise simple molecules as reporters, such as 4-aminothiophenol and 4-mercaptobenzoic acid (Figure 1.16).[91–93] These small molecules can be synthesised easily or bought commercially, and the process of binding the thiol to the gold surface is straightforward. However, their Raman signals can be improved upon, and so increasing research has gone towards more complex reporters with specific requirements.

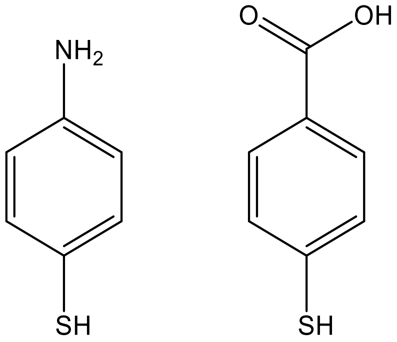

Figure 1.16: Structures of 4-aminothiophenol (left) and 4-mercaptobenzoic acid (right).

It is beneficial to match the absorption of the Raman reporter to the excitation wavelength to utilise the SERRS effect, as discussed in section 1.3. Therefore, commercially available organic dyes with absorption maxima close to the excitation wavelength are commonly used in SERS experiments.[94] Some common organic dyes used as Raman reporters on gold and silver SERS substrates are given in Table 1.2. The dyes can be split into categories defined by their linking mode to the metal surface; electrostatically binding, or covalent bond forming.

Binding mode	**Examples**
Binds electrostatically to metal surface	Crystal violet, rhodamine 6G, rhodamine B, nile blue, methylene blue
Links to surface via S-M interaction	Malachite green isothiocyanate, tetramethylrhodamine-5-isothiocyanate

Table 2: Examples of commercial dye molecules used as Raman reporters (note: these lists are not exhaustive). M= Au, Ag. [94]

Despite their weak binding, crystal violet and rhodamine 6G are widely used as Raman reporters due to their strong SERRS signals alongside common excitation wavelengths 532 nm and 633 nm. [95] Malachite green isothiocyanate has also been used in a range of SERS systems due to its strong bond formation with gold and silver substrates, via the isothiocyanate group.[96,97] These organic dyes are typically used to test novel new SERS substrates, although their high fluorescent backgrounds (with the exception of non-fluorescent methylene blue) in Raman spectra are a distinct disadvantage.[95]

As previously mentioned, red and near-infrared lasers are more popular than visible light for SERS experiments involving biological material, as autofluorescence is eliminated, and greater depth of penetration into tissue can be achieved (Figure 1.13). Therefore, dyes absorbing red and near-infrared light are commonly utilised as SERS reporters. One such dye is Prussian blue, an inorganic dye absorbing light in the region between 600-900 nm when bound to gold nanoparticles.[98,99] Prussian blue gives an intense Raman peak at 2156 cm^{-1}, in the area known as the biological silent region. This is the area above 1800 cm^{-1} (outside of the fingerprint region) where there are generally no vibrational modes in biological samples.[8,42] Focusing on this region avoids interference from the sample, allowing for clearer interpretation.[99] Prussian blue has been used as a Raman reporter in conjunction with gold nanoparticles for the detection of cervical cancer cells (Figure 1.17). The HeLa cervical cancer cell line is known to overexpress folic acid receptors; when Prussian blue coated gold nanoparticles were modified with folic acid, HeLa cells were selectively detected over the liver cancer cell line HepG2.[99]

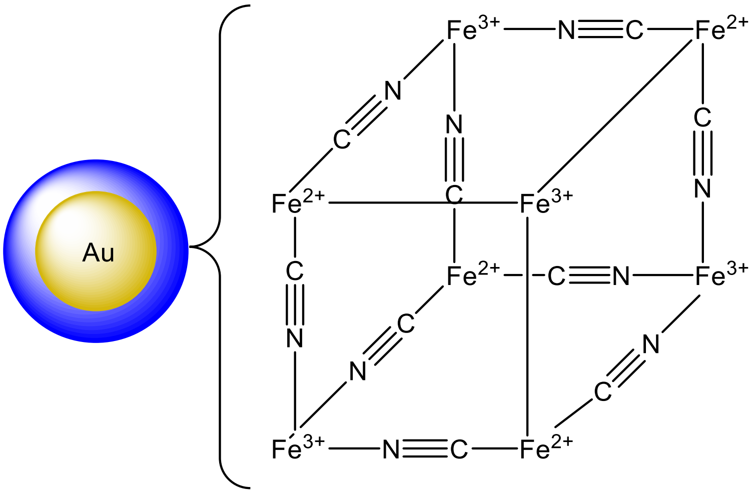

Figure 1.17: Structure of a Prussian blue coated gold nanoparticle.[99]

In addition to commercially available dyes, there is increasing research into the synthesis of novel dyes tailored specifically for SERS experiments. For example, Bedics *et al*. have synthesised chalcogenopyrylium based dyes absorbing in the region of 653-986 nm, making them promising for biological SERS applications.[100,101,102] One such example is shown in Figure 1.18. Furthermore, these dyes have been shown to give SERS signals with an excitation wavelength of 1550 nm, which is retina safe; a SERS system using a retina safe laser has desirable safety benefits. The dyes also possess thiophene groups, an ideal anchoring group for the functionalisation of gold surfaces.

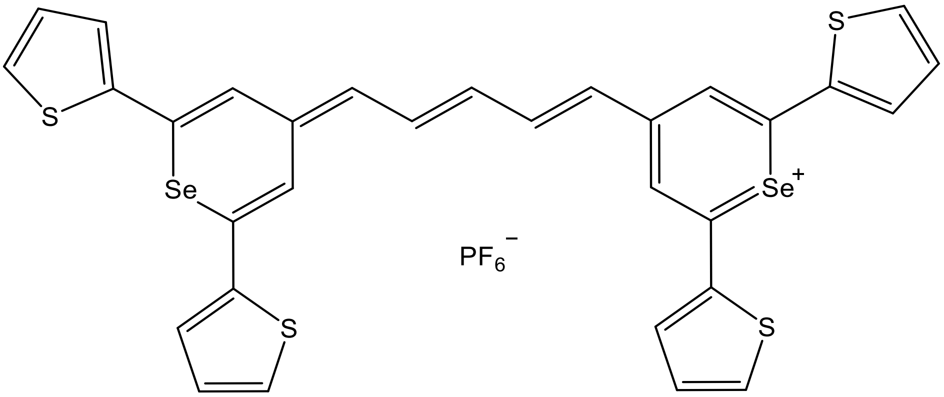

Figure 1.18: Structure of a chalcogenopyrylium dye with an absorbance maximum of 986 nm.[101]

1.5.2 Surface coatings

Nanorods and nanostars are often prepared using surfactants such as cetyl trimethylammonium bromide (CTAB) as a stabilising agent (Figure 1.19), as the strong repulsion between quaternary ammonium groups keeps the nanostructures effectively separated. CTAB can also act as a structure directing agent in the synthesis of these structures; in the case of gold nanorods, CTAB preferentially binds to side facets of the rods, allowing growth at the ends to produce the rod-type shape.[103] Although CTAB is generally regarded as safe when bound to a metal surface, some studies have shown an increase in toxicity of CTAB coated nanoparticles compared to uncoated particles.[104] This may be due to the non-covalent nature of CTAB binding, allowing it to easily dissociate from the surface, as unbound CTAB is damaging to cells.[105] In addition, the quaternary ammonium group can cause unwanted interaction with cells and molecules present in biological media.[106] For this reason, many other coatings have been explored.

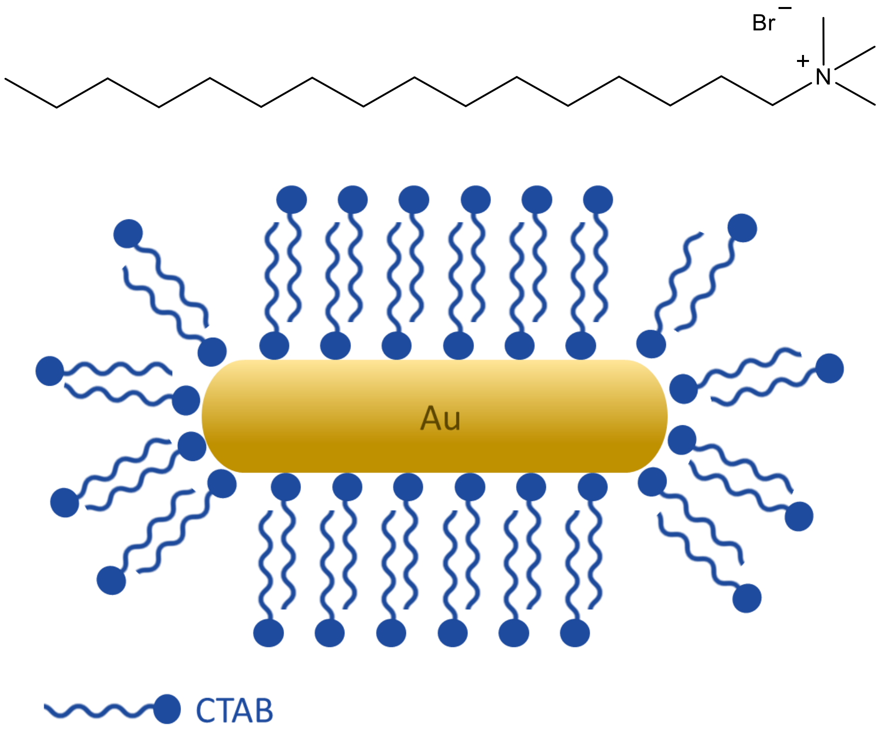

Figure 1.19: Structure of CTAB (top) and diagram of a CTAB stabilised gold nanorod.[103]

Silica coated gold nanoparticles (AuNP@SiO_2) have been utilised effectively in many extrinsic SERS studies.[76] Silica surface coatings have been shown to protect the Raman reporter from reacting with the surrounding environment, and prevent it from dissociating from the particle surface.[107,108] This is especially important if the reporter molecule has no anchoring group and instead binds to the surface via weak electrostatic forces. Another benefit of a silica shell is that it is chemically inert, meaning the particles can be applied to any material without chemically bonding to it, which may alter the Raman fingerprint of the material. The presence of a silica shell also acts as a spacer, reducing SERS hotspots caused by random aggregation of metal nanoparticles, improving the reproducibility of the SERS results.[107] These coatings are easily prepared using the Stöber method; the base catalysed hydrolysis of tetraethyl orthosilicate (TEOS) carried out in water/alcohol mixtures (Figure 1.20). [109–111] Using this method, silica coatings as thin as 0.5 nm have been reported, which is desirable as SERS is a distance-dependent technique; many groups have reported poor SERS signals for coated gold nanoparticles when the shell is thicker than 10 nm.[47,112,113]

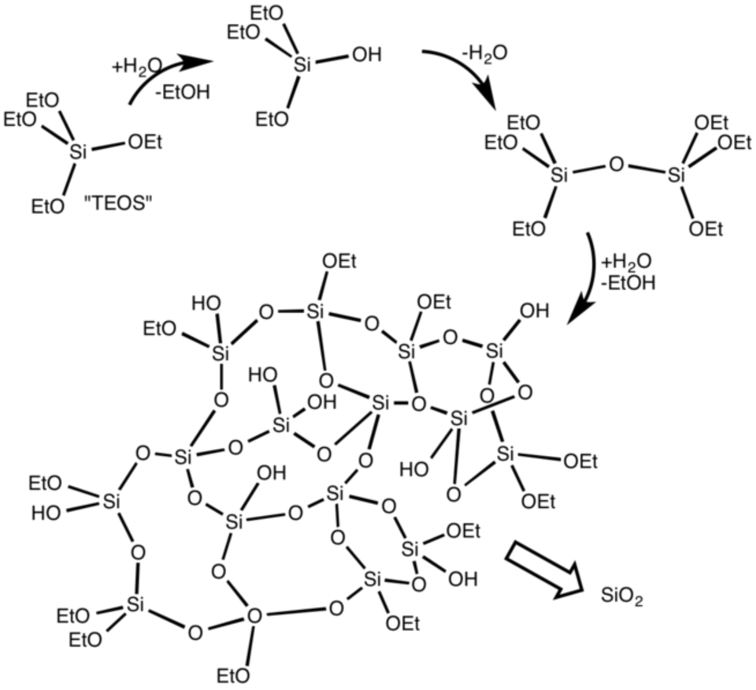

Figure 1.20: Simplified reaction Scheme depicting the Stöber process. [114]

Gold nanoparticles have also been coated with biocompatible materials such as peptides and biopolymers, to aid biocompatibility for SERS studies in biological systems.[115] Polyethylene glycol (PEG) is frequently used as a gold nanoparticle coating, due to its ability to increase the stability of the nanoparticles in biological media. In vitro studies have shown that PEGylated gold nanoparticles have reduced toxicity compared to uncoated nanoparticles, and increased cell uptake.[116] However, in vivo studies have found that PEG coated particles tend to accumulate in the liver significantly more than naked gold nanoparticles, which can cause liver damage.[117]

1.6 SERS probes for medical diagnostics

A previously stated, SERS has been utilised in a number of systems to detect simple molecules such as pesticides,[6] however its use in medical applications such as diagnostics is still in development. The use of SERS as a potential diagnostic technique has drawn interest due to the possibility to detect analytes at very low concentrations, with a strong signal.[118] The following examples have been chosen as they encompass the major types of SERS systems used for the detection of disease biomarkers; solution based SERS, and SERS substrates immobilised on a surface.

1.6.1 Solution state SERS probes for medical diagnostics

Harmsen *et al.* have fabricated surface enhanced resonance Raman spectroscopy (SERRS) substrates for the detection of various forms of cancer in mice. These substrates are unique due to their simple design, consisting of a gold nanostar core, and a Raman reporter trapped on the gold surface by a silica shell. Unlike most extrinsic probes, no component to selectively bind the target (such as a peptide or antibody) is incorporated.[119] Instead, the nanostars utilise the enhanced permeation and retention (EPR) effect. The EPR effect is a phenomenon in which nano-scale structures or macromolecules accumulate in cancerous tissue, but not healthy tissue. This is thought to be caused by the rapid formation of blood vessels in tumours, leading to gaps between endothelial cells, which facilitate the entry of macromolecules into the tumour from the bloodstream, as shown in Figure 1.21.[120] The molecules or nanostructures used to exploit this effect must meet certain requirements, including being above 40 kDa in mass and having a weakly negative surface charge.[121] The gold nanostars synthesised by Harmsen *et al.* do meet these requirements, allowing several forms of cancer including breast and prostate to be detected in mice.

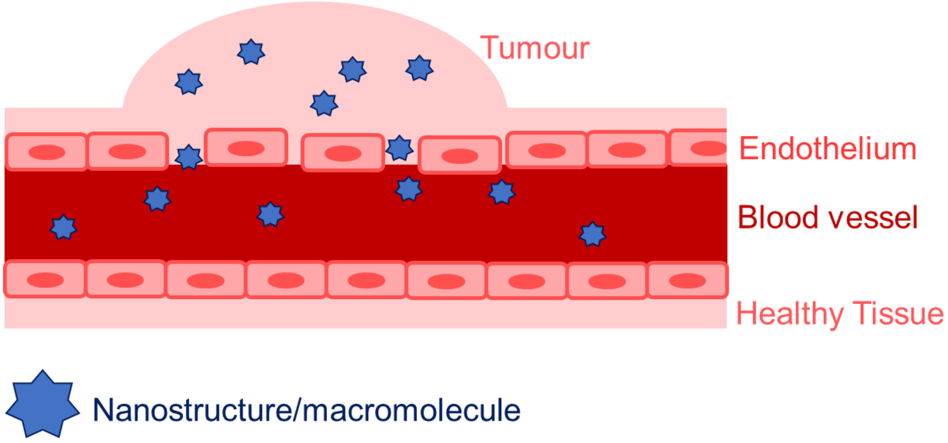

Figure 1.21: Depiction of the EPR effect

Intrinsic SERS probes have been used for the non-invasive detection of cervical cancer using blood plasma.[122] Cervical cancer is currently diagnosed following a cervical screening test, though studies have shown that attendance at cervical screening appointments has dropped amongst young people in recent years, possibly due to the invasive nature of the procedure.[123] The need for a non-invasive diagnostic method is therefore clear. Diagnosis of cervical cancer is also currently subjective and reliant on an experienced clinician.[124] A study by Feng *et al.* used silver colloids to obtain SERS spectra of blood plasma, identifying significant differences in the Raman fingerprints of plasma from cervical cancer patients compared to healthy plasma.[122] Notably, the spectra indicated higher levels of human serum albumin in the α-helix conformation in plasma from cancer patients. This SERS detection system was found to have a sensitivity of 96.7 %, although testing on other types of cancer was not carried out, so whether this system could differentiate cervical cancer from other types of cancer is uncertain.

The early detection of neurodegenerative conditions (such as Alzheimer's disease and Parkinson's disease) are also of interest due to the socioeconomic impact of these diseases.[125] Various examples of SERS systems for the detection of dementia biomarkers can be found in the literature. Zengin *et al.* have fabricated SERS sandwich probes for the detection of tau proteins, which are present in increased numbers in the cerebral spinal fluid of Alzheimer's patients.[126] The SERS substrate used in this system is a classic example of an extrinsic SERS probe, consisting of a gold nanoparticle (AuNP) core, a Raman reporter, and an antibody to bind the tau proteins. The Raman reporter used is 5,5'-dithiobis(2-nitrobenzoic acid) (DTNB), a small-molecule type reporter which binds to the gold surface when the disulfate bridge is cleaved and the subsequent thiolate molecules form a self-assembled monolayer (SAM). What makes this SERS system unique is the addition of iron oxide nanoparticles. These magnetic nanoparticles (MNPs) are also functionalised with antibodies, resulting in an MNP-tau-AuNP sandwich complex. Because of the magnetic properties of the MNPs, this complex can be separated from solution with magnets before SERS analysis, allowing for a clear, easy-to-read spectrum without interferents. This method also claims to be significantly faster and more cost-effective than current tau protein detection methods such as enzyme-linked immunosorbent assays (ELISA).[126]

A similar magnetic SERS 'sandwich probe' (Figure 1.22) has been synthesised by Vohra *et al*. for the diagnosis of squamous cell carcinoma (SCC).[127] Diagnosis of this cancer currently requires a trained clinician, however, SCC disproportionally effects people from low and middle income countries, where resources may be lacking. There is therefore an obvious need for a rapid point-of-contact test, requiring minimal training to operate. The aim of the study was to develop a SERS system to diagnose SCC by targeting cytokeratin 14 (CK 14), a protein expressed in carcinoma cells.[128] The SERS substrate consisted of a gold nanorattle core, functionalised with a DNA sequence acting as both a reporter and linker to bind CK 14. Magnetic nanoparticles were also functionalised with a DNA sequence to target CK 14. These sandwich probes successfully detected CK 14 in 93 % of SCC samples and 0 % of non-SCC samples, indicating good sensitivity and specificity.

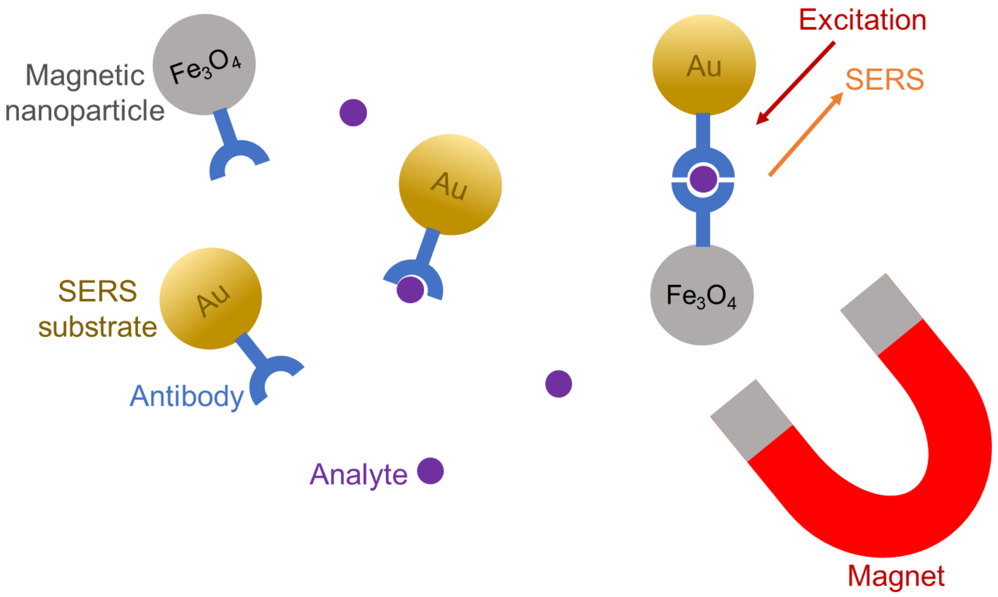

Figure 1.22: Simplified depiction of a typical magnetic SERS sandwich complex system.

1.6.2 Substrate Immobilised SERS probes for medical diagnostics

Because SERS is a technique which can only be applied diagnostically if the area of interest can be reached by a laser, many diagnostic techniques are focused on creating ‘lab on a chip’ systems for blood testing, in which the SERS substrate is immobilized on a surface.[129] For example, Lee *et al.* have used microfluidic chips alongside hollow gold nanoparticles for the detection of liver cancer. [130] In this system, a surface is functionalised with antibodies capable of binding alpha-fetoprotein (AFP), a protein which is present in high levels in hepatocellular carcinoma. Hollow gold nanoparticles (HGNs) are also coated with this antibody. The HGN solution and a sample containing AFP are then injected into the chip, where the AFP becomes immobilised on the antibody-coated surface. The HGNs bind to the immobilised AFP, creating ‘sandwich complexes’ on the surface, which can be detected by SERS, depicted in Figure 1.23. SERS based lateral flow assays such as these have also shown promising results for the detection of many other health conditions, including prostate cancer and HIV.[131,132]

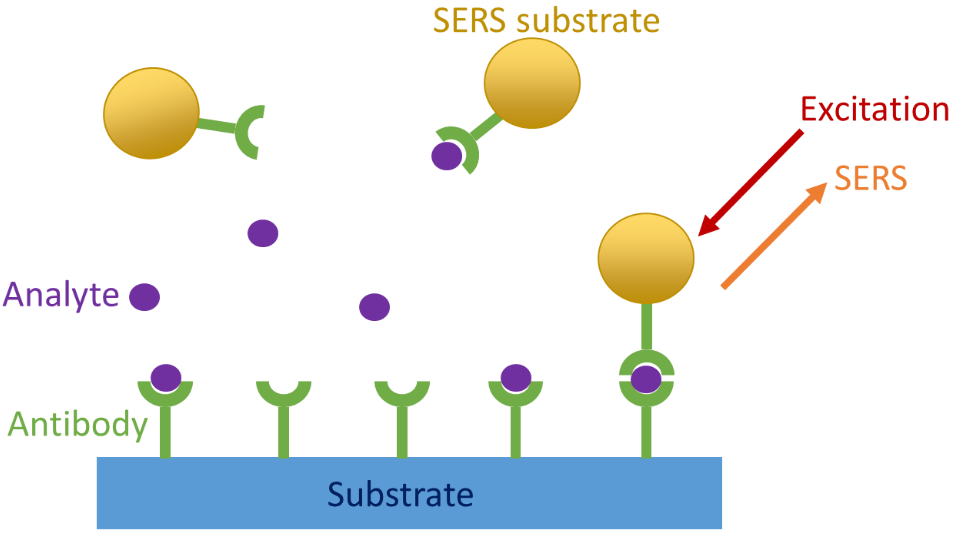

Figure 1.23: Depiction of a typical SERS-based lateral flow experiment.

Pseudomonas aeruginosa is a bacterium which can cause serious infection in people with compromised immune systems, with mortality rates of up to 60 %.[133] It is particularly dangerous to patients suffering chronic lung diseases such as cystic fibrosis, causing increased damage to the lungs. To be successfully treated by antibiotics, it is vital that the infection is caught early; however, the traditional diagnostic method of bacterial culture can take several days, demonstrating the need for a rapid, point-of-care SERS test for the bacterium. Wu *et al.* have used silver nanorods immobilized on glass as SERS substrate for the detection of pyocyanin, a toxin secreted by the bacterium. This is an intrinsic SERS system, as a positive test result relies on the presence of the biomarker pyocyanin's Raman fingerprint, rather than a reporter molecule. Using this method, pyocyanin can be detected at concentrations as low as 2.38 x10^{-8} mol dm^{-3}, which is lower than the average concentration found in sputum samples of cystic fibrosis patients who tested positive for pseudomonas aeruginosa. This SERS method is therefore promising for the rapid detection of pseudomonas aeruginosa in lung disease patients.

A similar intrinsic SERS method was utilised by Premasiri *et al.,* who immobilised gold nanoparticles on a silica substrate for the detection of bacteria in urine samples, with the intention of using this system for the rapid detection of urinary tract infections.[134] This SERS system is capable of detecting bacteria concentrations of 10^5 cfu cm^{-3}, the level required for effective diagnosis, with an accuracy greater than 95 % . Furthermore, by obtaining the Raman fingerprint of the bacteria, it is possible to identify the exact strain, so that the optimal antibiotic treatment can be chosen.

Many SERS systems incorporate closely packed metal nanostructures, as the nano-sized gaps between the structures creates a large quantity of SERS hotspots.[135] However, biomarkers for the detection of diseases are often large molecules such as proteins, which are unable to fit in these nanogaps. Thus, research has been carried out to created 'stretchable' SERS substrates (Figure 1.24), in which the gaps between metal structures can expand and shrink to fit the analyte. Mitomo *et al.* fabricated such a SERS system, in which gold nanoparticles are embedded onto a polyacrylic acid gel.[136] Results show that when the analyte (the protein cytochrome c) is deposited on top of a substrate with closely packed nanostructures, SERS signals are small, as the protein cannot fit within the hotspots. However, when the substrate is expanded and closed around the protein, SERS signals increase tenfold, making this a promising SERS substrate for diagnostic applications.

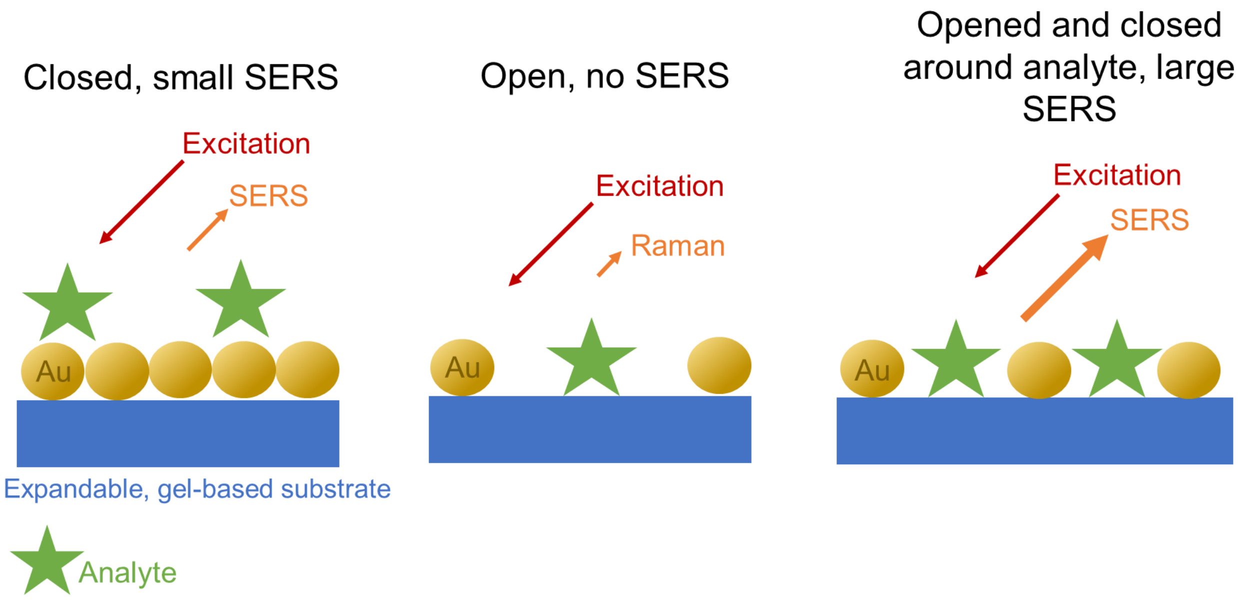

Figure 1.24: A 'stretchable' SERS substrate for large biomolecules.[136]

Despite these studies and many others, the use of SERS for biological applications is still a relatively new field, requiring a great deal of development. For example, studies on the toxicity of gold nanoparticles are few and at times contradictory; adsorption of proteins from biological media onto a nanoparticle surface can affect uptake into cells, hence the exact toxicity of a SERS substrate ultimately depends on its environment. [137] Currently, gold nanoparticles are not approved for human use, and have primarily been used *in vitro* and in live animal studies.[138] Overall, any probe designed for diagnostic use would require significant testing to ensure safety in clinical use and authorisation by the WHO and FDA.[139]

1.7 Melanoma Skin Cancer Diagnostic Methods: Present and Future

Melanoma skin cancer is currently diagnosed in a two-step procedure; examination by a clinician, followed by biopsy.[2,140] First, the skin is evaluated by a medical professional. When done with the unaided eye, the accuracy of melanoma diagnosis is around 60 %.[141] This can be improved using dermatoscopy, otherwise known as epiluminescence microscopy.[142] A dermatoscope is a handheld instrument comprising of a magnifying lens and light source (Figure 1.25). Because skin is highly reflective, basic dermatoscopy requires a liquid interface between the glass lens and the skin; by eliminating the air interface, reflection from the skin is reduced, thus increasing the penetration depth of light into the skin.[143]

Figure 1.25: A dermatoscope.[144]

An alternative technique is polarisation dermatoscopy (Figure 1.26), in which two polarizers with perpendicular axis are placed at the light source and detector, respectively.[145] Because polarized light reflected from the skin maintains its polarization, it is blocked from the detector by the second polarizer. However, polarized light which penetrates the skin is scattered in the dermis and emerges with random polarization, allowing it to pass through the second polarizer into the detector. This can allow the skin to be inspected in greater detail, revealing features beyond the outermost surface which are not otherwise visible. Although dermatoscopy can be an effective diagnostic technique, it is ultimately speculative, and the accuracy of diagnosis drops significantly when carried out by less experienced clinicians. [141,146]

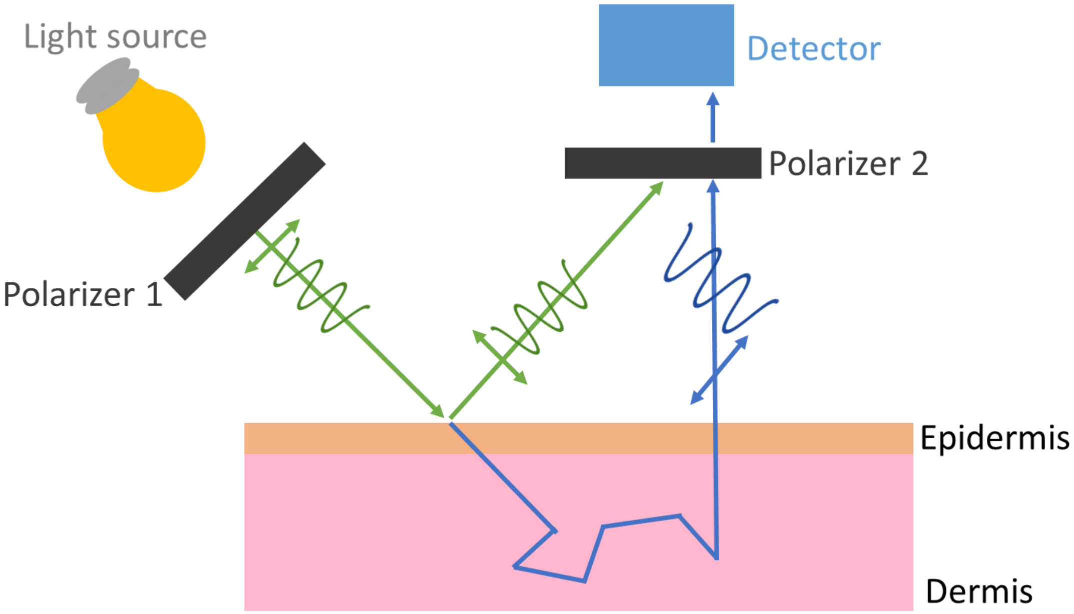

Figure 1.26: Diagram demonstrating how a polarisation dermatoscope uses cross polarisation to eliminate reflected light and view deeper into the skin.

If skin cancer is suspected, a biopsy is conducted, in which a small section of tissue is cut from the skin (excised) under local anaesthetic and preserved with a fixative. A histopathological examination is carried out, wherein the tissue is stained in order to see cellular components more clearly, and examined under a microscope.[147] This allows for a more detailed view of the tissue, but is still ultimately speculative, as well as invasive. In recent years there has been an increasing demand for point-of-care diagnostics, which would avoid the need for preserving and transporting tissue to a specialist facility, making the process more cost-effective.[135]

The efficiency of melanoma diagnosis is currently evaluated by the ‘number needed to excise’ (NNE), which is defined as the total number of legions excised divided by the number of melanomas excised.[148] A ten year study involving clinicians in thirteen countries found that between 1998 and 2007, the NNE value for melanoma diagnosis in non-specialised clinics did not improve at all, and only dropped slightly in specialist clinics, most likely due to the introduction of dermatoscopy.[142] This illustrates the need for an effective diagnostic technique requiring minimal training, making the process of receiving a diagnosis faster and more accessible. Furthermore, a non-invasive method would provide a more positive experience for the patient, as well as saving time and resources for other patients. In the following sections, examples of research into finding such a method are explored.

Melanoma tissue is often slightly darker in colour than that of benign lesions, and so many diagnostic techniques currently in research are based on the visual appearance of the skin.[149] One such technique is reflectance spectroscopy. Because melanoma tissue is darker, it frequently exhibits a lower reflectance value. Several groups have pursued this technique as a means of identifying melanoma, though the reflectance of cancerous tissue is often only very slightly lower than that of benign tissue, making it difficult to distinguish between the two using this method.[150,151] This uncertainty is exacerbated by the fact that many of these studies use small data sets; although a more comprehensive study by Tomatis *et al.* used data from over a thousand patients, other studies in this field have used as few as six human subjects.[152,153]

Another technique based on the visual appearance of the skin is machine learning. Using photographs of skin lesions, attempts have been made to implement machine learning algorithms for the identification of melanoma. However these are often unsuccessful, again due to the visual similarity between cancerous and benign growths, as well as poor contrast between the growth and surrounding skin.[154]

There have been some attempts at detecting biomarkers associated with various types of cancer using mass spectrometry.[155] Using MALDI-TOF-MS, Matharoo-Ball *et. al.* noted increased levels of alpha-1-acid glycoprotein (AAG) in serum samples from patients with stage IV melanoma, compared to healthy patients.[156] The group noted that this research could be expanded to detect melanoma in its earlier stages, however, critics of the method have voiced several disadvantages of using mass spectrometry as a diagnostic technique.[157] The major concerns are poor reproducibility, limited detection sensitivity, and the need for a skilled technician to operate the instrument. It should also be noted that several studies have found higher AAG levels in patients with various other types of cancer, so this is not necessarily an ideal biomarker for melanoma detection.[158,159]

A number of groups have attempted to identify melanoma by utilising fluorescent properties of skin tissue.[160] Although many fluorescence-based detection methods rely on the synthesis of fluorescent probes, visualising these probes would be difficult due to the autofluorescent nature of skin. Therefore, most research in this area is focused on the fluorescent substances already in skin, such as melanin, keratin, collagen, NAD(P)H and so on.[161] For instance, pheomelanin and eumelanin are the melanins responsible for red-yellow and brown-black pigmentation, respectively. It has been reported that the ratio of pheomelanin to eumelanin is higher in dysplastic nevi (atypical moles which although benign, are at high risk of becoming cancerous in future) than in healthy tissue, and higher still in malignant melanoma, resulting in red-shifted fluorescence spectra.[162]

Other studies have focused on the protonated form of nicotinamide adenine dinucleotide (NADH) and flavin adenine dinucleotide (FAD) as cancer biomarkers. Healthy cells primarily produce energy via mitochondrial oxidative phosphorylation, whereas cancerous cells use aerobic glycolysis; this is known as the Warburg effect.[163] NADH is a prominent electron acceptor in oxidative phosphorylation, and FAD is an electron donor. Therefore, the amounts of these molecules present in their bound or unbound states can indicate whether oxidative phosphorylation or glycolysis is the dominant process taking place in the cell, thus revealing whether the cell in cancerous or healthy.[164] Several groups have attempted to use fluorescence lifetimes of these biomarkers to distinguish healthy skin cells from melanoma, with no success.[165,166] However, Pires *et al.* reported noticeably longer fluorescent lifetimes in the melanoma cell line B16F10 as compared to healthy cells, reasoning that FAD in its free form has a longer lifetime than protein-bound FAD, and is present in higher amounts when glycolysis is the dominant process, indicating the presence of cancer cells. These results have not however been repeated in other melanoma cell lines.[161]

Radioactive labelling has also been pursued as a detection technique.[167] The use of melanocyte stimulating hormones labelled with ^{99m}Tc, ^{188}Re and ^{111}In have been reported for the detection of melanoma. Alpha-melanocyte stimulating hormone (α-MSH) is a peptide with a high binding affinity for the melanocortin receptor MC1R, which is overexpressed in melanoma. Radiolabelled derivates of this peptide are able to target MC1Rs in order to detect melanoma using SPECT/CT (the combination of single-photon emission computed tomography and computerised tomography).[167,168] Although these studies in mice have shown better specificity for targeting melanoma than other techniques, the overall process is equally as time consuming and invasive as a traditional biopsy.

Research has shown that melanoma can be detected by canine olfactory, the process in which dogs are trained to detect substances by scent.[169] A study by Pickel *et al.* showed that dogs are able to detect melanoma tissue samples planted on healthy patients. Following this, research continued to patients with suspected melanoma. The suspected lesions were covered with bandages, along with other bandages applied randomly about the patients' bodies. In six out of seven patients, the dogs were able to find the location of the lesion, and biopsies conducted several days later confirmed that these lesions were melanoma. In one of these patients, the melanoma detected by the dogs was not identified in the initial biopsy and required a second biopsy to confirm a diagnosis, indicating that in some cases dogs are able to identify early-stage melanoma before clinicians. Although promising, this study was small, using only two dogs and seven patients, and concerns were raised over whether the dogs actually detected the melanoma by scent, or cues by from patients. Furthermore, the training of dogs for olfactory is a time consuming and costly process requiring skilled animal handlers.

SERS has excellent potential for use in the diagnosis of melanoma due to its high enhancement factors, making it ideal for early stage detection.[170–172] However, the main challenge of using SERS in this area is acquiring spectra for malignant tissue which is distinct from benign tissue. Although some groups, using intrinsic SERS, have identified Raman peaks which are more intense in malignant tissue, the intensity of peaks can vary depending on the distribution of nanoparticles in the sample, and so reproducibility of this may be uncertain.[173–176] Few studies have attempted to create extrinsic SERS probes for the selective targeting of melanoma. One study successfully detected DNA mutations (BRAF V600E, c-Kit L576P and NRAS Q61K) in the plasma of melanoma patients, though these mutations are not present in all melanomas; this system may therefore be more useful for informing the treatment of already diagnosed melanoma patients, rather than for diagnosis.[177] Kumar *et al.* have created a SERS-based microchip for the detection of melanoma chondroitin sulfate proteogly (MCSP), a characteristic membrane protein found in melanoma cells.[178] However, the system has thus far only been tested with ‘simulated’ serum samples (human serum spiked with MCSP), which may not be representative of real-life samples. Furthermore, the acquisition of serum from blood samples is still an invasive and time-consuming process. Overall, although detection of melanoma skin cancer using SERS has been somewhat discussed in the literature, there is scope for more research to find an ideal probe.

The purpose of this work is to design and synthesise an extrinsic SERS probe able to selectively detect melanoma skin cancer, improving on current invasive and time-consuming methods of diagnosis.

1.8 References

1 A.-V. Giblin and J. M. Thomas, *J. Plast. Reconstr. Aesthetic Surg.*, 2007, **60**, 32–40.

2 J. L. Bong, R. M. Herd and J. A. A. Hunter, *J. Am. Acad. Dermatol.*, 2002, **46**, 690–694.

3 E. Smith and G. Dent, *Modern Raman spectroscopy: a practical approach*, John Wiley & Sons, 2019.

4 K. Kneipp, Y. Wang, H. Kneipp, L. T. Perelman, I. Itzkan, R. R. Dasari and M. S. Feld, *Phys. Rev. Lett.*, 1997, **78**, 1667–1670.

5 M. Fleischmann, P. J. Hendra and A. J. McQuillan, *Chem. Phys. Lett.*, 1974, **26**, 163–166.

6 B. Liu, P. Zhou, X. Liu, X. Sun, H. Li and M. Lin, *Food Bioprocess Technol.*, 2013, **6**, 710–718.

7 A. Chou, E. Jaatinen, R. Buividas, G. Seniutinas, S. Juodkazis, E. L. Izake and P. M. Fredericks, *Nanoscale*, 2012, **4**, 7419–7424.

8 E. C. Dreaden, A. M. Alkilany, X. Huang, C. J. Murphy and M. A. El-Sayed, *Chem. Soc. Rev.*, 2012, **41**, 2740–2779.

9 E. Smith and G. Dent, *Mod. Raman Spectrosc. – A Pract. Approach*, 2004, 1–21.

10 D. J. Lockwood, ed. M. R. Luo, Springer New York, New York, NY, 2016, pp. 1097–1107.

11 E. Smith and G. Dent, *Mod. Raman Spectrosc. – A Pract. Approach*, 2004, 71–92.

12 A. Campion and P. Kambhampati, *Chem. Soc. Rev.*, 1998, **27**, 241–250.

13 C. V RAMAN, *Nature*, 1928, **121**, 619.

14 M. Fleischmann, P. J. Hendra and A. J. McQuillan, *J. Chem. Soc.{,} Chem. Commun.*, 1973, 80–81.

15 F. J. Bezares, J. D. Caldwell, O. Glembocki, R. W. Rendell, M. Feygelson, M. Ukaegbu, R. Kasica, L. Shirey, N. D. Bassim and C. Hosten, *Plasmonics*, 2012, **7**, 143–150.

16 G. McNay, D. Eustace, W. E. Smith, K. Faulds and D. Graham, *Appl. Spectrosc.*, 2011, **65**, 825–837.

17 W. E. Smith and G. Dent, *Mod. Raman Spectrosc. – A Pract. Approach*, 2004, 113–133.

18 E. C. Le Ru and P. G. Etchegoin, eds. E. C. Le Ru and P. G. B. T.-P. of S.-E. R. S. Etchegoin, Elsevier, Amsterdam, 2009, pp. 185–264.

19 E. C. Le Ru and P. G. Etchegoin, *Chem. Phys. Lett.*, 2006, **423**, 63–66.

20 M. Moskovits, *Nature*, 2011, **469**, 307–308.

21 A. A. Stacy and R. P. Van Duyne, *Chem. Phys. Lett.*, 1983, **102**, 365–370.

22 R. J. H. Clark and T. J. Dines, *Angew. Chemie Int. Ed. English*, 1986, **25**, 131–158.

23 P. Shorygin, *Pure Appl. Chem.*, 1962, **4**, 87–96.

24 P. G. Etchegoin and E. C. Le Ru, *Phys. Chem. Chem. Phys.*, 2008, **10**, 6079–6089.

25 S. Nie and S. R. Emory, *Science (80-.).*, 1997, **275**, 1102 LP – 1106.

26 A. B. Zrimsek, N. Chiang, M. Mattei, S. Zaleski, M. O. McAnally, C. T. Chapman, A.-I. Henry, G. C. Schatz and R. P. Van Duyne, *Chem. Rev.*, 2017, **117**, 7583–7613.

27 Z. Zhang, T. Deckert-Gaudig, P. Singh and V. Deckert, *Chem. Commun. (Camb).*, 2015, **51**, 3069–3072.

28 Y. Fan, T. J. Anderson and B. Zhang, *Curr. Opin. Electrochem.*, 2018, **7**, 81–86.

29 E. Cortés, P. G. Etchegoin, E. C. Le Ru, A. Fainstein, M. E. Vela and R. C. Salvarezza, *J. Am. Chem. Soc.*, 2010, **132**, 18034–18037.

30 E. C. Le Ru, M. Meyer and P. G. Etchegoin, *J. Phys. Chem. B*, 2006, **110**, 1944–1948.

31 B.-S. Yeo, J. Stadler, T. Schmid, R. Zenobi and W. Zhang, *Chem. Phys. Lett.*, 2009, **472**, 1–13.

32 W. Zhang, B. S. Yeo, T. Schmid and R. Zenobi, *J. Phys. Chem. C*, 2007, **111**, 1733–1738.

33 R. M. Stöckle, Y. D. Suh, V. Deckert and R. Zenobi, *Chem. Phys. Lett.*, 2000, **318**, 131–136.

34 A. Rasmussen and V. Deckert, *J. Raman Spectrosc.*, 2006, **37**, 311–317.

35 R. Böhme, D. Cialla, M. Richter, P. Rösch, J. Popp and V. Deckert, *J. Biophotonics*, 2010, **3**, 455–461.

36 D. Kurouski, T. Deckert-Gaudig, V. Deckert and I. K. Lednev, *J. Am. Chem. Soc.*, 2012, **134**, 13323–13329.

37 W. Shen, X. Lin, C. Jiang, C. Li, H. Lin, J. Huang, S. Wang, G. Liu, X. Yan, Q. Zhong and B. Ren, *Angew. Chemie Int. Ed.*, 2015, **54**, 7308–7312.

38 Z. Jie, Y. Zenghe, Z. Xiaolei and Z. Yong, *Opt. Express*, 2018, **26**, 23534–23539.

39 S. Kasera, F. Biedermann, J. J. Baumberg, O. A. Scherman and S. Mahajan, *Nano Lett.*, 2012, **12**, 5924–5928.

40 O. Péron, E. Rinnert, T. Toury, M. de la Chapelle and C. Compère, *Analyst*, 2011, **136**, 1018–1022.

41 V. Peksa, M. Jahn, L. Štolcová, V. Schulz, J. Proška, M. Procházka, K. Weber, D. Cialla-May and J. Popp, *Anal. Chem.*, 2015, **87**, 2840–2844.

42 K. C. Bantz, A. F. Meyer, N. J. Wittenberg, H. Im, Ö. Kurtuluş, S. H. Lee, N. C. Lindquist, S.-H. Oh and C. L. Haynes, *Phys. Chem. Chem. Phys.*, 2011, **13**, 11551–11567.

43 P. R. West, S. Ishii, G. V Naik, N. K. Emani, V. M. Shalaev and A. Boltasseva, *Laser Photon. Rev.*, 2010, **4**, 795–808.

44 E. Le Ru and P. Etchegoin, *Principles of Surface-Enhanced Raman Spectroscopy: and related plasmonic effects*, Elsevier, 2008.

45 F. Benz, R. Chikkaraddy, A. Salmon, H. Ohadi, B. de Nijs, J. Mertens, C. Carnegie, R. W. Bowman and J. J. Baumberg, *J. Phys. Chem. Lett.*, 2016, **7**, 2264–2269.

46 T. B. Nguyen, T. K. T. Vu, Q. D. Nguyen, T. D. Nguyen, T. A. Nguyen and T. H. Trinh, *Adv. Nat. Sci. Nanosci. Nanotechnol.*, 2012, **3**, 25016.

47 N. D. Israelsen, C. Hanson and E. Vargis, *Sci. World J.*, 2015, **2015**, 124582.

48 B. Sharma, R. R. Frontiera, A.-I. Henry, E. Ringe and R. P. Van Duyne, *Mater. Today*, 2012, **15**, 16–25.

49 H. Keller, P. Simak, W. Schrepp and J. Dembowski, *Thin Solid Films*, 1994, **244**, 799–805.

50 M. Muniz-Miranda, C. Gellini and E. Giorgetti, *J. Phys. Chem. C*, 2011, **115**, 5021–5027.

51 K. Kneipp, R. R. Dasari and Y. Wang, *Appl. Spectrosc.*, 1994, **48**, 951–955.

52 M. Ahamed, M. S. AlSalhi and M. K. J. Siddiqui, *Clin. Chim. Acta*, 2010, **411**, 1841–1848.

53 S. Peulon, H. Antony, L. Legrand and A. Chausse, *Electrochim. Acta*, 2004, **49**, 2891–2899.

54 M. Dendisová-Vyškovská, V. Prokopec, M. Člupek and P. Matějka, *J. Raman Spectrosc.*, 2012, **43**, 181–186.

55 D. L. Jeanmaire and R. P. Van Duyne, *J. Electroanal. Chem. Interfacial Electrochem.*, 1977, **84**, 1–20.

56 C. Y. Chen, E. Burstein and S. Lundquist, *Solid State Commun.*, 1979, **32**, 63–66.

57 S. L. Kleinman, R. R. Frontiera, A.-I. Henry, J. A. Dieringer and R. P. Van Duyne, *Phys. Chem. Chem. Phys.*, 2013, **15**, 21–36.

58 M. Moskovits, *Rev. Mod. Phys.*, 1985, **57**, 783–826.

59 S. J. Oldenburg, R. D. Averitt, S. L. Westcott and N. J. Halas, *Chem. Phys. Lett.*, 1998, **288**, 243–247.

60 S. J. Oldenburg, G. D. Hale, J. B. Jackson and N. J. Halas, *Appl. Phys. Lett.*, 1999, **75**, 1063–1065.

61 H.-P. Liang, L.-J. Wan, C.-L. Bai and L. Jiang, *J. Phys. Chem. B*, 2005, **109**, 7795–7800.

62 S. Preciado-Flores, D. Wang, D. A. Wheeler, R. Newhouse, J. K. Hensel, A. Schwartzberg, L. Wang, J. Zhu, M. Barboza-Flores and J. Z. Zhang, *J. Mater. Chem.*, 2011, **21**, 2344–2350.

63 S. N. Abdollahi, M. Naderi and G. Amoabediny, *Colloids Surfaces A Physicochem. Eng. Asp.*, 2013, **436**, 1069–1075.

64 B. Li and H. C. Zeng, *Adv. Mater.*, 2019, **31**, 1801104.

65 Y. Yang, Q. Zhang, Z.-W. Fu and D. Qin, *ACS Appl. Mater. Interfaces*, 2014, **6**, 3750–3757.

66 Y. Khalavka, J. Becker and C. Sönnichsen, *J. Am. Chem. Soc.*, 2009, **131**, 1871–1875.

67 T. Zhang, G. Lu, W. Li, J. Liu, L. Hou, P. Perriat, M. Martini, O. Tillement and Q. Gong, *J. Phys. Chem. C*, 2012, **116**, 8804–8812.

68 M. A. Mahmoud, D. O'Neil and M. A. El-Sayed, *Chem. Mater.*, 2014, **26**, 44–58.

69 D. Radziuk and H. Moehwald, *Phys. Chem. Chem. Phys.*, 2015, **17**, 21072–21093.

70 M. Urbieta, M. Barbry, Y. Zhang, P. Koval, D. Sánchez-Portal, N. Zabala and J. Aizpurua, *ACS Nano*, 2018, **12**, 585–595.

71 F. Tian, F. Bonnier, A. Casey, A. E. Shanahan and H. J. Byrne, *Anal. Methods*, 2014, **6**, 9116–9123.

72 P. F. Liao and A. Wokaun, *J. Chem. Phys.*, 1982, **76**, 751–752.

73 D. Barolet, *Semin. Cutan. Med. Surg.*, 2008, **27**, 227–238.

74 A. Garcia-Leis, J. V. Garcia-Ramos and S. Sanchez-Cortes, *J. Phys. Chem. C*, 2013, **117**, 7791–7795.

75 H. Yuan, C. G. Khoury, H. Hwang, C. M. Wilson, G. A. Grant and T. Vo-Dinh, *Nanotechnology*, 2012, **23**, 75102.

76 X.-D. Tian, B.-J. Liu, J.-F. Li, Z.-L. Yang, B. Ren and Z.-Q. Tian, *J. Raman Spectrosc.*, 2013, **44**, 994–998.

77 S. Abalde-Cela, P. Aldeanueva-Potel, C. Mateo-Mateo, L. Rodriguez-Lorenzo, R. A. Alvarez-Puebla and L. M. Liz-Marzán, *J. R. Soc. Interface*, 2010, **7**, 435–450.

78 M. Martin, *J. Raman Spectrosc.*, **36**, 485–496.

79 B. D. Chithrani, A. A. Ghazani and W. C. W. Chan, *Nano Lett.*, 2006, **6**, 662–668.

80 Y. Jiang, S. Huo, T. Mizuhara, R. Das, Y.-W. Lee, S. Hou, D. F. Moyano, B. Duncan, X.-J. Liang and V. M. Rotello, *ACS Nano*, 2015, **9**, 9986–9993.

81 K. A. Willets, *Anal. Bioanal. Chem.*, 2009, **394**, 85–94.

82 L. Sun, Y. A. Diaz-Fernandez, T. A. Gschneidtner, F. Westerlund, S. Lara-Avila and K. Moth-Poulsen, *Chem. Soc. Rev.*, 2014, **43**, 7378–7411.

83 M. Brust and C. J. Kiely, *Colloids Surfaces A Physicochem. Eng. Asp.*, 2002, **202**, 175–186.

84 E. Leary, A. La Rosa, M. T. Gonzalez, G. Rubio-Bollinger, N. Agrait and N. Martin, *Chem. Soc. Rev.*, 2015, **44**, 920–942.

85 Y. Kang, D.-J. Won, S. R. Kim, K. Seo, H.-S. Choi, G. Lee, Z. Noh, T. S. Lee and C. Lee, *Mater. Sci. Eng. C*, 2004, **24**, 43–46.

86 S. Nath, S. K. Ghosh, S. Kundu, S. Praharaj, S. Panigrahi and T. Pal, *J. Nanoparticle Res.*, 2006, **8**, 111–116.

87 F. Chen, X. Li, J. Hihath, Z. Huang and N. Tao, *J. Am. Chem. Soc.*, 2006, **128**, 15874–15881.

88 D. V Leff, L. Brandt and J. R. Heath, *Langmuir*, 1996, **12**, 4723–4730.

89 A. Krzykawska, J. Ossowski, T. Żaba and P. Cyganik, *Chem. Commun.*, 2017, **53**, 5748–5751.

90 L. Guo, L. Ma, Y. Zhang, X. Cheng, Y. Xu, J. Wang, E. Wang and Z. Peng, *Langmuir*, 2016, **32**, 11514–11519.

91 C. Wang, Y. Chen, T. Wang, Z. Ma and Z. Su, *Adv. Funct. Mater.*, 2008, **18**, 355–361.

92 Y. Feng, L. He, L. Wang, R. Mo, C. Zhou, P. Hong and C. Li, *Nanomaterials*, 2020, **10**, 1000.

93 C. Song, Z. Wang, R. Zhang, J. Yang, X. Tan and Y. Cui, *Biosens. Bioelectron.*, 2009, **25**, 826–831.

94 Y. Wang, B. Yan and L. Chen, *Chem. Rev.*, 2013, **113**, 1391–1428.

95 S. E. J. Bell, G. Charron, E. Cortés, J. Kneipp, M. L. de la Chapelle, J. Langer, M. Procházka, V. Tran and S. Schlücker, *Angew. Chemie Int. Ed.*, 2020, **59**, 5454–5462.

96 N. Yang, T.-T. You, Y.-K. Gao, C.-M. Zhang and P.-G. Yin, *J. Agric. Food Chem.*, 2018, **66**, 6889–6896.

97 S. Lee, H. Chon, S.-Y. Yoon, E. K. Lee, S.-I. Chang, D. W. Lim and J. Choo,

Nanoscale, 2012, **4**, 124–129.

98 D. Liang, Q. Jin, N. Yan, J. Feng, J. Wang and X. Tang, *Adv. Biosyst.*, 2018, **2**, 1800100.

99 Y. Yin, Q. Li, S. Ma, H. Liu, B. Dong, J. Yang and D. Liu, *Anal. Chem.*, 2017, **89**, 1551–1557.

100 M. A. Bedics, H. Kearns, J. M. Cox, S. Mabbott, F. Ali, N. C. Shand, K. Faulds, J. B. Benedict, D. Graham and M. R. Detty, *Chem. Sci.*, 2015, **6**, 2302–2306.

101 H. Kearns, M. A. Bedics, N. C. Shand, K. Faulds, M. R. Detty and D. Graham, *Analyst*, 2016, **141**, 5062–5065.

102 F. Bonnier, S. M. Ali, P. Knief, H. Lambkin, K. Flynn, V. McDonagh, C. Healy, T. C. Lee, F. M. Lyng and H. J. Byrne, *Vib. Spectrosc.*, 2012, **61**, 124–132.

103 A. McLintock, H. J. Lee and A. W. Wark, *Phys. Chem. Chem. Phys.*, 2013, **15**, 18835–18843.

104 A. M. Alkilany and C. J. Murphy, *J. Nanoparticle Res.*, 2010, **12**, 2313–2333.

105 S. Wang, W. Lu, O. Tovmachenko, U. S. Rai, H. Yu and P. C. Ray, *Chem. Phys. Lett.*, 2008, **463**, 145–149.

106 X. Hu and X. Gao, *Phys. Chem. Chem. Phys.*, 2011, **13**, 10028–10035.

107 A. M. Fales, H. Yuan and T. Vo-Dinh, *Langmuir*, 2011, **27**, 12186–12190.

108 J. Han, X. Qian, Q. Wu, R. Jha, J. Duan, Z. Yang, K. O. Maher, S. Nie and C. Xu, *Biomaterials*, 2016, **105**, 66–76.

109 K. Lee, A. N. Sathyagal and A. V McCormick, *Colloids Surfaces A Physicochem. Eng. Asp.*, 1998, **144**, 115–125.

110 Y. Kobayashi, H. Katakami, E. Mine, D. Nagao, M. Konno and L. M. Liz-Marzán, *J. Colloid Interface Sci.*, 2005, **283**, 392–396.

111 W. Stöber, A. Fink and E. Bohn, *J. Colloid Interface Sci.*, 1968, **26**, 62–69.

112 J. F. Li, X. D. Tian, S. B. Li, J. R. Anema, Z. L. Yang, Y. Ding, Y. F. Wu, Y. M. Zeng, Q. Z. Chen, B. Ren, Z. L. Wang and Z. Q. Tian, *Nat. Protoc.*, 2012, **8**, 52.

113 S. Kralj, D. Makovec, S. Čampelj and M. Drofenik, *J. Magn. Magn. Mater.*, 2010, **322**, 1847–1853.

114 via W. C. Smokefoot, CC BY-SA 3.0 <https://creativecommons.org/licenses/by-sa/3.0>, Highly simplified representation of the condensation of TEOS in sol gel process.

115 C. J. Murphy, A. M. Gole, J. W. Stone, P. N. Sisco, A. M. Alkilany, E. C. Goldsmith and S. C. Baxter, *Acc. Chem. Res.*, 2008, **41**, 1721–1730.

116 X.-D. Zhang, D. Wu, X. Shen, J. Chen, Y.-M. Sun, P.-X. Liu and X.-J. Liang, *Biomaterials*, 2012, **33**, 6408–6419.

117 X.-D. Zhang, D. Wu, X. Shen, P.-X. Liu, N. Yang, B. Zhao, H. Zhang, Y.-M. Sun, L.-A. Zhang and F.-Y. Fan, *Int. J. Nanomedicine*, 2011, **6**, 2071–2081.

118 A. J. Mieszawska, W. J. M. Mulder, Z. A. Fayad and D. P. Cormode, *Mol. Pharm.*, 2013, **10**, 831–847.

119 S. Harmsen, R. Huang, M. A. Wall, H. Karabeber, J. M. Samii, M. Spaliviero, J. R. White, S. Monette, R. O\textquoterightConnor, K. L. Pitter, S. A. Sastra, M. Saborowski, E. C. Holland, S. Singer, K. P. Olive, S. W. Lowe, R. G. Blasberg and M. F. Kircher, *Sci. Transl. Med.*, 2015, **7**, 271ra7--271ra7.

120 J. Fang, H. Nakamura and H. Maeda, *Adv. Drug Deliv. Rev.*, 2011, **63**, 136–151.

121 H. Maeda, H. Nakamura and J. Fang, *Adv. Drug Deliv. Rev.*, 2013, **65**, 71–79.

122 S. Feng, D. Lin, J. Lin, B. Li, Z. Huang, G. Chen, W. Zhang, L. Wang, J. Pan, R. Chen and H. Zeng, *Analyst*, 2013, **138**, 3967–3974.

123 P. Petignat and M. Roy, *BMJ*, 2007, **335**, 765–768.

124 B. J. Willoughby, K. Faulkner, E. C. Stamp and C. J. Whitaker, *J. Public Health (Bangkok).*, 2006, **28**, 355–360.

125 C. D. Keating, *Proc. Natl. Acad. Sci.*, 2005, **102**, 2263–2264.

126 A. Zengin, U. Tamer and T. Caykara, *Biomacromolecules*, 2013, **14**, 3001–3009.

127 P. Vohra, H. T. Ngo, W. T. Lee and T. Vo-Dinh, *Anal. Methods*, 2017, **9**, 5550–5556.

128 P. G. Chu, M. H. Lyda and L. M. Weiss, *Histopathology*, 2001, **39**, 9–16.

129 L. Chen and J. Choo, *Electrophoresis*, 2008, **29**, 1815–1828.

130 M. Lee, K. Lee, K. H. Kim, K. W. Oh and J. Choo, *Lab Chip*, 2012, **12**, 3720–3727.

131 Z. Cheng, N. Choi, R. Wang, S. Lee, K. C. Moon, S.-Y. Yoon, L. Chen and J. Choo, *ACS Nano*, 2017, **11**, 4926–4933.

132 X. Fu, Z. Cheng, J. Yu, P. Choo, L. Chen and J. Choo, *Biosens. Bioelectron.*, 2016, **78**, 530–537.

133 X. Wu, J. Chen, X. Li, Y. Zhao and S. M. Zughaier, *Nanomedicine Nanotechnology, Biol. Med.*, 2014, **10**, 1863–1870.

134 W. R. Premasiri, Y. Chen, P. M. Williamson, D. C. Bandarage, C. Pyles and L. D. Ziegler, *Anal. Bioanal. Chem.*, 2017, **409**, 3043–3054.

135 K. Xu, R. Zhou, K. Takei and M. Hong, *Adv. Sci.*, 2019, **6**, 1900925.

136 H. Mitomo, K. Horie, Y. Matsuo, K. Niikura, T. Tani, M. Naya and K. Ijiro, *Adv. Opt. Mater.*, 2016, **4**, 259–263.

137 Y.-P. Jia, B.-Y. Ma, X.-W. Wei and Z.-Y. Qian, *Chinese Chem. Lett.*, 2017, **28**, 691–702.

138 D. Bobo, K. J. Robinson, J. Islam, K. J. Thurecht and S. R. Corrie, *Pharm. Res.*, 2016, **33**, 2373–2387.

139 S. Mulaje, *J. Drug Deliv. Ther.*, , DOI:10.22270/jddt.v3i2.409.

140 M. Helfand, S. M. Mahon, K. B. Eden, P. S. Frame and C. T. Orleans, *Am. J. Prev. Med.*, 2001, **20**, 47–58.

141 H. Kittler, H. Pehamberger, K. Wolff and M. Binder, *Lancet Oncol.*, 2002, **3**, 159–165.

142 G. Argenziano, L. Cerroni, I. Zalaudek, S. Staibano, R. Hofmann-Wellenhof, N. Arpaia, R. M. Bakos, B. Balme, J. Bandic, R. Bandelloni, A. M. G. Brunasso, H. Cabo, D. A. Calcara, B. Carlos-Ortega, A. C. Carvalho, G. Casas, H. Dong, G. Ferrara, R. Filotico, G. Gómez, A. Halpern, G. Ilardi, A. Ishiko, G. Kandiloglu, H. Kawasaki, K. Kobayashi, H. Koga, I. Kovalyshyn, D. Langford, X. Liu, A. A. Marghoob, M. Mascolo, C. Massone, L. Mazzoni, S. Menzies, A. Minagawa, L. Nugnes, F. Ozdemir, G. Pellacani, S. Seidenari, K. Siamas, I. Stanganelli, W. V Stoecker, M. Tanaka, L. Thomas, P. Tschandl and H. Kittler, *J. Am. Acad. Dermatol.*, 2012, **67**, 54-59.e1.

143 C. Benvenuto-Andrade, S. W. Dusza, A. L. C. Agero, A. Scope, M. Rajadhyaksha, A. C. Halpern and A. A. Marghoob, *Arch. Dermatol.*, 2007, **143**, 329–338.

144 via W. C. I, Frank33, CC BY-SA 3.0 <http://creativecommons.org/licenses/by-sa/3.0/>, Dermatoscope (Heine, delta-10).

145 Y. Pan, D. S. Gareau, A. Scope, M. Rajadhyaksha, N. A. Mullani and A. A. Marghoob, *Arch. Dermatol.*, 2008, **144**, 828–829.

146 H. Lorentzen, K. Weismann, C. S. Petersen, F. Grønhøj Larsen, L. Secher and V. Skødt, *Acta Derm. Venereol.*

147 I. H. Wolf, J. Smolle, H. P. Soyer and H. Kerl, *Melanoma Res.*, 1998, **8**, 425–429.

148 L. Chen, S. Dusza, M. Grazzini, A. Blum and A. Marghoob, *Australas. J. Dermatol.*, 2013, **54**, 310–312.

149 J. A. N. BOROVANSKÝ, E. VEDRALOVÁ and P. HACH, *Pigment Cell Res.*, 1991, **4**, 222–224.

150 B. W. Murphy, R. J. Webster, B. A. Turlach, C. J. Quirk, C. D. Clay, P. J. Heenan and D. D. Sampson, *J. Biomed. Opt.*, 2005, **10**, 1–9.

151 R. Marchesini, M. Brambilla, C. Clemente, M. Maniezzo, A. E. Sichirollo, A. Testori, D. R. Venturoli and N. Cascinelli, *Photochem. Photobiol.*, 1991, **53**, 77–84.

152 S. Tomatis, M. Carrara, A. Bono, C. Bartoli, M. Lualdi, G. Tragni, A. Colombo and R. Marchesini, *Phys. Med. Biol.*, 2005, **50**, 1675–1687.

153 G. Zonios, A. Dimou, I. Bassukas, D. Galaris, A. Tsolakidis and E. Kaxiras, *J. Biomed. Opt.*, 2008, **13**, 1–8.

154 Y. Li and L. Shen, *Sensors* , 2018, 18.

155 C. E. Parker and C. H. Borchers, *Mol. Oncol.*, 2014, **8**, 840–858.

156 B. Matharoo-Ball, L. Ratcliffe, L. Lancashire, S. Ugurel, A. K. Miles, D. J. Weston, R. Rees, D. Schadendorf, G. Ball and C. S. Creaser, *PROTEOMICS – Clin. Appl.*, 2007, **1**, 605–620.

157 S. Y. Lim, J. H. Lee, R. J. Diefenbach, R. F. Kefford and H. Rizos, *Mol. Cancer*, 2018, **17**, 8.

158 H. Alexander, A. L. Stegner, C. Wagner-Mann, G. C. Du Bois, S. Alexander and E. R. Sauter, *Clin. Cancer Res.*, 2004, **10**, 7500–7510.

159 A. J. Bleasby, J. C. Knowles and N. J. Cooke, *Clin. Chim. Acta*, 1985, **150**, 231–235.

160 B. W. Chwirot, N. Sypniewska, Z. Michniewicz, J. Redzinski, S. Chwirot, G. Kurzawski and W. Ruka, *J. Invest. Dermatol.*, 2001, **117**, 1449–1451.

161 L. Pires, M. S. Nogueira, S. Pratavieira, L. T. Moriyama and C. Kurachi, *Biomed. Opt. Express*, 2014, **5**, 3080–3089.

162 D. Leupold, M. Scholz, G. Stankovic, J. Reda, S. Buder, R. Eichhorn, G. Wessler, M. Stücker, K. Hoffmann, J. Bauer and C. Garbe, *Pigment Cell Melanoma Res.*, 2011, **24**, 438–445.

163 M. G. Vander Heiden, L. C. Cantley and C. B. Thompson, *Science (80-.).*, 2009, **324**, 1029 LP – 1033.

164 A. F. Santidrian, A. Matsuno-Yagi, M. Ritland, B. B. Seo, S. E. LeBoeuf, L. J. Gay, T. Yagi and B. Felding-Habermann, *J. Clin. Invest.*, 2013, **123**, 1068–1081.

165 S. Seidenari, F. Arginelli, C. Dunsby, P. M. W. French, K. König, C. Magnoni, C. Talbot and G. Ponti, *PLoS One*, 2013, **8**, e70682–e70682.

166 E. Dimitrow, I. Riemann, A. Ehlers, M. J. Koehler, J. Norgauer, P. Elsner, K. König and M. Kaatz, *Exp. Dermatol.*, 2009, **18**, 509–515.

167 J. Chen, M. F. Giblin, N. Wang, S. S. Jurisson and T. P. Quinn, *Nucl. Med. Biol.*, 1999, **26**, 687–693.

168 Y. Miao, K. Benwell and T. P. Quinn, *J. Nucl. Med.*, 2007, **48**, 73–80.

169 D. Pickel, G. P. Manucy, D. B. Walker, S. B. Hall and J. C. Walker, *Appl. Anim. Behav. Sci.*, 2004, **89**, 107–116.

170 M. M. Joseph, N. Narayanan, J. B. Nair, V. Karunakaran, A. N. Ramya, P. T. Sujai, G. Saranya, J. S. Arya, V. M. Vijayan and K. K. Maiti, *Biomaterials*, 2018, **181**, 140–181.

171 J. H. Granger, M. C. Granger, M. A. Firpo, S. J. Mulvihill and M. D. Porter, *Analyst*, 2013, **138**, 410–416.

172 J. H. Granger, N. E. Schlotter, A. C. Crawford and M. D. Porter, *Chem. Soc. Rev.*,

2016, **45**, 3865–3882.

173 S. C. Pinzaru, C. A. Dehelean, A. Falamas, N. Leopold and C. Lehene, 2010, vol. 7376, pp. 73760T-7376–6.

174 F. Zeng, D. Xu, C. Zhan, C. Liang, W. Zhao, J. Zhang, H. Feng and X. Ma, *ACS Appl. Nano Mater.*, , DOI:10.1021/acsanm.8b00444.

175 S. Cinta Pinzaru, A. Falamas, C. Dehelean, C. Morari and M. Venter, *Double Amino Functionalized Ag Nanoparticles as SERS Tags in Raman Diagnostic*, 2013, vol. 86.

176 A. Falamas, C. A. Dehelean and S. Cinta Pinzaru, *Vib. Spectrosc.*, 2018, **95**, 44–50.

177 E. J.H. Wee, Y. Wang, S. C.-H Tsao and Matt Trau, *Theranostics*. 2016, **6**, 1506–1513.

178 A. R. Kumar, K. B. Shanmugasundaram, J. Li, Z. Zhang, A. A. Ibn Sina, A. Wuethrich and M. Trau, *RSC Adv.*, 2020, **10**, 28778

2. Surface Enhanced Raman Spectroscopy Probes: Design and Initial Testing

A rapid, unspeculative detection system for melanoma detection would allow the disease to be caught at an early, treatable stage. SERS is a promising technique for such an application due to its low detection limits.[1–6] By combining a targeted SERS probe with a table-top Raman spectrometer, it could be possible to detect early-stage melanoma at the point-of-care, without a specialist present. In the following chapter, the design and synthesis of a SERS probe for the detection of melanoma is discussed; first focusing on the synthesis of a basic intrinsic probe, followed by the incorporation of Raman reporters. The probe was then functionalised with a peptide for targeting the human breast cancer cell line MCF7 for the purposes of testing. Functionalisation of the probe to target melanoma is discussed in the following chapter.

2.1 Synthesis of Gold Nanoparticles and Size Dependence

The size of a metal nanoparticle plays a key role in signal enhancement, as a larger particle has more free electrons to contribute to a surface plasmon wave, resulting in a greater plasmon effect.[7] However, it has been reported that when nanoparticles become too large (greater than 100 nm), signal enhancement ceases to improve and can even diminish.[8,9] Before a probe was synthesised, the optimal diameter for signal enhancement was explored by synthesising gold nanoparticles of various sizes. The signal enhancing properties of these particles were explored by comparing their ability to enhance fluorescence.

2.1.1 The Metal Enhanced Fluorescence Effect

Metal enhanced fluorescence is the amplification of fluorescence signals as a result of adding plasmonic structures (such as gold nanoparticles) in close proximity to the fluorophore. [10] The mechanism by which this occurs is analogous to the SERS effect; the localised electric field at the metal surface E_{Loc} (created by coupling of the LSP field to the electric field of incident light, Section 1.2) enhances the intensity of fluorescence.[11] The metal also enhances fluorescence by radiative decay engineering.[12] This is a phenomenon in which the presence of the metal surface increases the overall radiative decay rate Γ by introducing a new, additional radiative decay rate, Γ_m (Figure 2.1), increasing quantum yield. Much like SERS, metal enhanced fluorescence has attracted attention as it facilitates the detection of very small traces of analyte, creating the potential for ultra-sensitive fluorescence spectroscopy techniques for sensing applications, with minimal cost.[13]

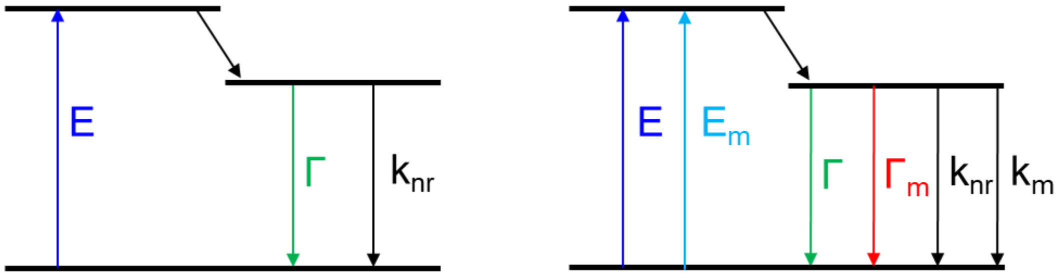

Figure 2.1: Jablonski diagram for a fluorophore without (left) and with (right) metal-enhancing effects. E_m, $Γ_m$ *and* k_m *represent the additional excitation, radiative decay and non-radiative decay in the presence of a metal surface, respectively.*[12]

2.1.2 Synthesis of Gold Nanoparticles

Gold nanoparticles of varying sizes were synthesised for these tests. Gold nanoparticles were initially chosen for their ease of synthesis compared to more elaborate shapes as well as being stable, non-toxic, and efficient supporters of surface plasmons. The nanoparticles were synthesised via the Turkevich method, in which sodium chloroaurate is reduced with sodium citrate (Scheme 2.1). This is the most frequently used method for gold nanoparticle synthesis since it was first developed in 1951.[14] The initiation step involves the reduction of Au (III) to Au (0) to form gold clusters, which in turn combine to form 'seed particles' approximately 1.5 nm or less in diameter; this seed particle formation is the size determining step of the reaction.[15]

The citrate in solution causes an increase in pH which shifts the equilibrium of gold species from $[AuCl_4]^-$ to the less reactive $[Au(Cl)_{4-x}(OH)_x]^-$, which can be understood by considering the coupling of equations 2.1 and 2.2.[15] The decreased amount of reactive $[AuCl_4]^-$ species results in the termination of the seed formation step.

$$[AuCl_4]^- + xH_2O \rightleftharpoons [AuCl_{4-x}(OH)_x]^- + xH^+ + xCl^- \qquad \textit{(eq. 2.1)}$$

$$Cit^{3-} + xH^+ \rightleftharpoons H_xCit^{(3-x)} \qquad \textit{(eq. 2.2)}$$

It was initially speculated that the blue colour of the solution after this step is caused by the formation of large gold aggregates, which then fragment to form smaller particles. However, X-ray scattering data from Wuithschick *et. al* suggests that the next step actually involves $[Au(Cl)_{4-x}(OH)_x]^-$ ions becoming attracted into the electric double layer of the seed particles, where they are reduced at the particle surface.[16]

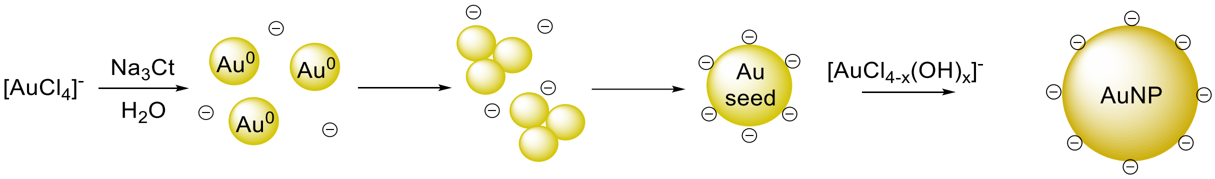

Scheme 2.1: Turkevich synthesis of gold nanoparticles using sodium chloroaurate and sodium citrate (represented with ϴ).

2.1.3 Seed mediated growth and modification

Seed particles were first synthesised by the Turkevich method as described above. A 0.01 w.t.% solution of sodium chloroaurate was heated to boiling with sodium citrate until a colour change was observed. The seed solution and all subsequent nanoparticle solutions were washed by centrifuging at 4400 rpm three times before re-suspending in water.

In order to reliably synthesise nanoparticles absorbing at specific wavelengths, a controlled seed growth method was developed. A seed solution of particles with an absorbance maximum of 528 nm, corresponding approximately to a diameter of 9 nm,[17] were synthesised, before heating to 65 °C with 3 ml sodium citrate (1 w.t.%) and adding 3 mM sodium chloroaurate solution dropwise. The UV-Vis spectrum of the reaction mixture was recorded at regular intervals until the desired absorbance was achieved (Figure 2.2).

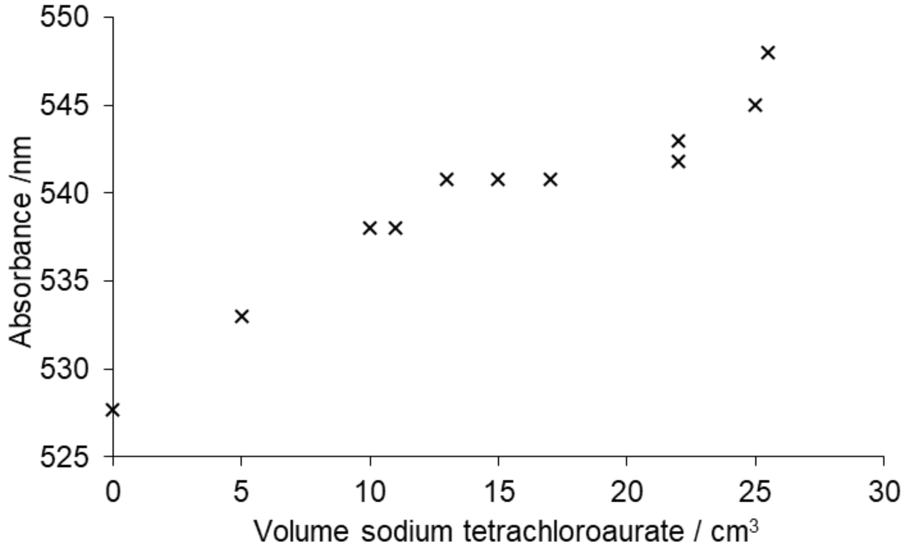

Figure 2.2: Absorbance of nanoparticles against amount sodium chloroaurate added to growth solution. 2 ml sodium citrate was initially added, and a plateau can be seen around 540 nm; at this point an additional 1 ml citrate was added.

This method was preferable over many of the seed growth methods in the literature, as it does not require a strong reducing agent, such as hydroxylamine hydrochloride. Another drawback to many methods stated in the literature is that the absorbance of the final product may vary by several nanometres, making them unreliable when a specific wavelength is required, as is often the case for SERS applications. Although the size distribution of particles synthesised by this method is relatively broad, it was the most reliable method of obtaining solutions with a specific absorption. This method was primarily used to synthesise particles with an absorbance maximum of 548 nm, as these were determined to give the best enhancement of fluorescence and Raman signals (as discussed in Section 2.1.4), although a range of particles of varying absorbances up to 559 nm were synthesised.

TEM images were used to determine nanoparticle size, as estimating size from the absorption maximum, i.e. the plasmon resonance, is not accurate for particles with broad size distribution or surface coatings.[17] The size distribution of nanoparticles with λ_{max}= 548 nm (Figure 2.3) was obtained by measuring the diameters of 196 individual nanoparticles with ImageJ software. Using this method, the mean diameter was found to be 62 nm with a standard deviation of 26 nm. The large standard deviation and broad size distribution of the nanoparticles, skewed towards smaller diameters, was presumed to be due to the formation of new seeds alongside seed growth. The icosahedral geometry of the nanoparticles synthesised by this method may attribute to their signal enhancing properties, discussed in Chapter 1.

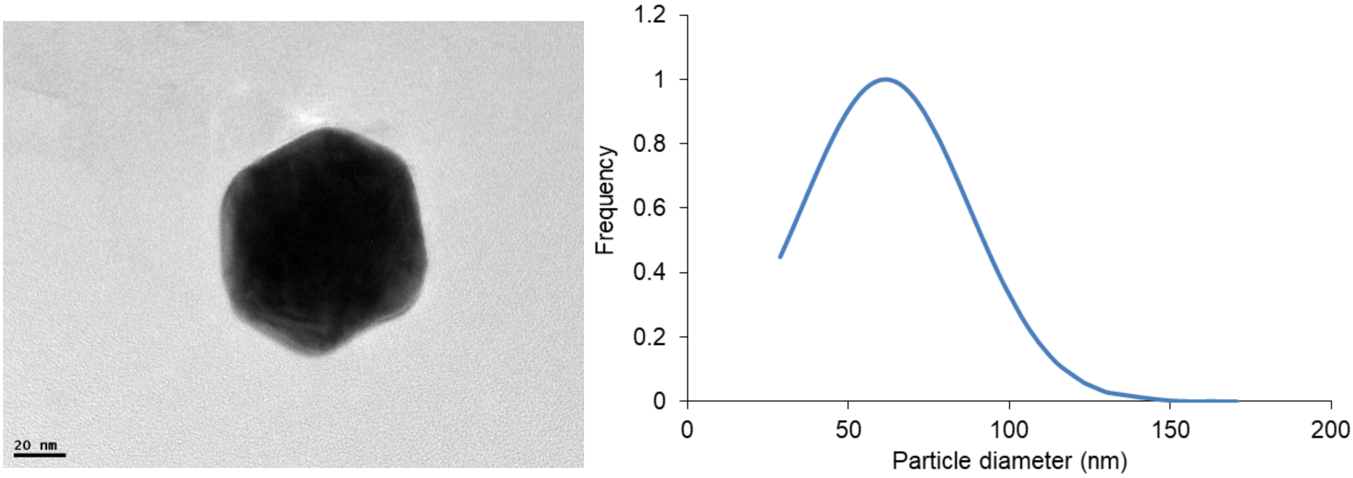

Figure 2.3: TEM image of gold nanoparticle (ʎ$_{max}$ = 548 nm), with size distribution. Mean particle diameter= 62 nm.

2.1.4 Synthesis of silica coated gold nanoparticles

The nanoparticles were coated in silica, as studies have shown that silica coatings provide improved reproducibility in SERS experiments by reducing random hotspots caused by aggregation, and eliminating the possibility of varying signals due to different analyte interactions with the bare gold surface.[18] The silica coating method used was the Stöber method (Schemes 2.2-2.3), a hydrolysis of TEOS where silica is deposited on the surface of the gold nanoparticles.[19,20] TEOS is first undergoes base catalysed hydrolysis to yield $SiOH(EtO)_3$, followed by a condensation reaction to give a Si-O-Si containing species. Subsequent condensation reactions occur until a SiO_2 polymer network with hydroxy and ethoxy terminal groups is produced.[21,22] A solution of TEOS in ethanol was added to nanoparticles suspended in water, adjusted to pH 10 with ammonia.

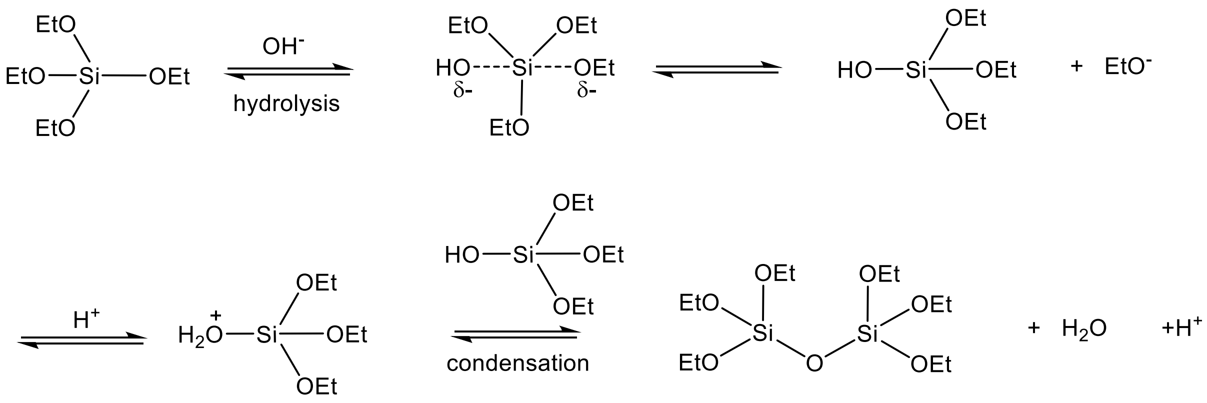

Scheme 2.2: Hydrolysis and condensation of TEOS to form silica.[20]

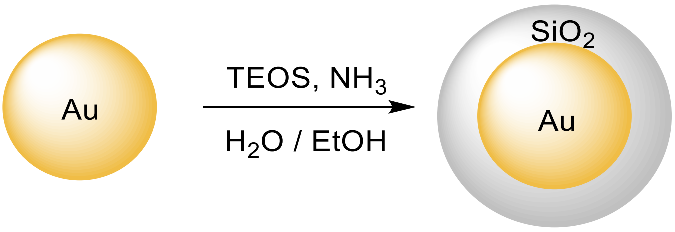

Scheme 2.3: Synthesis of silica coated gold nanoparticles

The resulting nanoparticles were centrifuged and suspended in ethanol, as silica coated nanoparticles tend to be less stable in water than ethanol, due to the lower zeta potential of silica in water.[23] Visually, the nanoparticles appeared to be well dispersed, with no aggregate visible by eye.

TEM images of the silica coated nanoparticles (Figure 2.4) do not show a visible silica layer, although analysis of the samples by EDX indicates that silica is present (Figure 2.5). The presence of the silica layer was confirmed by the addition of a linker group. 3-(Aminopropyl)trimethoxysilane (APTMS) was attached to the silica surface; the terminal amine groups of the APTMS were then detectable following the attachment a fluorescent marker. This is discussed in greater detail in Section 2.2.1. The fact that the silica coating is not visible by TEM, though determined to be present via other methods, may suggest that the coating is too thin to observe, though this is not certain, as the few nanoparticles imaged by TEM may not be representative of the sample as a whole. However, if the coating is indeed as thin as the images suggest, then this is ideal for SERS applications, as the electromagnetic field associated with the surface plasmons (responsible for SERS enhancement) decays exponentially from the surface.[24]

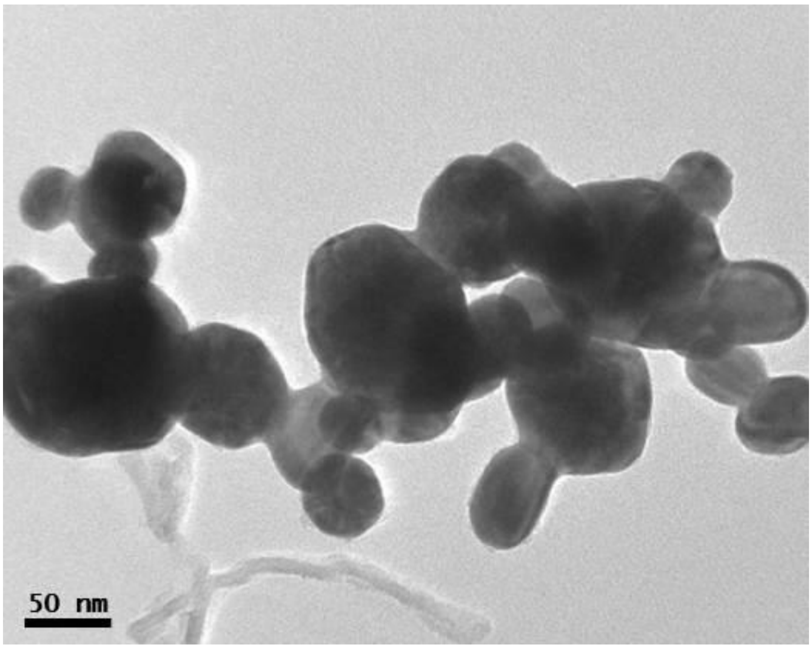

Figure 2.4: TEM images of AuNP@SiO$_2$ nanoparticles.

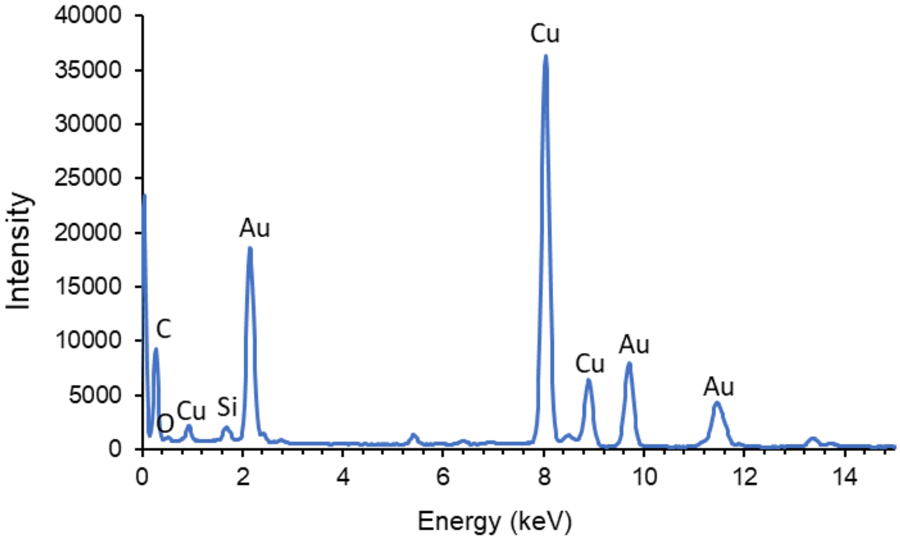

Figure 2.5: EDX spectrum of AuNP@SiO$_2$ nanoparticles.

2.1.5 MEF in solution

To explore the signal enhancing effects of the nanoparticles, the effect of the nanoparticles on the fluorescence emission of rhodamine 6G was recorded, both in solution and on gold slides.

The phenomenon of metal enhanced fluorescence is analogous to surface enhanced Raman signals, and therefore is an effective precursory study to show the signal enhancing effects of the various nanoparticle solutions. Solutions of 0.1 mM rhodamine 6G were prepared by dissolving rhodamine in 10 mg cm^{-3} solutions of citrate stabilised gold nanoparticles of varying λ_{max} values, suspended in water.

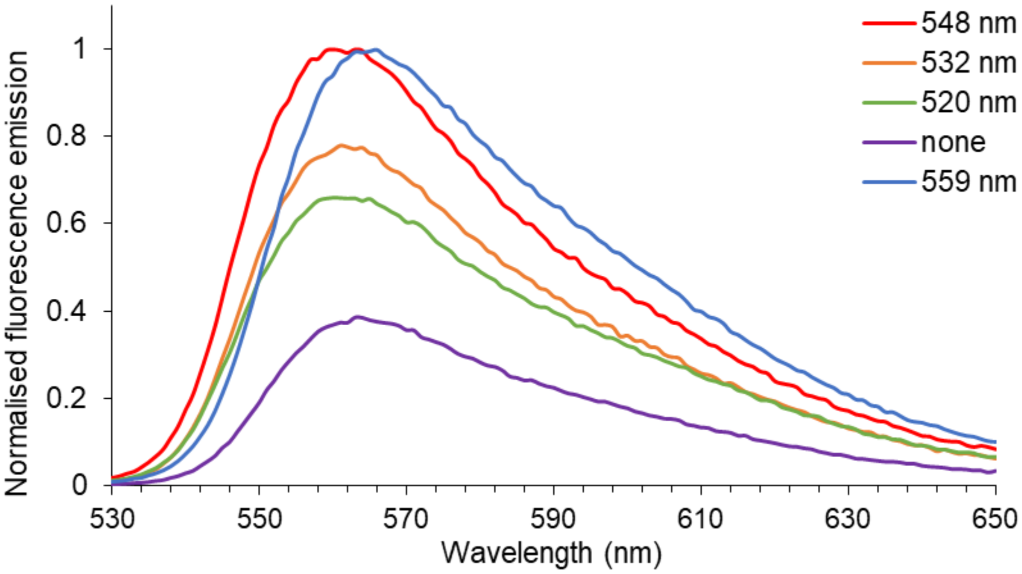

Figure 2.6: Fluorescence spectra of rhodamine 6G in solution with gold nanoparticles of varying absorbance maxima.

The results in Figure 2.6 show that generally, as the nanoparticle absorbance maximum increases, so does the enhancement of fluorescence emission. The absorption of gold nanoparticle solution, indicating the plasmon resonance of the particles, is proportional to nanoparticle size.[17] It is therefore to be expected that solutions absorbing longer wavelengths, indicative of larger particles in solution, give the largest fluorescence enhancement, as plasmon enhancing effects are size dependent.[25] A maximum enhancement is achieved from the nanoparticles with an absorbance of 548 nm, after which there is no further enhancement, which is consistent with the generally accepted rule that SERS nanoparticles tend to have an optimum size, after which signal enhancement ceases or is diminished.[8,9] The reason for the shift in emission with 559 nm absorbing nanoparticles is unclear.

2.1.5 MEF on metal surfaces

Solutions of rhodamine 6G and nanoparticles were prepared in the same way, with added polyvinyl alcohol (PVA) to form a more viscous liquid. Gold coated glass coverslips were then spin coated with the solutions, to create thin layers of rhodamine, with and without gold nanoparticles, on a gold surface, and the fluorescence spectra of each of these surfaces was measured (Figure 2.7), to determine the effects of a gold film on the fluorescence emission, as well as gold nanoparticles.

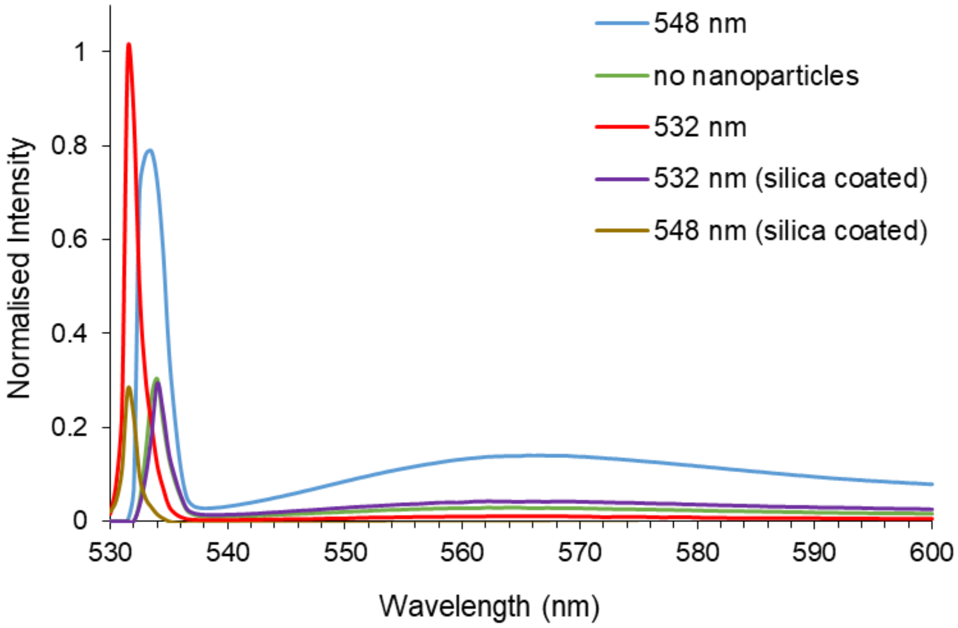

Figure 2.7: Fluorescence spectra of rhodamine 6G and gold nanoparticle solutions of varying absorbances on gold films.

In this thin layer, the low concentration of rhodamine resulted in a less intense fluorescence emission peak, and a very sharp prominent peak attributed to the Raman scattering of water, which tended to increase as the fluorescence emission decreased. The gold surface enhances the Raman peak, which is usually too insignificant to be observed in a fluorescence spectrum. As expected, although metal nanoparticles have the ability to enhance fluorescence, metals with little or no nanoscale structure do not, and metals in very close contact with fluorophore (less than 5 nm) can cause quenching of fluorescence.[10] Therefore, although metal nanoparticles in solution enhance fluorescence emission, it is quenched when the rhodamine is deposited onto a solid gold slide.

Figure 2.7 also indicates that the signal enhancement diminishes on silica coating, despite TEM images suggesting that the coating is thin enough that the LSP wave can penetrate it. The lack of signal enhancement may be due to the instability of silica coated particles in solution, which experience some aggregation due to the coating causing the particles to ‘stick together’ as shown by TEM (Figure 2.4), and a large amount of aggregation may result in a poor distribution of the gold particles throughout the film.

It is also possible that the silica layer prevents hotspot formation between the surfaces of the gold nanoparticles, resulting in insufficient signal enhancement. Suspending the particles in ethanol:water (1:1) helps to prevent aggregation, although this is not ideal for particles to be tested in biological systems, as ethanol is toxic to cells. Silica coating may therefore be a more appropriate technique for nanostructures which do not require aggregation between particles for hotspots formation, such as nanostars as opposed to spheres.

Overall, the results show a strong correlation between signal enhancing effects and nanoparticle size, which is consistent with the literature, and therefore the nanoparticles absorbing at 548 nm were used to synthesise the intrinsic probe described in section 2.2 The results for silica coated nanoparticles show little signal enhancement of the Raman peak in the fluorescence spectrum, likely because the protective layer prevents hotspot formation between particles. It therefore may be ideal to devise a probe which does not rely on aggregation for hotspot formation, such as gold nanostars.

2.2 Synthesis of a Surface Enhanced Raman Probe

To begin, a simple intrinsic SERS probe consisting of a gold nanoparticle core and silica coating was synthesised, before elaborating on the design by incorporating a reporter, a more complex shaped gold core, and a unique cell-surface receptor targeting-peptide for the selective detection of various cell lines.

2.2.1 Addition of a Linking Group

The silica coating of the nanoparticles as prepared in section 2.1 allowed the particles to be functionalised with (3-aminopropyl)trimethoxysilane (APTMS) as shown in Schemes 2.4-2.5, providing a terminal amine group to allow a peptide to be attached, for the selective targeting of cell lines.

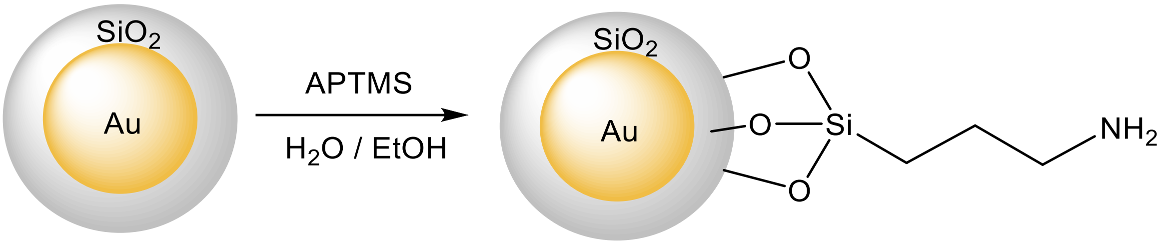

Scheme 2.4: Synthesis of APTMS functionalised gold nanoparticles.

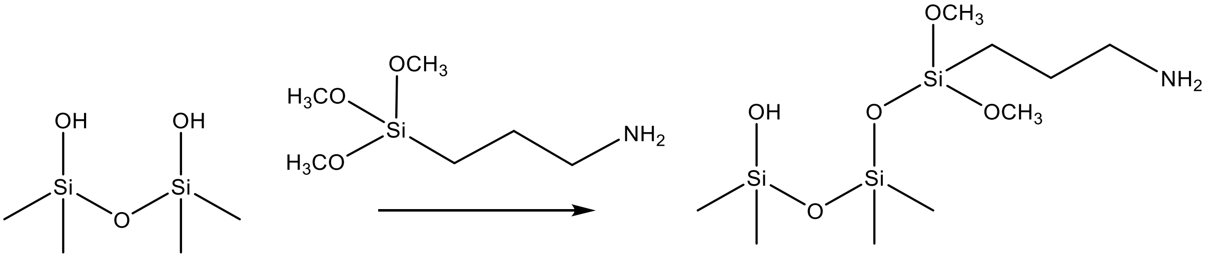

Scheme 2.5: Reaction of silica with APTMS [26]

To determine success of the reaction, the terminal amine of the APTMS functionalised probe coupled with dansyl chloride (Scheme 2.6). Excess danysl chloride was removed by centrifuging four times before re-suspending in ethanol. The fluorescence of the nanoparticles (Figure 2.8) indicates the presence of dansyl groups on the particle surface, which suggests that the functionalisation of the nanoparticles with APTMS to give amine linker groups was successful. To further characterise the nanoparticles, the fluorescence was compared to that of 3-dansylpropyl trimethoxysilane (APTMS-DNS, 1.3 mmol), in order to determine the number of linking groups on each particle surface.

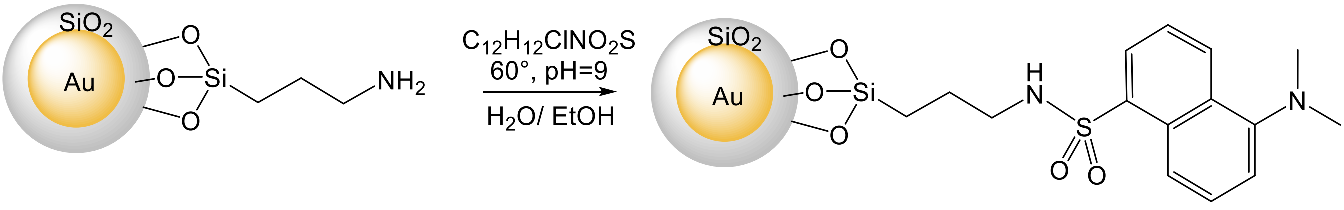

Scheme 2.6: Synthesis of dansylated nanoparticles.

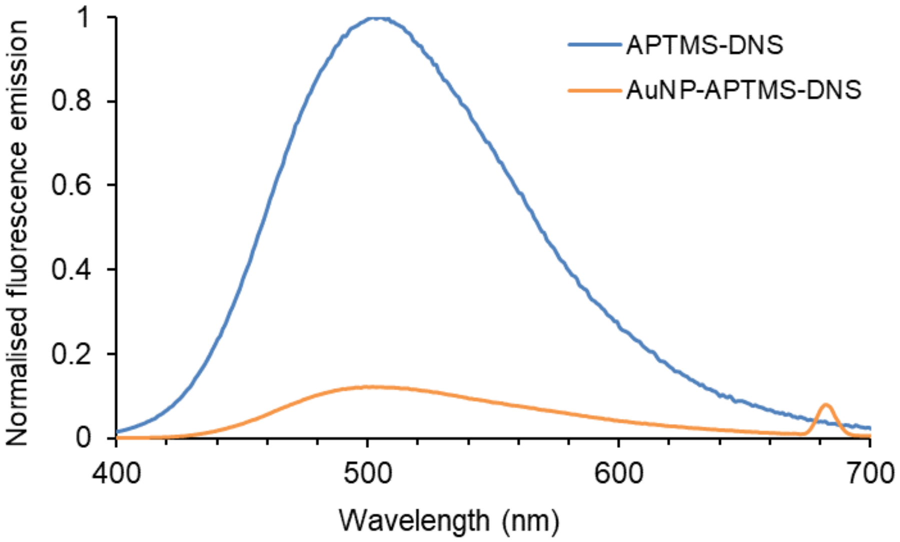

Figure 2.8: Fluorescence emission spectra of the intrinsic probe with attached dansyl group, as shown in Scheme 2.6, with unbound dansylated trimethoxysilane for comparison.

By comparison of the fluorescence emission and using Beer-Lambert law, the total surface concentration of dansylated trimethoxysilane in the nanoparticle solution was calculated to be 0.16 mM. In a 5.45 x10^{-8} M solution of gold nanoparticles this gives approximately 2845 dansyl groups per particle. Assuming all amino groups were dansylated, as an excess of dansyl chloride was added, for a solution of nanoparticles with a mean diameter of 62 nm (size distribution provided in Figure 2.3) this gives a surface distribution of around one amino trimethoxysilane linker group per 5 nm^2 of nanoparticle surface. Figure 2.8 also shows an emission peak at 684 nm, most likely a 2nd order scattering artifact.

2.2.2 SERS Probe Design

Following the successful fabrication of silica coated gold nanoparticles functionalised with APTMS, focus was shifted to create a more complex SERS probe (Figure 2.9), consisting of a gold nanostar core, methylene blue Raman reporter, silica coating, and APTMS linker group to eventually bind a peptide for the selective detection of a chosen cell line.

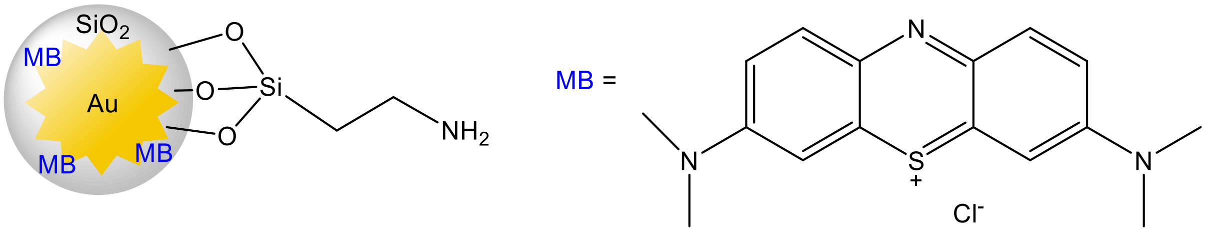

Figure 2.9: Probe design, where 'MB' represents the methylene blue reporter.

The new probe design consists again of a gold core, though the shape was changed from a nanosphere to a nanostars. It has been established that gold nanostars produce a greater signal enhancement that nanoparticles, due to the well-known 'lightening rod effect' in which the points of the stars effectively act as antennae.[27,28] Nanostars also tend to absorb longer wavelengths than nanoparticles, absorbing in the visible red region [29,30]. This is beneficial as it increases the likelihood for resonance Raman enhancement, as the wavelength used for Raman experiments was 785 nm.

The probe also has a Raman reporter, making it 'extrinsic'; this means that a spectrum of the reporter is acquired in experiments, as opposed to the analyte. This system requires the probe to specifically bind to the analyte, such that a signal would be observed if the target is present, and no signal would be observed if the target was not present (assuming excess probe is rinsed away). [31] Extrinsic probes are idea for analysing biological samples, which often have noisy spectra due to the many compounds present and can lack favourably strong Raman bands. Over the reporter layer, there is a thin silica coating to keep the methylene blue in place and improve reproducibility, followed by the addition of linker molecule (3-aminopropyl)trimethoxysilane (APTMS), which can then be used to bind a peptide with specific uptake in breast cancer cells. A peptide with specificity to breast cancer has been used initially for proof of concept, as this cell line was readily available. The system was later altered for the detection of human melanoma cells as described in Chapter 3.

2.2.3 Choice of Reporter

It was decided for several reasons that methylene blue (Figure 2.9) would be used as a Raman reporter. Most importantly, methylene blue has a λ_{max} value of 665 nm (Figure 2.10). When selecting a suitable Raman reporter, the main priority was to find a molecule absorbing close to the laser wavelength being used in Raman experiments, in order to utilise the SERRS effect.[32] The laser used for Raman experiments was 785 nm, both for its ability to penetrate several micrometres into the skin, and because autofluorescence of biological tissue is negligible at this wavelength. A reporter absorbing in the red region was therefore required.

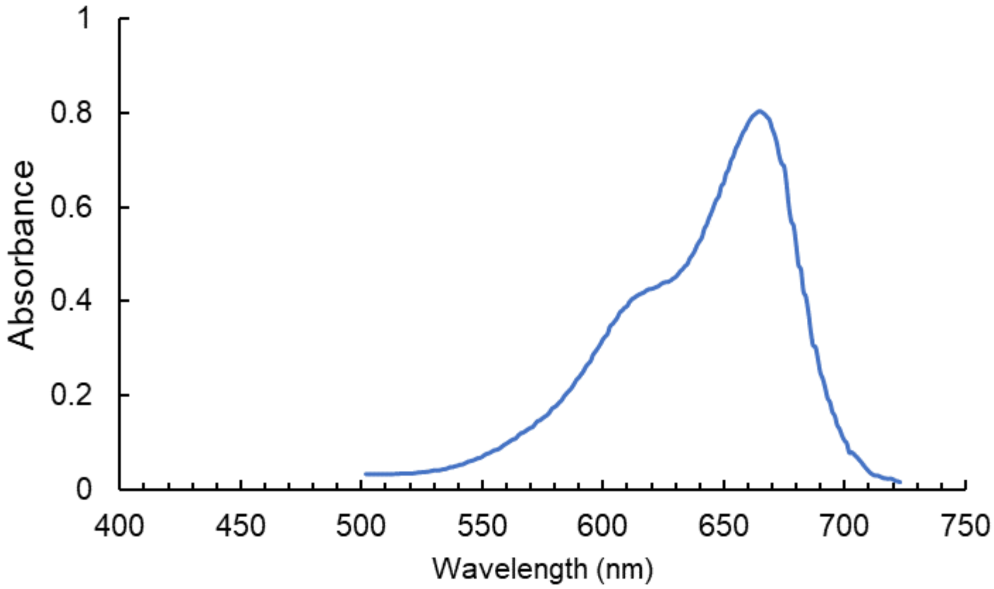

Figure 2.10: UV-Vis spectrum of methylene blue. Spectral data was acquired from Fluorophores.org.

Although it would be possible to find molecules with a λ_{max} value closer to 785 nm, there are other benefits to using methylene blue: it is a non-fluorescent dye, minimising background noise in Raman spectral acquisition; it gives strong Raman signals which allow the probe to be easily identified in spectra; and it has been FDA approved for medical use.[33] Methylene blue has also been shown to bind to gold surfaces via electrostatic interactions,[34] meaning it can be deposited directly onto the surface of the gold without any further modifications to the molecule. Granted, methylene blue does not adhere to the surface as strongly as a covalently bonded reporter would, however this issue can be overcome by applying a silica coating to the probe, trapping the methylene blue layer in place.

2.2.4 Gold nanostar synthesis

Gold nanostar (AuNS) synthesis is typically a two-step process in which 'seed particles' (gold nanoparticles around 5 nm in diameter) are synthesised using a sodium chloroaurate or chloroauric acid, and a reducing agent. A structure directing agent such as silver nitrate is then reduced in situ and silver is deposited on {110} facets of the gold surface, before further choroaurate is added to build up the gold 'points' of the stars on top of these silver deposits (Scheme 2.7 a).[35]

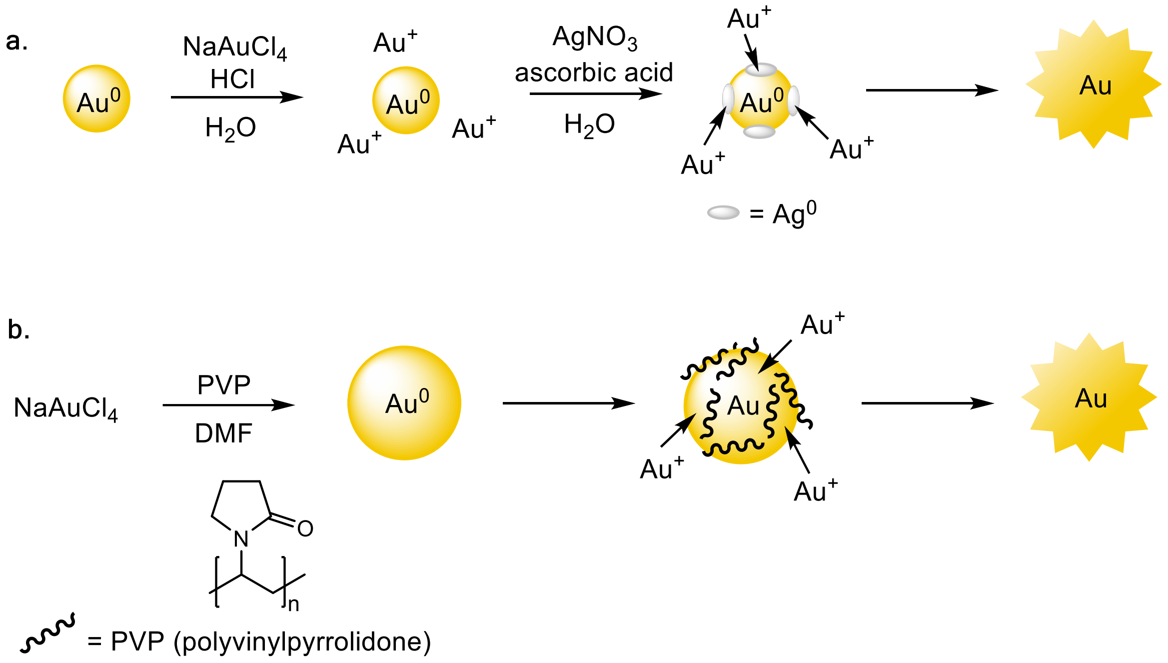

Scheme 2.7: Two methods for gold nanostar synthesis. A, the most common 'two step' method, using pre-made gold seed particles; and B, a 'one pot' method.

Other groups such as Kedia *et al.* have reported one pot methods, in which a single reagent such as polyvinylpyrrolidone (PVP) can act as a reducing agent for seed formation, a structure directing agent for point growth, and a stabilising agent (Scheme 2.7 b).[36] There are numerous theories as to the mechanism for reduction of chloroaurate by PVP. Several groups suggest that Au^{3+} forms a weak coordination complex with an enolate form of PVP, and this unstable complex (the exact structure of which is disputed) rearranges to give Au(0) and pyrrolidone in its amide form, or chlorinated PVP byproducts.[36–39] On the other hand, Hoppe *et al.* proposes two mechanisms involving radicals (Scheme 2.8), in which either the metal ion directly abstracts a hydrogen atom from PVP to form an organic radical (which can then react further with the metal ion) or PVP degrades in the presence of the metal to form an organic radical.[40]

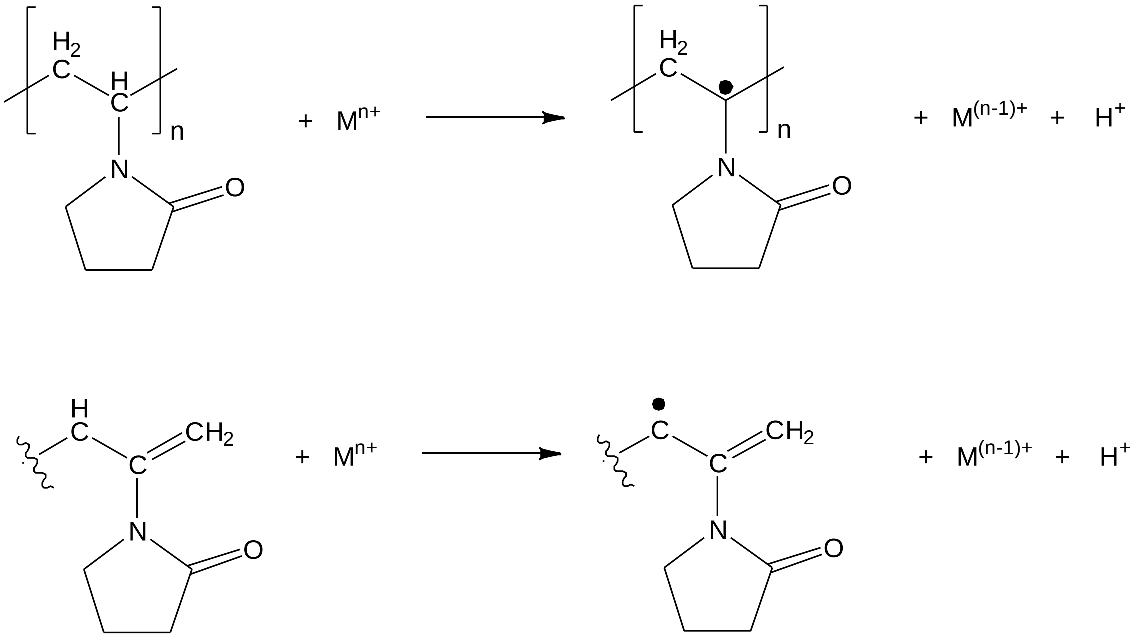

Scheme 2.8: Proposed mechanisms for the reduction of gold by PVP via radical intermediates.

PVP acts as a structure directing agent by binding selectively to Au{100} facets, preventing Au(0) deposits from building up in those areas.[36] PVP is also a good stabilising agent due to its hydrophobic carbon chains, which extend into the solvent and repel one another, thus stabilising the particles with steric hindrance.[41] The ‘two-step’ and ‘one-pot’ methods for gold nanostar synthesis from the literature (Schemes 2.7 a and b) were compared and adapted.

By comparing TEM images (Figure 2.11), it is clear that the two-step-method creates stars with more defined points, which have the potential for good signal enhancement. However, these points are not symmetrical or homogenous in length, and uniformity is preferred to ensure repeatable signal enhancement results. The one pot method on the other hand produced nanostars with many points roughly equal in length, although these points were not long or ‘sharp’ in appearance, such that the shape could be likened to popcorn more than stars.

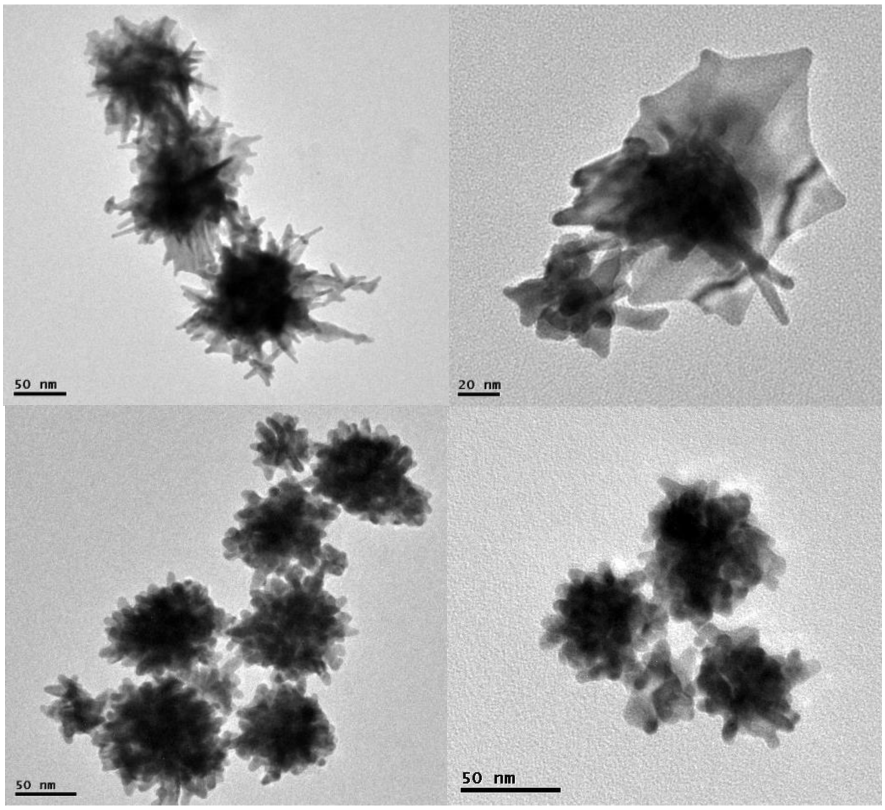

Figure 2.11: Top: gold nanostars made by the two-step method, without (left) and with (right) silica coating. Bottom: Gold nanostars made by the one pot method, without (left) and with (right) silica coating

Methylene blue and silica were applied to both nanostar batches, as shown in Scheme 2.9. These products are referred to as AuNS-MB@SiO_2, with MB denoting methylene blue and @SiO_2 denoting the silica coating.

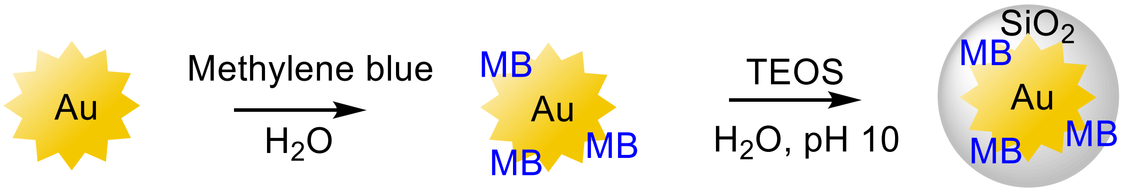

Scheme 2.9: Synthesis of AuNS-MB@SiO_2

Raman spectra (Figures 2.12-2.13) showed that the methylene blue peaks were significantly more enhanced, with less noise, using stars made by the one-pot method, as opposed to the two-step method. The most likely explanation for this is the thickness of the silica coating. Because the two-step-method produced stars with fewer points, the spaces between these points became clogged with silica in the coating process, as shown by TEM in Figure 2.11. The thickness of this coating most likely caused the reduction in Raman enhancement, as the SERS effect is distance-dependent. The one-pot method produced stars with more closely packed points; since the surface of these stars has fewer large troughs where silica build-up can occur, a much thinner more even coating was achieved. Considering all of this, the one-pot method was used for all syntheses going forward. These stars have an average point-to-point diameter of 55 nm, confirmed by TEM, and star-point plasmon resonance of 975 nm (Figure 2.14).

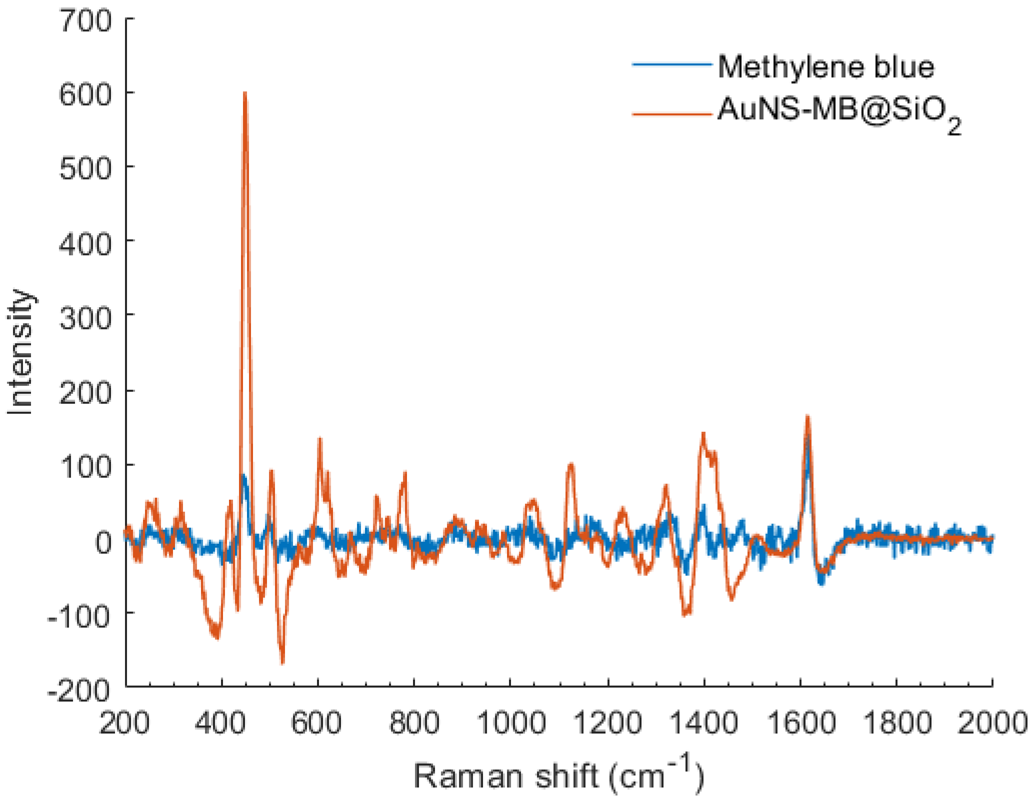

Figure 2.12: Raman spectrum of the SERS probe made by the one pot method, overlayed with the spectrum of the Raman reporter methylene blue (MB).

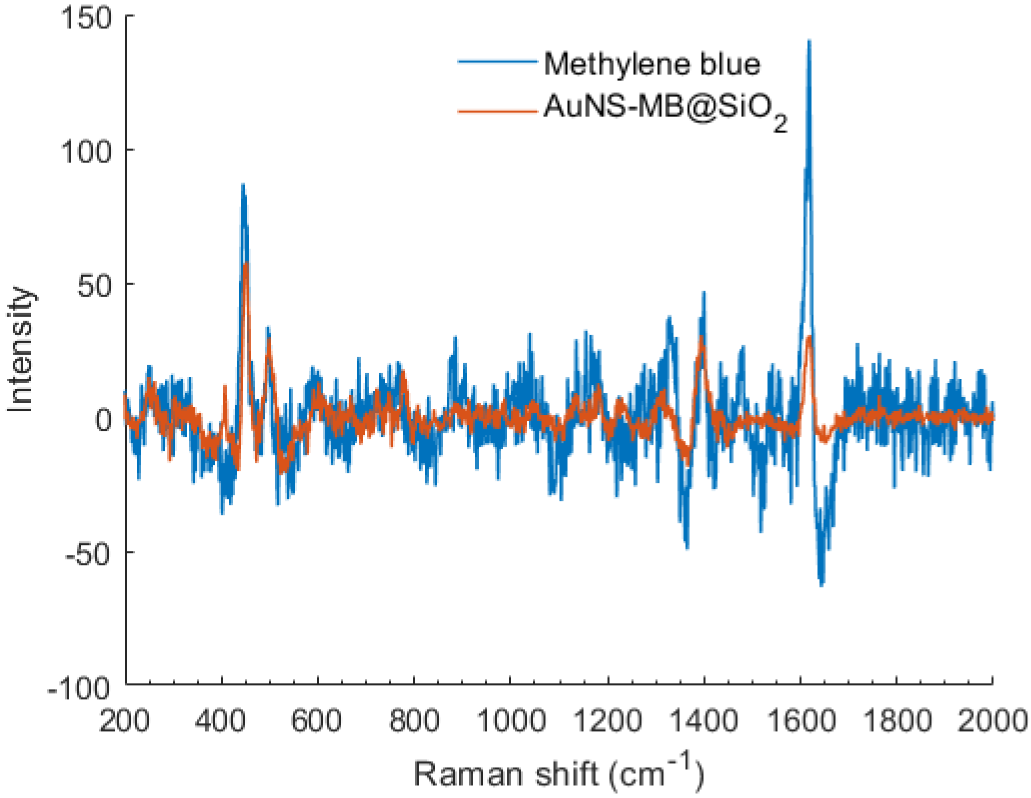

Figure 2.13: Raman spectrum of the SERS probe AuNS-MB@SiO$_2$ made by the two-step method, overlayed with the spectrum of the Raman reporter methylene blue (MB).

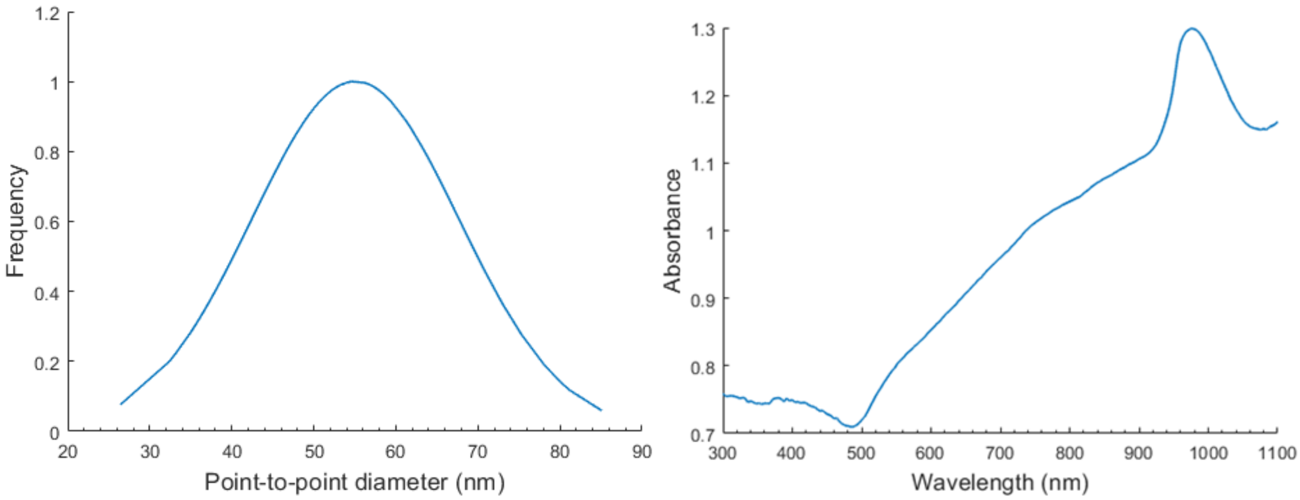

Figure 2.14: Size distribution (left) and UV-Vis spectrum (right) of gold nanostars. λ_{max} indicates plasmon resonance of the star points, while the broader peak across much of the spectrum indicates the plasmon resonance of the star core. The broadness of the peak can be attributed to the amorphous shape of the stars.

2.2.5 Probe Synthesis: Silica Coating Optimisation

The silica coating method, as used in previous synthesis, was adapted to produce the thinnest possible layer. The initial method of silica coating involved stirring the nanostars in a solution of TEOS for 16 hours, according to literature, and is the same method used in Section 2.1 for the coating of gold nanoparticles.[42] In contrast to particles, using this method with stars resulted in a thick coating, likely due to silica build-up between the points of the stars. This excess silica causes particles to stick together (Figure 2.15).

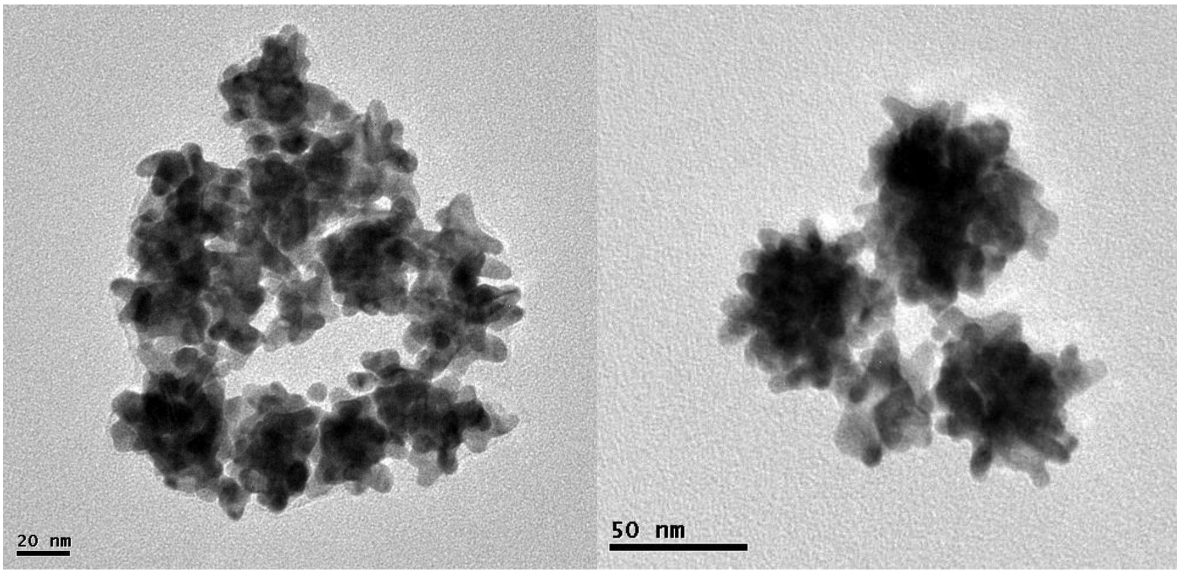

Figure 2.15: Left: silica coated nanostars before optimisation. An outline can be seen around the particles indicating a thicker coating, and the particles can also be seen sticking together in a 'clump'. Right: silica coated nanostars after optimisation.

Although this aggregation can cause increased SERS hotspots, the disordered nature of the aggregation makes signal enhancement too variable, and therefore is best avoided. An alternate coating method as described for use with gold nanoparticles by Li *et al.* was attempted, in which silica coating is carried out using (3-aminopropyl)trimethoxysilane (APTMS) and sodium silicate solution as opposed to tetraethyl orthosilicate (TEOS),[18] however this did not yield any coating and so it was decided instead that the best course of action would be to optimise the TEOS method. It was found that reducing the TEOS concentration any more resulted in no reaction occurring, so instead shorter stirring times were used. It was found that the reaction still took place after reducing stirring time from overnight to one hour, and a much thinner coating was produced (Figure 2.15, right). This resulted in enhanced signals of the methylene blue Raman reporter, and less noise (Figure 2.16).

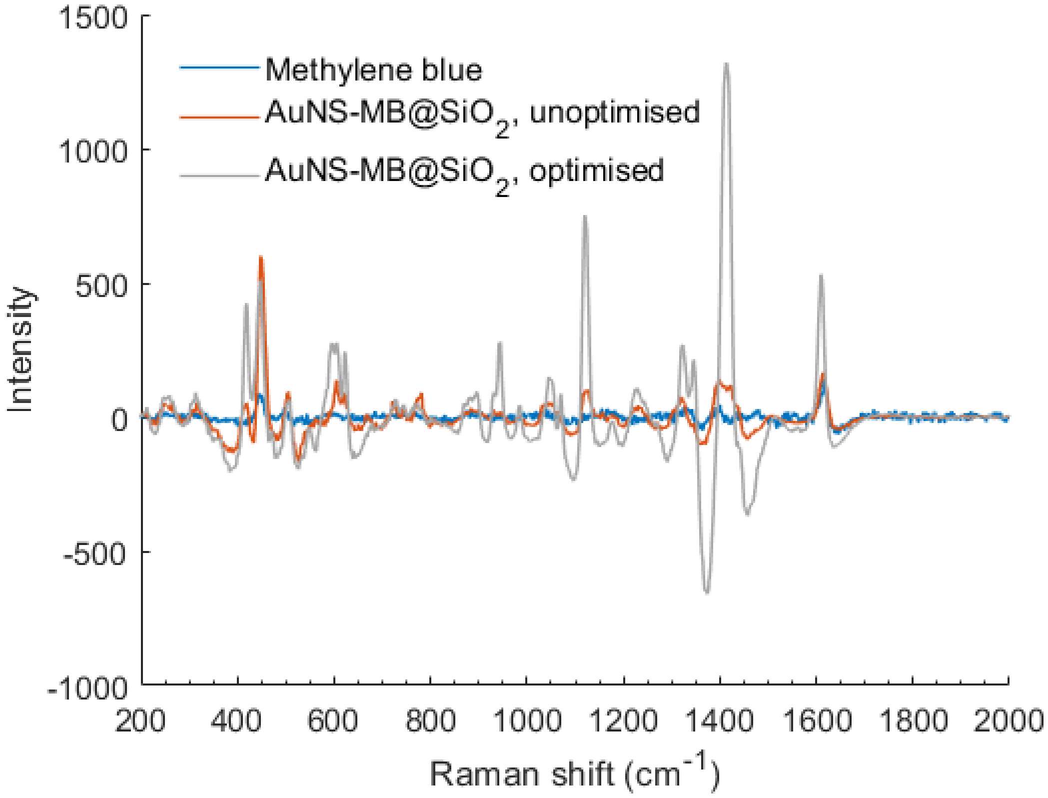

Figure 2.16: Raman spectra of the probe before and after optimising the silica coating method, with the spectrum of the methylene blue Raman reporter overlaid (MB).

The coating is not obvious via TEM at this resolution, however it is assumed to be present as it was possible to attach and observe the APTMS linker group, which bonds to the silica coating (Section 2.2.6). Silicone and oxygen are also observed in the EDX spectrum (Figure 2.17).

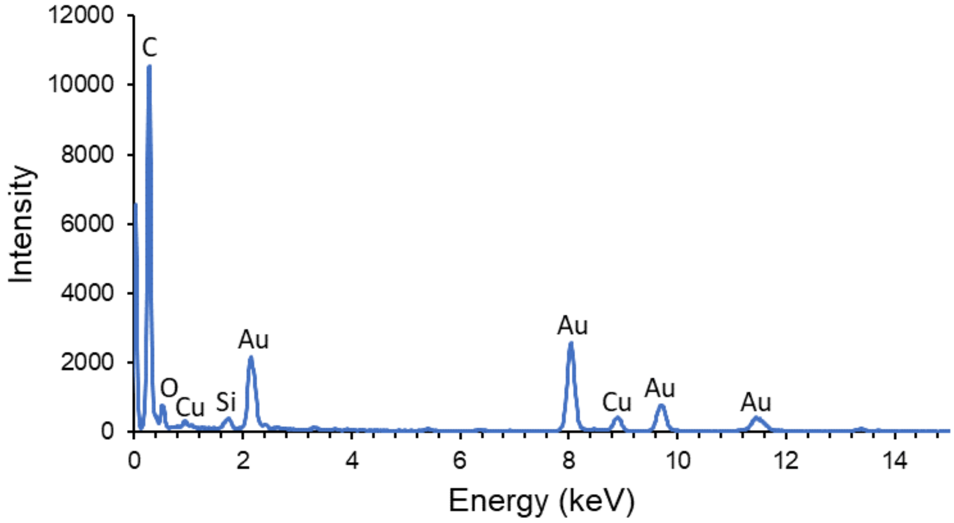

Figure 2.17: EDX spectrum of AuNS-MB@SiO₂

2.2.6 Linker Group Attachment

APTMS could be added immediately after the silica coating step, meaning that silica coating and linker addition could be carried out as a one-pot reaction (with reagents added sequentially). The ease of this optimised synthetic route, and its reduced reaction time, would greatly simplify the process of producing the probe commercially, if the final product reaches this stage.

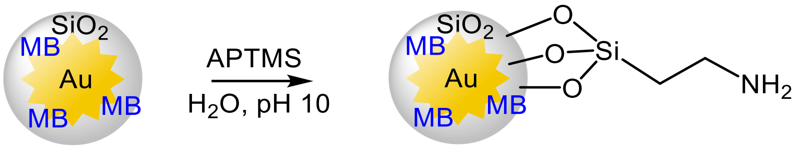

Scheme 2.10: APTMS functionalisation of AuNS-MB@SiO₂

The number of linker groups on the surface was determined by addition of a fluorescent dansylate group (Scheme 2.11) and calculating the moles of fluorescent species via Beer-Lambert Law (see Figure 2.18 for fluorescence spectra). By this method, it was determined that two in every three probes has a linker group, although results may be inaccurate due to surface enhanced fluorescence of the dansylate group caused by the nanostars. Failure to attach APTMS to some nanostars may be due to aggregation, making the star surface inaccessible.

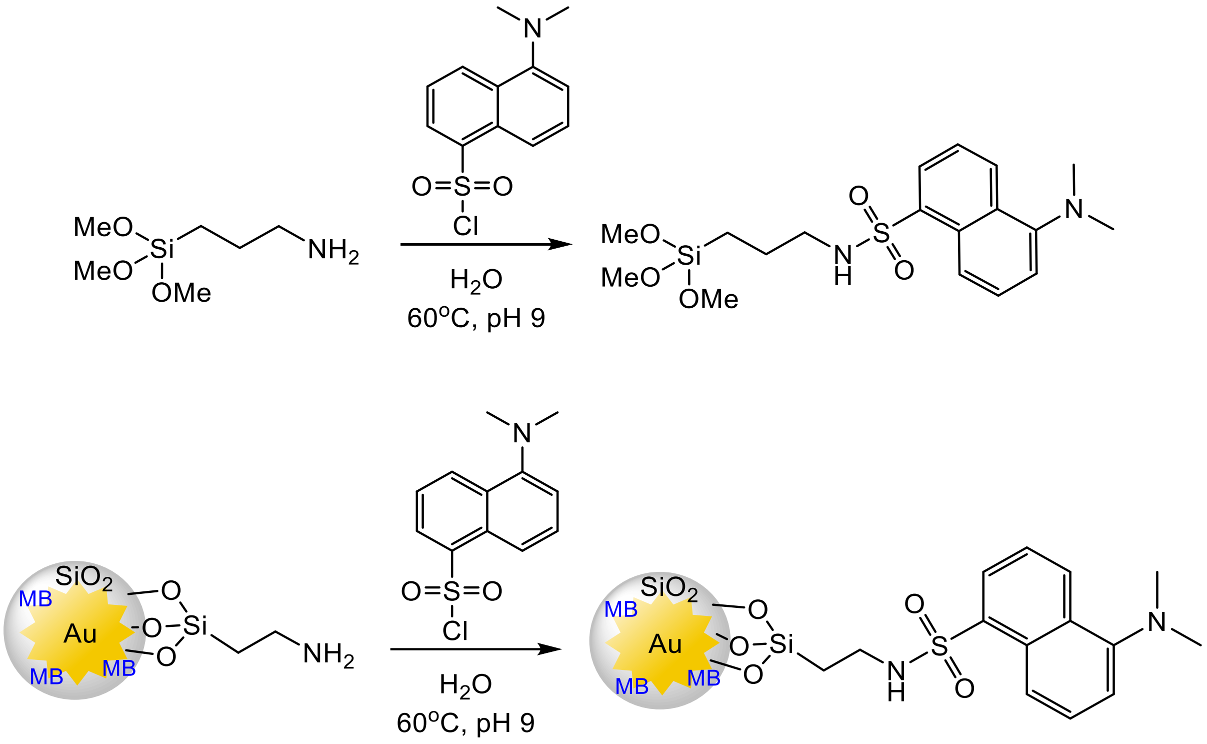

Scheme 2.11: Synthesis of dansylated APTMS and dansylated SERS probe

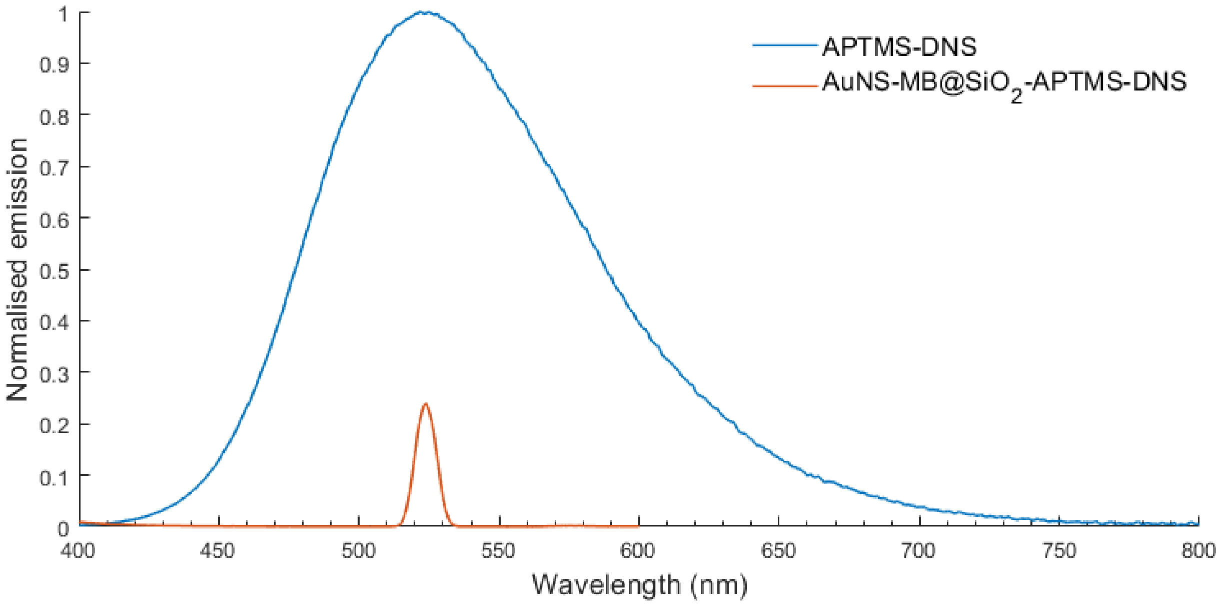

Figure 2.18: Fluorescence spectrum of the dansylated SERS probe with the fluorescence spectrum of dansylated APTMS solution on its own.

2.2.7 Specificity for MCF7

The APTMS linker group, with a terminal amine, allowed a peptide to be attached for specific binding to the human breast cancer cell line MCF7 (Scheme 2.12). This cell line was used for initial testing as it was readily available; the probe was later modified for melanoma targeting (Chapter 3). The peptide chosen was the chain DMPGTVLP (Figure 2.19), purchased from Biopeptek Ltd. This peptide has been utilised in numerous studies for targeting MCF7.[44] Studies by Bedi et al. show that this peptide binds to the surface of MCF7 cells, and that binding of a drug delivery vessel with this peptide incorporated into its structure was 2000 times higher than that of a non-specific vessel.[43] The effectiveness of this DMPGTVLP for creating a selective SERS probe to target MCF7 is explored in Section 2.4.

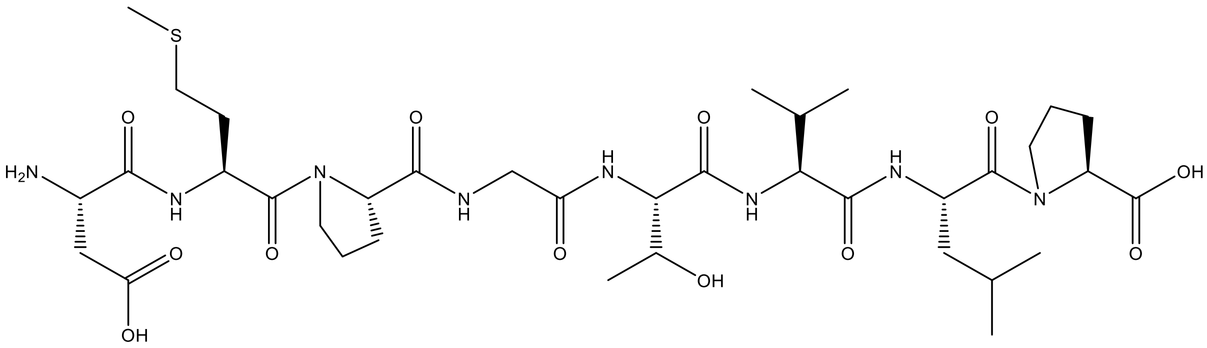

Figure 2.19: Structure of MCF7 selective peptide DMPGTVLP.

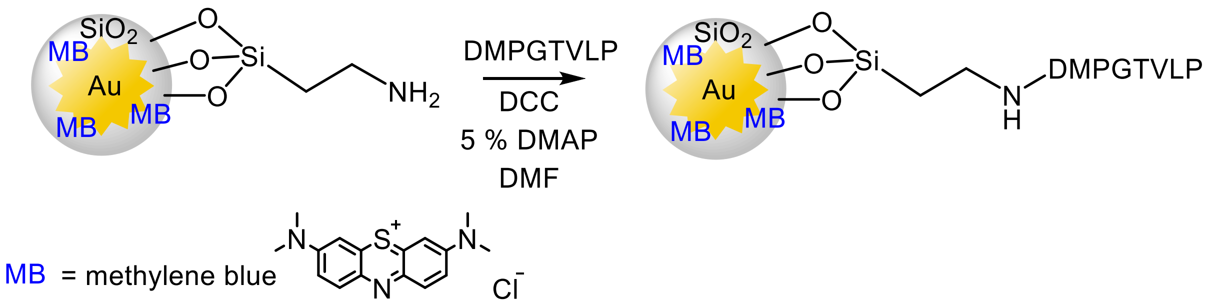

Scheme 2.12: Attachment of peptide DMPGTVLP to AuNS-MB@SiO$_2$-APTMS

2.3 Probe Characterisation

2.3.1 Limit of Detection

Raman spectra were acquired for the probe at varying concentrations, and the intensity of a prominent methylene blue peak at 512 cm^{-1} was plotted for each, showing a linear relationship between intensity and probe concentration (Figure 2.20). The limit of detection of the probe (the lowest theoretical concentration at which it is possible to detect the reporter, with the Raman instrumentation used in this report) was calculated using this linear relationship[45] and found to be 0.0025 mg ml^{-1}. Only three repetitions were used for this experiment, and a greater number would be required for more in-depth analysis.

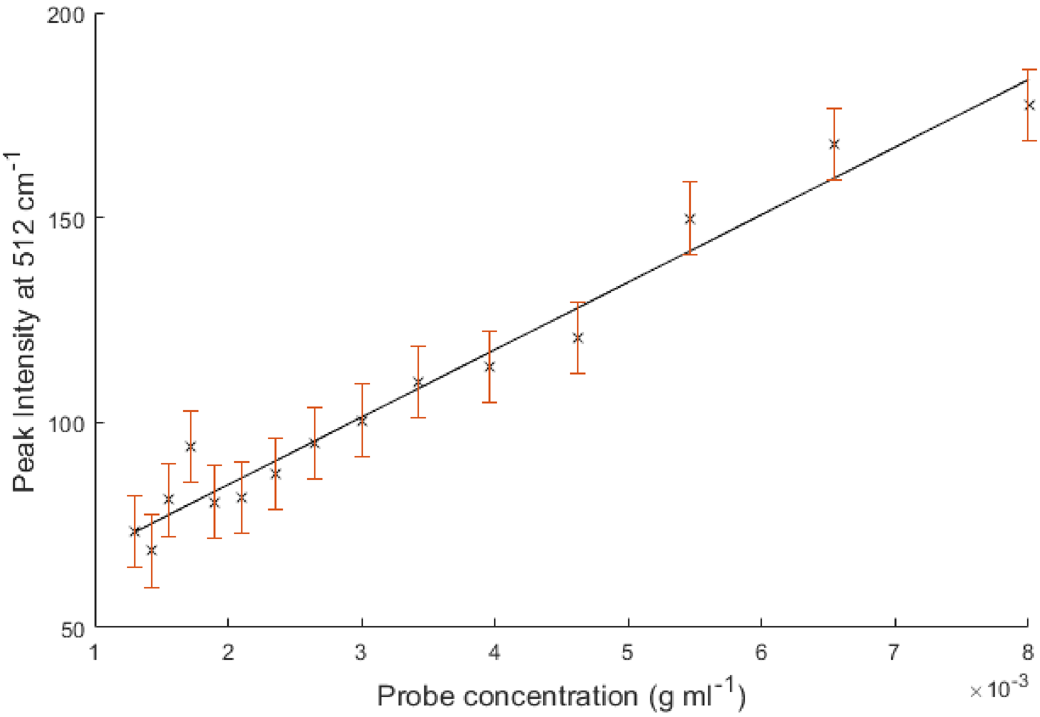

Figure 2.20: Plot of probe concentration against peak intensity of the methylene blue Raman reporter, for Raman spectra of the probe in solution. Error bars represent standard error.

2.3.2 Toxicity

To determine the toxicity of the probe, measurements were carried out as described in the experimental section. Toxicity experiments were carried out with all cell lines used in this work; MCF7 (chemotherapeutically resistant human breast cancer) for which the probe was initially designed, A375 (human melanoma cells) which the probe was later modified to target

(Chapter 3), and NIH 3T3 (mouse skin fibroblasts cells) which are used throughout as a control cell line. Results in Figures 2.21-2.23 show that the probe is non-toxic at working concentrations (concentrations of 0.5 mg ml^{-1} are applied to samples for SERS experiments), as there is no visible drop in cell viability with increasing probe concentration.

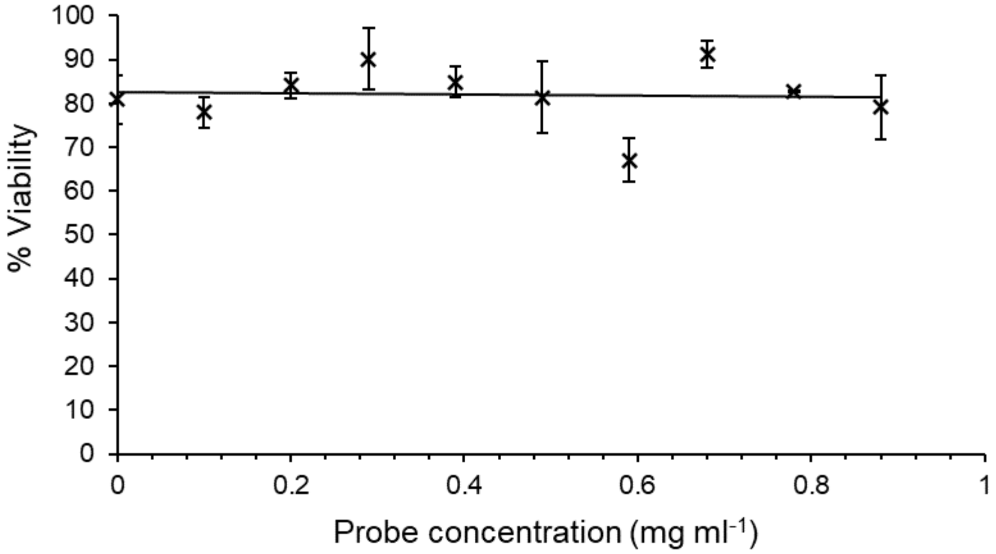

Figure 2.21: Plot of probe concentration against cell viability for MCF7. Error bars represent standard error

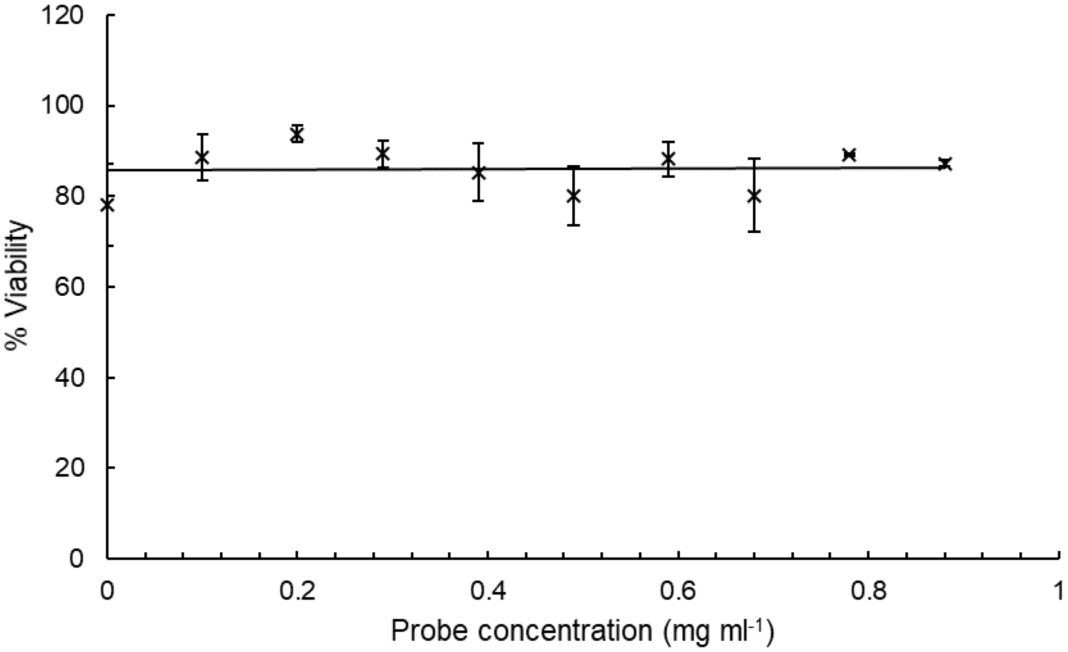

Figure 2.22: Plot of probe concentration against cell viability for NIH 3T3. Error bars represent standard error

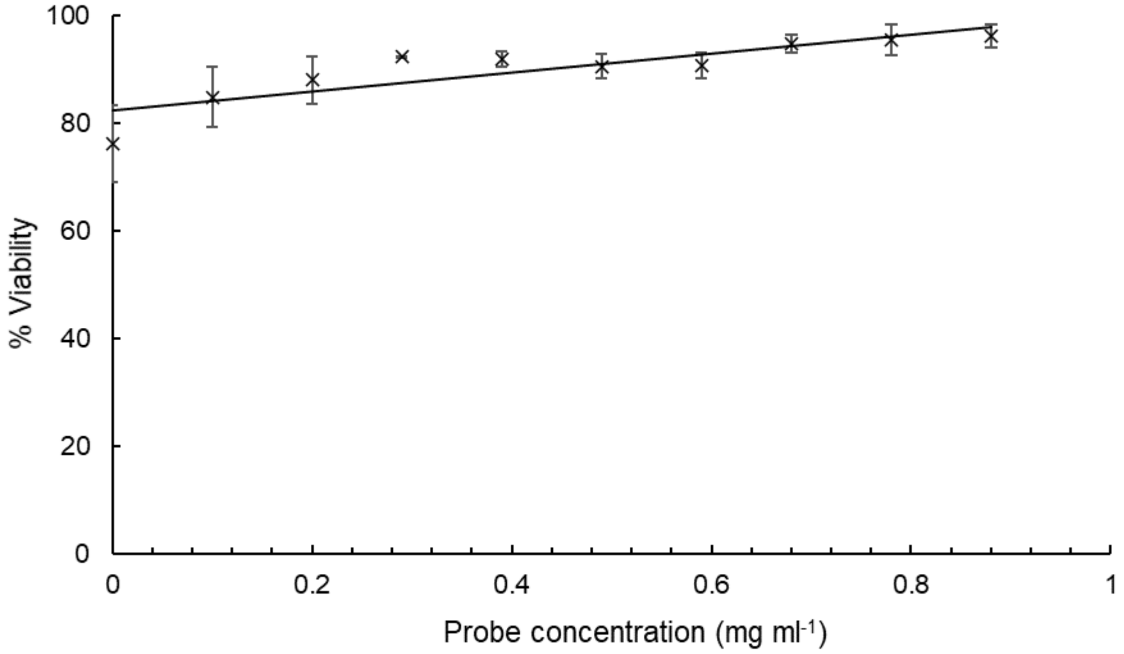

Figure 2.23: Plot of probe concentration against cell viability for A375. Error bars represent standard error

2.4 SERS Studies

Surface enhanced Raman experiments were carried out with MCF7 and NIH 3T3 cell lines to determine the selectivity of the probe for MCF7. The probe was applied to cell samples, and a Raman spectrum was acquired, before rinsing thoroughly with deionised water. A spectrum was then acquired again, to determine whether the probe would ‘rinse off’ non-target NIH 3T3 cells and bind selectively to MCF7. The experiments were also repeated using a ‘control probe’, *i.e.* a probe without an attached peptide, to determine whether the peptide was responsible for selective binding. Spectra are shown in Figures 2.24-2.27. Negative Raman intensities are a result of baseline correction carried out using MATLAB.

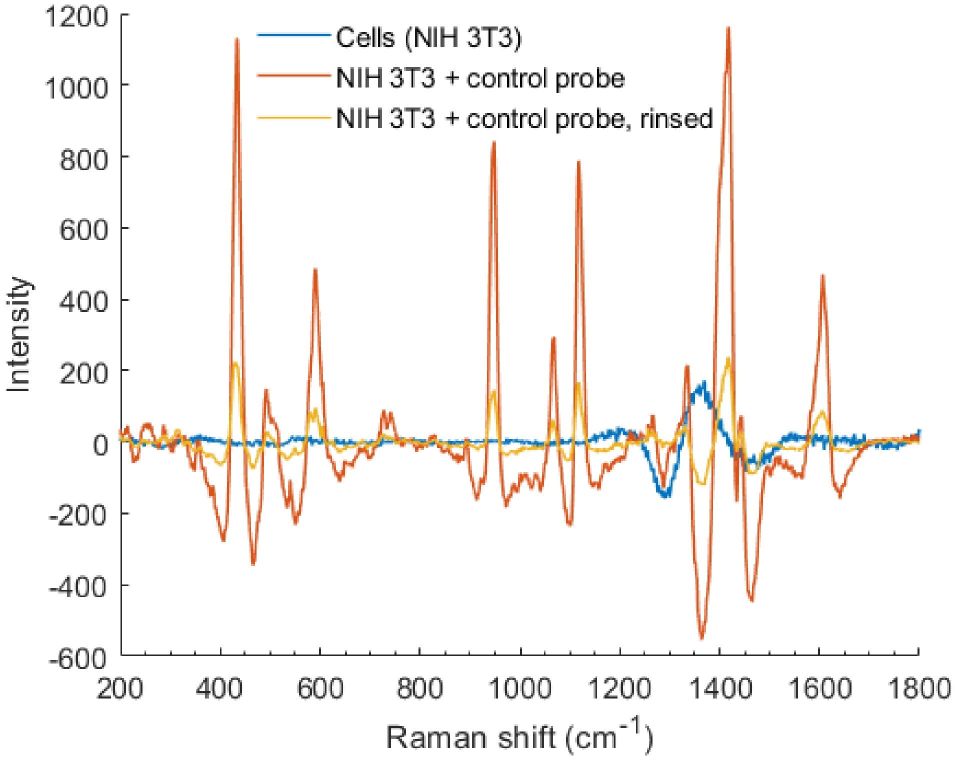

Figure 2.24: Raman spectra of NIH 3T3 cells with non-selective control probe, before and after rinsing.

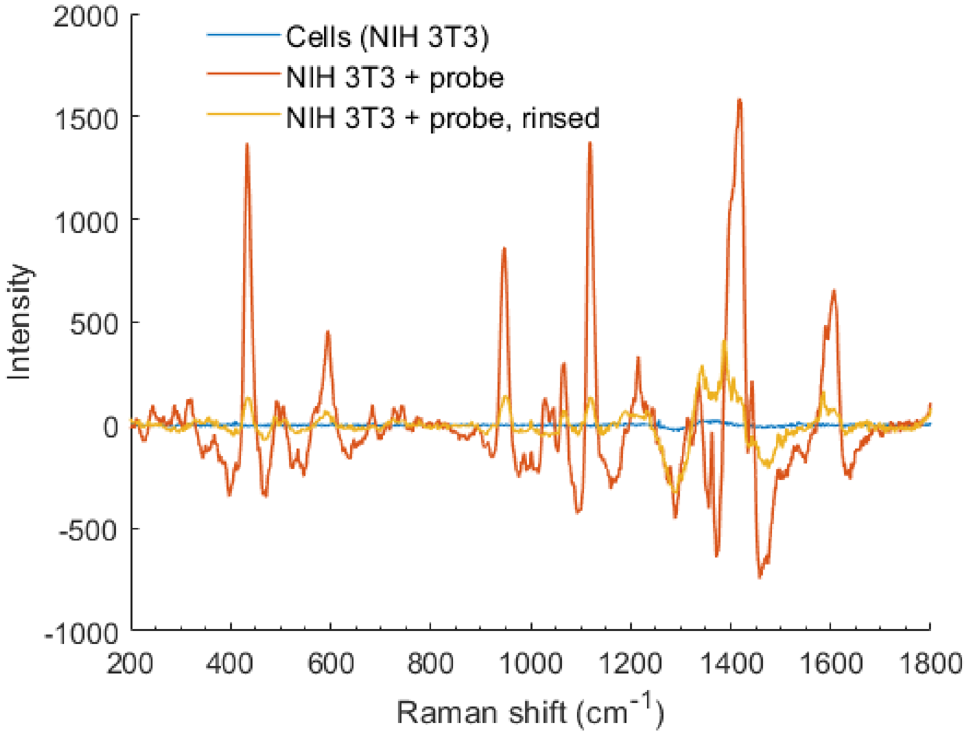

Figure 2.25: Raman spectra of NIH 3T3 cells with probe, before and after rinsing.

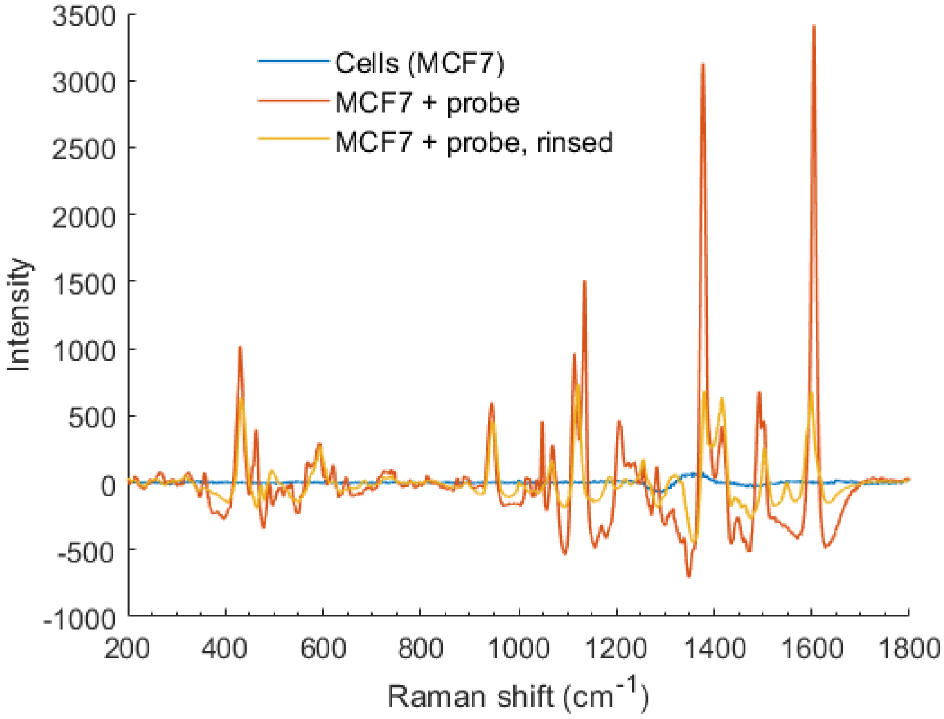

Figure 2.26: Raman spectra of MCF7 cells with probe, before and after rinsing.

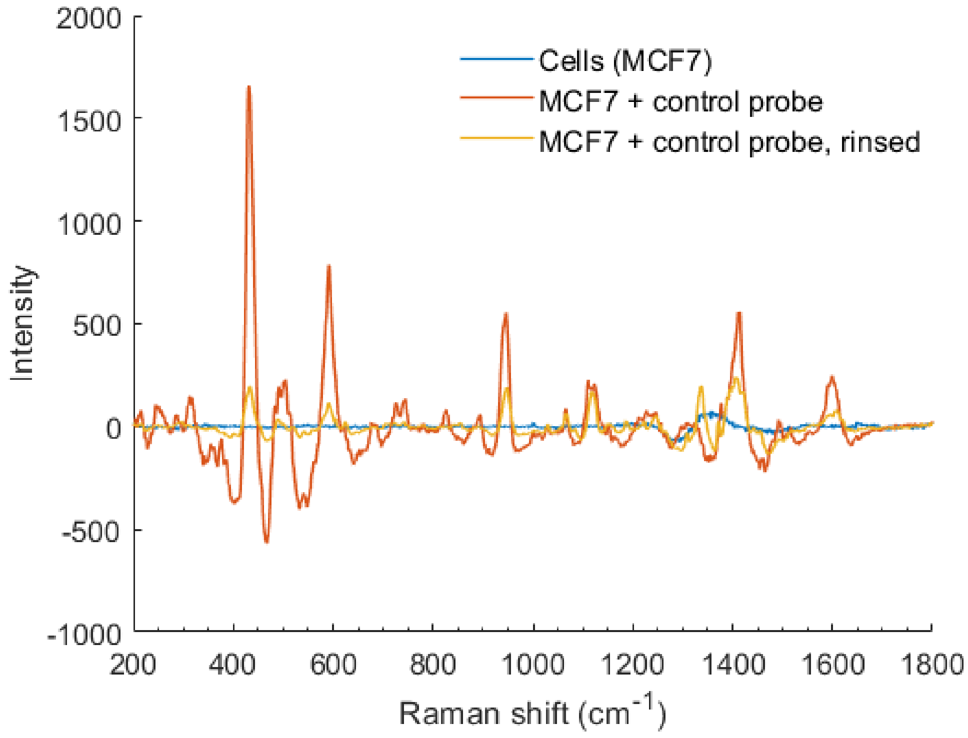

Figure 2.27: Raman spectra of MCF7 cells with non-selective control probe, before and after rinsing.

Figures 2.24-2.25 show that the probe (both the selective probe and the unselective control) does indeed rinse out of NIH 3T3 cells, as a distinct drop in signal is observed. Signal loss is also observed when the dosed MCF7 cells are rinsed (Figure 2.26), though not as much as in NIH 3T3, particularly in the region 400-1000 cm^{-1}. This suggests that probe does bind selectively to MCF7. Signal loss is also observed when MCF7 cell samples containing the non-selective control probe are rinsed (Figure 2.27), however a significant amount of signal remains, suggesting that not all of the probes have been removed on rinsing.

The residual amounts of probe in NIH 3T3 after rinsing, as well as the residual control probe in MCF7 after rinsing, could be attributed to the EPR effect. These experiments are also flawed as it is not possible to rinse the cells vigorously enough to remove all residual probe, without rinsing the cells themselves off the slides, which may also be the reason that signal is not completely lost from NIH 3T3, or from MCF7 with the control probe, upon rinsing. However, it is clear that SERS signals after rinsing are much less diminished in MCF7 with the selective probe, suggesting that the peptide does contribute to selectivity. Because removal of all traces of unbound probe may not be possible with rinsing, a 'minimum signal height' must be decided upon for clinical use, in order for an operator to confirm selective probe binding, based on peak intensity.

2.5 Confocal Microscopy

To further evaluate the specificity of the probe, laser scanning confocal microscopy (LSCM) was carried out with MCF7, using NIH-3T3 cells as a control. As an additional control, the probe was also tested with and without the MCF7 specific peptide. Because the probe is non-fluorescent, the structure needed to be modified to make it visible by LSCM, which usually requires samples to be stained with a fluorophore. The methylene blue reporter was therefore replaced with cresyl violet (Figure 2.28), a structurally similar but fluorescent dye. This fluorescent probe was again made with and without the MCF7 specific peptide; these analogues will be referred to as 'CV-probe' and 'CV- control probe' respectively.

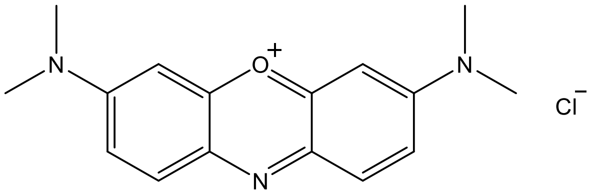

Figure 2.28: Structure of cresyl violet fluorescent dye.

The CV-control probe, without peptide, goes into both MCF7 and NIH 3T3 cells indiscriminately (Figure 2.29). A likely reason for this is that the silica coating, which is highly hydrophilic, is readily taken up by both cell lines. It is of course preferable that the CV-control probe would not go into the cells at all, so it can be assured that the probe will only give a signal when it is bound to the target cells via the selective peptide. One way to work around this could be to implement a hydrophobic coating. Alternatively, if methylene blue was replaced with an alternative reporter, binding more strongly to the surface, the need for a protective polymer coating may be all together redundant.

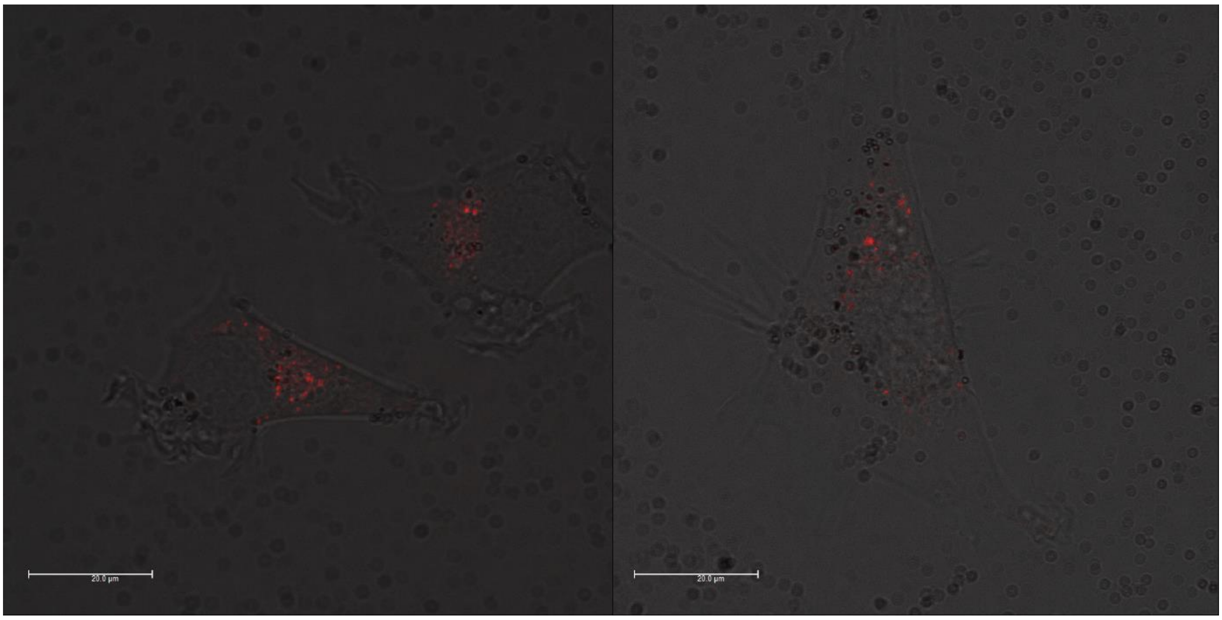

Figure 2.29: LSCM images of MCF7 (left) and NIH 3T3 (right) cells with the cresyl violet non-specific control probe, overlaid with bright field transmission light microscopy images. Transmission λ_{ex} 488nm; fluorescence λ_{ex} 633 nm, λ_{em} 650-800 nm. Uptake of the probe is evident from the red emission seen inside the cells. Scale bar 20 µm. Spots in the background are caused by the silica coated probe adhering to the glass coverslip.

The CV probe with the peptide attached is taken up into MCF7, as can be seen in Figure 2.30. In contrast, no uptake is observed with NIH 3T3. The reduced uptake into NIH 3T3 with the peptide-functionalised probe compared to the control probe is possibly caused by the peptide allowing the probe to be coated with proteins from the cell media, making it too large to be taken up by the cell. Despite this effect, the probe still has a greater affinity for the MCF7 cells due to the selective targeting peptide.

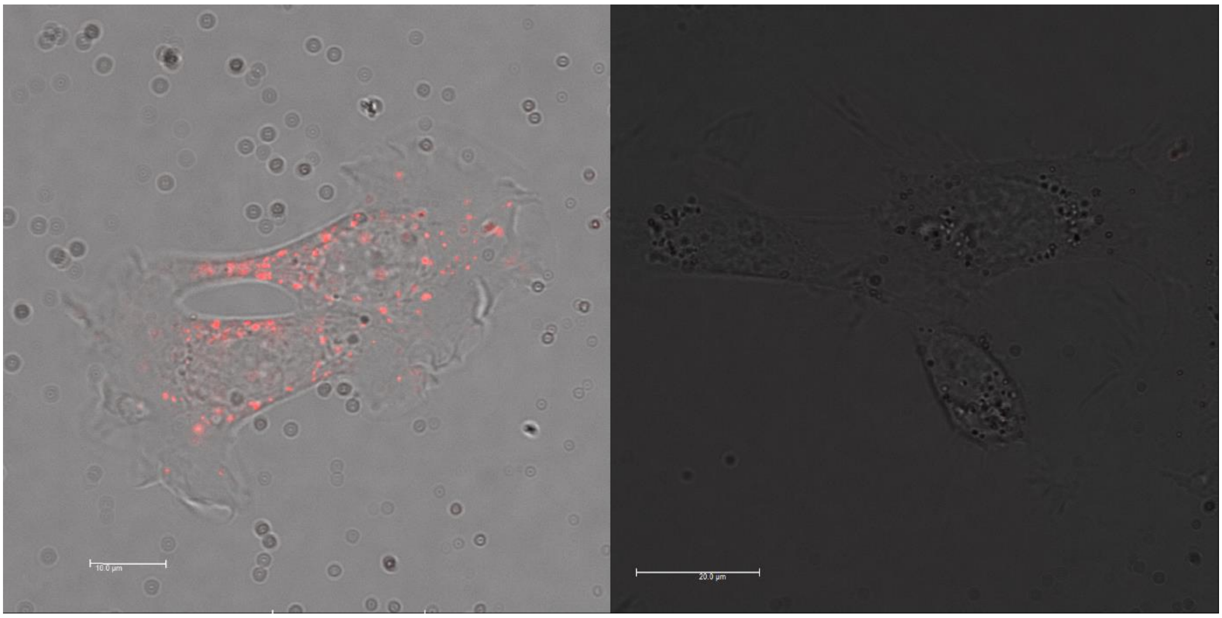

Figure 2.30: LSCM images of MCF7 (left) and NIH 3T3 (right) cells with the cresyl violet MCF7-specific probe overlaid with bright field transmission light microscopy images. Transmission λ_{ex} 488nm; fluorescence λ_{ex} 633 nm, λ_{em} 650-800 nm. In MCF7, uptake of the probe is evident from the red emission seen inside the cells; scale bar 10 µm. In NIH 3T3, no such uptake is observed; scale bar 20 µm.

2.6 Alternative Reporter Molecules

One of the challenges of designing an extrinsic SERS probe is finding a suitable Raman reporter. The main factors explored in most cases are the signal enhancing effects of the reporter, and whether it produces a strong, clear Raman signal. However, there is less emphasis on ease of synthesis, and cost. Following the success of the methylene blue reporter, the use of other commercially available red and near-infra red absorbing dyes were explored, as an economical alternative to current Raman reporters in the literature.

2.6.1 Comparison of Dyes

When choosing a reporter, it is desirable to have a molecule which absorbs close to the laser wavelength being used in Raman experiments, in order to utilise the SERRS effect. The laser wavelength used for experiments in this section is 785 nm, chosen for its ability to penetrate into tissue, and because it eliminates noise cause by the autofluorescence of biological material often observed with shorter wavelengths.

As an alternative to novel, custom-made reporters, which can be difficult and costly to synthesise, commercial dyes were tested as Raman reporters.[46–49] Several commercial dyes were incorporated into extrinsic probes and tested as an alternative to bespoke reporters. The structures and absorbance of four commercial near infra-red (NIR) dyes: HITCI, Styryl 9, and RH800, and IR806 are shown in Figures 2.31-2.34, with their corresponding Raman spectra in Table 2.1.

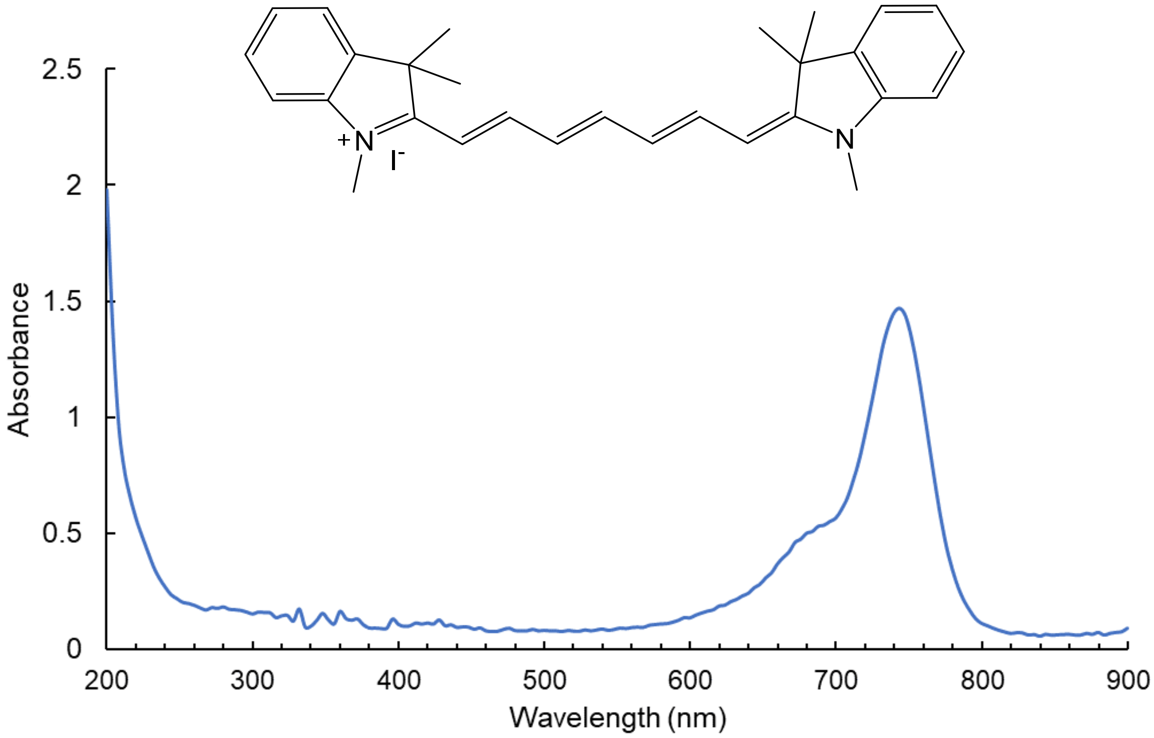

Figure 2.31: Structure and UV-Vis spectrum of HITCI in ethanol. Spectrum acquired by Dr Robert Pal.

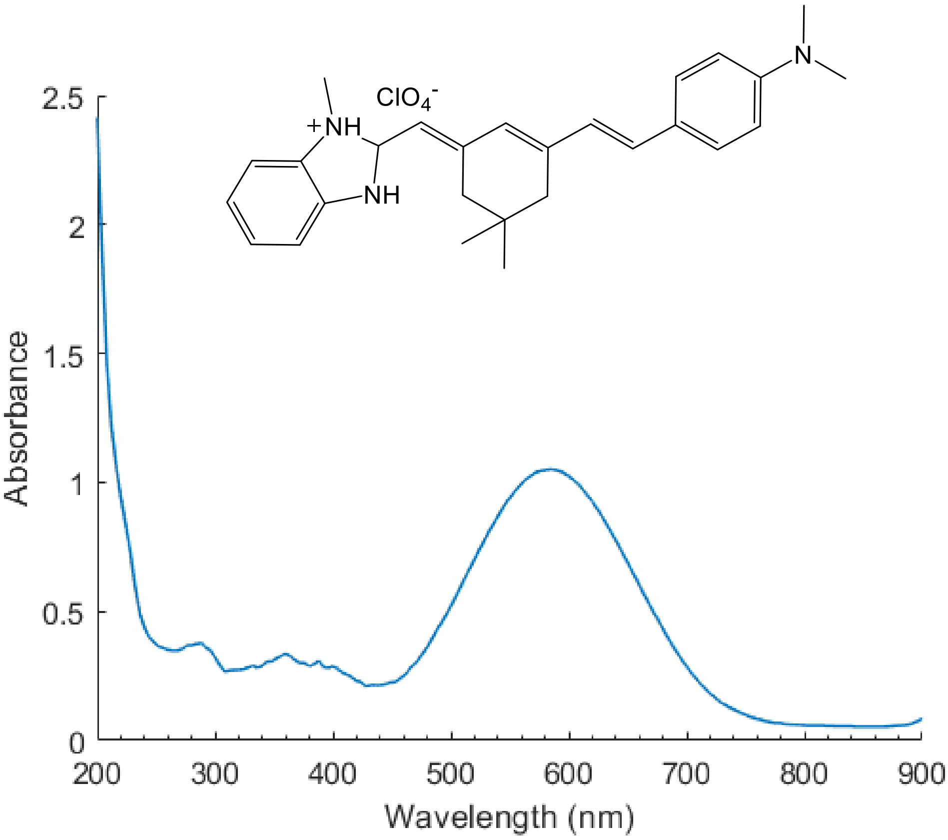

Figure 2.32: Structure and UV-Vis spectrum of Styryl 9 in ethanol.

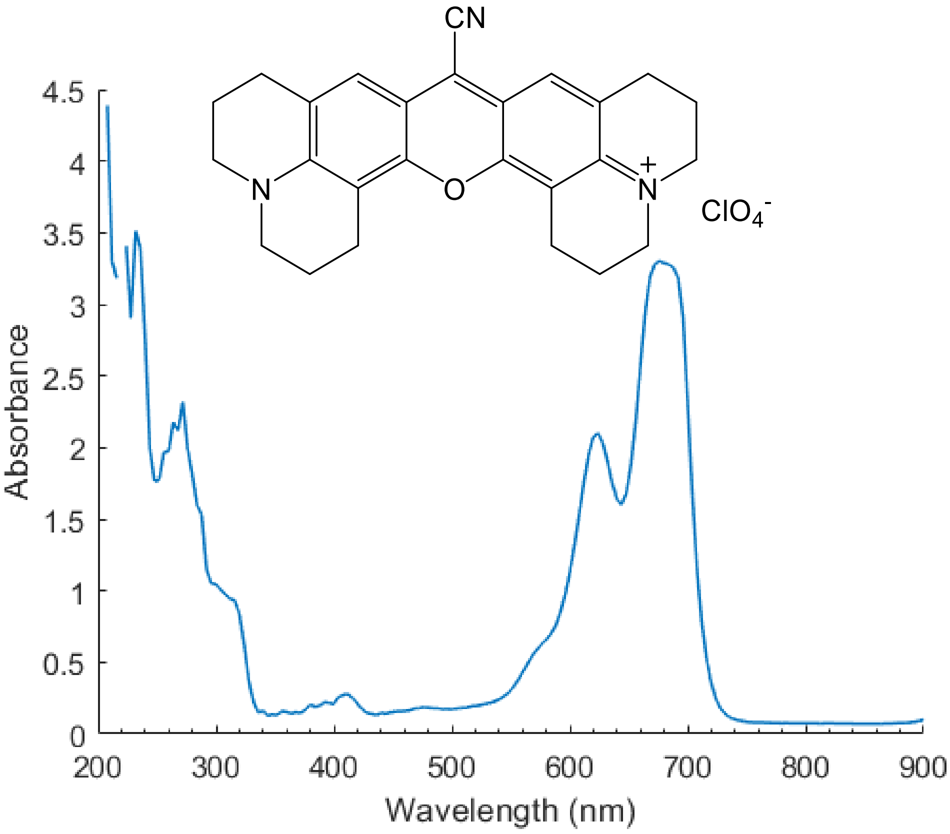

Figure 2.33: Structure and UV-Vis spectrum of Rhodamine 800 in ethanol.

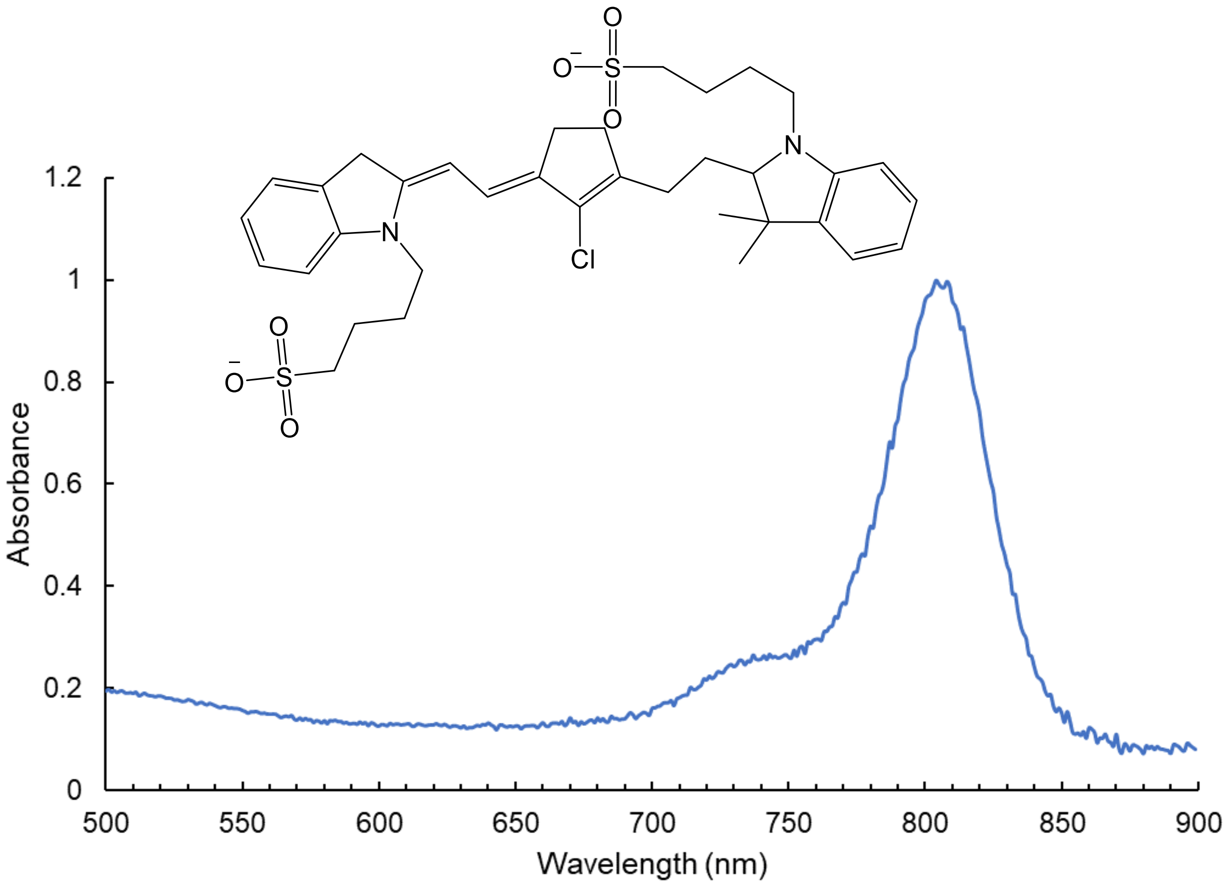

Figure 2.34: Structure and UV-Vis spectrum of IR 806 in chloroform. Spectral data was obtained from Fluorophores.org.

As can be seen by the UV-Vis spectra in Figures 2.31-2.34, all three dyes have some absorbance at 785 nm, which is ideal for resonance Raman effects. It is not necessary for the absorbance maximum to match 785 nm exactly; this may in fact cause a great deal of interference due to the florescence of the reporter.

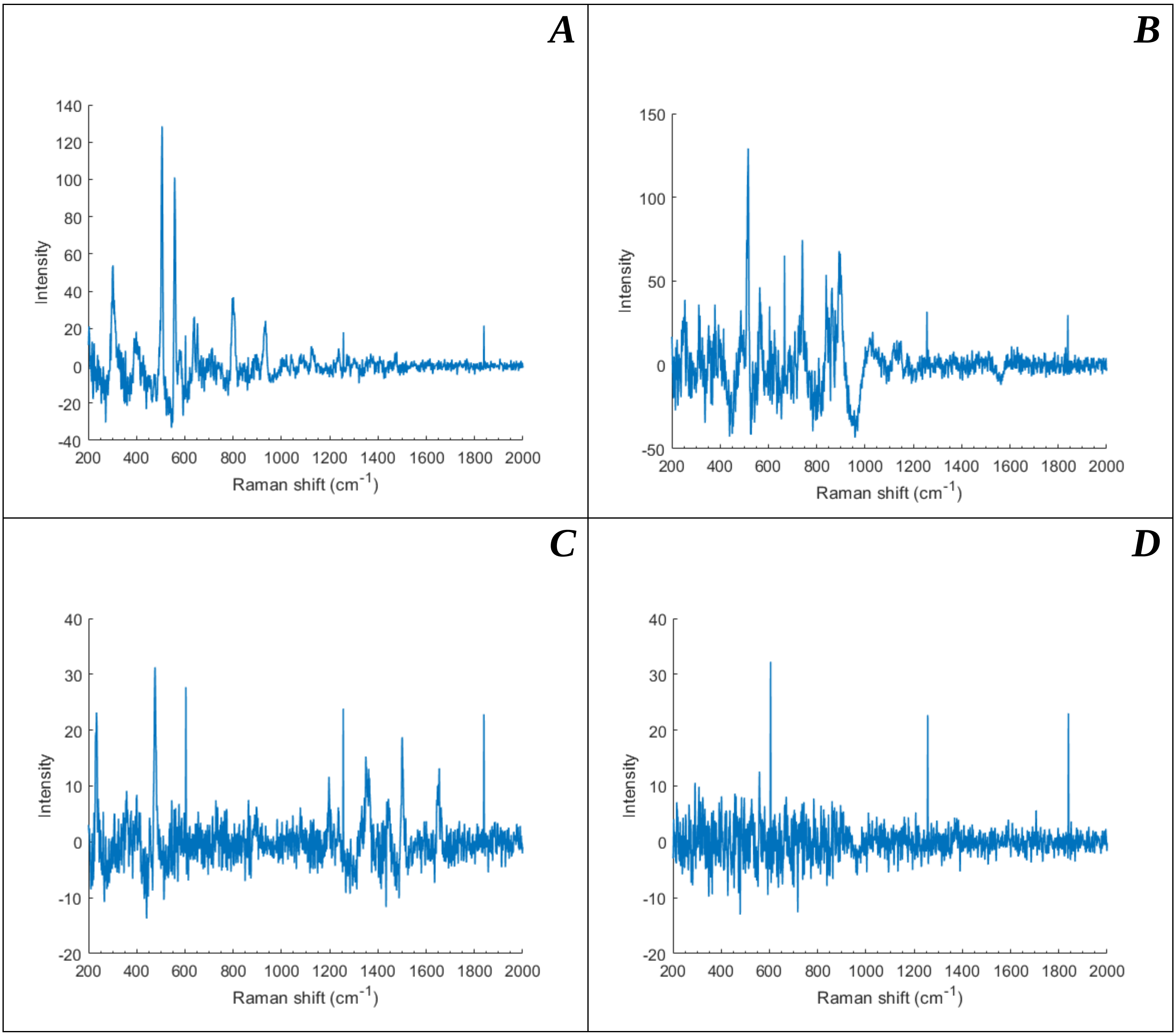

Table 2.1: Raman spectra of HITCI (A), Styryl 9 (B), Rhodamine 800 (C) and IR806 (D).

The Raman spectra of all four dyes were recorded as shown in Table 2.1. The spectra of IR 806 and rhodamine 800 do not have significant strong peaks, and although the spectrum of styryl 9 has some notable peaks, these are noisy and lack definition. These dyes were therefore not taken any further. HITCI however showed strong peaks at 506 and 558 cm^{-1}, as well as some defined peaks at 797 and 933 cm^{-1}, making it potentially an ideal reporter. A probe was therefore synthesised with HITCI as the reporter *(*Scheme 2.13). As with the previous probe using methylene blue, this was modified to be made selective with MCF7 cells and initially tested with this cell line.

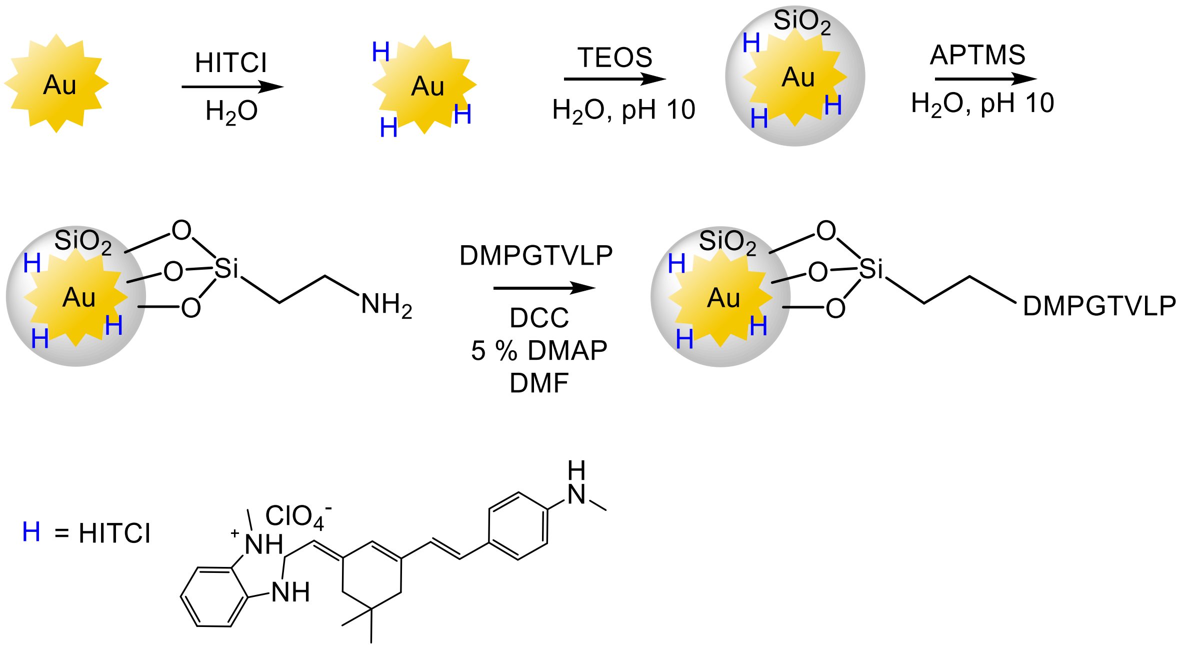

Scheme 2.13: Synthesis of AuNS-HITCI@SiO₂-APTMS-DMPGTVLP

2.7 Alternative Probe Characterisation

2.7.1 Limit of Detection

The limit of detection of the HITCI reporter probe was investigated. The intensity of a prominent peak in the Raman spectrum of HITCI, 503 cm^{-1}, was recorded at varying concentrations (Figure 2.35). The signal intensity is seen to increase with increasing concentration, though the exact relationship cannot be said to be linear due to the amount of error, as shown by the standard error bars on the graph below. This large difference in measurements at a given concentration, resulting in a large error, is likely caused by aggregation. Aggregation of the sample will lead to large clusters of the probe in certain areas of the sample, with very few individual probes between these clusters. Following from this, it is logical that some spectra would have amplified signals, due to the Raman hotspots of the aggregate cluster, and some spectra would have weak signals, due to large areas of sample with little probe at all. This lack of stability is a stark contrast to the methylene blue probe, which appeared stable in solution to the eye (the solution remained a deep blue, suggesting an evenly dispersed colloid, and the probe was not seen to ‘crash out’ of solution and collect at the bottom of the sample bottle) for around one month; much longer than the HITCI probe which would show visible signs of aggregation after around 3 days. This is also reflected in the limit of detection study of the methylene blue probe, as the margin of error is much lower. The reason for this disparity in stability is unclear.

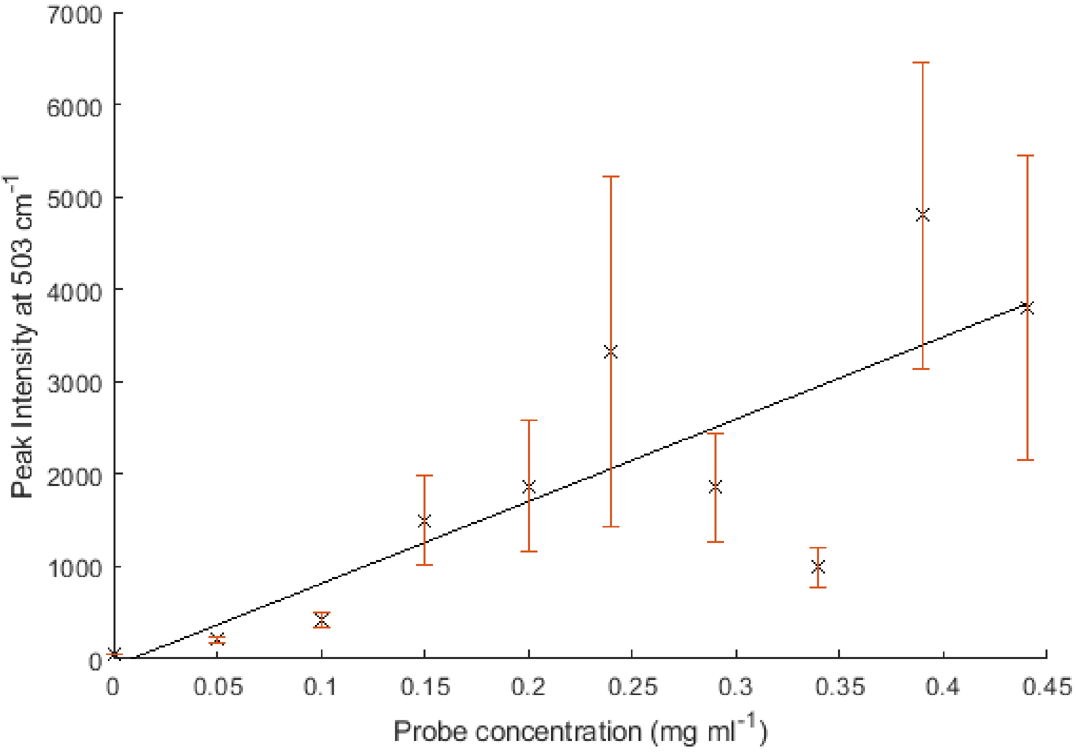

Figure 2.35: Limit of detection study of AuNS-HITCI@SiO$_2$, showing probe concentration against the intensity of a prominent peak at 503 cm^{-1} the Raman spectrum of HITCI . Error bars represent standard error, which is large due to instability of the probe in solution.

2.7.2 Toxicity

Dosing relevant cell lines (MCF7, NIH 3T3 and A375) for 24 hours showed no clear correlation between cell viability and probe concentration, as can be seen in Figures 2.36-2.38 below, so it can be said that AuNS-HITCI@SiO$_2$ is non-toxic at working concentrations.

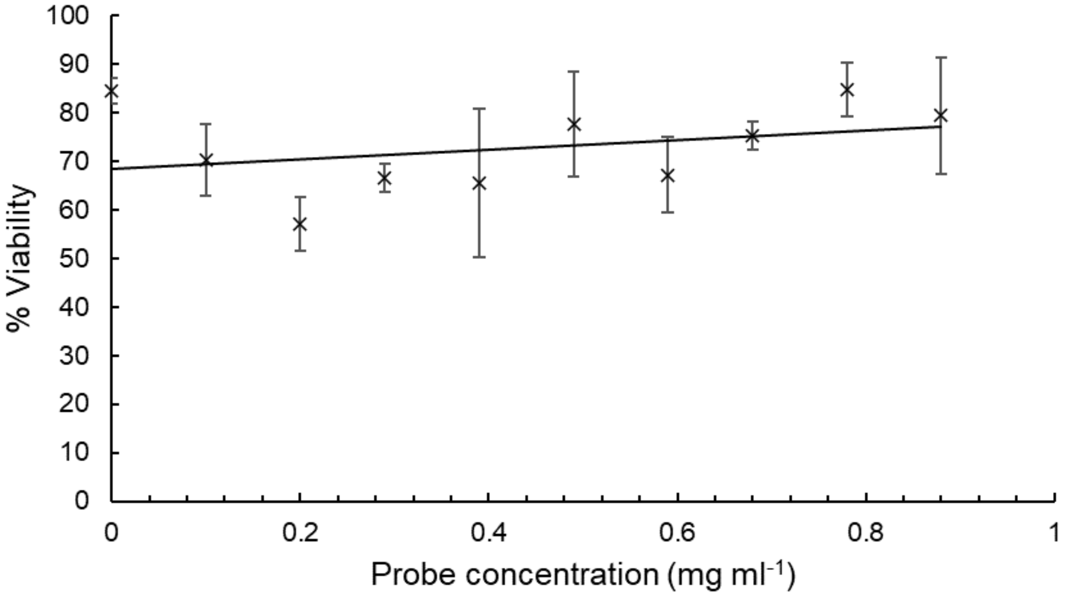

Figure 2.36: Plot of probe concentration vs cell viability for MCF7. Error bars represent standard error

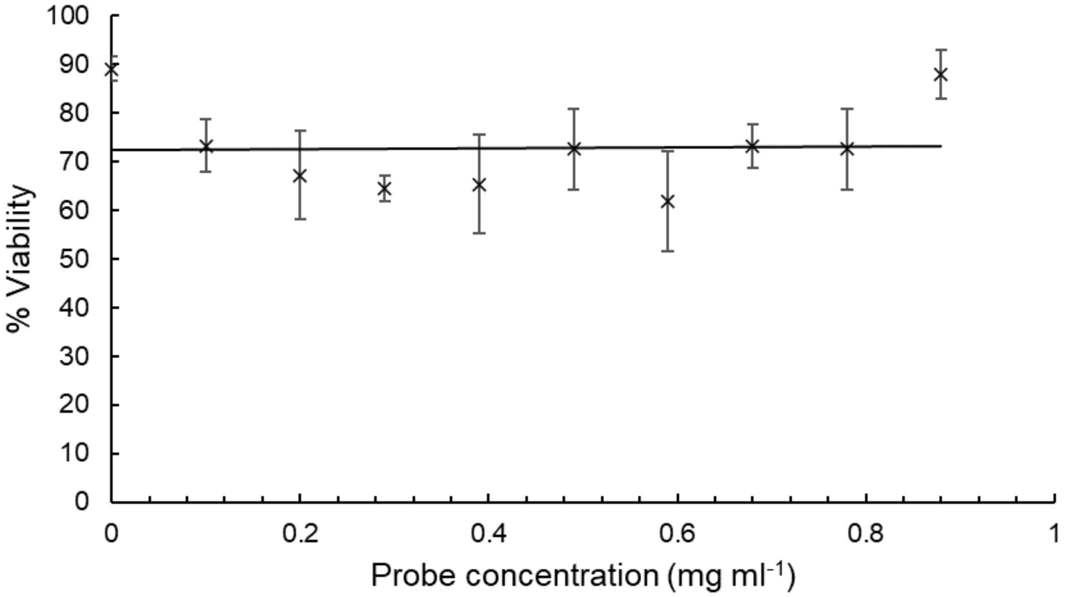

Figure 2.37: Plot of probe concentration vs cell viability for NIH 3T3. Error bars represent standard error

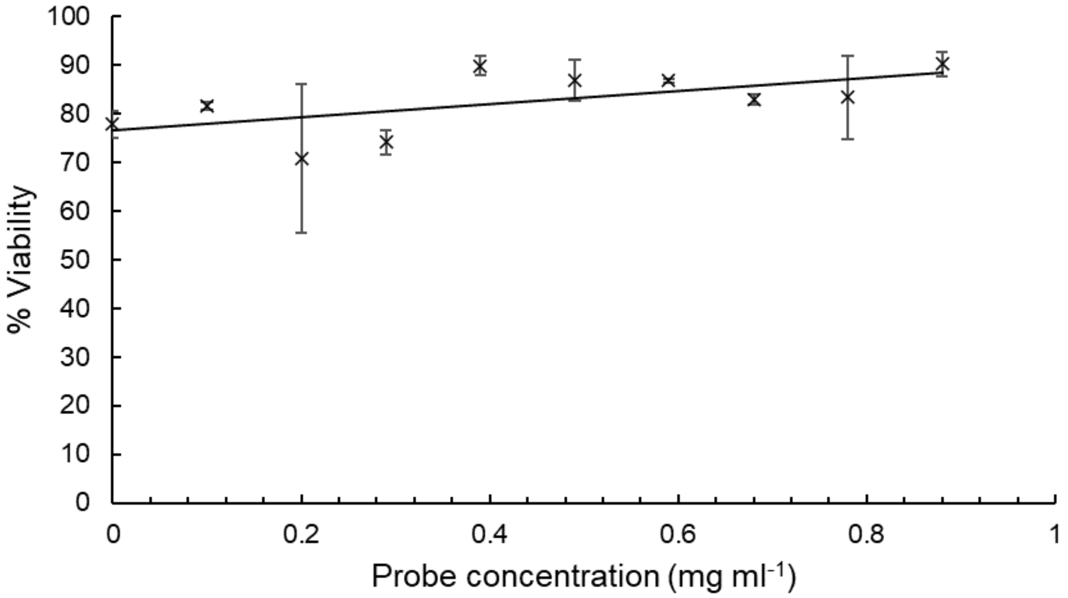

Figure 2.38: Plot of probe concentration vs cell viability for A375. Error bars represent standard error

2.7.3 SERS Studies

Surface enhanced Raman experiments were carried out using the peptide modified HITCI probe in order to determine its selectivity for the MCF7 cell line. After these preliminary tests, the probe could be modified for the A375 skin cancer cell line, as described in Chapter 3. Two different controls were used in these experiments. First, a control cell line, NIH 3T3, was compared with MCF7 to determine selectivity for MCF7. The experiment was also repeated with and without the peptide DMPGTVLP to determine that it was this component of the probe affecting selectivity. The term ‘control probe’ is used to refer to the probe without the selective peptide attached. Results are displayed and discussed below. Experimental set-up is detailed in Chapter 6. Negative Raman intensities are a result of baseline correction carried out using MATLAB.

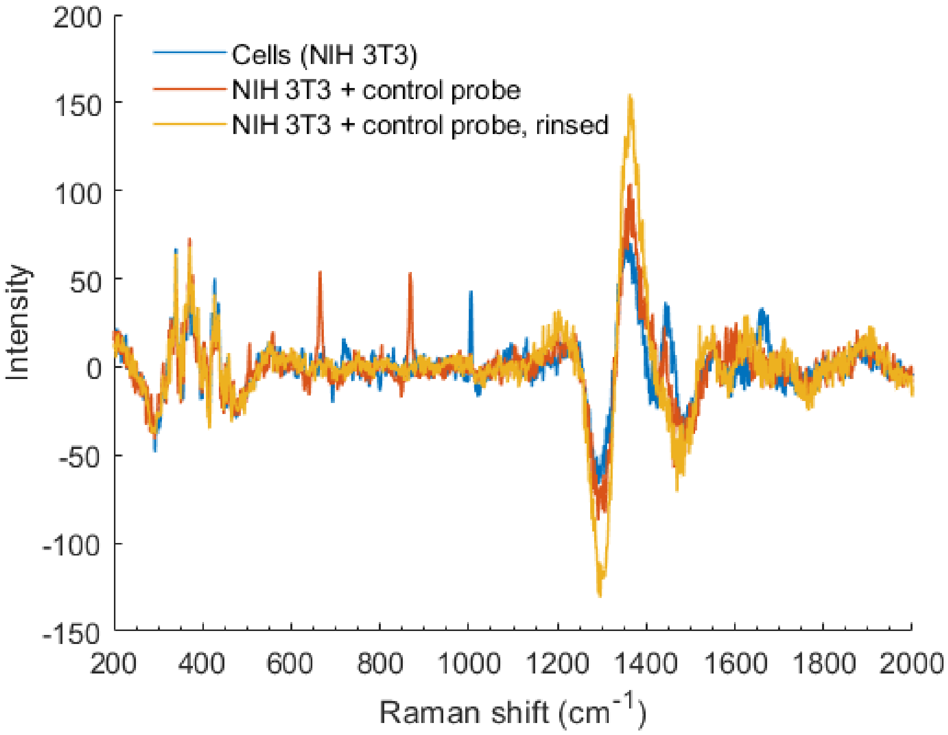

Figure 2.39: SERS spectra of NIH 3T3 cell pellets with AuNS-HITCI@SiO$_2$, without peptide

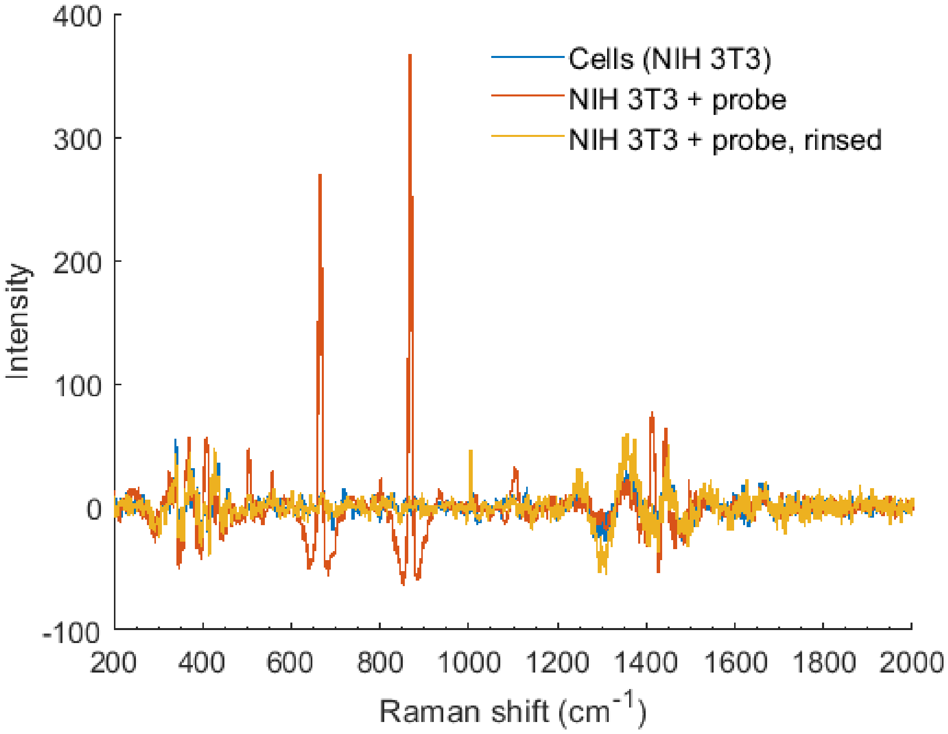

Figure 2.40: SERS spectra of NIH 3T3 cell pellets with AuNS-HITCI@SiO$_2$-DMPGTVLP

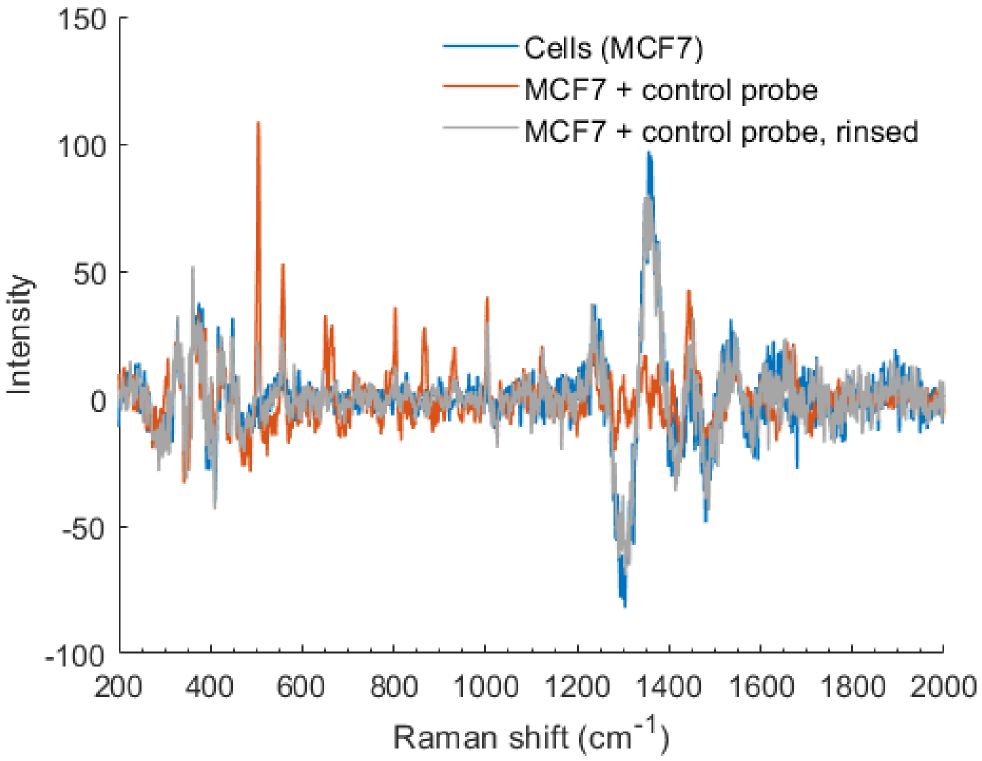

Figure 2.41: SERS spectra of MCF7 cell pellets with AuNS-HITCI@SiO$_2$

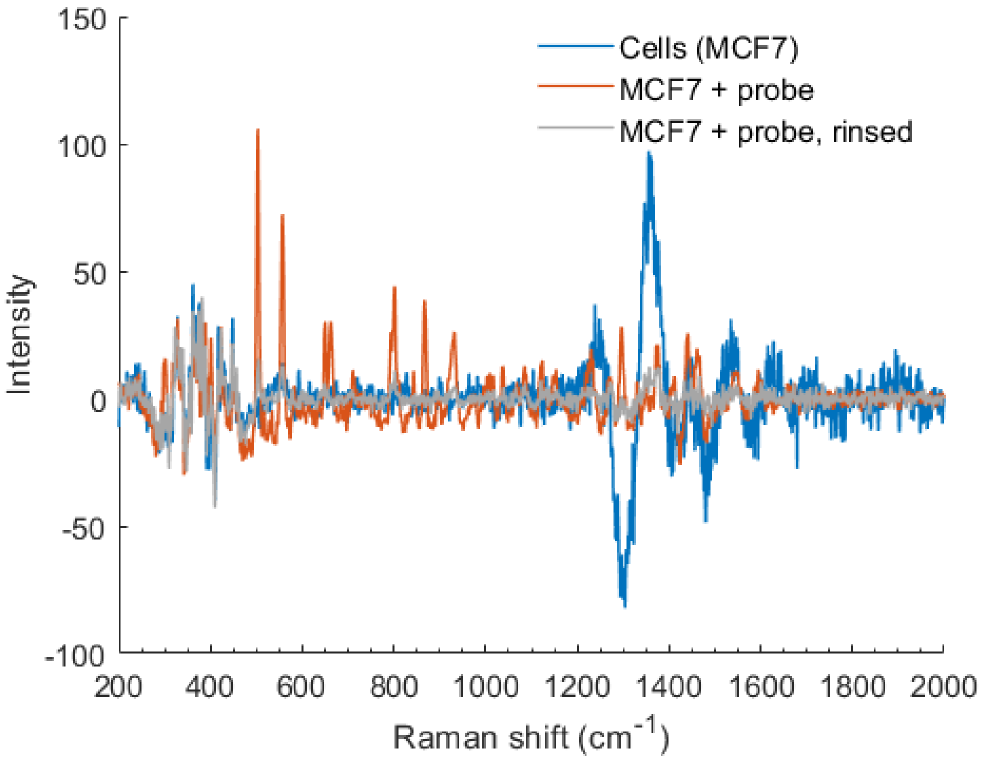

Figure 2.42: SERS spectra of MCF7 cell pellets with AuNS-HITCI@SiO$_2$-DMPGTVLP

Figure 2.39 shows the spectrum of the control probe dosed onto NIH 3T3. As expected, when the probe is rinsed from the cells, the signal of the HITCI reporter disappears, as there is no peptide to target the cells and bind the probe to them. The NIH 3T3 cells were then dosed with AuNS-HITCI@SiO_2-DMPGTVLP, the peptide functionalised probe, which again rinsed from the probe (Figure 2.40). Both of these experiments were repeated with the MCF7 cell line. However, the selective probe containing the MCF7 targeting peptide failed to remain in the cells after rinsing (Figure 2.42). Since this peptide successfully targeted MCF7 cells in previous experiments with the methylene blue reporter, the reason for this is likely due to the poor stability of the probe, which showed visible signs of aggregation (the solution was a less deep shade of blue with some aggregate visible by eye). A small amount of aggregation can cause increased SERS signals due to hotspot formation, as discussed previously. However, too much aggregation causes the probe to accumulate in large, widely separated clusters, making the concentration of the probe in solution effectively much lower. It is therefore likely that the probe was not sufficiently spread throughout the cell sample to give a SERS signal. Overall, the results suggest that the HITCI probe is not suitably reliable, due to poor stability.

The purpose of the work herein was to construct the foundations of a SERS probe to be later modified for selective melanoma detection. Each aspect of the probe; core material, shape, coating, and reporter, has been selected to optimise signal enhancement, biocompatibility, stability, and ease of synthesis. Finding a suitable NIR dye for use as a Raman reporter was of particular interest. Often, NIR reporters presented in the literature are novel molecules requiring multi-step synthesis, which can be costly and time-consuming.[47,48,50,51] Commercial dyes are regularly utilised as SERS reporters due to their availability; however, these dyes do not typically absorb in the NIR region, and are thus unable to fully utilise the SERRS effect when used alongside a NIR laser.[51-52] Of the red and NIR absorbing dyes explored in this work, it can be concluded that the methylene blue was the most successful Raman reporter, giving a clear signal which was present when bound to MCF7 target cells via the selective peptide, but rinsing away to give diminished signal when it was unable to selectively bind a target. HITCI, though giving promising Raman signals, was unstable when incorporated into a probe. Moving forward, the suitability of the methylene blue probe to detect human melanoma is explored in the following chapter.

2.8 References

1 M. Helfand, S. M. Mahon, K. B. Eden, P. S. Frame and C. T. Orleans, *Am. J. Prev. Med.*, 2001, **20**, 47–58.

2 H. Lorentzen, K. Weismann, C. S. Petersen, F. Grønhøj Larsen, L. Secher and V. Skødt, *Acta Derm. Venereol.*

3 A.-V. Giblin and J. M. Thomas, *J. Plast. Reconstr. Aesthetic Surg.*, 2007, **60**, 32–40.

4 E. C. Dreaden, A. M. Alkilany, X. Huang, C. J. Murphy and M. A. El-Sayed, *Chem. Soc. Rev.*, 2012, **41**, 2740–2779.

5 J. H. Granger, N. E. Schlotter, A. C. Crawford and M. D. Porter, *Chem. Soc. Rev.*, 2016, **45**, 3865–3882.

6 K. Kong, C. Kendall, N. Stone and I. Notingher, *Adv. Drug Deliv. Rev.*, 2015, **89**, 121–134.

7 F. Benz, R. Chikkaraddy, A. Salmon, H. Ohadi, B. de Nijs, J. Mertens, C. Carnegie, R. W. Bowman and J. J. Baumberg, *J. Phys. Chem. Lett.*, 2016, **7**, 2264–2269.

8 S. Abalde-Cela, P. Aldeanueva-Potel, C. Mateo-Mateo, L. Rodriguez-Lorenzo, R. A. Alvarez-Puebla and L. M. Liz-Marzán, *J. R. Soc. Interface*, 2010, **7**, 435–450.

9 M. Moskovits, *J. Raman Spectrosc.*, 2005, **36**, 485–496.

10 K. Aslan, I. Gryczynski, J. Malicka, E. Matveeva, J. R. Lakowicz and C. D. Geddes, *Curr. Opin. Biotechnol.*, 2005, **16**, 55–62.

11 Y. Jeong, Y.-M. Kook, K. Lee and W.-G. Koh, *Biosens. Bioelectron.*, 2018, **111**, 102–116.

12 J. R. Lakowicz, *Anal. Biochem.*, 2001, **298**, 1–24.

13 Z. Gryczynski, J. Malicka, I. Gryczynski, E. Matveeva, C. D. Geddes, K. Aslan and J. R. Lakowicz, *Proc. SPIE--the Int. Soc. Opt. Eng.*, 2004, **5321**, 275–282.

14 J. Turkevich, P. C. Stevenson and J. Hillier, *Discuss. Faraday Soc.*, 1951, **11**, 55–75.

15 H. Tyagi, A. Kushwaha, A. Kumar and M. Aslam, *Nanoscale Res. Lett.*, 2016, **11**, 362.

16 M. Wuithschick, A. Birnbaum, S. Witte, M. Sztucki, U. Vainio, N. Pinna, K. Rademann, F. Emmerling, R. Kraehnert and J. Polte, *ACS Nano*, 2015, **9**, 7052–7071.

17 W. Haiss, N. T. K. Thanh, J. Aveyard and D. G. Fernig, *Anal. Chem.*, 2007, **79**, 4215–4221.

18 J. F. Li, X. D. Tian, S. B. Li, J. R. Anema, Z. L. Yang, Y. Ding, Y. F. Wu, Y. M. Zeng, Q. Z. Chen, B. Ren, Z. L. Wang and Z. Q. Tian, *Nat. Protoc.*, 2012, **8**, 52.

19 Y. Kobayashi, H. Katakami, E. Mine, D. Nagao, M. Konno and L. M. Liz-Marzán, *J. Colloid Interface Sci.*, 2005, **283**, 392–396.

20 S. Yun, H. Luo and Y. Gao, *RSC Adv.*, 2014, **4**, 4535–4542.

21 O. Malay, I. Yilgor and Y. Z. Menceloglu, *J. Sol-Gel Sci. Technol.*, 2013, **67**, 351–361.

22 C. J. Brinker, *J. Non. Cryst. Solids*, 1988, **100**, 31–50.

23 C. Graf, Q. Gao, I. Schütz, C. N. Noufele, W. Ruan, U. Posselt, E. Korotianskiy, D. Nordmeyer, F. Rancan, S. Hadam, A. Vogt, J. Lademann, V. Haucke and E. Rühl, *Langmuir*, 2012, **28**, 7598–7613.

24 O. Benson, *Nature*, 2011, **480**, 193–199.

25 F. Tian, F. Bonnier, A. Casey, A. E. Shanahan and H. J. Byrne, *Anal. Methods*, 2014, **6**, 9116–9123.

26 A. C. Borges-Muñoz, D. P. Miller, E. Zurek and L. A. Colón, *Microchem. J.*, 2019, **147**, 263–268.

27 P. F. Liao and A. Wokaun, *J. Chem. Phys.*, 1982, **76**, 751–752.

28 M. Urbieta, M. Barbry, Y. Zhang, P. Koval, D. Sánchez-Portal, N. Zabala and J. Aizpurua, *ACS Nano*, 2018, **12**, 585–595.

29 H. Yuan, C. G. Khoury, H. Hwang, C. M. Wilson, G. A. Grant and T. Vo-Dinh, *Nanotechnology*, 2012, **23**, 75102.

30 S. Chatterjee, A. B. Ringane, A. Arya, G. M. Das, V. R. Dantham, R. Laha and S. Hussian, *J. Nanoparticle Res.*, 2016, **18**, 242.

31 K. C. Bantz, A. F. Meyer, N. J. Wittenberg, H. Im, Ö. Kurtuluş, S. H. Lee, N. C.

Lindquist, S.-H. Oh and C. L. Haynes, *Phys. Chem. Chem. Phys.*, 2011, **13**, 11551–11567.

32 G. McNay, D. Eustace, W. E. Smith, K. Faulds and D. Graham, *Appl. Spectrosc.*, 2011, **65**, 825–837.

33 R. A. Floyd, 1990.

34 N. Narband, I. P. Parkin, J. J. Gil-Tomas, M. Wilson and S. Tubby, in *2007 NSTI Nanotechnology Conference and Trade Show-NSTI Nanotech 2007, Technical Proceedings*, 2007, vol. 4, pp. 359–362.

35 S. Atta, M. Beetz and L. Fabris, *Nanoscale*, 2019, **11**, 2946–2958.

36 A. Kedia, H. Kumar and P. S. Kumar, *RSC Adv.*, 2015, **5**, 5205–5212.

37 A. Kedia and P. Senthil Kumar, *J. Phys. Chem. C*, 2012, **116**, 1679–1686.

38 M. Behera and S. Ram, *Appl. Nanosci.*, 2014, **4**, 247–254.

39 S. Ram and H.-J. Fecht, *J. Phys. Chem. C*, 2011, **115**, 7817–7828.

40 C. E. Hoppe, M. Lazzari, I. Pardiñas-Blanco and M. A. López-Quintela, *Langmuir*, 2006, **22**, 7027–7034.

41 K. M. Koczkur, S. Mourdikoudis, L. Polavarapu and S. E. Skrabalak, *Dalt. Trans.*, 2015, **44**, 17883–17905.

42 A. M. Fales, H. Yuan and T. Vo-Dinh, *Langmuir*, 2011, **27**, 12186–12190.

43 D. Bedi, T. Musacchio, O. A. Fagbohun, J. W. Gillespie, P. Deinnocentes, R. C. Bird, L. Bookbinder, V. P. Torchilin and V. A. Petrenko, *Nanomedicine Nanotechnology, Biol. Med.*, 2011, **7**, 315–323.

44 V. García-López, F. Chen, L. G. Nilewski, G. Duret, A. Aliyan, A. B. Kolomeisky, J. T. Robinson, G. Wang, R. Pal and J. M. Tour, *Nature*, 2017, **548**, 567.

45 T. Little, *BioPharm Int.*, 2015, **28**, 48–51.

46 K. K. Maiti, U. S. Dinish, A. Samanta, M. Vendrell, K.-S. Soh, S.-J. Park, M. Olivo and Y.-T. Chang, *Nano Today*, 2012, **7**, 85–93.

47 A. Samanta, K. K. Maiti, K.-S. Soh, X. Liao, M. Vendrell, U. S. Dinish, S.-W. Yun, R.

Bhuvaneswari, H. Kim, S. Rautela, J. Chung, M. Olivo and Y.-T. Chang, *Angew. Chemie Int. Ed.*, 2011, **50**, 6089–6092.

48 S. J. Cho, Y.-H. Ahn, K. K. Maiti, U. S. Dinish, C. Y. Fu, P. Thoniyot, M. Olivo and Y.-T. Chang, *Chem. Commun.*, 2010, **46**, 722–724.

49 R. J. Mallia, P. Z. McVeigh, C. J. Fisher, I. Veilleux and B. C. Wilson, *Nanomedicine*, 2015, **10**, 89–101.

50 G. von Maltzhan, A Centrone, J. Park, R. Ramanathan, M. J. Sailor, T. A. Hatton and S. N. Bhata, *Adv. Mater.,* 2009, **21**, 3175–3180.

51 M. A. Bedics, H. Kearns, J. M. Cox, S. Mabbott, F. Ali, N. C. Shand, K. Faulds, J. B. Benedict, D. Graham and M. R. Detty, Chem. Sci., 2015, 6, 2302–2306

51 J. Kneipp, H. Kneipp, A. Rajadurai, R. W. Redmonda, and K. Kneipp, *J. Raman Spectrosc*., 2009, **40**, 1–5.

52 A. Jaworska, T. Wojcik, K. Malek, U. Kwolek, M. Kepczynski, A. A. Ansary, S. Chlopicki and M. Baranska, *Microchim Acta*., 2015, **182**, 119–127

3. Selective Targeting of Human Melanoma

Skin cancer is the 5th most common cancer in the UK, and appears to be rising.[1] It can be divided into two categories: melanoma, arising from melanocytes (melanin producing cells in the epidermis) and carcinoma, arising from basal and squamous cells (also found in the epidermis).[2,3] Of these two types, melanoma accounts for the vast majority of skin cancer deaths, being significantly less treatable than carninoma.[4] Skin cancer deaths have risen dramatically in recent years, increasing 149 % since the early 1970s. As with all types of cancer, the key to treatment is to detect the cancer as early as possible. In the case of melanoma, by the time the melanoma has grown to a thickness of over 4 mm, the probability of five-year survival drops from around 70 % to 45 %, so the need for early detection is clear.[5] However, current diagnostic methods for melanoma skin cancer could do with improvement. In the first instance, the melanoma is examined by eye; the human error associated with this method is obvious. If melanoma is suspected, the patient will then be sent for a biopsy, an invasive and time consuming procedure.[6]

In this project, it is proposed that melanoma skin cancer could be detected using SERS, in a method which would involve applying a SERS probe to the skin, rinsing the area with water to remove any probe which has not selectively bound to the target, and analysing this area with a Table-top, eye-safe Raman spectrometer. In theory, if melanoma is present, a SERS signal would be observed. This method would make melanoma detection fast, taking mere minutes, non-invasive, and would give a definitive diagnosis without human error. Furthermore, this method negates the need for a specialist, as it would require minimal training and could be carried out by any member of staff. A schematic demonstrating the concept is given in Figure 3.1.

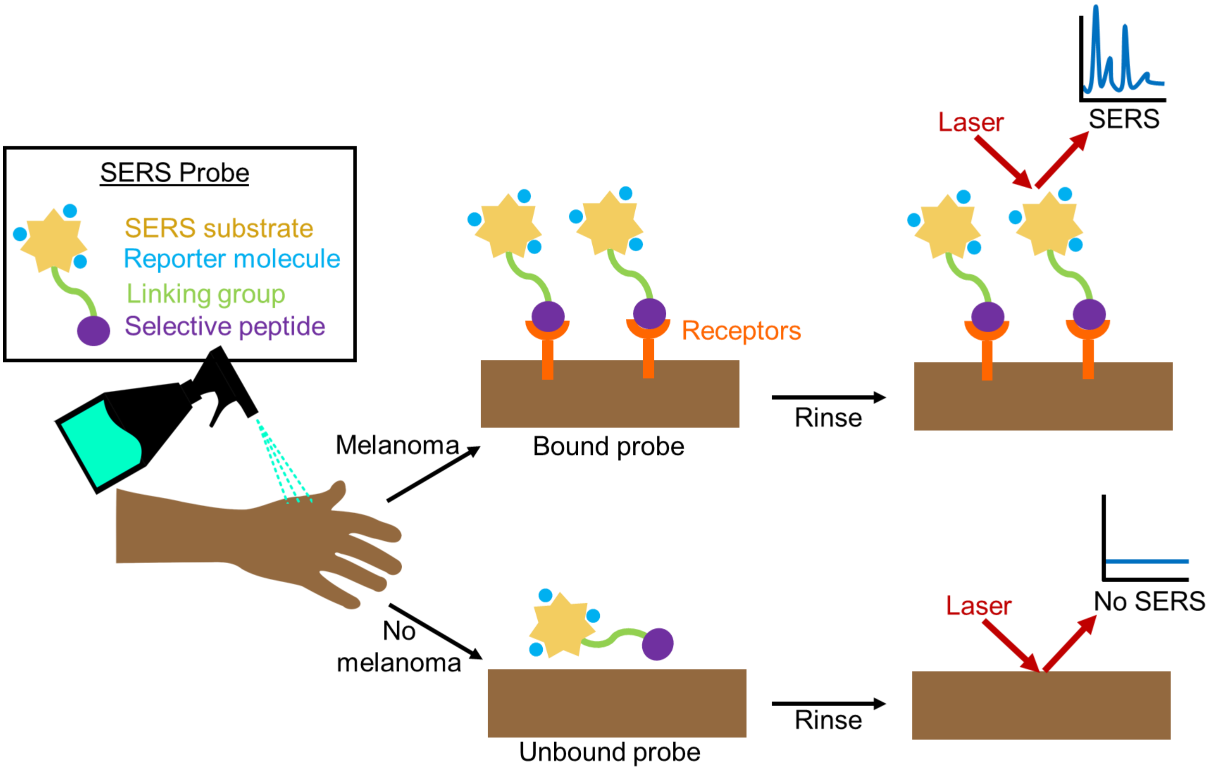

Figure 3.1: Concept of SERS diagnostic system for melanoma.

In previous chapters, the development of a SERS probe for melanoma detection has been discussed, although the key aspect of the probe has not yet been addressed; a peptide to selectively bind the SERS probe to its target, malignant melanoma cells. In this section, a method for targeting malignant melanoma is discussed.

3.1 Identifying an appropriate peptide

Most of the research into melanoma detection is focused on utilising melanocortin receptors. Melanocortin receptors are a family of G-protein coupled receptors (GPCRs), activated by melanocortins (peptide hormones). The known members of this group are MC1R, MC2R, MC3R, MC4R, and MC5R. The group as a whole are responsible for numerous processes such as appetite control and immune function.[7–9] Sometimes known as melanocyte-stimulating hormone receptor (MSHR), MC1R is one of the main proteins involved in controlling skin and hair pigmentation, and is therefore of key interest in skin cancer research. Studies have shown that MC1R is overexpressed in melanoma, compared to healthy skin cells.[10–14] Therefore, a probe which is able to detect unusually high levels of MC1R could indicate the presence of skin cancer.

Numerous studies have been conducted to find peptides which target MC1R effectively; the majority of these peptides are, logically, derived from melanocortins; in particular, melanocyte stimulating hormones (MSHs). This family of hormones consists of α-MSH, β-MSH and γ-MSH, although α-MSH (Figure 3.2) is the most prevalent MSH being utilised in this area, due to its superior affinity for MC1Rs.[15] α-MSH consists of the following sequence: Ac-Ser-Tyr-Ser-Met-Glu-His-Phe-Arg-Trp-Gly-Lys-Pro-Val-NH_2.[16] The critical 'messenger sequence' of this peptide is His-Phe-Arg-Trp. This is the minimum fragment required to stimulate a response from MC1Rs; the other amino acids can be substituted to varying effects.[17,18]

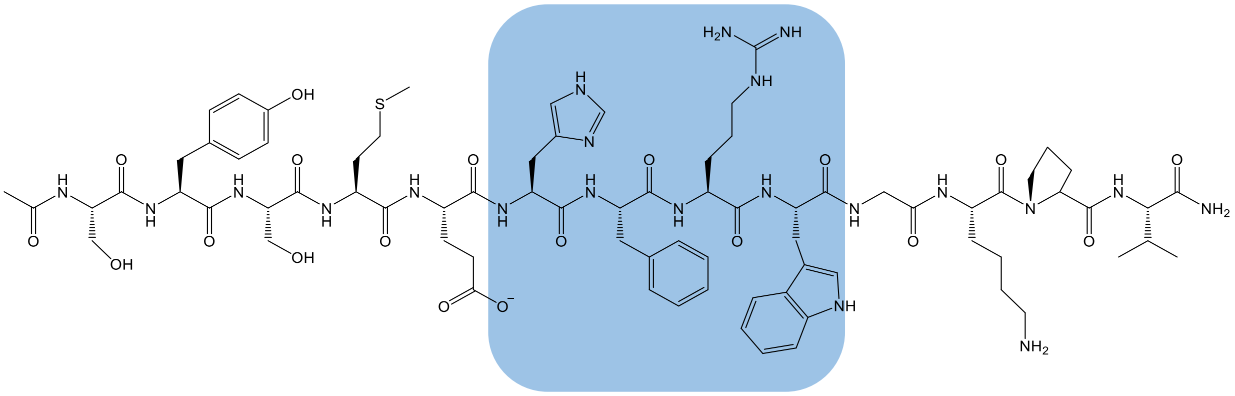

Figure 3.2: Structure of α-MSH with messenger sequence highlighted.

One of the most widely researched derivatives of this peptide is [Nleu^4-D-Phe^7]α-MSH, also known as NPD-MSH (Figure 3.3). This peptide incorporates norleucine, an isomer of leucine, at position four in the peptide chain, in place of methionine. At position seven phenylaniline is replaced by its stereoisomer D-phenylaniline. NPD-MSH was first synthesised by Sawyer *et. al* in 1980, who noted its improved stability in biological media compared to unmodified α-MSH.[19] Most notably, NPD-MSH has been found to bind to MC1Rs more effectively, in some cases exhibiting a potency up to twenty six times greater than α-MSH.[19–21] Binding of NPD-MSH and unmodified α-MSH to MC1R receptors is shown in Figure 3.4.

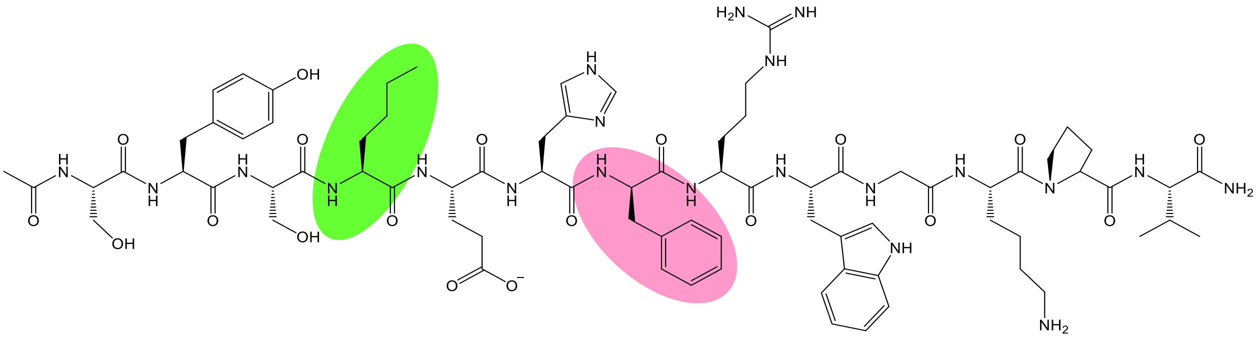

Figure 3.3: Structure of NPD-MSH with structural differences from α-MSH highlighted.

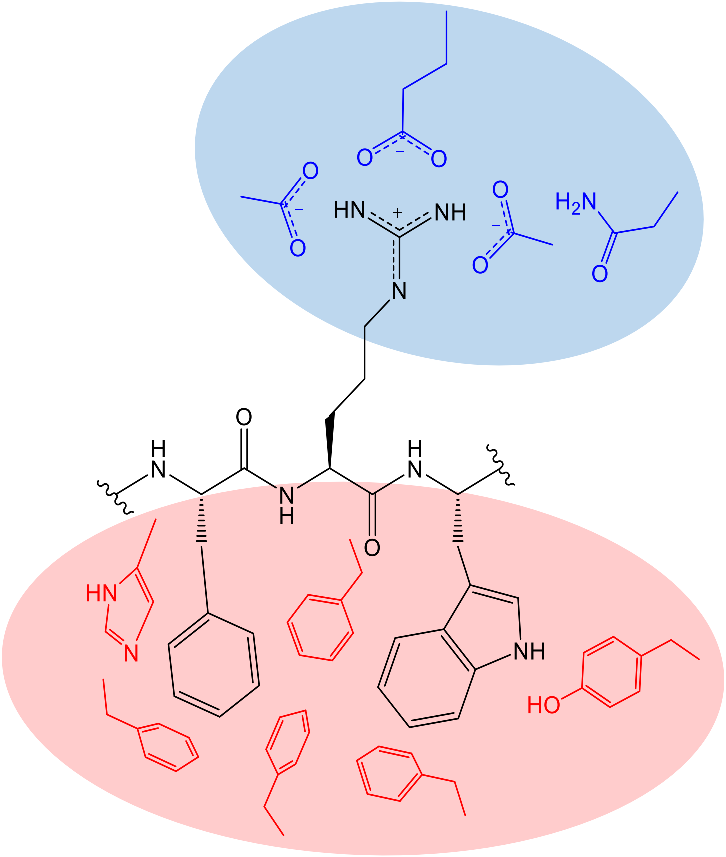

Figure 3.4: Schematic diagram showing binding of the messenger sequence of α-MSH and NPD-MSH to hydrophobic (red) and ionic (blue) binding pockets in MC1R.[20]

NDP-MSH is the gold standard for MC1R targeting; although some groups have modified it, few have sought a different structure all together.[22–25] One of the major reasons for modification of NDP-MSH is its tendency to accumulate in the liver and kidneys.[26,27] However, if used topically, this would not occur and is therefore not a concern for a skin cancer detection system applied directly to the skin surface. Going forward, the probe synthesised in Chapter 2, using methylene blue as a Raman reporter, was modified to incorporate the peptide NDP-MSH for targeting skin cancer cells.

It was also necessary to identify an appropriate cell line for targeting. There are a number of human melanoma cell lines available commercially, all expressing differing amounts of MC1Rs. The human melanoma cell line A375 is widely used in skin cancer research and has been confirmed by several groups to express MC1Rs, making it an appropriate cell line for this work.[28–30]

3.2 Peptide coupling to SERS probes

In Chapter 2, the basis of a SERS probe was synthesised, incorporating a gold nanostar core, methylene blue Raman reporter, a silica shell to 'trap' the reporter in place, and an APTMS linker group to bind a selective peptide. Following initial tests with the human breast cancer line MCF7 using the peptide DMPGTVLP, which proved successful, peptide coupling was carried out with NDP-MSH, in order to test the probe with the cell line A375. Peptide coupling between the SERS probe and NDP-MSH was carried out using the same method as the previous peptide coupling, with dicyclohexylmethanediimine (DCC) as a coupling agent (Scheme 3.1).

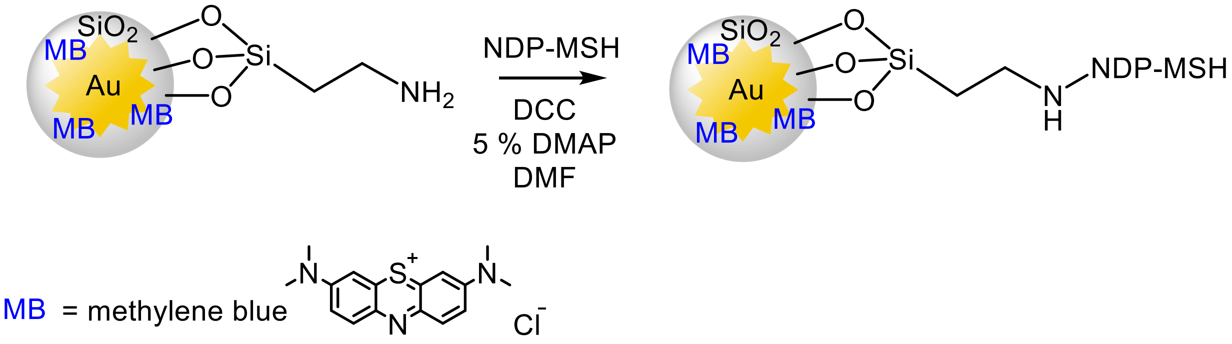

Scheme 3.1: Peptide coupling of NDP-MSH to the linker group of the SERS probe

3.3 Toxicity of the final probe

Toxicity of the control probe AuNS-MB@SiO_2 was tested with various cell lines in Chapter 2. These measurements were repeated for the final selective probe AuNS-MB@SiO_2-NDPMSH with the human melanoma cell line A375 to ensure the presence of the peptide did not affect toxicity. Cell were dosed with the probe for 24 hours as described in Chapter 6.

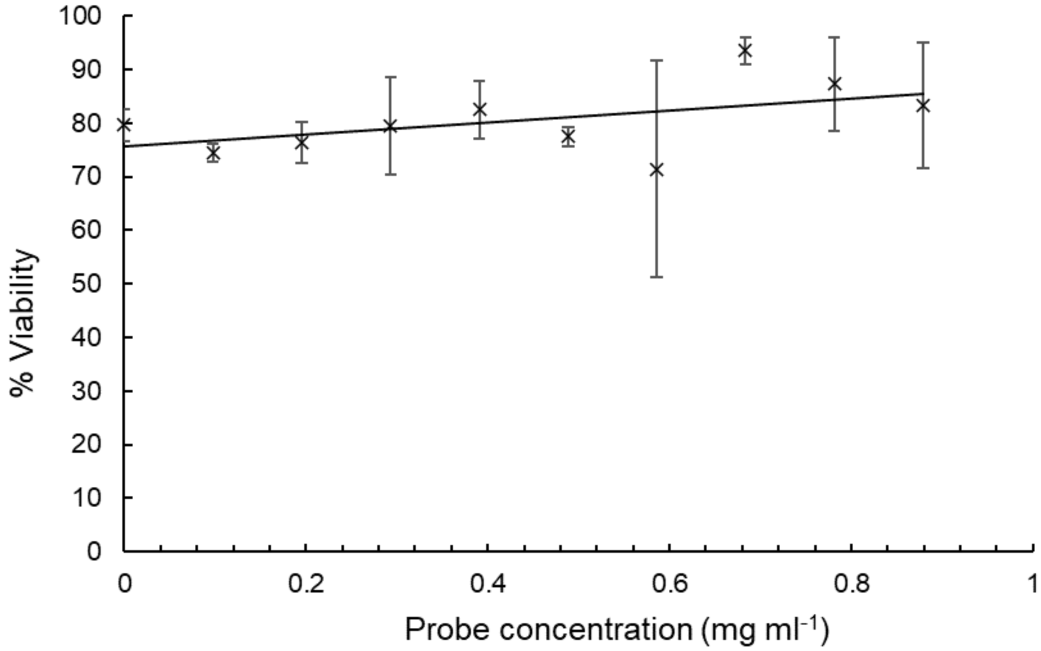

Figure 3.5: Plot of selective probe AuNS-MB@SiO$_2$-NDPMSH concentration against cell viability for A375. Error bars represent standard error.

Figure 3.5 shows the dose-response data for AuNS-MB@SiO$_2$-NDPMSH with the A375 cell line. Due to some variation in the quality of live-cell samples, several error bars are large; the slight positive gradient in the dose-response data can be attributed to this error, as an increase in cell viability with increased probe concentration is highly unlikely. The lack of a significant negative gradient suggests that the probe is non-toxic at working concentrations.

3.3 Confocal Microscopy

As in Chapter 2, an analogous probe was synthesised using the cresyl violet as the reporter (Figure 3.6). The fluorescent nature of the dye allows the probe to be imaged via LSCM, and because cresyl violet is structurally similar to methylene blue, it is assumed that this fluorescent probe behaves in a similar way to the methylene blue SERS probe.

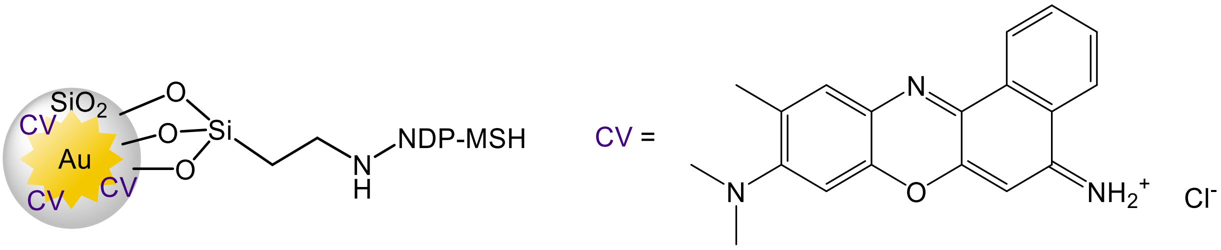

Figure 3.6: Cresyl violet probe fabricated for fluorescence microscopy.

This cresyl violet probe without the selective peptide was incubated for two hours with both the NIH 3T3 cell line and the A375 cell line. Confocal microscopy images (Figure 3.7) show the interaction of the fluorescent probe with the cells. The fluorescent control probe (red) is not visible at all in NIH 3T3 cells, though some probe can be seen alongside A375 cells, despite the lack of a selective peptide. This is possibly due to the EPR effect.[31] However, it is clear that significantly more probe is present in the A375 cell line when the A375 selective peptide is coupled, as shown in Figure 3.8. Even with this peptide present, none of the probe is visible in or around NIH 3T3 cells, suggesting good selectivity for the A375 cell line. The spots in the background of the images are caused by the silica coated probe adhering to the glass coverslip.

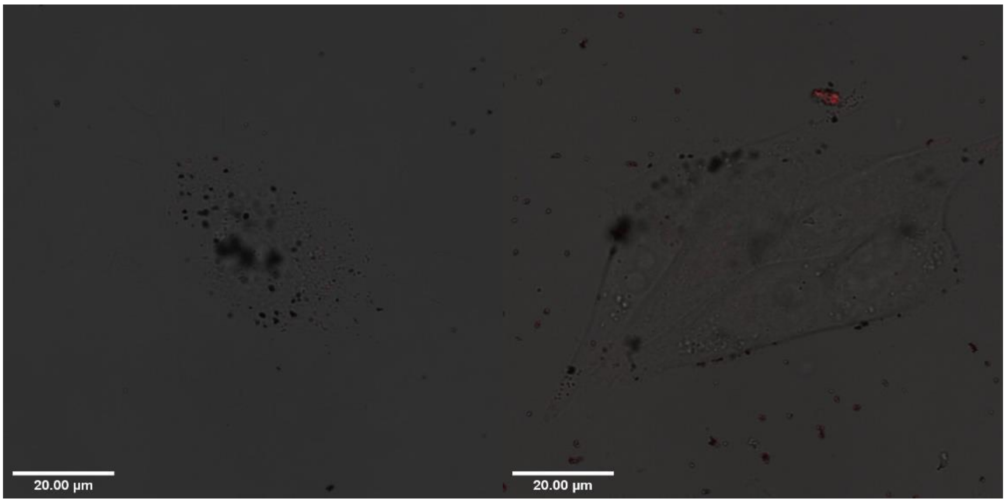

Figure 3.7: LSCM images of NIH 3T3 (left) and A375 (right) cells with the cresyl violet non-specific control probe, overlaid with bright field transmission light microscopy images. Transmission λ_{ex} 488nm; fluorescence λ_{ex} 633 nm, λ_{em} 650-800 nm. The presence of a small amount of probe is evident from the red emission seen about the cells.

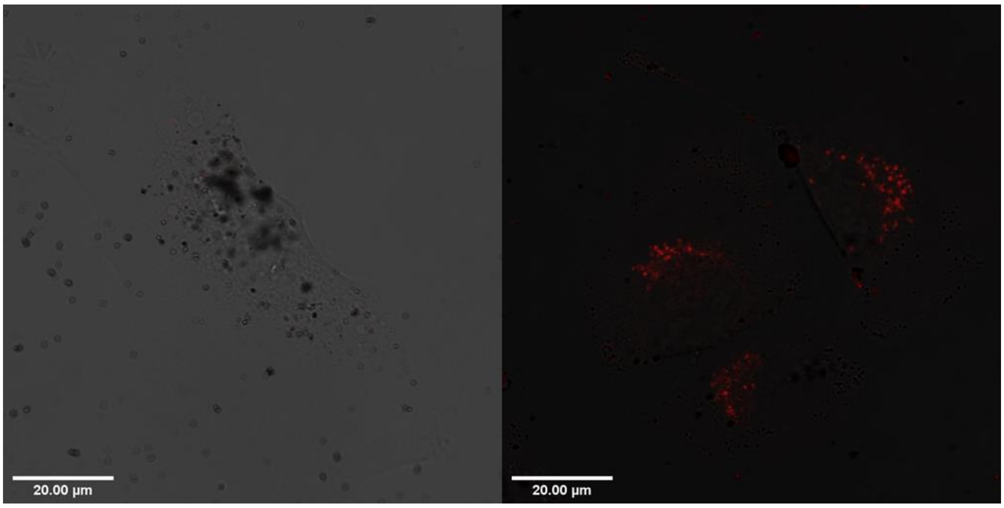

Figure 3.8: LSCM images of NIH 3T3 (left) and A375 (right) cells with the cresyl violet A375-specific probe, overlaid with bright field transmission light microscopy images. Transmission λ_{ex} *488nm; fluorescence* λ_{ex} *633 nm,* λ_{em} *650-800 nm. Uptake of the probe is evident from the red emission seen inside the cells.*

3.4 SERS Testing with Human Melanoma Cells

The effectiveness of the SERS probe in targeting human melanoma was evaluated against the cell line A375. Similar to tests carried out previously with MCF7 breast cancer cells, the selective probe was applied to cells by the method described in Chapter 6, and Raman spectra were collected. The cells were then rinsed with deionised water, and Raman spectra were collected again. If the selective SERS probe modified with the peptide NDP-MSH were to give SERS signals with human melanoma cells after rinsing, but ‘rinse out’ of other cells, giving no signal, this would prove that the probe is suitably selective to detect melanoma. Two controls were used; the control cell line NIH 3T3 (mouse skin fibroblasts), and a SERS probe with no peptide attached. These spectra are shown in Figures 3.9-3.12. Negative Raman intensities are a result of baseline correction carried out using MATLAB.

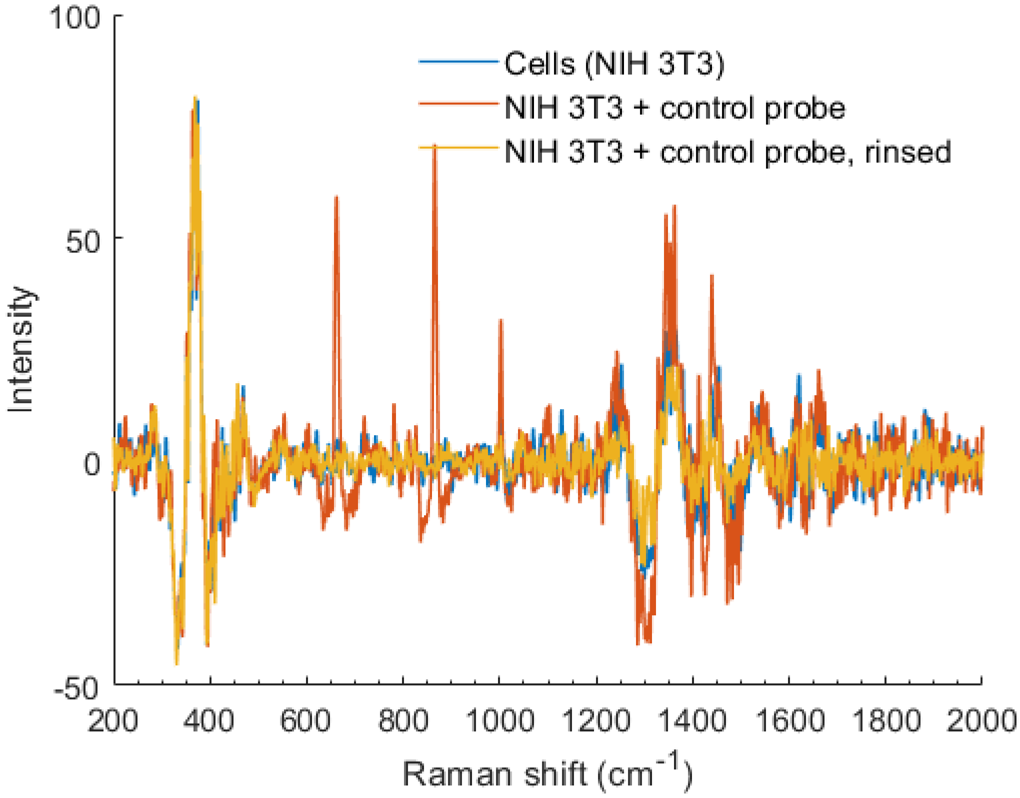

Figure 3.9: SERS spectra of NIH 3T3 cells dosed with non-selective control probe AuNS-MB@SiO$_2$, before and after rinsing.

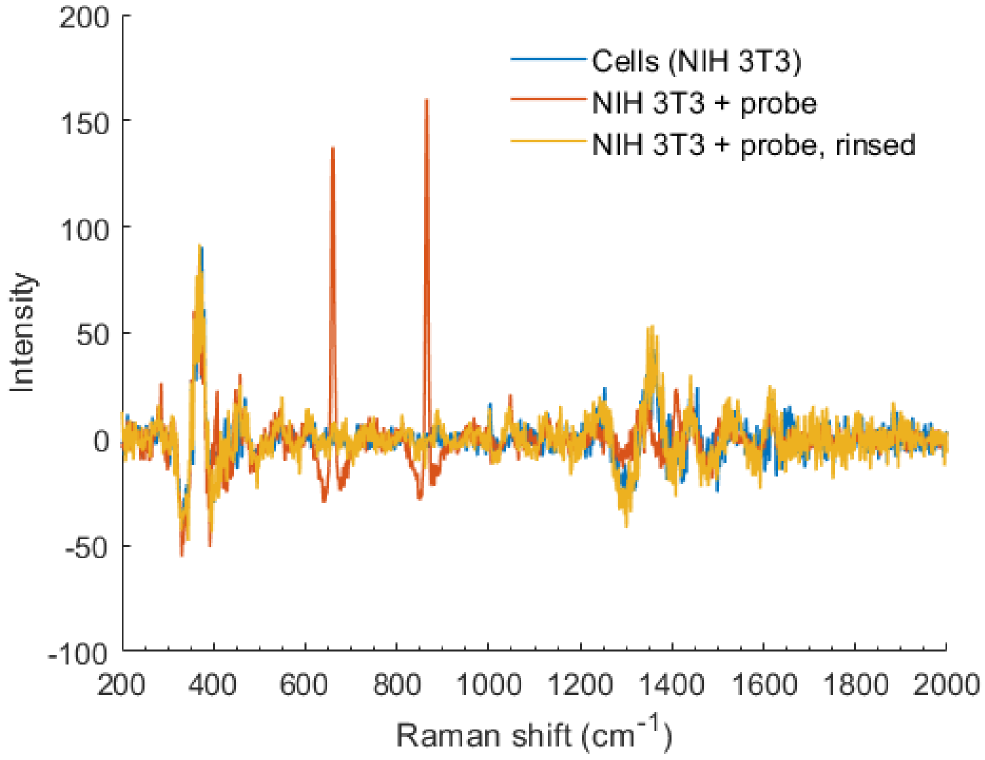

Figure 3.10: SERS spectra of NIH 3T3 cells dosed with selective probe AuNS-MB@SiO$_2$-NDPMSH before and after rinsing.

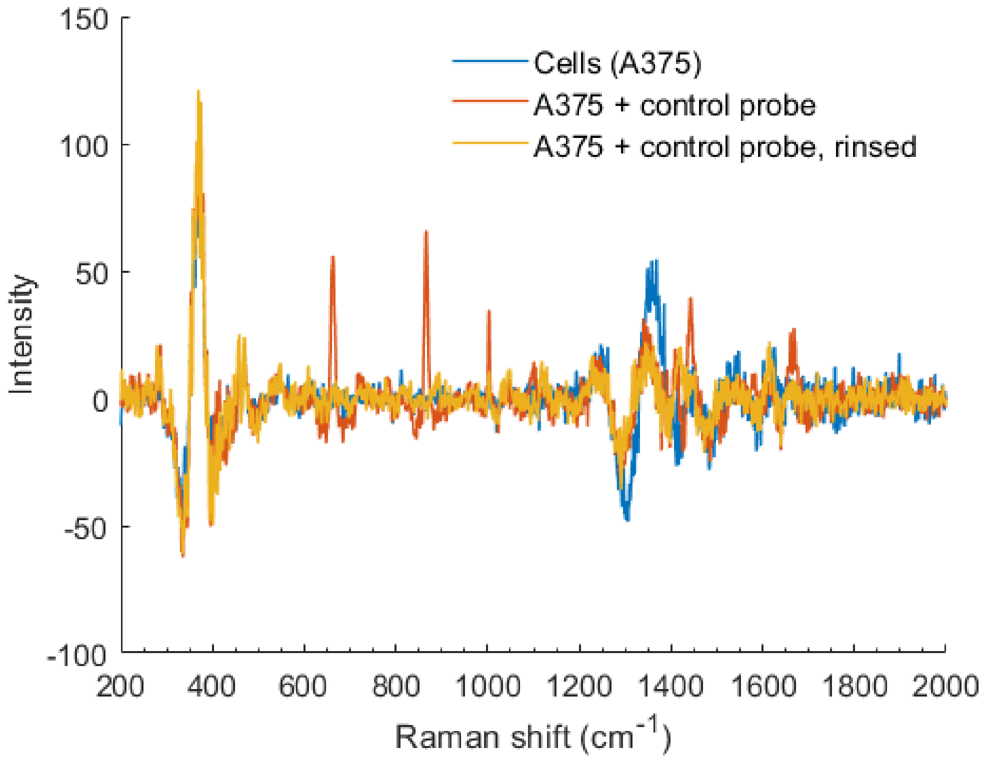

Figure 3.11: SERS spectra of A375 cells dosed with non-selective control probe AuNS-MB@SiO_2 before and after rinsing

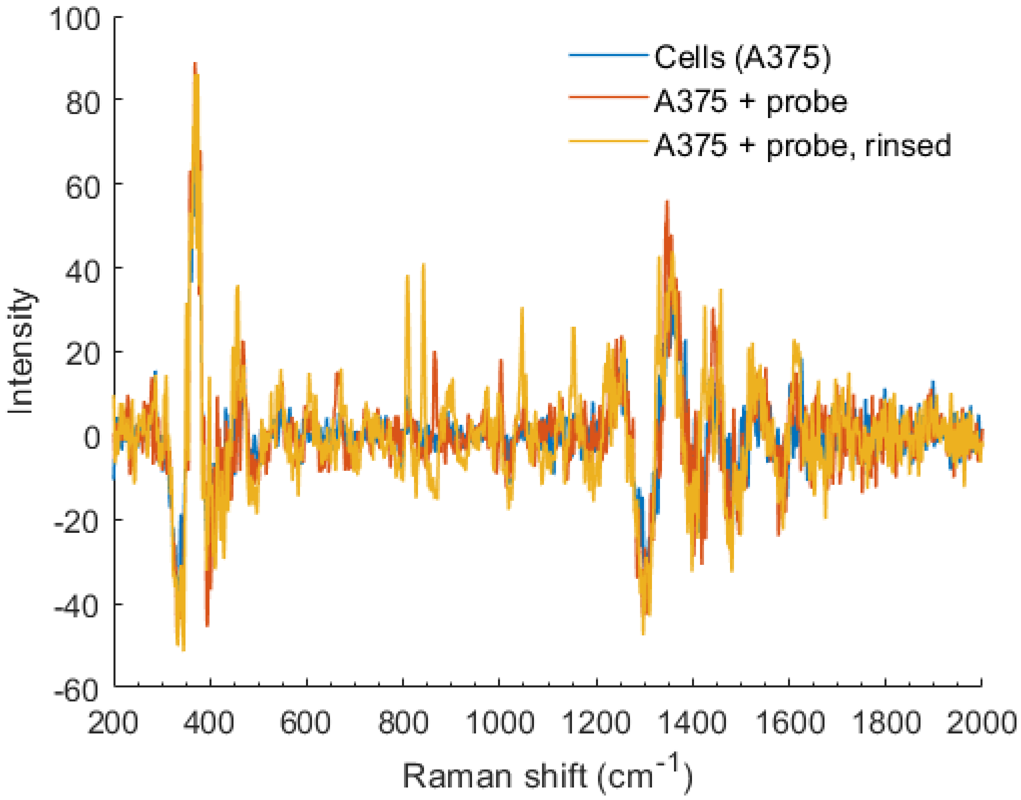

Figure 3.12: SERS spectra of A375 cells dosed with selective probe AuNS-MB@SiO_2-NDPMSH before and after rinsing.

In Figures 3.9-3.11, the most prominent peaks are those at 663 and 866 cm^{-1}, attributed to in plane and out of plane bending of C-H in methylene blue respectively.[32] To be clear, for the purposes of this research a ‘prominent peak’ is defined as a peak in the SERS spectrum which is not present in the background spectrum of cells without any probe, and is significantly higher than background noise. This peak at 663 cm^{-1} also appears in Figure 3.12, though somewhat diminished. Figure 3.12 also has a prominent peak close to 866 cm^{-1}, at 841 cm^{-1}. It is not clear whether this signal also arises from methylene blue, but has shifted slightly, or whether this peak can be attributed to C-C stretching of the amino acid norleucine in the peptide chain.[33] Other prominent peaks of Figure 3.12 are those at 808, 1047 and 1154 cm^{-1} the latter two can be most likely attributed to in plane and out of plane bending of C-H bonds in methylene blue, respectively. The cause of the peak at 808 cm^{-1} is uncertain. Regardless of specific peak assignations, what is clear is that Figure 3.12 does not show significant reduction in Raman signals on rinsing. In Figures 3.9-3.11, the Raman spectra of cells between 500 and 1200 cm^{-1} are flat- besides some minor noise- on rinsing, indicating that the probe is no longer present. However, in Figure 3.12, clear signals are visible after rinsing, indicating that the probe remains in the cell sample. The evidence therefore suggests that the Raman probe with selective peptide NPD-MSH does bind to A375 skin cancer cells. The lack of Raman signal in Figures 3.9-3.10, where a different cell line is used, and Figure 3.11, where a ‘control probe’ without NPD-MSH is used, suggest the probe is selective for A375 skin cancer cells, and that this can be attributed to the presence of the peptide.

This suggests that the SERS probe designed and constructed as shown in Scheme 3.1 is suitable for the selective detection of skin cancer in humans. However, further research may be required to find a Raman reporter with stronger, clearer SERS signals. Nonetheless, this is a promising initial step towards a SERS-based melanoma diagnostic system, which would be an improvement on the current slow and speculative methods of diagnosis, and has been attempted successfully by few other studies.[34]

3.5 References

1 Cancer Research UK, https://www.cancerresearchuk.org/health-professional/cancer-statistics/statistics-by-cancer-type/melanoma-skin-cancer, (accessed 31 May 2020).

2 R. P. Gallagher, B. Ma, D. I. McLean, C. P. Yang, V. Ho, J. A. Carruthers and L. M. Warshawski, *J. Am. Acad. Dermatol.*, 1990, **23**, 413–421.

3 R. Zanetti, S. Rosso, C. Martinez, A. Nieto, A. Miranda, M. Mercier, D. I. Loria, A. Østerlind, R. Greinert, C. Navarro, G. Fabbrocini, C. Barbera, H. Sancho-Garnier, L. Gafà, A. Chiarugi, R. Mossotti and for the H. W. Group, *Br. J. Cancer*, 2006, **94**, 743–751.

4 F. M.-L. Robertson and L. Fitzgerald, *J. cancer policy*, 2017, **12**, 67–71.

5 M. Helfand, S. M. Mahon, K. B. Eden, P. S. Frame and C. T. Orleans, *Am. J. Prev. Med.*, 2001, **20**, 47–58.

6 J. E. Mayer, S. M. Swetter, T. Fu and A. C. Geller, *J. Am. Acad. Dermatol.*, 2014, **71**, 599.e1-599.e12.

7 V. J. and C. L. and van D. A., *Curr. Drug Targets*, 2003, 4, 586–597.

8 J. Wikberg, R. Muceniece, I. Mandrika, P. Prūsis, J. Lindblom, C. Post and A. Skottner, *Pharmacol. Res.*, 2000, **42**, 393–420.

9 M. E. Hadley and R. T. Dorr, *Peptides*, 2006, **27**, 921–930.

10 E. B. Hawryluk and H. Tsao, *Cold Spring Harb. Perspect. Med.*, 2014, **4**, a015388–a015388.

11 R. M. Dores, *Ann. N. Y. Acad. Sci.*, 2009, **1163**, 93–100.

12 N. K. Tafreshi, X. Huang, V. E. Moberg, N. M. Barkey, V. K. Sondak, H. Tian, D. L. Morse and J. Vagner, *Bioconjug. Chem.*, 2012, **23**, 2451–2459.

13 J. E. S. Wikberg, *Eur. J. Pharmacol.*, 1999, **375**, 295–310.

14 A. A. Rosenkranz, T. A. Slastnikova, M. O. Durymanov and A. S. Sobolev, *Biochemistry. (Mosc).*, 2013, **78**, 1228–1237.

15 W. Wang, D.-Y. Guo, Y.-J. Lin and Y.-X. Tao, *Front. Endocrinol. (Lausanne).*, 2019,

10, 683.

16 A. M. L. Castrucci, M. E. Hadley, T. K. Sawyer, B. C. Wilkes, F. Al-Obeidi, D. J. Staples, A. E. de Vaux, O. Dym, M. F. Hintz, J. P. Riehm, K. R. Rao and V. J. Hruby, *Gen. Comp. Endocrinol.*, 1989, **73**, 157–163.

17 J. Chen, M. F. Giblin, N. Wang, S. S. Jurisson and T. P. Quinn, *Nucl. Med. Biol.*, 1999, **26**, 687–693.

18 C. Haskell-Luevano, T. K. Sawyer, S. Hendrata, C. North, L. Panahinia, M. Stum, D. J. Staples, A. M. De Lauro Castrucci, M. E. Hadley and V. J. Hruby, *Peptides*, 1996, **17**, 995–1002.

19 T. K. Sawyer, P. J. Sanfilippo, V. J. Hruby, M. H. Engel, C. B. Heward, J. B. Burnett and M. E. Hadley, *Proc. Natl. Acad. Sci.*, 1980, **77**, 5754–5758.

20 Y. Yang, C. Dickinson, C. Haskell-Luevano and I. Gantz, *J. Biol. Chem.*, 1997, **272**, 23000–23010.

21 C. Haskell-Luevano, J. R. Holder, E. K. Monck and R. M. Bauzo, *J. Med. Chem.*, 2001, **44**, 2247–2252.

22 H. B. Schiöth, F. Mutulis, R. Muceniece, P. Prusis and J. E. S. Wikberg, *Br. J. Pharmacol.*, 1998, **124**, 75–82.

23 M. F. Giblin, N. Wang, T. J. Hoffman, S. S. Jurisson and T. P. Quinn, *Proc. Natl. Acad. Sci.*, 1998, **95**, 12814–12818.

24 V. B. Swope and Z. A. Abdel-Malek, *Int. J. Mol. Sci.* , 2018, 19.

25 Y. Zhou, S. Mowlazadeh Haghighi, I. Zoi, J. R. Sawyer, V. J. Hruby and M. Cai, *J. Med. Chem.*, 2017, **60**, 9320–9329.

26 S. Froidevaux, M. Calame-Christe, H. Tanner and A. N. Eberle, *J. Nucl. Med.*, 2005, **46**, 887–895.

27 Z. Cheng, J. Chen, Y. Miao, N. K. Owen, T. P. Quinn and S. S. Jurisson, *J. Med. Chem.*, 2002, **45**, 3048–3056.

28 H. Chung, J. Lee, D. Jeong, I.-O. Han and E.-S. Oh, *J. Biol. Chem.* , 2012, **287**, 19326–19335.

29 A. Lindskog Jonsson, A. Granqvist, J. Elvin, M. E. Johansson, B. Haraldsson and J. Nyström, *PLoS One*, 2014, **9**, e87816.

30 P. Eves, J. Haycock, C. Layton, M. Wagner, H. Kemp, M. Szabo, R. Morandini, G. Ghanem, J. C. García-Borrón, C. Jiménez-Cervantes and S. Mac Neil, *Br. J. Cancer*, 2003, **89**, 2004–2015.

31 J. Fang, H. Nakamura and H. Maeda, *Adv. Drug Deliv. Rev.*, 2011, **63**, 136–151.

32 G.-N. Xiao and S.-Q. Man, *Chem. Phys. Lett.*, 2007, **447**, 305–309.

33 S. Stewart and P. M. Fredericks, *Spectrochim. Acta Part A Mol. Biomol. Spectrosc.*, 1999, **55**, 1615–1640.

34 A. R. Kumar, K. B. Shanmugasundaram, J. Li, Z. Zhang, A. A. Ibn Sina, A. Wuethrich and M. Trau, *RSC Adv.*, 2020, **10**, 28778

4. Molecular Wire Effects on Surface Enhanced Raman

In 1959, prominent physicist Richard Feynman speculated that computers could one day shrink to nanoscale proportions. His lecture “There’s plenty of room at the bottom” discussed the possibility of circuits being built on a molecular scale, with single molecules constituting electrical components such as wires and resistors.[1] It wasn’t until the 1970’s that the first research on the conductivity of molecules was published; one of the earliest instances of this being Bernhard Mann and Hans Kuhn’s 1971 paper reporting the conductivity of fatty acid monolayers on metal surfaces.[2] Since then, the area of molecular electronics has grown massively in the pursuit of building ångström scale devices. In this chapter, another use for molecular wires is explored; the possibility of molecular wires being used as ‘antennae’ to amplify the surface enhanced Raman phenomenon.

A molecular wire is defined as a molecule which conducts charge along its length. Some examples of these molecules include alkanes, oligophenylene ethynylenes (OPEs) and oligothiophenes; the conductive properties of these types of molecules are explored often in literature. In this chapter, it is proposed that the conductive properties of these molecules could be used to improve SERS signals.

To understand how this might work, we must readdress the origins of the SERS effect. As mentioned previously, incident light on a solution of metal nanoparticles can induce a localised surface plasmon (LSP).[3–5] When LSPs become confined by features such as crevices, points, or junctions between adjacent particles, they interact to form ‘hotspots’; areas of highly localised, intense electromagnetic fields, and it is in these hotspots that enhancement of the incident and scattered light occurs, resulting in the surface enhanced Raman effect. Here it is proposed that a molecular wire could conduct LSPs, extending the reach of the enhancing effect further from the metal surface, as surface plasmons are evanescent and decay exponentially from the metal surface. The molecular wire could in effect act as an antenna, overall augmenting the SERS effect. At this stage, this theory is speculative, though previous work does suggest that molecular wires can propagate evanescent waves from a metal surface with PSPs.[6]

4.1 Molecular Wire Design

Careful consideration was taken into the design of molecular wires. First, the wire should contain a suitable anchoring group, to bind to the surface of gold nanostars in order to create a SERS probe. The backbone of the wire should be sufficiently conjugated to conduct charge, and give a strong Raman signal, acting both as a wire and Raman reporter in one. Finally, the wire should have a linker group to attach a selective peptide in order to bind the SERS target, as detailed in Chapter 3. The general structure is show in in Figure 4.1

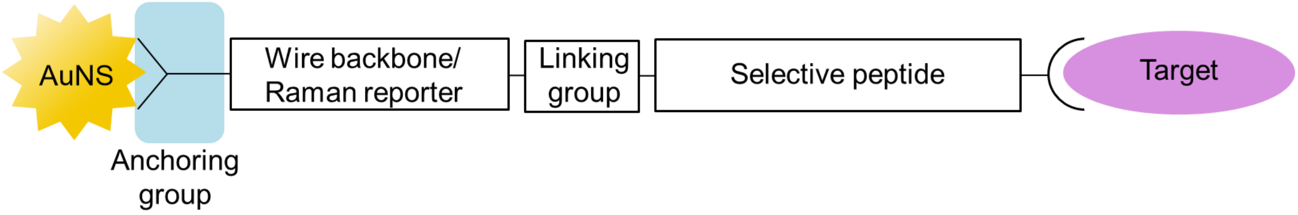

Figure 4.1: Schematic diagram of molecular wire SERS probe structure (not to scale).

4.1.1 Anchoring Group

In order to attach the molecular wire to a gold surface, the wire must possess a suitable anchoring group, as discussed in Chapter 1. Thiols tend to be the most common due to their ability to form self-assembled monolayers (SAMs) under mild conditions, without the need for any additional reagents.[7] Furthermore, anchoring groups have a significant effect on the ability of a molecular wire to transport charge; Au-SH anchoring groups have been shown to have greater conductance than Au-NH_2 and Au-COOH, most likely due to superior bond strength.[7,8]

Although thiols have been shown to have the best aurophilicity of the many functional groups tested in the literature, many other sulphur containing functional groups such as thioacetates and thioethers will bind to gold in a similar way, as shown in Figure 4.2.[9] The syntheses detailed in this chapter contain several different sulphur containing functional groups; starting materials were often altered if a reaction did not work, hence functional groups were changed slightly. The chosen functional group also depended on the cost of reagents.

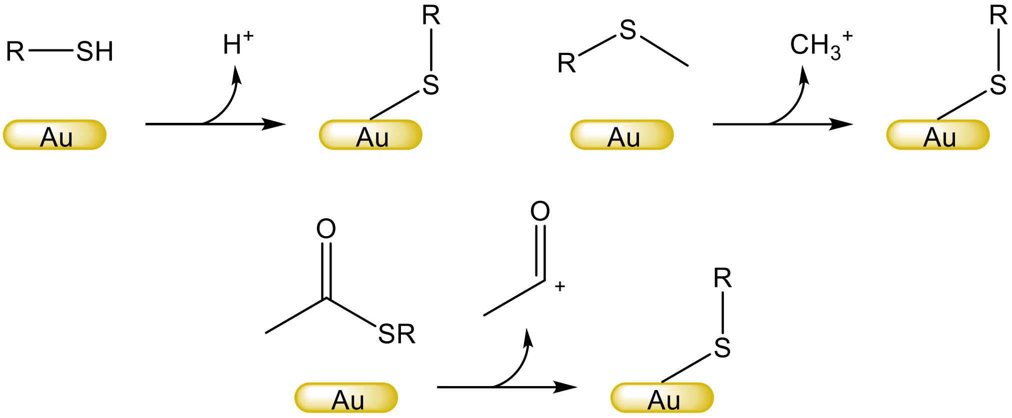

Figure 4.2: Mechanisms of sulphur-containing anchoring groups (top left- thiol; top right- thioether; bottom- thioacetate) binding to gold surfaces.

4.1.2 Linking Group

At the opposing end to the anchoring group, the molecular wire must possess a suitable linker for the selective peptide, in order to be used as a probe for melanoma detection. Molecules synthesised therefore contained amine or carboxylic acid terminal groups, in order to attach the peptide using a simple peptide bond-forming reaction, as in Chapter 3. Because these groups can also act as anchoring groups, it is important to use a very aurophillic anchoring group which can 'outcompete' the amine or carboxylic acid in binding to the gold surface. Another possible work-around for this problem is the 'stepwise' approach, discussed in section 4.1.3.

4.1.3 Wire Backbone

Two different backbone structures were synthesised; oligo(phenylene triazole) (OPT), and oligo(phenylene ethynylene) (OPE). These structures were chosen for their high levels of conjugation and ease of synthesis via coupling reactions. The general structures of these backbones are given in Figure 4.3, along with some other common molecular wire backbone structures.

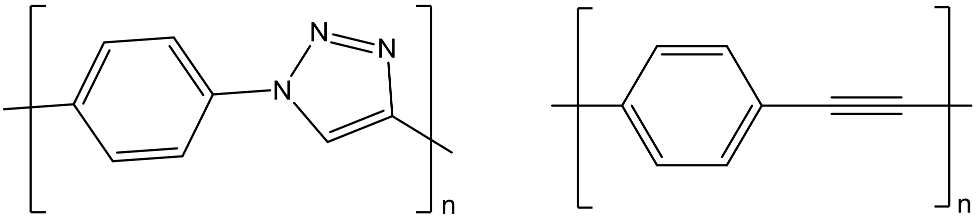

Oligo(phenylene triazole) (OPT)   Oligo(phenylene ethynylene) (OPE)

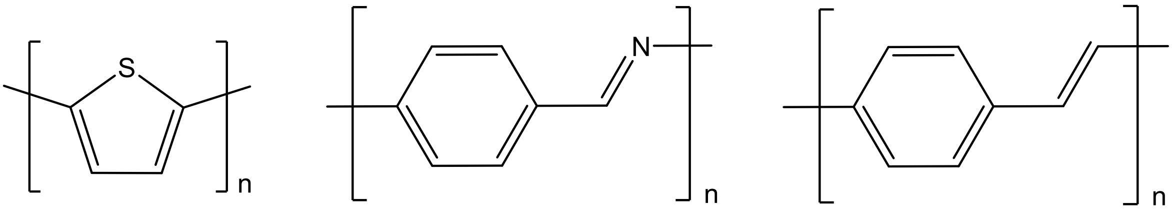

Oligothiophene   Oligo(phenylene imine) (OPI)   Oligo(phenylene vinylene) (OPV)

Figure 4.3: Example structures of common molecular wires.

It was initially decided that the wires should be built ‘step-wise’ on the gold nanostar surface, as depicted in Figure 4.4. The first ‘building block’ of the oligomer would be attached to the gold surface via the anchoring group, forming a SAM. A coupling reaction could then be carried out on the gold surface, hence building the molecule step by step on the gold surface. This approach was deemed to be advantageous for several reasons. Firstly, should the final molecular wire product be insoluble, attaching the wire to the gold nanostars in the final stage of the probe synthesis would therefore prove challenging. It was also speculated that a stepwise approach would allow for more of the molecules to bind to the gold surface, as steric hindrance may prevent long-chain molecules from forming a closely packed monolayer. Finally, because the probe linking group could also act as an anchoring group, the stepwise approach could prevent wires attaching themselves to the gold surface ‘upside down’. The molecules were first synthesised on their own, without the gold nanostars, however the idea of using this stepwise approach to eventually construct a probe was taken into account in these initial syntheses, as reactions must have suitably mild conditions to be carried out on the gold surface without causing the nanostars to aggregate.

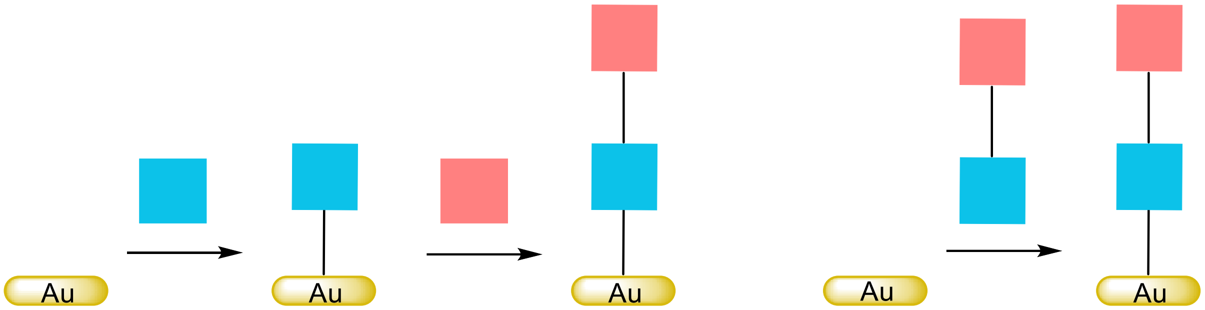

Figure 4.4: Schematic diagram of the stepwise approach (left) compared to a direct approach (right).

4.2 Molecular Wire Synthesis: OPTs

The first set of novel molecular wires, OPT wires, were synthesised by combining an aromatic azide and alkyne using a 1,3-cycloaddition or Huisgen cycloaddition, to create the benzene-triazole-benzene conjugated chain. This type of reaction was chosen as it is also known as a 'click reaction'.[10–13] A click reaction is defined as a reaction which can occur under mild conditions, quickly, and with high yield. These mild conditions are ideal for building the wire stepwise on the gold surface. In order to synthesis these triazole wires, azides were synthesised for the coupling reaction with the alkynes.

4.2.1 Azide synthesis

The first azide synthesis attempted was a substitution reaction of 1,4-bromothiophenol using sodium azide. This method was adapted from that of Zhu et. al.[14], though proved to be unsuccessful; it was quickly realised that due to the lack of an electron-withdrawing group, it was not possible for the S_NAr addition-elimination reaction to take place as the appropriate intermediate cannot form. Because the electron-donating thiol is necessary as an anchoring group, a different approach had to be found.

Azides were therefore synthesised from their analogous amines, using sodium nitrite and sodium azide. The mechanism for this is detailed in Scheme 4.1; in acidic conditions, the amine reacts with sodium nitrite to form a diazonium salt. The diazonium group then leaves and is substituted for the azide group by an aromatic S_N1 reaction. The reaction was initially attempted with 1,4-thioaniline, using a literature technique modified from Mach et. al.[15], although this was unsuccessful. However, the same method did work using 1,4-methylthioaniline. The reason for this is unclear.

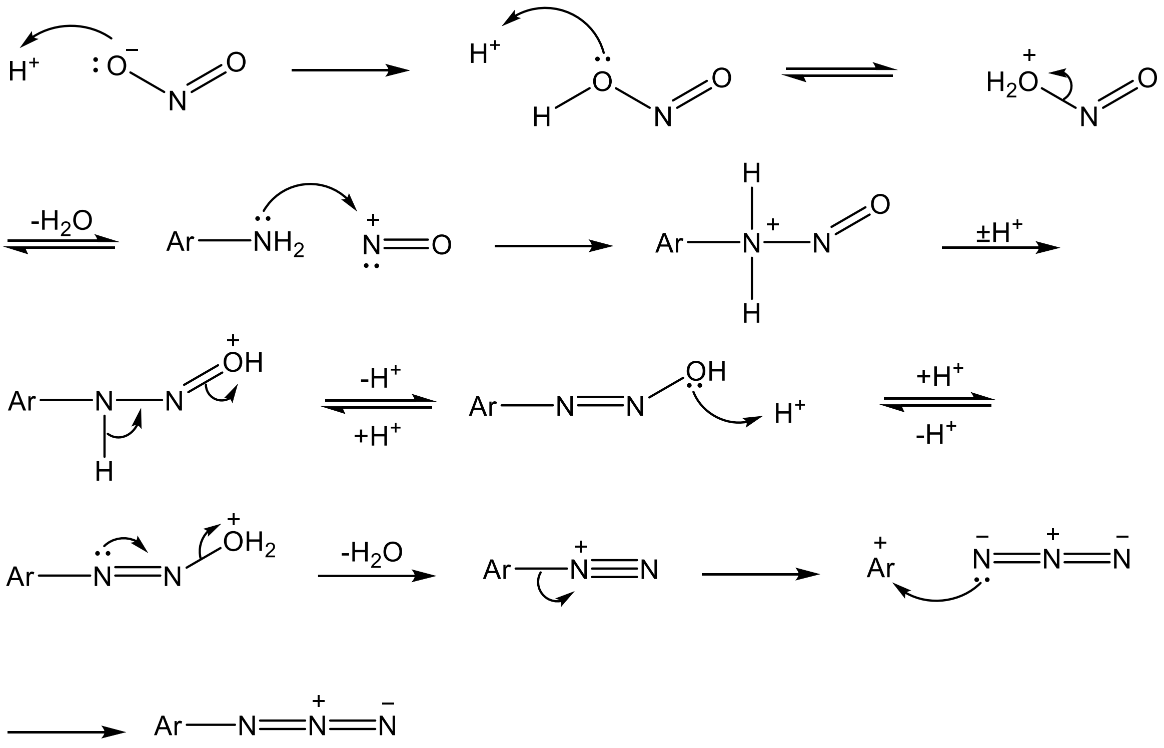

Scheme 4.1: Synthesis of an aromatic azide from an amine.

4.2.2 Azide-alkyne Click Reactions

The general mechanism for the copper catalysed Huisgen cycloaddition, as proposed by Worrell et. al., is given in Scheme 4.2. A variety of novel molecular wire syntheses were attempted by adapting literature procedures;[22] the proposed structures, starting materials, solvent, copper catalyst and accompanying co-catalyst used, and success of the reaction are summarised in Table 4.1.

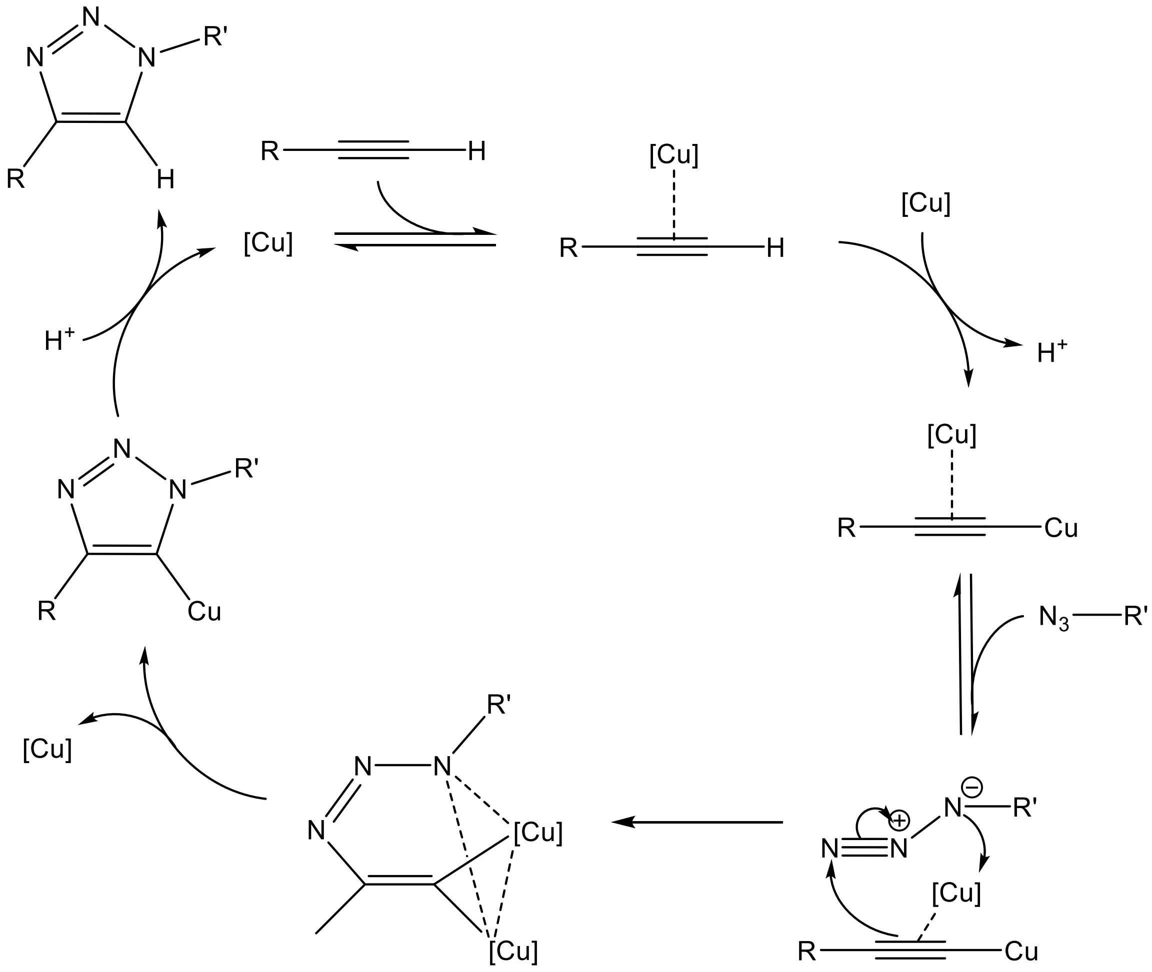

Scheme 4.2: The mechanism for the copper (I) catalysed Huisgen cycloaddition.[16]

The Huisgen reaction is catalysed by Cu(I), however due to the instability of simple Cu(I) salts this is typically generated in situ from Cu(II) and the use of a co-catalyst to reduce the copper.[17] This is the case for reactions using $CuSO_4$ and sodium ascorbate. However, this limits the reaction to aqueous conditions. The alternative catalyst $[CuBr(PPh_3)_3]$ is a stable form of Cu(I), using bulky ligands to protect the copper centre from oxidation, negating the need for a co-catalyst.[18] It is important to protect the Cu(I) from oxidising agents, not only to allow the reaction to take place, but to prevent Cu(II) mediated alkyne homocoupling (known as the Eglinton reaction) from taking place to a form a diacetylene biproduct.[19,20,21] It should be noted that alkyne homocoupling can also take place in the presence of a Cu (I) catalyst (i.e. Glaser coupling), although due to the nature of click reactions, the cycloaddition should be far preferable. This catalyst can be used in a wide range of organic solvents, making it useful for reactions with water-insoluble reagents.[18] Another copper catalyst with the benefit of being soluble in a range of organic solvents is $[Cu(CH_3CN)_4PF_6]$. This catalyst is used in conjunction with tetrabutylammonium difluorotriphenylsilicate (TBAT), a supporting ligand which binds to Cu(I) coordination sites to protect the metal centre from oxidation.[22] [$Cu(CH_3CN)_4PF_6$] is also often used with a base such as $^iPr_2NH$ to aid deprotonation of the alkyne and subsequent formation of the copper-alkyne complex, as alkynes are not very acidic (this step is shown in the top-right of Scheme 4.2). There is some debate on whether this is necessary, as the formation of the acetylide is already fast without the need for further assistance, and the presence of a base may hinder the protonation of the triazole (this step is shown in the top-left of Scheme 4.2).[19] However, a base was used in the syntheses detailed in this chapter, in accordance with most protocols in the literature.[23] Table 4.1 summarises the outcomes of these syntheses.

Structure	Starting materials	Catalyst/ other additives	Solvent	Reaction Success
1. 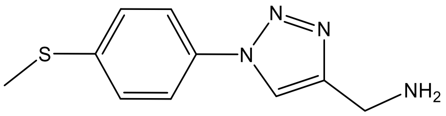	1,4-azido(methylthio) phenol, propargylamine	$CuSO_4$ / sodium ascorbate	H_2O/ EtOH 1:1	No
			H_2O/ ^tBuOH 1:1	No
			H_2O / DMF 4:1	No
		[$CuBr(PPh_3)_3$]	MeCN	No
2. 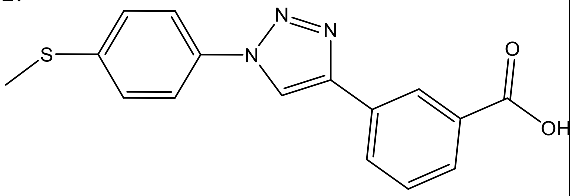	1,4-azido(methylthio) phenol ,3-ethynyl benzoic acid	$CuSO_4$ / sodium ascorbate	H_2O / EtOH 1:1	No
		[$CuBr(PPh_3)_3$]	MeCN	No
		[$Cu(CH_3CN)_4PF_6$] / TBAT / $^iPr_2NH$	MeCN	Yes
3. 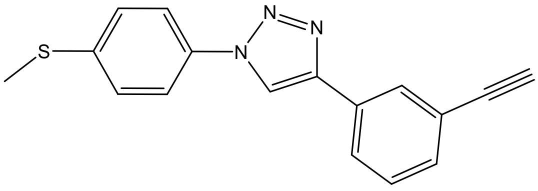	1,4-azido(methylthio) phenol, 1,3-diethynylbenzene	[$Cu(CH_3CN)_4PF_6$] / TBAT / $^iPr_2NH$	MeCN	No

Structure	Starting materials	Catalyst/ other additives	Solvent	Reaction Success
4. 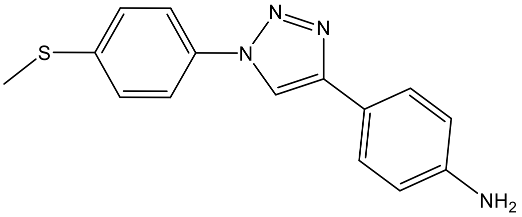	1,4-azido(methylthio) phenol, 4-ethynylaniline	[$Cu(CH_3CN)_4PF_6$] / TBAT / $^iPr_2NH$	MeCN	Yes

Table 4.1: Summary of molecular wire synthesis attempts

Molecular wire 1 is the most straightforward of the proposed structures, combining 1,4-azidothiophenol with a simple amine to act as a linking group. This synthesis was first attempted with $CuSO_4$; a cheap catalyst and therefore a good starting point for the synthesis. The azide starting material was not soluble in water, and so mixtures of ethanol and butanol with water were attempted, though neither were successful due to poor solubility. [$CuBr(PPh_3)_3$] was therefore obtained as a catalyst in order to carry out the reaction in acetonitrile, which the azide did dissolve in. However, this reaction too did not go to completion for reasons which are unclear. It was decided that a number of different structures would be attempted to obtain a molecular wire product, and so procedures for structures 2-4 were carried out. These structures are longer and more conjugated, incorporating an additional benzene ring, and so should act as more effective molecular wires.

This first of these new designs, Structure 2, incorporates a carboxylic acid to act as a linking group. It would have been preferable to carry out this reaction using 4-ethynyl benzoic acid, as opposed to the meta isomer; this would have improved the conductive properties of the wire, as the presence of the carboxyl group on the meta position breaks the conjugation of the molecule, reducing electronic communication. Unfortunately, this isomer was not available to purchase. The synthesis of Structure 2 was again unsuccessful in aqueous conditions due to poor solubility. Despite the frequent use of [$CuBr(PPh_3)_3$] for click reactions in the literature, this catalyst again did not yield results, and so a third catalyst, [$Cu(CH_3CN)_4PF_6$], was purchased. The synthesis of structure 2 with this catalyst was successful, however, the product could not be used to functionalise gold nanostars due to its poor solubility in all of the standard solvents available. Although poor solubility would a make it impossible to attach the structure to a gold nanostar using a direct approach, a stepwise approach was attempted to overcome this, detailed in section 4.4. Following the apparent success of [Cu(CH_3CN)$_4$$PF_6$] as compared to the other catalysts, all further reactions were attempted using this catalyst only.

Structure 3 does not have a linking group, however, it was proposed that it would make a good Raman reporter nonetheless, as alkyne groups give strong Raman signals outside of the biological region. Again, it would have been preferable to carry out the reaction with the para isomer of 1,3-diethynylbenzene, though this reagent was unavailable to purchase. The only downside to the lack of a linking group is that when the final probe is constructed, a second, separate molecule would have to be added to the gold nanostars, alongside the molecular wire reporter, in order to bind the selective peptide, making the synthesis overall less efficient as an extra step would be required. Unfortunately, the synthesis never reached this stage, as the reaction yielded an unwanted bi-product caused 1-methylthio-4-azido-bezene reacting again with the initial product (Scheme 4.3), confirmed by a mass spectrometry M+1 peak at 457 m/z.

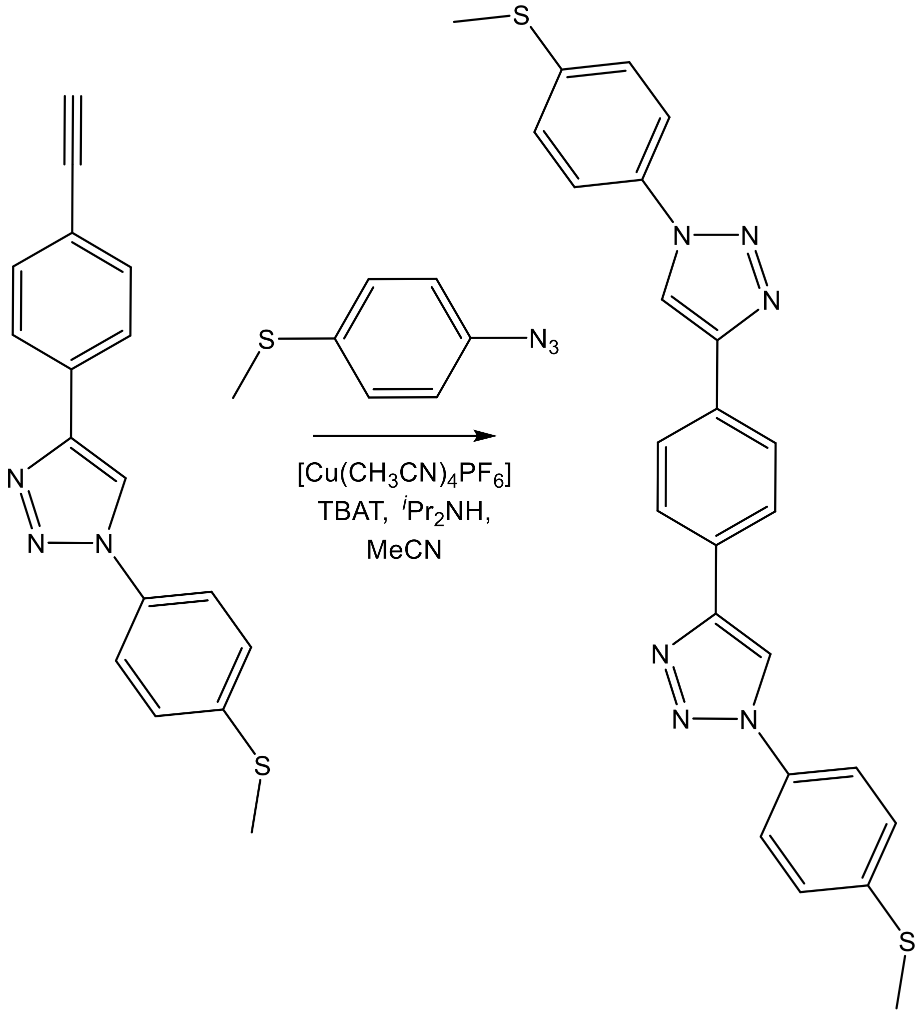

Scheme 4.3: Formation of unwanted biproduct from Structure 3.

Finally, the synthesis of Structure 4 was not only successful, but yielded a product soluble enough to work with. Going forward, this molecular wire would be used to construct a SERS probe.

4.3 Molecular Wire Synthesis: OPEs

An OPE molecular wire synthesis was also attempted. As previously mentions OPEs have a relatively facile synthesis by Sonogashira coupling; the palladium catalysed coupling of an alkyne and a halide alongside a copper cocatalyst, as shown in Scheme 4.4. In addition, they have the benefit of an alkyne group, giving a strong Raman signal outside of the biological region, where it would not be obscured by other signals. For this reason, an OPE would make an ideal Raman reporter. Incorporating an alkyne into the backbone has the added benefit of increasing rigidity of the molecule. Research by Sukegawa *et. al*. suggests that increasing rigidity can improve the conductivity of a molecular wire due to electron-vibration coupling, although this study was conducted using the significantly more rigid carbon-bridged oligo-p-phenylenevinylenes (COPVs).[24]

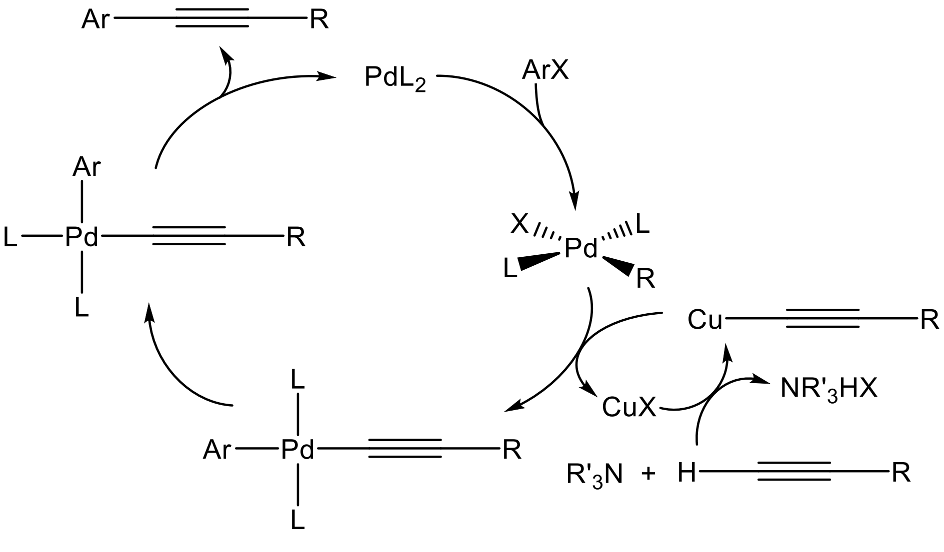

Scheme 4.4: Catalytic cycle of the Sonogashira reaction.

A synthetic route for a novel molecular wire Raman reporter was designed from a precursor OPE provided by Dr N. Sim (Scheme 4.5). Since the precursor already had an appropriate backbone, the only necessary steps were to convert the alcohol groups into thiol anchoring groups. In addition to the OPE backbone, the molecule features a carboxylic acid terminal linking group to bind a peptide, and two thiol groups to securely anchor the molecule to the gold surface. The extra thiol group has the added benefit of keeping the molecule in a more upright position on the gold surface; this is preferable to allow peptide coupling to take place on the terminal carboxylic acid group, which is less likely to occur if the wires are lying flat on the surface of the gold, sterically crowding the linking group. This upright position also ensures consistent binding geometry of the thiol; conductive properties of thiol anchored molecular wires have been shown to differ vastly due to the different possible binding geometries of the thiol, thus ensuring consistent binding will yield more consistent results.[25] The syntheses given in Scheme 4.5 were assisted by Ms Y. Ermakova (4th year MSc. 2019/20).

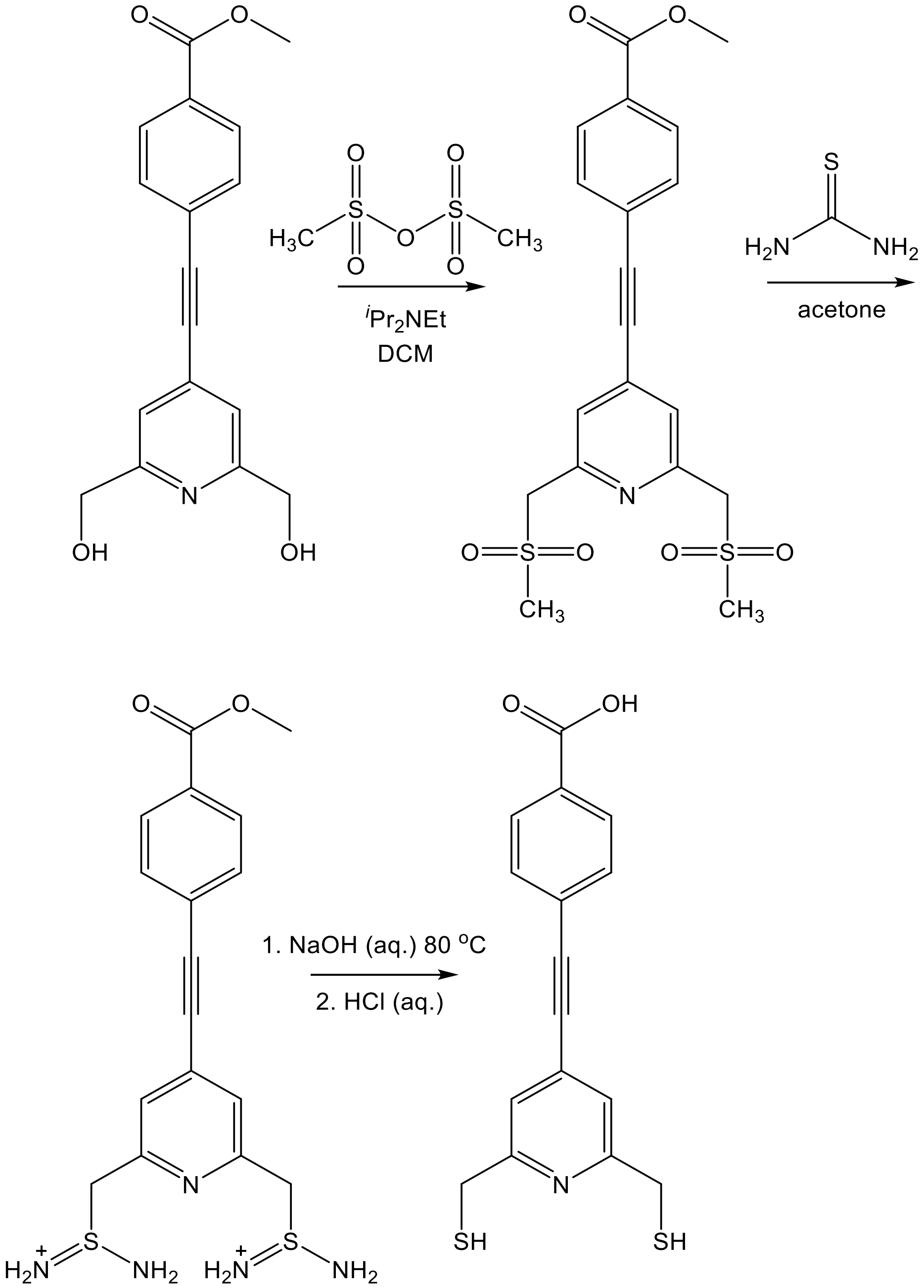

Scheme 4.5: Synthetic route for OPE molecular wire

The first step of this Scheme involves the conversion of the alcohol to a mesylate group, a considerably better leaving group than the alcohol. The mesylate is then substituted for thiourea via an S_N2 mechanism, providing the C-S bond required to form the thiol. Finally, hydrolysis of the thiourea groups and the ester was carried out using three equivalents of NaOH, giving the thiol anchoring groups and terminal carboxylic acid in one step. The product was acidified to enable separation into the organic phase. The main product of this sequence, however, was not an alkyne but its alkene derivative, most likely formed in the acidification step. The mechanism for this reaction is given below (Scheme 4.6). Although it would have been preferable to repeat the reaction under different conditions to obtain the alkyne product, this was not possible due to time constraints caused by COVID-19. As the alkene is still a molecular wire, having a conjugated backbone, and will still give a Raman signal, it was deemed acceptable to proceed with this product.

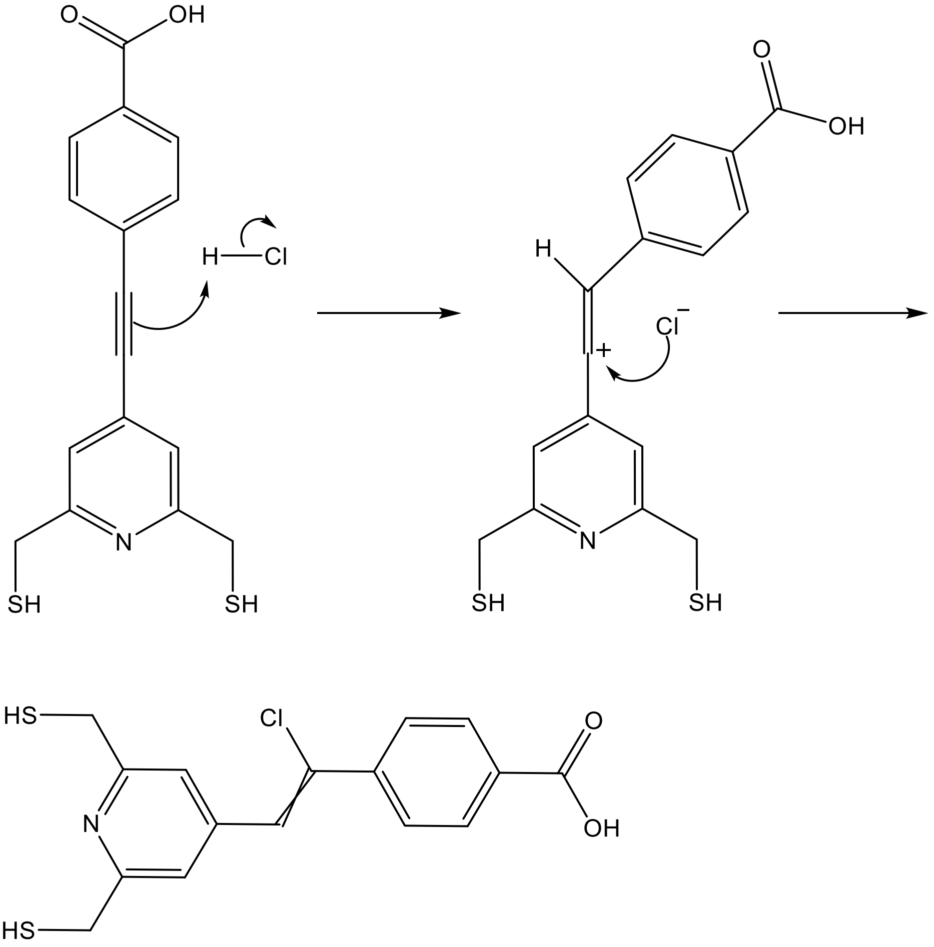

Scheme 4.6: Formation of 4-{2-[2,6-bis(sulfonylmethyl)pyridin-4-yl]-1-chloroethenyl}benzoic acid used in SERS experiments

The position of the chlorine atom on the double bond was not determined due to time constraints. The addition of the hydrogen to the carbon atom closest to the benzoic acid group could give a more stable intermediate due to stabilisation of the carbocation by the p-benzoic acid group, although this is purely speculative. The configuration of the alkene was not determined as this is not relevant to its function as a molecular wire or Raman reporter.

4.4 Functionalisation of Gold Nanostars

The next step of the synthetic process was to attach the molecular wires to the gold nanostar surface, in order to test the theory of molecular wire augmented SERS. If the probes proved to be successful at this stage, they could then be further functionalised with a peptide and used in cell testing.

Two methods were attempted for the functionalisation of gold nanostars with 4-{1-[4-(methylsulfanyl)phenyl]-1H-1,2,3-triazol-4-yl}aniline (structure 4 of Table 4.1). The first was the stepwise method (Scheme 4.7) followed by the direct method (Scheme 4.8). A stepwise approach was also attempted for 3-{1-[4-(methylsulfanyl)phenyl]-1H-1,2,3-triazol-4-yl}benzoic acid (structure 2, Table 4.1), as the poor solubility of this molecule made a direct approach impossible. It was therefore speculated that a stepwise approach could overcome this to yield structure 2 on the gold surface.

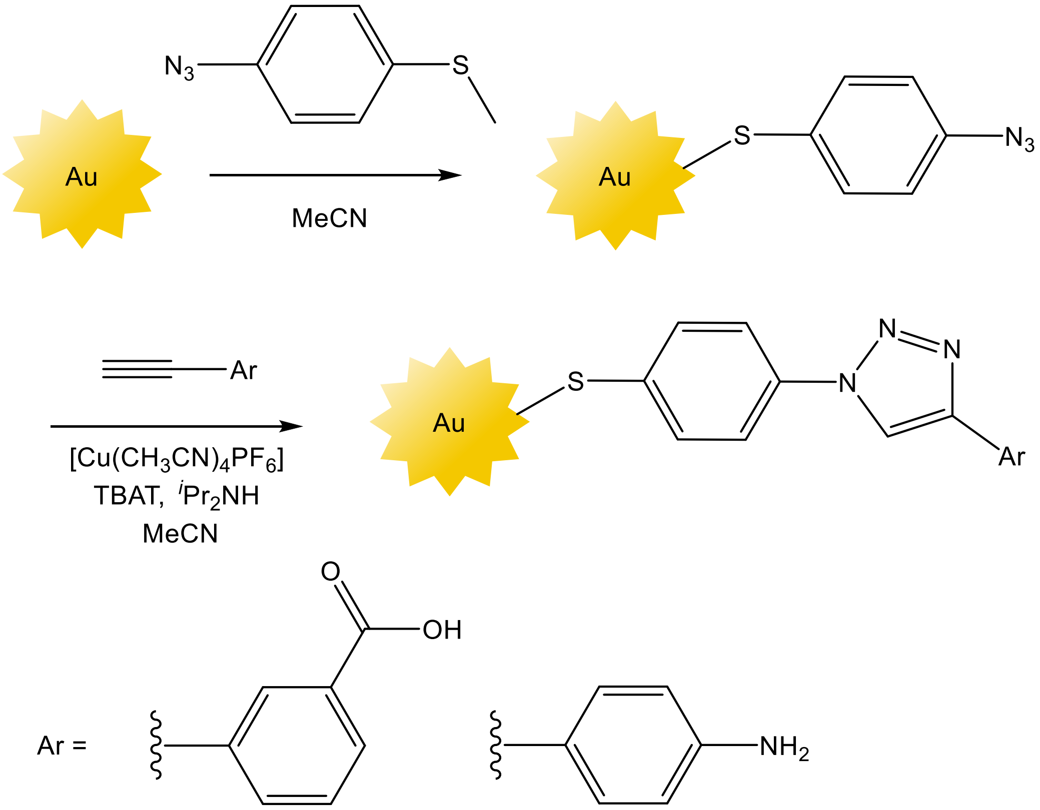

Scheme 4.7: Synthetic route for building structures 2 and 4 stepwise on gold nanoparticles (not to scale).

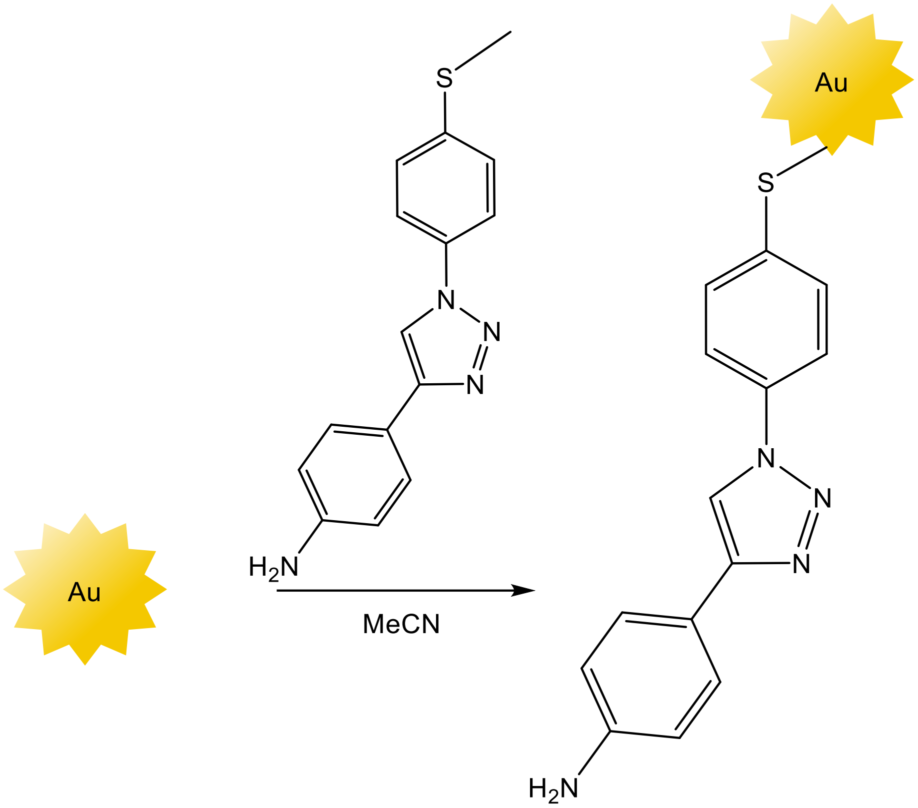

Scheme 4.8: Direct addition of structure 4 to gold nanostar surface (not to scale).

After step one of the stepwise method (in which the self-assembled monolayer is formed), the mixture was centrifuged at 4000 rpm, the supernatant was decanted, and the nanostars resuspended to ensure the click reaction only occurred on the gold surface, and not with residual azide in solution. Despite the very mild reaction conditions of the click reactions, attempts at stepwise synthesis resulted in total aggregation of the gold nanostars. It is plausible that both 1,4-azido(methylthio)phenol starting material, and any molecular wires which may have formed, could bind gold nanostars at both ends, facilitating aggregation. Aggregation could also be caused by hydrogen bonding of the terminal groups of molecular wires (Figure 4.5).

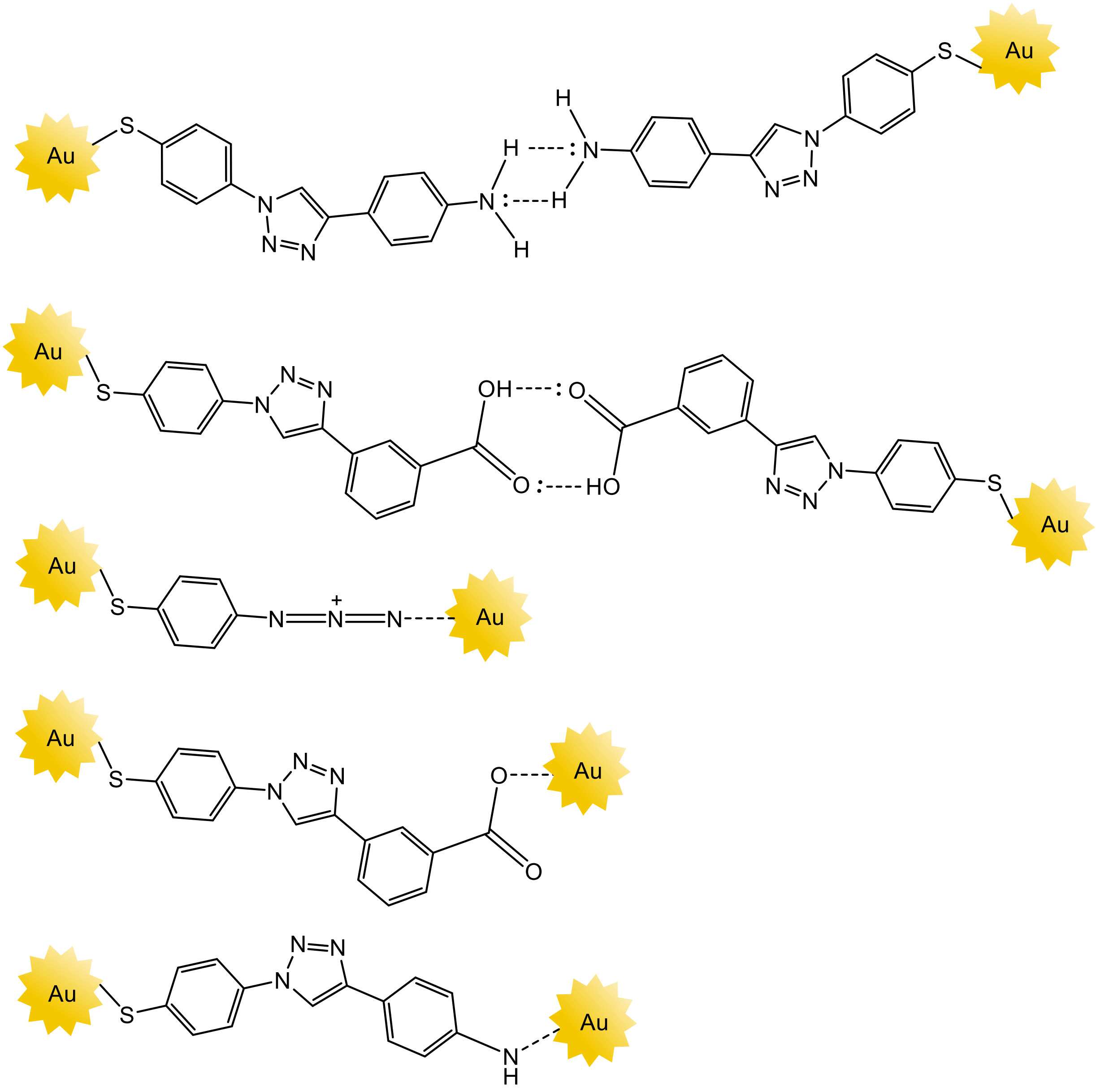

Figure 4.5: Possible modes of aggregation during stepwise synthesis of molecular wires on gold nanostars.

However, if the presence of the molecular wires were the cause of the aggregation, this would also be observed in the direct approach. Although some aggregation was observed in the direct approach (this was apparent, as the gold nanostar solution appeared to be a less deep shade of blue to the eye after the reaction was left overnight, suggesting that the nanostars were less evenly dispersed), the extent of this was much less than that of the stepwise approach, in which the nanostars aggregated completely, suggesting that the main cause was either the 1,4-azido(methylthio)phenol, solvent, or the presence of TBAT and ^{i}Pr$_2$NH . Solvent is an unlikely cause, as PVP stabilised metal nanoparticles are well known to be stable in a wide variety of organic solvents, due to the amphiphilic nature of PVP.[26–28] Evidence suggest that the presence of a base may accelerate degradation of PVP, thus decreasing stability of the particles.[28] It can therefore be concluded that the presence of TBAT, $^{i}Pr_2NH$ and 1,4-azido(methylthio)phenol could all be the cause of aggregation; since these factors cannot be removed (particularly the azide, a key reactant), the stepwise approach was deemed not feasible. However, the direct approach proved successful for Structure 4. The Raman spectrum of the gold nanostars after the addition of the molecular wire (Figure 4.6) shows that the prominent peaks of the wire are present, indicating the molecular wire is bound to the surface. The nanostars were centrifuged, washed and resuspended in water 3 times to ensure that these signals are from the gold nanostars and not residual molecular wire in solution. Negative Raman intensities are a result of baseline correction carried out using MATLAB.

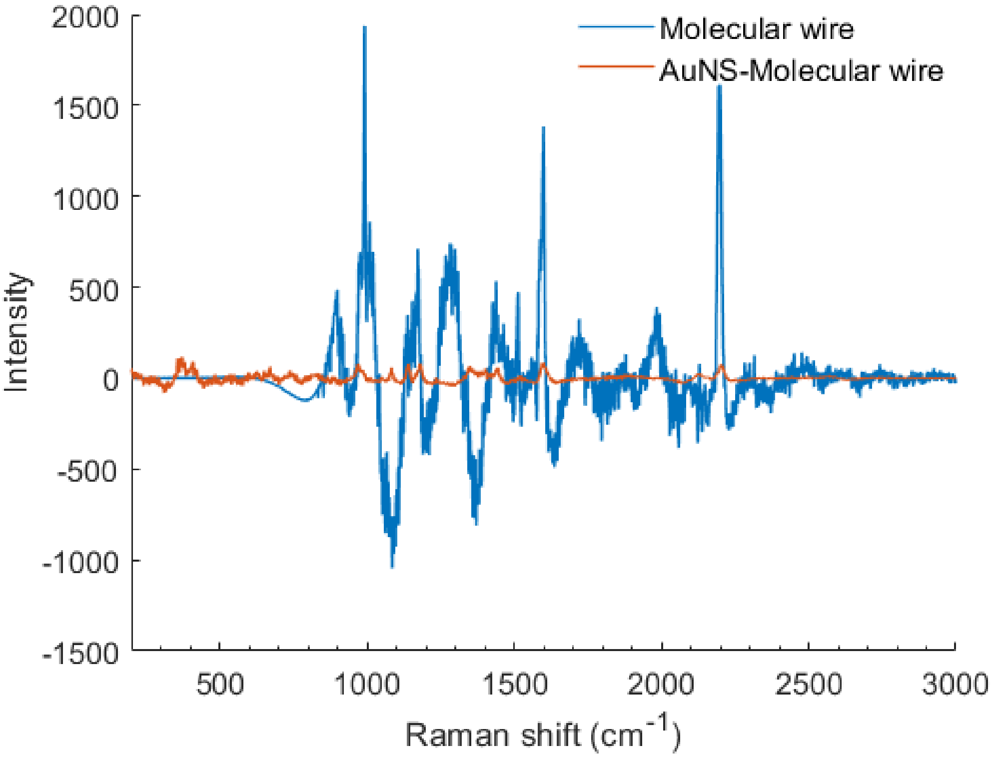

Figure 4.6: Raman spectra of 4-{1-[4-(methylsulfanyl)phenyl]-1H-1,2,3-triazol-4-yl}aniline on the surface of gold nanostars, and isolated as a solid.

4-{2-[2,6-bis(sulfanylmethyl)pyridin-4-yl]-1-chloroethenyl}benzoic acid was added to the gold nanostar surface via the direct approach. Again, some aggregation was visible by eye, as the gold nanostar solution was visibly less blue after stirring; this is likely caused by the carboxylic acid terminal group, causing aggregation in the same way as the previous molecular wire shown in Figure 4.5. Unfortunately, this aggregation resulted in few features in the Raman spectrum (Figure 4.7). The most prominent peak is at 398 cm^{-1}, indicating PVP on the gold nanostar surface, followed by a slight broad peak about 1500 cm^{-1} caused by interference of the glass microscope slide below the sample. There is a weak peak at 872 cm^{-1}, which could be said to match the peak at 901 cm^{-1} in the spectrum of the isolated molecular wire; besides this, it is difficult to say if the molecular wire is indeed present on the gold surface.

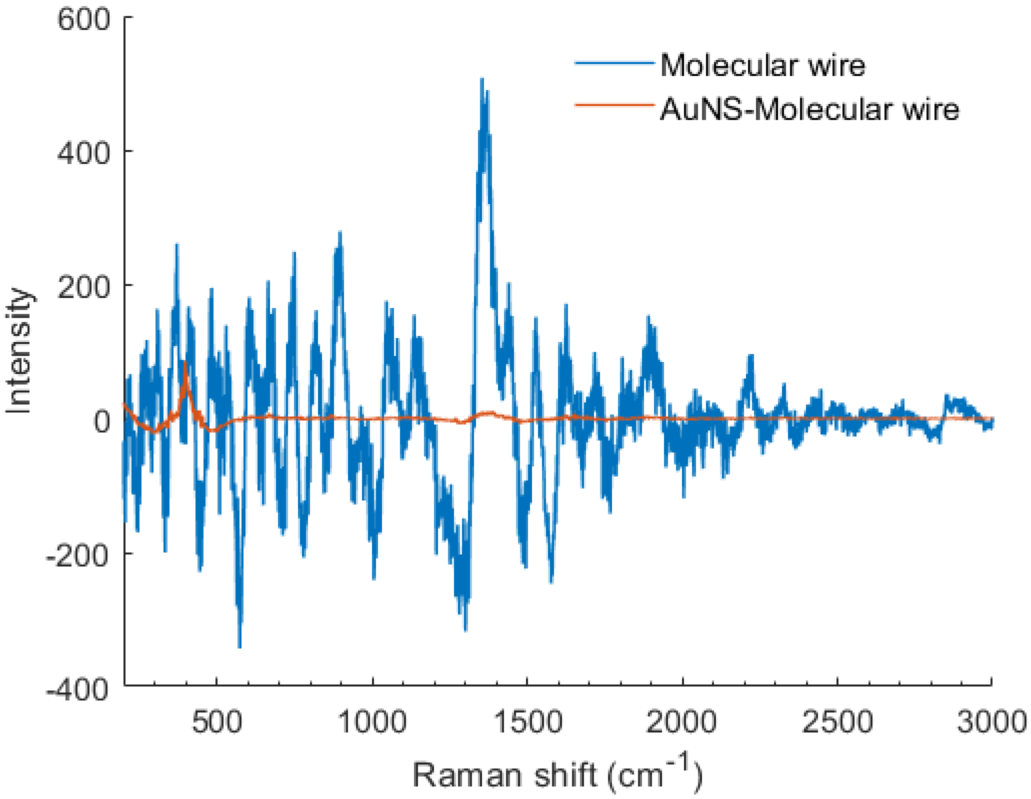

Figure 4.7: Raman spectra of 4-{2-[2,6-bis(sulfonylmethyl)pyridin-4-yl]-1-chloroethenyl}benzoic acid on the surface of gold nanostars, and isolated as a solid.

4.5 Conclusions and Further Synthetic Work

In summary, a number of synthetic methods were trialled in order to obtain a molecular wire on a gold nanostar surface; the effectiveness of these functionalised nanostars to amplify SERS signals is explored in the next section. It was initially speculated that a stepwise approach would be ideal, though this was unsuccessful; it is possible that removal of ^{i}PrNH$_2$ from the reaction mixture could improve this, as studies show that basic conditions may be a cause of aggregation, and this reagent may not be essential to the success of the reaction. This could be investigated further, however was not explored at this time due to time constraints, and the fact that a satisfactory product was obtained by the alternative direct approach.

The ‘probes’ constructed in this section are technically unfinished, consisting only of a gold nanostar and molecular wire reporter. To classify these as complete probes, it would be necessary to add the selective peptide. Before carrying out this final synthetic step, the effects of the molecular wires on SERS were investigated, and peptide coupling would be carried out if these tests were deemed successful.

4.6 Enhancement Effects

To assess potential SERS amplifying effects of molecular wires, it was necessary to create a suitable control. Control molecules should have two essential features; firstly, they must have the same functional groups as the molecular wires, thus giving similar Raman signals. In addition, they must be small molecules, allowing electronic communication over a much shorter range than the molecular wires synthesised in the previous section. A control molecule meeting these two requirements could be bound to a gold nanostar surface and compared to the molecular wire functionalised nanostars. It was theorised that if this ‘control probe’ were to give weaker SERS signals than the molecular wire functionalised nanostars, it could then be concluded that SERS signals are enhanced by molecular wires.

The search for a suitable control molecule was a compromise between optimal structure and time. In an ideal world, a molecule would be synthesised with as much structural similarity to its analogous molecular wire as possible. However, given time constraints, it was more favourable to buy commercially available molecules than to synthesise new compounds.

4.6.1 OPT Wire Controls

For comparison with the OPT wire 4-{1-[4-(methylsulfanyl)phenyl]-1H-1,2,3-triazol-4-yl}aniline (Table 1 structure 4), the first most simple control molecule proposed was 1,2,3-triazole. It was speculated that the triazole could adhere to a gold nanostar surface via either lone pairs on nitrogen 2 or 3.[29] It is not necessary for a control molecule to have a linking group, as a peptide will not be added at this initial testing stage. However, triazoles form very weak coordinate bonds with metals; it is therefore likely that it would be difficult to synthesise a stable AuNS-(1,2,3-triazole) colloid, as the washing step of the synthesis may remove the triazole from the surface all together. This was evident in Raman spectrum of AuNS-(1,2,3-

triazole) (Figure 4.8), which exhibited few strong features besides the characteristic PVP peak from the gold nanostars at 398 cm^{-1}, and a peak from the glass microscope slide at 1377 cm^{-1}. Negative Raman intensities are a result of baseline correction carried out using MATLAB.

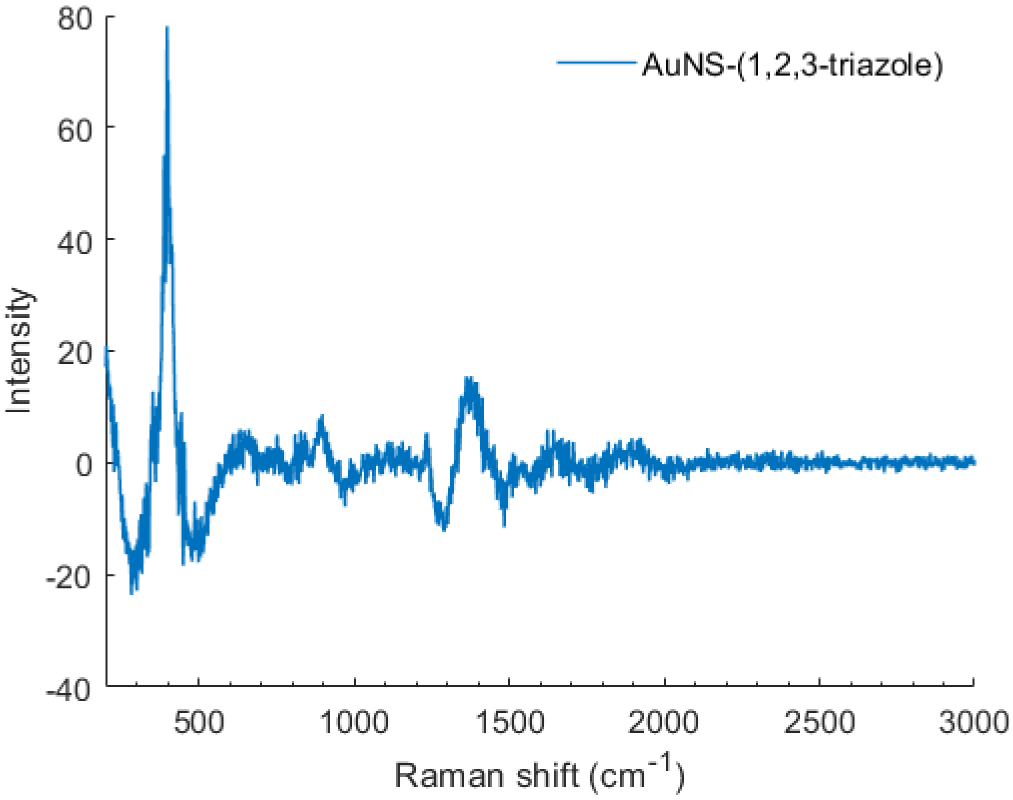

Figure 4.8: Raman spectrum of AuNS-(1,2,3-triazole).

As well as its weak bonding, unfunctionalized 1,2,3-triazole is also a poor control due to its lack of a sulphur-containing anchoring group. Evidence shows that the anchoring group of a molecular wire has a significant impact on conductivity, and sulphur-containing anchoring groups in particular have excellent conductive properties.[25,30] Therefore, a molecule with a different anchoring group to the molecular wire is not a suitable control. Additionally, the highly aurophillic nature of a sulphur-containing anchoring group will likely result in many molecules binding to the gold surface. In comparison, a molecule with a much less aurophillic anchoring group such as triazole will bind to the gold surface more sparsely. Therefore, the AuNS-OPT probe (AuNS-S-(4-phenyl-1H-1,2,3-triazol-4-yl)aniline) would likely give higher SERS signals than the AuNS-(1,2,3-triazole) control due to a higher number of molecules bound to the gold surface, as opposed to being a result of the conductive properties of the molecular wire. For these reasons it is essential to find a control with a similar anchoring group. Sodium 5-thiolate-1,2,3,-triazole was purchased from Fisher Scientific as an acceptable control. It was assumed that in solution, the thiolate ion would bind to gold in much the same way as any other sulphur-containing anchoring group.

It should be noted that this is not an ideal control, as the anchoring group is directly attached to the triazole. This is not the case in the original molecular wire, which has a benzene spacer between the anchoring group and the triazole. This difference in groups bonded to the triazole could affect the conductive properties of the triazole or even its Raman signals, thus making it a sub-optimal control. However, inclusion of a benzene ring in the control molecule would make it a molecular wire, contradicting one of the key requirements of the control. Although it would be a shorter molecular wire than the original, and so the effects of wire length could be compared, the difference in length is not significant enough to make a decent comparison.

Despite the aforementioned concerns, a control probe was synthesised from sodium 5-thiolate-1,2,3,-triazole, as shown in Scheme 4.9. All control probes in this section were centrifuged, washed and resuspended in purite water three times before testing unless otherwise stated. The Raman spectrum of these functionalised gold nanostars is given in in Figure 4.9. Negative Raman intensities are a result of baseline correction carried out using MATLAB.

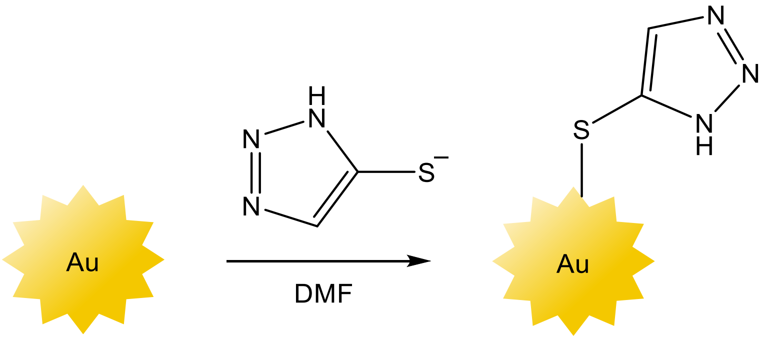

Scheme 4.9: Synthesis of AuNS-S-(1,2,3-triazole) control probe for comparison with AuNS-S-(4-phenyl-1H-1,2,3-triazol-4-yl)aniline.

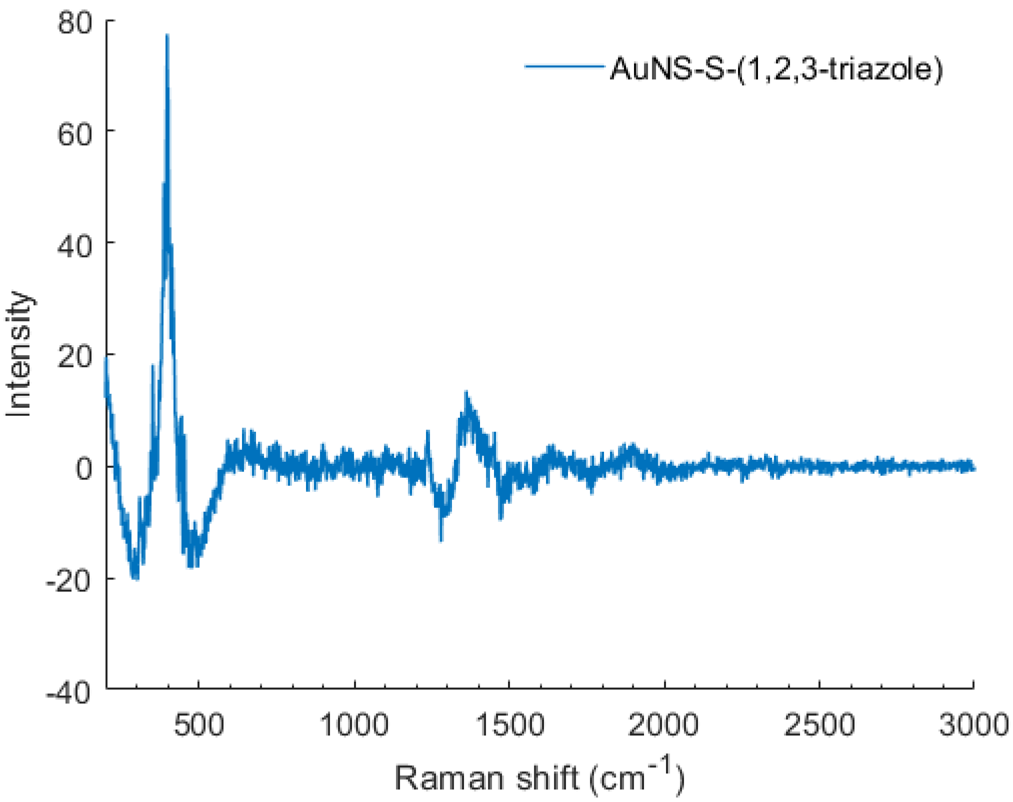

Figure 4.9: Raman spectrum of AuNS-S-(1,2,3-triazole) control probe.

Despite the presence of sulphur in this triazole derivative, which should improve binding to gold, it is clear from the Raman spectrum that the molecule is not present on the gold surface (the peaks present at 399 cm^{-1} and 1363 cm^{-1} can be attributed to PVP and the glass microscope slide, respectively) and so AuNS-S-(1,2,3-triazole) was deemed an unsuitable control. The reasons for this are unclear, but it is possible that the presence of a salt may have caused aggregation of the nanostars (though little aggregation was observed by eye). Following the unsuccessful results with triazole molecules, a new control probe was synthesised using an aniline derivative as a control molecule, as this fragment is also present in the molecular wire. The control probe was synthesised using 4-methylthioaniline (Scheme 4.10), and the Raman peaks of this molecule were visible on the gold nanostar surface (Figure 4.10). Notably, peaks at 1075, 1142 and 1437 cm^{-1} were prominent. Negative Raman intensities are a result of baseline correction carried out using MATLAB.

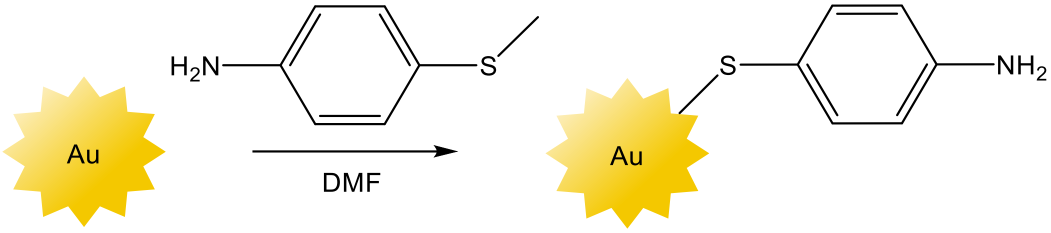

Scheme 4.10: Synthesis of AuNS-S-(aniline) control probe for comparison with AuNS-S-(4-phenyl-1H-1,2,3-triazol-4-yl)aniline.

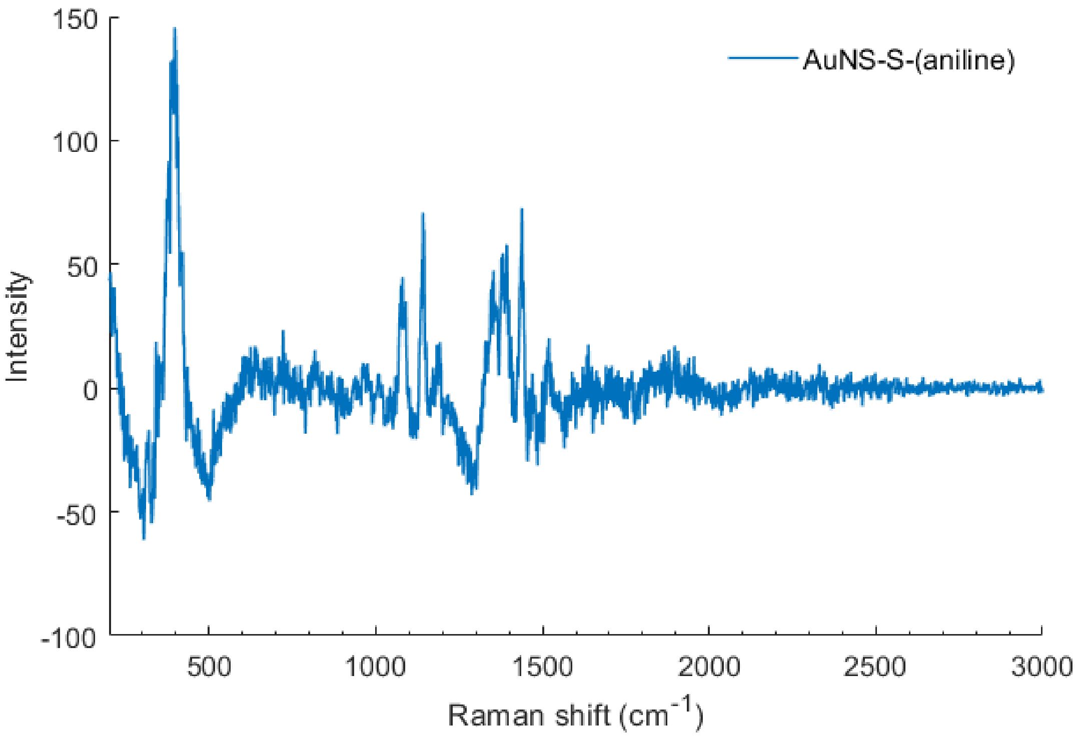

Figure 4.10: Raman spectrum of AuNS-S-(aniline) control probe.

4.6.3 OPE Wire Controls

The original control molecule designed to complement this molecular wire was but-3-yne-1-thiol. As the initial molecular wire design incorporated an alkyne bond to give strong Raman signals, so did the control design, as well as a thiol for binding the gold surface. Although two thiol groups would have been preferable, as this would make the control more structurally similar to the molecular wire, finding a molecule with this functionality from commercial sources was difficult and as previously mentioned, time for synthetic work was limited. The control molecule features a four-carbon chain, as it was speculated that a shorter molecule would be too volatile to work with. When it was discovered that the carbon-carbon triple bond of the molecular wire had been halogenated to yield an alkene, the same was done in the synthesis of the control molecule, so that alkene signals could be compared as opposed to alkyne. Hence the final control molecule became 2-chlorobut-3-ene-1-thiol. This synthesis of this molecule, given in Scheme 4.11, was assisted by Ms Y. Ermakova (4th year MSc. 2018/19). Gold nanostars were then functionalised with the molecule as shown in Scheme 4.12.

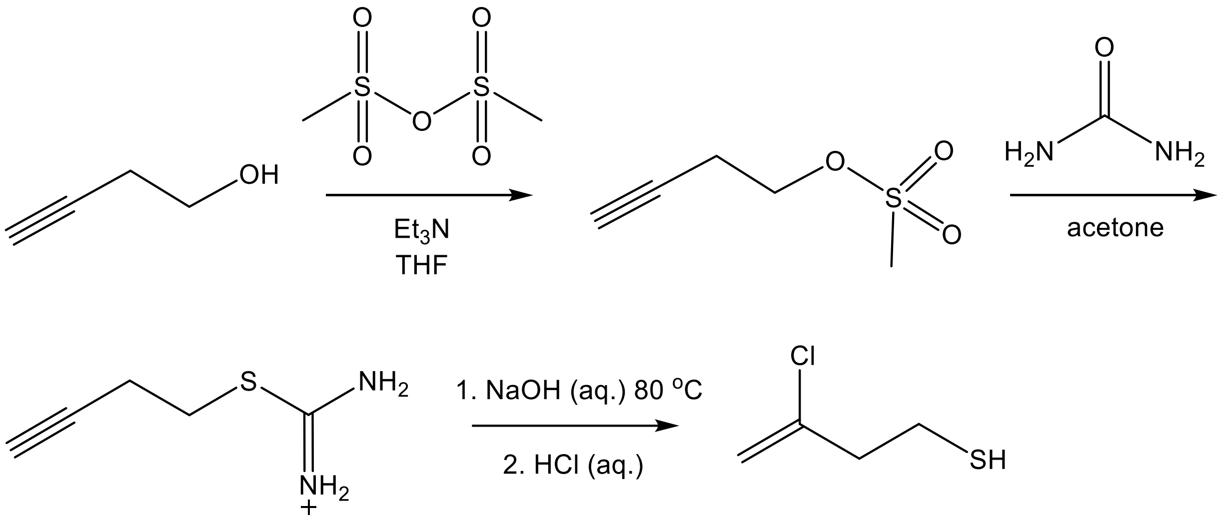

Scheme 4.11: Synthesis of 2-chlorobut-3-ene-1-thiol.

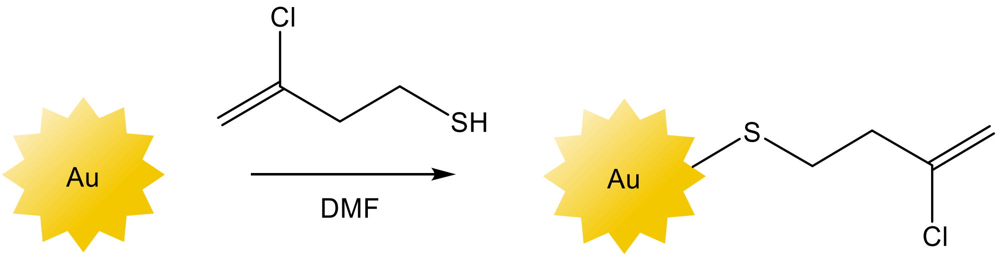

Scheme 4.12: Synthesis of control probe 3 for comparison with AuNS-S-(2-chloro-but-3-ene)

Unfortunately, the Raman spectrum of this probe (Figure 4.11) also shows a lack of significant features, probably due to aggregation of the probe, as the nanostar solution became visibly paler on stirring, though the reason for this is unclear. Negative Raman intensities are a result of baseline correction carried out using MATLAB.

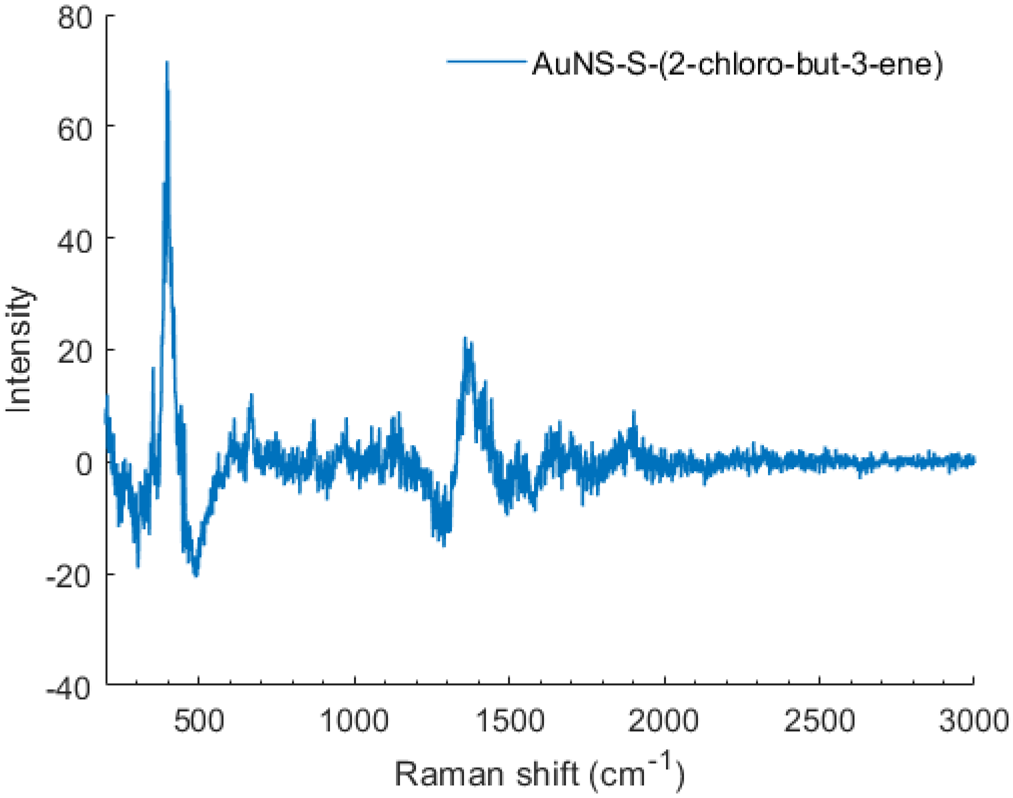

Figure 4.11: Raman spectrum of AuNS-S-(2-chloro-but-3-ene) control probe.

4.6.3 Enhancement Effects: Results

Due to the poor stability of the AuNS-4-{2-[2,6-bis(sulfanylmethyl)pyridin-4-yl]-1-chloroethenyl}benzoic acid and its analogous control, this probe was not explored further. Raman spectra of AuNS-S-(4-phenyl-1H-1,2,3-triazol-4-yl)aniline and AuNS-S-(aniline) are given below (Figure 4.12). Negative Raman intensities are a result of baseline correction carried out using MATLAB.

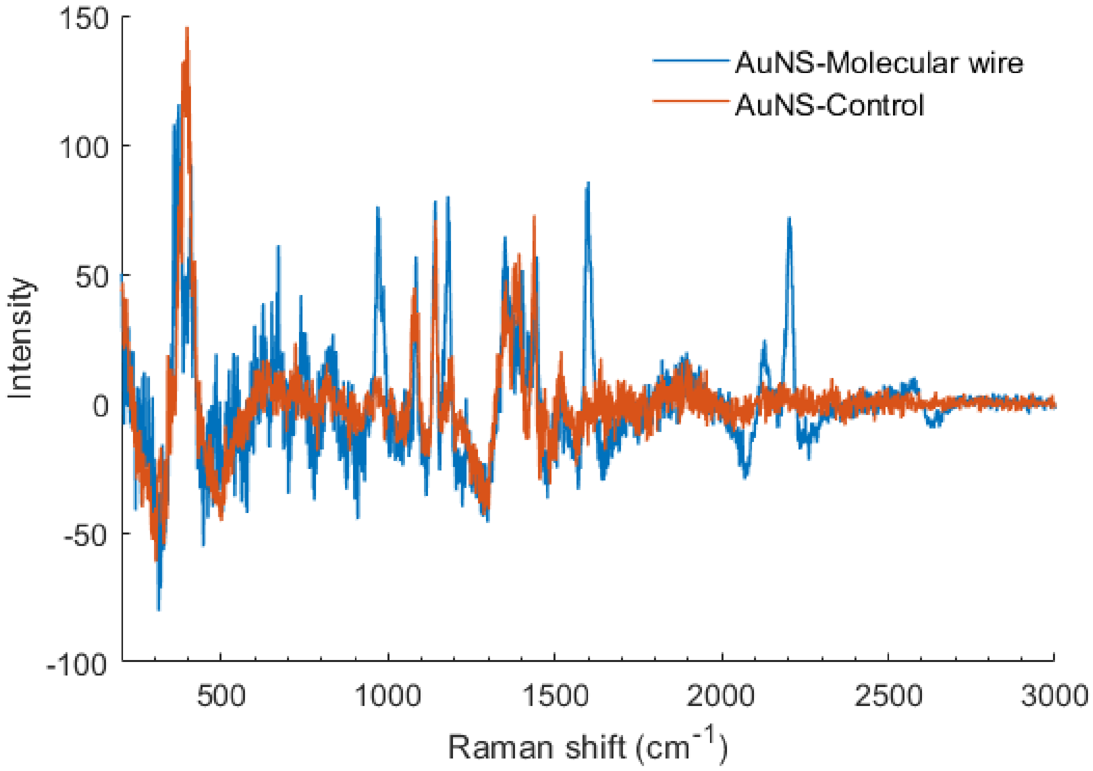

Figure 4.12: Raman spectra of AuNS-S-(4-phenyl-1H-1,2,3-triazol-4-yl)aniline (blue) and *AuNS-S-(aniline).*

The most noticeable matching peaks which can be compared are those at 1080, 1142, 1184, and 1437 cm^{-1}. It is clear that the peaks at these positions are not significantly larger than those of the control, and so we can conclude from this data that molecular wires do not enhance SERS signals in this instance.

4.7 Conclusions and Further Work

These experiments conclude that no noticeable SERS signal enhancement could be observed in the presence of molecular wires. However, it would have been valuable to try different wire structures and lengths. Of the two molecular wire functionalised AuNS structures synthesised in this chapter, only one could be tested against a control, due to instability of the gold nanostars in solution following the wire attachment step. Despite difficulties faced in this project, many different molecular wire monolayers have been constructed on gold surfaces in the literature.[31–34] It may be valuable to analyse the effect of these known molecular wire monolayers on SERS, as a more tried-and-tested system could prove more stable.

In addition, constructing wires with a greater variety of lengths may have made for a more stark contrast, although this was not attempted in this project due to the challenges of synthesising long molecular wires, which can be highly insoluble. Although the control probes used in this chapter were sub-optimal, it is unlikely that a control probe with a closer structure to its analogous molecular wire would have yielded different results; clearly, the problem lies with the AuNS-molecular wire structures themselves, which gave poor Raman signals due to instability. It was noted that the probes in this chapter appeared to have less visible aggregation when suspended in DMF as opposed to water, and so different solvents could have been explored to aid stability, although any probe deemed successful would need to be water soluble for biological compatibility in melanoma-targeting experiments.

In addition, it may be useful take these experiments ‘back to basics’ by attaching the molecular wires to gold nanospheres, as opposed to nanostars. Simple gold nanospheres are known to be more stable than elaborate shapes such as stars.[35] Use of a more reliable gold colloid may have improved stability; it could be said that starting with gold nanostars was too ambitious. However, time constraints would not allow these syntheses to be repeated with gold nanospheres.

In conclusion, the idea that molecular wires could improve SERS signals could not be proven by these experiments, although more research would need to be conducted to rule out this hypothesis entirely.

4.8 References

1 R. P. Feynman, *Calif. Inst. Technol. Eng. Sci. Mag.*

2 B. Mann and H. Kuhn, *J. Appl. Phys.*, 1971, **42**, 4398–4405.

3 F. J. Bezares, J. D. Caldwell, O. Glembocki, R. W. Rendell, M. Feygelson, M. Ukaegbu, R. Kasica, L. Shirey, N. D. Bassim and C. Hosten, *Plasmonics*, 2012, **7**, 143–150.

4 E. Smith and G. Dent, *Mod. Raman Spectrosc. – A Pract. Approach*, 2004, 1–21.

5 E. Le Ru and P. Etchegoin, *Principles of Surface-Enhanced Raman Spectroscopy: and related plasmonic effects*, Elsevier, 2008.

6 K. Bowes, Durham University, 2017.

7 F. Chen, X. Li, J. Hihath, Z. Huang and N. Tao, *J. Am. Chem. Soc.*, 2006, **128**, 15874–15881.

8 V. Kaliginedi, A. V. Rudnev, P. Moreno-García, M. Baghernejad, C. Huang, W. Hong and T. Wandlowski, *Phys. Chem. Chem. Phys.*, 2014, **16**, 23529–23539.

9 Y. Kang, D.-J. Won, S. R. Kim, K. Seo, H.-S. Choi, G. Lee, Z. Noh, T. S. Lee and C. Lee, *Mater. Sci. Eng. C*, 2004, **24**, 43–46.

10 V. V Rostovtsev, L. G. Green, V. V Fokin and K. B. Sharpless, *Angew. Chemie Int. Ed.*, 2002, **41**, 2596–2599.

11 J. E. Moses and A. D. Moorhouse, *Chem. Soc. Rev.*, 2007, **36**, 1249–1262.

12 H. C. Kolb, M. G. Finn and K. B. Sharpless, *Angew. Chemie Int. Ed.*, 2001, **40**, 2004–2021.

13 R. Huisgen, *Angew. Chemie Int. Ed. English*, 1963, **2**, 565–598.

14 Z. Jia and Q. Zhu, *Bioorg. Med. Chem. Lett.*, 2010, **20**, 6222–6225.

15 X. Peng, Q. Wang, Y. Mishra, J. Xu, D. E. Reichert, M. Malik, M. Taylor, R. R. Luedtke and R. H. Mach, *Bioorg. Med. Chem. Lett.*, 2015, **25**, 519–523.

16 B. T. Worrell, J. A. Malik and V. V Fokin, *Science (80-.).*, 2013, **340**, 457–460.

17 L. Liang and D. Astruc, *Coord. Chem. Rev.*, 2011, **255**, 2933–2945.

18 S. Lal and S. Díez-González, *J. Org. Chem.*, 2011, **76**, 2367–2373.

19 S. I. Presolski, V. P. Hong and M. G. Finn, *Curr. Protoc. Chem. Biol.*, 2011, **3**, 153–162.

20 J. E. Hein and V. V Fokin, *Chem. Soc. Rev.*, 2010, **39**, 1302–1315.

21 J. Jover, *J. Chem.*, 2015, **2015**, 430358.

22 R. Berg and B. F. Straub, *Beilstein J. Org. Chem.*, 2013, **9**, 2715–2750.

23 G. C. Tron, T. Pirali, R. A. Billington, P. L. Canonico, G. Sorba and A. A. Genazzani, *Med. Res. Rev.*, 2008, **28**, 278–308.

24 J. Sukegawa, C. Schubert, X. Zhu, H. Tsuji, D. M. Guldi and E. Nakamura, *Nat.*

Chem., 2014, **6**, 899–905.

25 V. Obersteiner, D. A. Egger and E. Zojer, *J. Phys. Chem. C*, 2015, **119**, 21198–21208.

26 K. M. Koczkur, S. Mourdikoudis, L. Polavarapu and S. E. Skrabalak, *Dalt. Trans.*, 2015, **44**, 17883–17905.

27 S. K. Seol, D. Kim, S. Jung, W. S. Chang, Y. M. Bae, K. H. Lee and Y. Hwu, *Mater. Chem. Phys.*, 2012, **137**, 135–139.

28 M. Zhou, B. Wang, Z. Rozynek, Z. Xie, J. O. Fossum, X. Yu and S. Raaen, *Nanotechnology*, 2009, **20**, 505606.

29 P. I. P. Elliott, in *Organometallic Chemistry: Volume 39*, The Royal Society of Chemistry, 2014, vol. 39, pp. 1–25.

30 E. Leary, A. La Rosa, M. T. Gonzalez, G. Rubio-Bollinger, N. Agrait and N. Martin, *Chem. Soc. Rev.*, 2015, **44**, 920–942.

31 M. Miyachi, Y. Yamanoi, Y. Shibata, H. Matsumoto, K. Nakazato, M. Konno, K. Ito, Y. Inoue and H. Nishihara, *Chem. Commun.*, 2010, **46**, 2557–2559.

32 M. Minamoto, M. M. Matsushita and T. Sugawara, *Polyhedron*, 2005, **24**, 2263–2268.

33 S. Taniguchi, M. Minamoto, M. M. Matsushita, T. Sugawara, Y. Kawada and D. Bethell, *J. Mater. Chem.*, 2006, **16**, 3459–3465.

34 C. Lee, Y. Kang, K. Lee, S. Rim Kim, D.-J. Won, J. Sung Noh, H. Kyu Shin, C. Keun Song, Y. Soo Kwon, H.-M. So and J. Kim, *Curr. Appl. Phys.*, 2002, **2**, 39–45.

35 M. Chirea, *Catal.* , 2013, 3.

5. Conclusions

The goal of this work has been to create a surface enhanced Raman probe for the selective detection of melanoma skin cancer. Melanoma is the deadliest type of skin cancer, though survival rates improve significantly when it is caught in the early stages; catching the disease early on is therefore vital to reducing mortality rates.[1,2] Unfortunately, current diagnostic methods are invasive and rely on speculative examination of the lesion by an experienced clinician, taking up precious time and resources, as well as having potential for human error.[3–5] A rapid detection system could save time and circumvent the need for an expert, making diagnosis faster and more accessible, especially in areas where experienced specialists are scarce.

SERS offers a promising alternative; having the potential for accuracy down to the single molecule, SERS could be used to detect biomarkers of cancer early in the disease.[6,7] However, the use of this technique to detect melanoma has not been fully explored in the literature.

5.1 Evaluation of the SERS probe

A SERS probe was designed and fabricated using gold nanostars as the SERS substrate, methylene as a Raman reporter, a silica coating, and the linking group APTMS to bind the selective peptide [Nle^4, D-Phe^7]-α-MSH. This probe was applied to the human melanoma cell line A375, as well as the mouse skin fibroblast cell line NIH 3T3 (acting as a control), and Raman spectra of the cell samples applied to glass coverslips were recorded before and after rinsing the sample, to determine selectivity. Results in Chapter 3 show that when the probe is applied to the control cell line, the Raman signals of the reporter molecules are significantly diminished after rinsing, implying that the probe has not adhered to the cells. However, after rinsing A375 cells dosed with the probe, the Raman signals remain sufficiently prominent to suggest that the probe has bound to the target and is therefore selective. These results suggest that the probe has achieved its goal; a Raman signal is observed in the presence of melanoma cells, and when no melanoma is present, the unbound probe rinses away from the sample to give no signal. While this result is significant, the probe requires further optimization before it could be applied in a clinical setting.

5.1.2 Structural Optimisation

Further research into creating a gold nanostar core with a more controlled number of points could improve reproducibility. Although longer, sharper points could create a greater lightening rod effect, results showed that silica coating nanostars of this type resulted in large deposits of silica between points, which reduced SERS signals; further optimization of the silica coating method to address this could result in better enhancing effects.

In Chapter 2, it was speculated that a SERS probe with a silica coating may give false-positive results in cells, as the hydrophilic nature of silica could facilitate probe adhesion to the cell, regardless of functionalisation with a peptide. It is possible that a SERS probe could be designed with a hydrophobic polymer coating, such that the probe would be repelled from the cell surface, unless forced into contact with a selective peptide, ensuring that there would be no false-positive results. The most obvious setback of this idea is finding a method to bind a hydrophobic polymer to gold nanostars, as such a polymer would have no suitable functional groups capable of binding to gold. Nonetheless, the prospect of eliminating false positives with a hydrophobic coating remains of interest, and given more time, this avenue could have been pursued further. Alternatively, the use of a different Raman reporter molecule which binds to the gold surface more strongly than methylene blue could negate the need for a surface coating all together (although the lack of a coating to provide space between the gold nanostars may result hotspot formation via aggregation of the stars, reducing reproducibility).

5.1.3 Reporter Optimisation

In Chapter 2 several NIR dyes were investigated as potential reporter molecules. Commercially available dyes were explored as these are easily obtainable, and utilise the SERRS effect when used alongside a 785 nm laser. Due to poor SERS signals and stability issues of other dyes bound to gold nanostars, only methylene blue was determined to be suitable. This dye does have many benefits, including being inexpensive, non-fluorescent (minimising background noise) and approved by the US FDA for medical use. Despite these advantages, to further optimise the probe it would be beneficial to find a molecule with stronger SERS signals. A molecule containing functional groups with vibrational frequencies outside of the biological window, such as an alkyne, could also improve spectral interpretation, as there would be minimal noise from the biological sample in this region. As mentioned previously, a molecule which binds covalently to the gold surface may prove beneficial as it would negate the need for a silica coating, which could improve Raman signals (as the SERS effect is distance dependent) as well as potentially reducing false-positive results. Furthermore, a molecule such as a thiol could form a densely-packed SAM on the gold nanostar surface, improving SERS signals by increasing reporter concentration. However, finding a SERRS reporter with all of these qualities would likely require a novel molecule to be designed and synthesised, while the use of the commercially available methylene blue would keep the cost of producing the probe to a minimum.

5.1.3 Peptide Optimisation and Cell Lines

The peptide [Nle^4, D-Phe^7]-α-MSH was chosen for its ability to target MC1Rs as shown in the literature. Although further research could have been done to find a peptide with optimal selectivity, Raman spectra in Chapter 3 show that SERS signals of the selective probe in melanoma cells are not significantly diminished on rinsing as they are in the control cell line, suggesting that this peptide is sufficiently selective.

Of the many melanoma cell lines available commercially, A375 was selected as it has been proven to express MC1Rs, making it suitable for these experiments. However, microscopy images given in Chapter 3 show some uptake of the non-selective (peptide free) probe into A375. This suggests that some of the selectivity may be contributed to the EPR effect rather than the peptide. In order to fully rule this out, it would be beneficial to test the probe with a range of cancer cell lines from different types of cancer besides melanoma. Still, it is clear that there is a great deal more probe about the A357 cells when the peptide is present, so it is reasonable to assume that most of the selectivity is due to the peptide. The possibility of probe being taken up by other cancer cells via the EPR effect does present the possibility of false positive test results when melanoma is not present but another cancer such as squamous cell carcinoma is present. Therefore, any future work on this probe would require the researcher to define a minimum signal output for melanoma to be confirmed.

5.2 Evaluation of Molecular Wire SERS

It was speculated that molecular wires could possess the ability to enhance SERS signals. Previous work suggests that molecular wires are able to propagate evanescent waves from a metal surface with propagating surface plasmons.[8] Following this, it was suggested that molecular wires could be used to extend the reach of the SERS effect further from the metal surface, effectively acting as antennae to improve SERS signals.

Two molecular wires were synthesized and adhered to gold nanostar surfaces, along with ‘control molecules’; shorter molecules with similar functional groups, which would therefore have similar peaks in their Raman fingerprints. ‘Molecular wire augmented SERS’ would be evident if the Raman intensities were significantly greater in the molecular wire SERS spectra compared to the SERS spectra of the control molecules. Overall, no such signal difference was observed.

One of the major difficulties encountered in this chapter was the synthesis of stable molecular wire functionalized gold nanostars, as these had a tendency to aggregate, possibly due to various interactions of the wires between nanostars as discussed in Chapter 4. To counter this, more simple wires without terminal functional groups could be trialed, to minimize interaction between wires. However, a terminal functional group would eventually be a necessity, in order to bind a selective peptide and build a complete SERS probe, as in Chapter 3.

It is also possible that stability could be improved if simpler gold nanoshapes, such as nanospheres, were used, as these are generally more stable than nanostars. Overall, the possibility of molecular wire enhanced SERS could be known for certain if a more stable probe were fabricated, though this would take many optimization steps (including finding an ideal molecular wire and SERS substrate), which could not be fully explored in this work due to time constraints.

5.3 Further Work

In conclusion, the SERS reporter synthesized and tested in Chapters 2 and 3 can be classified as a selective probe in that Raman signals were observed in melanoma cells after rinsing, but not in control cells. In order to improve this probe, it would be beneficial to further optimize the nanostar core and reporter to maximise SERS output, though at this stage the results are promising. An optimized version of the probe presented in this work could then be tested with human tissue samples, and potentially progress to clinical trials in melanoma patients. Used in conjunction with a table-top Raman spectrometer, the probe could be used by any non-specialist healthcare worker to give rapid, point-of-care diagnosis of melanoma.

5.4 References

1 A.-V. Giblin and J. M. Thomas, *J. Plast. Reconstr. Aesthetic Surg.*, 2007, **60**, 32–40.

2 J. E. Mayer, S. M. Swetter, T. Fu and A. C. Geller, *J. Am. Acad. Dermatol.*, 2014, **71**, 599.e1-599.e12.

3 I. H. Wolf, J. Smolle, H. P. Soyer and H. Kerl, *Melanoma Res.*, 1998, **8**, 425–429.

4 H. Kittler, H. Pehamberger, K. Wolff and M. Binder, *Lancet Oncol.*, 2002, **3**, 159–165.

5 J. L. Bong, R. M. Herd and J. A. A. Hunter, *J. Am. Acad. Dermatol.*, 2002, **46**, 690–694.

6 J. H. Granger, N. E. Schlotter, A. C. Crawford and M. D. Porter, *Chem. Soc. Rev.*, 2016, **45**, 3865–3882.

7 E. C. Dreaden, A. M. Alkilany, X. Huang, C. J. Murphy and M. A. El-Sayed, *Chem. Soc. Rev.*, 2012, **41**, 2740–2779.

8 K. Bowes, Durham University, 2017.

6. Experimental

6.1 General Conditions

Instrumental set up

UV-Vis spectra were recorded with a UV-100 spectrometer, using a 1 cm quartz cell. Raman spectra were acquired using a Horiba Jobin Yvon LabRAM HR confocal Raman microscope, with a peltier-cooled CCD, 50× LWD objective lens, and diode laser. An excitation wavelength of 785 nm was used unless stated otherwise, with <1 mW laser power at the sample. TEM images were obtained by using a JEOL 2100F TEM. Samples for TEM were deposited onto carbon films on 200 mesh copper grids and allowed to air dry before use. Fluorescence emission spectra were recorded using a Horiba Jobin Yvon SPEX Fluorolog 3-22 spectrofluorometer. NMR spectra were obtained using a Bruker Avance-400 spectrometer. Laser scanning confocal microscopy (LSCM) images were acquired with a Leica SP5 II LSCM confocal microscope with a HCX APO x63/1.4 NA Lambda-Blue objective. Excitation was 633 nm, with an emission detection window of 650-800 nm, and scan speed of 100 Hz. Transmission images were collected using a 488 nm laser line. The field of view was 1024 x 1024 pixels, with a pixel size of 98.5 x 98.5 µm.

General Synthetic Conditions

Standard starting materials were purchased from Sigma Aldrich. Peptides DMPGTVLP and [Nle^4,D-Phe^7]-α-MSH were purchased from Biopeptek Ltd. and GenScript Biotech respectively. Reactions were carried out at room temperature and in normal atmospheric conditions unless stated otherwise.

6.2 SERS Probes with Dye-Based Reporters and Related Syntheses

Citrate stabilised gold nanoparticles (AuNP)

A 100 ml aqueous solution of sodium chloroaurate (0.01 wt. %, 0.01g) was heated to boiling and 7 ml sodium citrate added (1 wt. %, 0.07 g). The mixture was boiled for 30 mins until a colour change from yellow to red was observed, consistent with the Turkevich method.[1] $\lambda_{max}(H_2O)$/nm 530.

Gold nanoparticle seed growth

20 ml of AuNP seed solution was made up to 100 ml with water and the solution was heated to 65 °C, before adding 3 ml of sodium citrate solution (1 wt. %, 0.03 g). An aqueous solution of sodium chloroaurate (3 mM) was added dropwise until the desired absorbance was achieved. For AuNP with an average diameter of 62 nm (ʎ = 548 nm), 25 ml $NaAuCl_4$ solution was added in total. The nanoparticle solution was centrifuged twice at 4400 rpm and resuspended in water.

Silica coated AuNP (AuNP@SiO_2)

Following a modified Stöber method [2], the pH of a 20 ml solution of citrate stabilised AuNP suspended in water (ʎ = 548 nm, 0.02 mg cm^{-2}) was adjusted to 10.5 by dropwise addition of ammonia. A 2 ml solution of tetraethylorthosilicate (TEOS) in EtOH (1 mM) was added dropwise over 1.5 h, and the mixture stirred was stirred for 24h. The nanoparticle solution was then centrifuged twice at 4400 rpm and suspended in EtOH:H_2O (1:1). λ_{max}(EtOH)/nm 530.

AuNP@SiO_2-(3-aminopropyl) trimethoxysilane (AuNP@SiO_2-APTMS)

A 10 ml solution of AuNP@SiO_2 (0.02 mg cm^{-2}) was made up to 100 ml in EtOH:H_2O (1:1) and adjusted to pH 10.5 by dropwise addition of ammonia. A 20 mM solution of 3-aminopropyl trimethoxysilane (17.4 µl) in EtOH was added and the mixture stirred for 3h at room temperature. The nanoparticle solution was then centrifuged twice at 4400 rpm and suspended in EtOH:H_2O (1:1). λ_{max}(EtOH)/nm 530.

3-dansylpropyl trimethoxysilane (APTMS-DNS)

Dansyl chloride (7 mg, 1 mmol) was dissolved in DCM, and 3-aminopropyl trimethoxysilane (4.5 mg, 1 mmol) was added. 9 µl tributylamine (1.5 mmol) was then added, and the mixture was stirred for 2 hours. The solvent was then removed *in vacuo* and filtered through a silica plug yielding the product as a yellow oil (18 mg, 67 %). ^{1}H NMR (400 MHz, $CDCl_3$): δ_H 0.54 (m, 2H, H5), 2.93 (m, 8H, H1 and H3), 3.50 (s, 9H, H6), 7.22 (d, 1H, aromatic), 7.55 (m, 2H, aromatic), 8.26 (dd, 2H, aromatic), 8.55 (d, 1H, aromatic). Consistent with literature.[3]

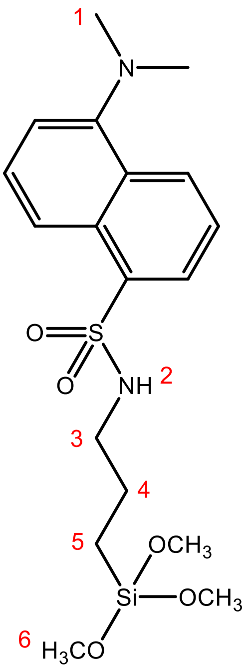

$Au@SiO_2$-(3-dansylpropyl triethoxysilane) ($Au@SiO_2$-APTMS-DNS)

A 5ml solution of $Au@SiO_2$-APTMS (0.2 mg cm^{-2}) was centrifuged and resuspended in 2 ml $NaHCO_3$ buffer solution (pH 10, 25 mM). A 1 ml solution of dansyl chloride in acetone (20 mM) was added and the mixture was stirred in the dark for 1h at 60°C. The nanoparticle solution was then centrifuged twice at 4400 rpm and suspended in EtOH. λ_{max}(EtOH)/nm 320, 530.

Gold nanostars (AuNS): 'one-step' method

5 g polyvinylpyrrolidone (PVP) was dissolved in 150 ml DMF with stirring at 8000 rpm. 240 µl aqueous sodium chloroaurate solution (0.17 M) was added and a colour change from yellow to blue was observed within 30 mins. Particles were washed by centrifuging at 2400 rpm for 20 mins. Excessive centrifuging was avoided to prevent aggregation.[4] The supernatant was removed and particles were resuspended in purite water, and characterised using TEM. λ_{max}(EtOH)/nm 976.

Gold nanoparticle seeds (nanostar precursors for 'two-step' method)

A 10 ml aqueous solution of sodium chloroaurate (1 mM) was brought to boil, and 1.5 ml of sodium citrate solution (1 wt%, 15 mg) was added quickly. A colour change from yellow to red was observed immediately. The solution was refluxed a further 15 mins before cooling to room temperature.[5] The resulting seeds were not centrifuged to minimise aggregation (additives in this synthesis were minimal and not detrimental to nanostar synthesis). λ_{max}(H_2O)/nm 527.

Gold nanostars: 'two-step' method

A 100 ml solution of sodium chloroaurate (0.25 mM in water) was stirred at 700 rpm with 100 µl conc. HCl and 1 ml seed solution. 1 ml silver nitrate solution (2mM in water) and 500 µl ascorbic acid solution (100 mM in water) were added simultaneously, and a colour change from yellow to blue was observed within one minute. The nanostars were centrifuged for 15 mins at 2400 rpm to halt nucleation, and resuspended in purite water.[5] λ_{max}(EtOH)/nm 568, 983.

Silica coated gold nanostars with methylene blue Raman reporter and linker (AuNS-MB@SiO_2-APTMS)

50 mg methylene blue was added to a 20 ml solution of AuNS suspended in purite water. The solution was stirred for 1h before centrifuging at 2400 rpm for 20 mins, to remove excess methylene blue. The particles were resuspended in 20 ml purite water, and the pH was made up to 10.5 by dropwise addition of ammonia. 1.5 ml tetraethyl orthosilicate (TEOS) solution in ethanol (5 mM) was added dropwise over 40 mins with stirring. The solution was stirred for a further 20 mins, before adding 5 ml (3-aminopropyl)trimethoxysilane (APTMS) solution in ethanol (10 mM) dropwise over 30 mins. The solution was stirred for 1h, and the particles were washed by centrifuging twice at 2400 rpm for 20 mins, resuspended in purite water, and characterised by TEM. λ_{max}(EtOH)/nm 650, 974.

Silica coated gold nanostars with methylene blue Raman reporter, linker and MCF7 selective peptide (AuNS-MB@SiO_2-APTMS-DMPGTVLP)

A 20 ml solution of AuNS-MB@SiO2-APTMS, prepared as stated above, was resuspended in DMF and cooled to 0 °C. 0.5 mg of the peptide DMPGTVLP, 37 µL 4-dimethylaminopyridine (3.7 nmol) and 125 µL dicyclohexyl carbodiimide (60 nmol) were added. The solution was then allowed to warm to room temperature and stirred for 16 hr, before centrifuging at 4400 rpm for 20 mins and resuspending in water.

Silica coated gold nanostars with methylene blue Raman reporter, linker and A375 selective peptide (AuNS-MB@SiO_2-APTMS-[Nle^4,D-Phe^7]-α-MSH)

A 20 ml solution of AuNS-MB@SiO2-APTMS, prepared as stated above, was resuspended in DMF and cooled to 0 °C. A 100 µL solution of the peptide [Nle^4,D-Phe^7]-α-MSH in DMF (60 nmol) , 37 µL 4-dimethylaminopyridine (3.7 nmol) and 125 µL dicyclohexyl carbodiimide (60 nmol) were added. The solution was then allowed to warm to room temperature and stirred for 16 hr, before centrifuging at 4400 rpm for 20 mins and resuspending in water.

Silica coated gold nanostars with cresyl violet fluorescent reporter/ HITCI reporter and linker (AuNS-CV@SiO_2-APTMS, AuNS-HT@SiO_2-APTMS)

Prepared in the same way as the methylene blue analogue, substituting methylene blue for cresyl violet and HITCI respectively. $\lambda_{max\text{-}CV}$(EtOH)/nm 679, 974 $\lambda_{max\text{-}HT}$(EtOH)/nm 674, 974.

Silica coated gold nanostars with crystal violet fluorescent reporter/ HITCI reporter, linker and MCF7 selective peptide (AuNS-CV@SiO_2-APTMS- DMPGTVLP, AuNS-HT@SiO_2-APTMS- DMPGTVLP)

Prepared in the same way as the methylene blue analogue, substituting AuNS-MB@SiO_2-APTMS for AuNS-CV@SiO_2-APTMS and AuNS-HT@SiO_2-APTMS respectively.

Silica coated gold nanostars with crystal violet fluorescent reporter, linker and A375 selective peptide (AuNS-CV@SiO2-APTMS-[Nle^4,D-Phe^7]-α-MSH)

Prepared in the same way as the methylene blue analogue, substituting AuNS-MB@SiO_2-APTMS for AuNS-CV@SiO_2-APTMS.

6.3 Molecular Wires and Related Syntheses.

1,4-azido(methylthio)phenol

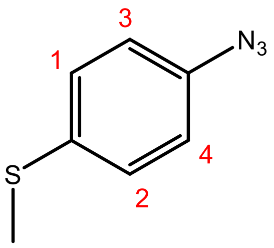

Methylthioaniline (306 mg, 2.20 mmol) was dissolved in a 1:1 solution of water and HCl at 0 °C. Sodium nitrite (495 mg, 7.20 mmol) was dissolved in water (1 ml) and added dropwise, and the mixture was stirred for 1 h. The mixture was then poured into a solution of sodium acetate (4 g, 48.8 mmol) and sodium azide (508 mg, 7.82 mmol) in water (30 ml) and stirred 15 h. The product was extracted with DCM, washed with brine and dried over Na_2SO_4 before removing the solvent *in vacuo* to give 1,4-azido(methylthio)phenol as a yellow oil (225 mg, 62 %). ^{1}H NMR (400 MHz, $CDCl_3$): δ_H 2.40 (3H, s, CH_3), 6.98 (2H, dd, J = 6.6, 2.1, H1 H2), 7.28 (2H, dd, J = 6.6, 2.1, H3 H4). Consistent with literature.[6]

General method for synthesis of triazole molecular wires using $CuSO_4$

1,4-azido(methylthio)phenol (50 mg, 0.30 mmol) was dissolved in either a 1:1 solution of water and ethanol or t-butanol. Copper sulphate (1.26 mg, 5.04 x10^{-3} mmol, 2 %) and sodium ascorbate (9.98 mg, 0.05 mmol, 20 %) were added, followed by the appropriate alkyne (0.25 mmol), before stirring 16 h at RT. Potential product was extracted with dichloromethane, washed with brine and $NaHCO_3$ and dried over $MgSO_4$ before removing solvent *in vacuo.*[7] This method did not yield any product.

General method for synthesis of triazole molecular wires using [CuBr(PPh$_3$)$_3$]

1,4-azido(methylthio)phenol (50 mg, 0.30 mmol) and bromotris(triphenylphosphine)copper(I) (14 mg, 1.52 x10^{-2} mmol, 5 %) were dissolved in acetonitrile. The appropriate alkyne was added (0.30 mmol) and the mixture was stirred for 16 h at RT. Potential product was extracted with ethyl acetate and dried over MgSO$_4$ before removing solvent *in vacuo*.[8] This method did not yield any product.

General method for synthesis of triazole molecular wires using [Cu(CH$_3$CN)$_4$PF$_6$]

1,4-azido(methylthio)phenol (50 mg, 0.30 mmol) was dissolved in acetonitrile (50 ml) with tetrakis(acetonitrile)copper(I) hexafluorophosphate (56 mg, 0.15 mmol, 0.5 eq), tetrabutylammonium difluorotriphenylsilicate (81 mg, 0.15 mmol, 0.5 eq.), and diisopropylamine (168 µl, 1.2 mmol, 4 eq.). The appropriate alkyne was added (0.30 mmol) and the mixture was stirred 16 h at RT. Any precipitate formed was isolated via Buchner filtration and washed with THF.[9]

3-{1-[4-(methylsulfanyl)phenyl]-1H-1,2,3-triazol-4-yl}benzoic acid

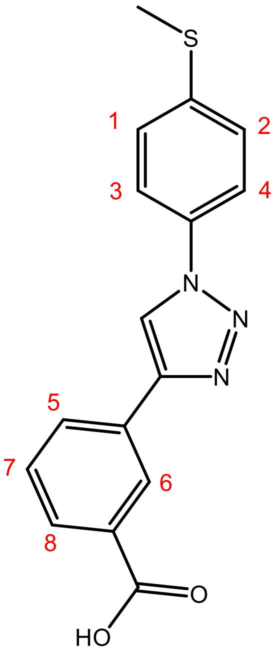

1,4-azido(methylthio)phenol (50 mg, 0.30 mmol) was dissolved in acetonitrile (50 ml) with tetrakis(acetonitrile)copper(I) hexafluorophosphate (56 mg, 0.15 mmol, 0.5 eq), tetrabutylammonium difluorotriphenylsilicate (81 mg, 0.15 mmol, 0.5 eq.), and diisopropylamine (168 µl, 1.2 mmol, 4 eq.). 4-ethynyl benzoic acid (44 mg, 0.30 mmol) was added and the mixture was stirred 16 h at RT. A precipitate was isolated by Buchner filtration and washed with THF to yield the crude product as a green solid (70 mg, 75 %). m/z (ASAP) 312 (M$^+$, 100%). ^{1}H NMR(400 MHz, DMSO): δ_H 5.77 (3H, s, SC*H*$_3$), 6.51 (2H, d, *J* = 12, H1 H2), 6.65 (1H, d, *J* = 8, H7), 7.11 (1H, d, *J* = 8, H8), 7.14 (1H, s, triazole), 7.49 (2H, d, *J* = 12, H3 H4), 7.59 (1H, d, *J* = 8, H5), 7.87 (1H, d, *J* = 8, H6), 8.98 (1H, s, COOH).

4-{1-[4-(Methylsulfanyl)phenyl]-1H-1,2,3-triazol-4-yl}aniline

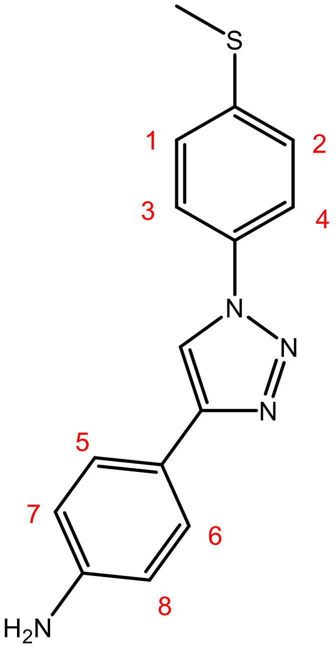

1,4-azido(methylthio)phenol (71 mg, 0.43 mmol) was dissolved in acetonitrile (50 ml) with tetrakis(acetonitrile)copper(I) hexafluorophosphate (78 mg, 0.21 mmol, 0.5 eq), tetrabutylammonium difluorotriphenylsilicate (113 mg, 0.21 mmol, 0.5 eq.), and diisopropylamine (238 µl, 1.7 mmol, 4 eq.). 4-ethynyl aniline (44 mg, 0.43 mmol) was and the mixture was stirred 16 h at RT. A precipitate was isolated by Buchner filtration and washed with THF to yield the crude product as a yellow solid (81.3 mg, 67 %) solid (70 mg, 75 %). m/z (ASAP) 283 (M^+, 100%). ^{1}H NMR (400 MHz, $CDCl_3$): δ_H 3.40 (2H, s, N*H*$_2$) 5.32 (3H, s, SC*H*$_3$), 6.62 (2H, d, *J* = 8, H7 H8), 6.68 (2H, d, *J* = 12, H1 H2), 7.59 (2H, d, *J* = 8, H5 H6), 7.84 (2H, d, *J* = 12, H3 H4). ^{13}C NMR data of the final product could not be acquired due to COVID-19 restrictions.

Methyl 4-{2-[2,6-bis(methanesulfonylmethyl)pyridin-4-yl]ethynyl}benzoate

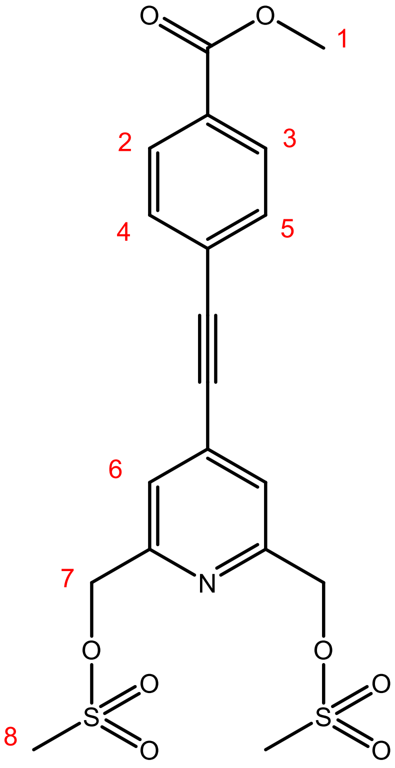

DIEA (217 mg, 1.68 mmol) was added to a mixture of methyl 4-{2-[2,6-bis(hydroxymethyl)pyridine-4-yl]ethynyl}benzoate. (100 mg, 0.336 mmol) and $O(SO_2CH_3)_2$ (293 mg, 1.68 mmol) in dry THF (2 ml) under argon and allowed to react with stirring for 2 h. The solvent was then removed *in vacuo* and the product was redissolved in DCM (10 ml) and washed with purite water (3 × 10 ml), then the combined organic phases were dried over Na_2SO_4 and solvent was removed *in vacuo* to give 3-{1-[4-(methylsulfanyl)phenyl]-1H-1,2,3-triazol-4-yl}benzoic acid as a brown solid (125 mg, 82 %). ^{1}H NMR (400 MHz, $CDCl_3$): δ_H 8.08-8.11 (2H, m, H2 H3), 7.64-7.68 (2H, m, H4 H5), 7.59 (2H, s, pyridine), 5.35 (4H, s, H7), 3.97 (3H, s, H1), 3.16 (6H, s, H8).

Methyl 4-(4-ethynyl-2,6-((carbamimidoylsulfanyl)methyl)pyridine)benzoate

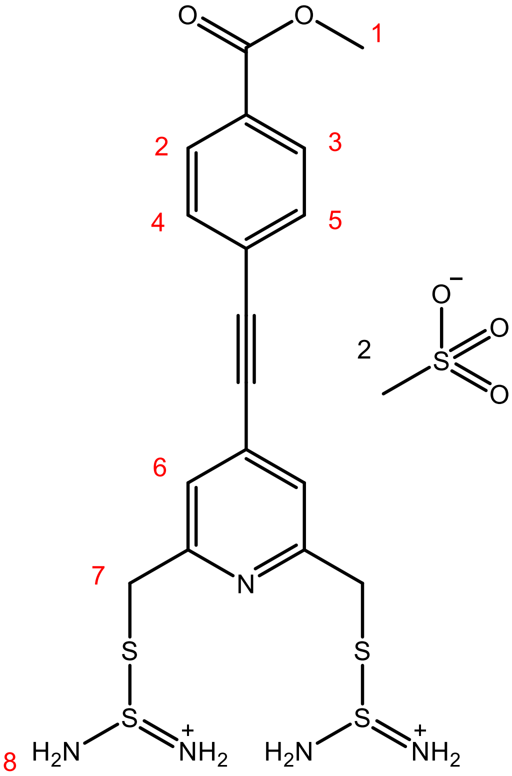

Thiourea (13 mg, 0.176 mmol) and methyl 4-{2-[2,6-bis(methanesulfonylmethyl)pyridin-4-yl]ethynyl}benzoate (40 mg, 0.088 mmol) were dissolved in acetone (4 ml) and left to react for 48 h with stirring. A brown precipitate formed which was filtered off using a Buchner funnel and washed with diethyl ether to give methyl 4-(4-ethynyl-2,6-((carbamimidoylsulfanyl)-methyl)pyridine)benzoate as the isothiouronium salt. (25.5 mg, 57 %). %). ^1H NMR (400 MHz, $CDCl_3$): δ_H 8.06 (2H, d, J = *8*, H2 H3), 7.76 (2H, d, J = *8*, H4 H5), 7.68 (2H, s, H6), 4.62 (4H, s, H7), 3.89 (3H, s, H1), 2.33 (6H, s, H8).

4-{2-[2,6-Bis(sulfanylmethyl)pyridin-4-yl]-1-chloroethenyl}benzoic acid

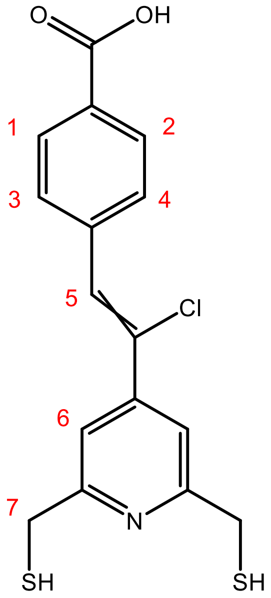

Methyl 4-(4-ethynyl-2,6-((carbamimidoylsulfanyl)methyl)pyridine)benzoate (10 mg, 0.020 mmol) was dissolved in 2M aqueous NaOH (5 ml) and heated at 80 °C in an argon atmosphere with stirring for 3 h. After cooling to room temperature the solution was acidified to pH 2 with 2M HCl and extracted with DCM (3 × 10 ml). The organic phases were combined, washed with deionised water (3 × 10 ml), dried over Na_2SO_4 and the solvent removed *in vacuo* then passed through a Celite plug for purification to yield 4-{2-[2,6-bis(sulfanylmethyl)pyridin-4-yl]-1-chloroethenyl}benzoic acid as a green solid (3.3 mg, 52 %). ^1H NMR (400 MHz, $CDCl_3$): δ_H 8.11-8.12 (2H, m, H1 H2), 7.71-7.74 (2H, m, H3 H4), 7.54-7.56 (2H, m, H6), 7.02 (1H, s, COOH), 5.37 (4H, s, H7), 4.73 (1H, s, H5), 3.69 (2H, s, SH). Mass spectrometry and ^{13}C NMR data of the final product could not be acquired due to COVID-19 restrictions.

But-3-yn-1-yl methanesulfonate

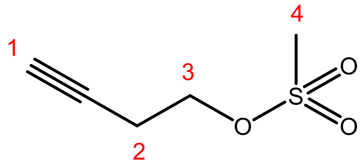

Et_3N(178 mg, 1.76 mmol) was added to a mixture of but-3-yn-1-ol (49.3 mg, 0.703 mmol) and $O(SO_2CH_3)_2$ (306 mg, 1.76 mmol) in dry THF (2 ml) and under argon and left to react with stirring for 2 h. The solvent was then removed *in vacuo* and the product was redissolved in DCM (10 ml) and washed with deionised water (3 × 10 ml), then the combined organic phases were dried over Na_2SO_4 and solvent was removed *in vacuo* to give but-3-yn-1-yl methanesulfonate as a yellow oil (118 mg, 45 %). ^{1}H NMR (400 MHz, $CDCl_3$): δ_H 4.33 (2H, t, J = 6.69, H3), 3.08 (3H, s, H4), 2.68 (2H, dt, J = 2.68, 6.69, H2), 2.09 (1H, t, J = 2.68, H1).

3-Butyn-1-yl carbamimidothioate

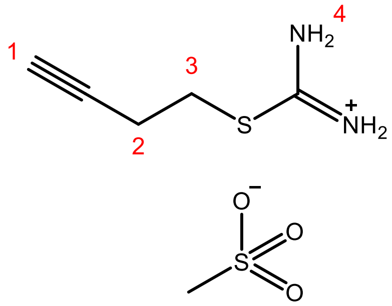

Thiourea (130 mg, 1.70 mmol) and but-3-yn-1-yl methanesulfonate (118 mg, 0.796 mmol) were dissolved in acetone (4 ml) and left to react for 48 h with stirring. A white precipitate formed which was too fine to be filtered off. Solvent was decanted off and the precipitate was washed with DCM to yield 3-butyn-1-yl carbamimidothioate as the isothiouronium salt (55 mg, 60%). ^{1}H NMR (400 MHz, $CDCl_3$): δ_H 4.25 (2H, t, J = 6.36, H3), 3.21 (3H, s, H4), 2.97 (1H, t, J = 2.63 H2), 2.63 (1H, td, J = 2.68, 6.36 H1).

2-Chlorobut-3-ene-1-thiol

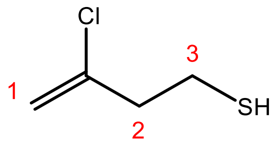

The isothiouronium salt of 3-butyn-1-yl carbamimidothioate (25 mg, 0.119 mmol) was dissolved in 2M aqueous NaOH (5 ml) and heated at 50 °C in an argon atmosphere with stirring overnight. After cooling to room temperature the solution was acidified to pH 2 with 2M HCl and extracted with diethyl ether (3 × 10 ml). The organic phases were combined, washed with deionised water (3 × 10 ml), dried over Na_2SO_4 and the solvent removed by gentle heating at atmospheric pressure. The resulting solid was washed with DCM to yield 2-chlorobut-3-ene-1-thiol as a yellow powder (5 mg, 34 %). ^{1}H NMR (400 MHz, $CDCl_3$): δ_H 4.70 (1H, s, SH), 3.69 (2H, s, H1), 3.60-3.62 (2H, m, H3), 3.26-3.30 (2H, m, H2). Mass spectrometry and ^{13}C NMR data of the final product could not be acquired due to COVID-19 restrictions.

General method for the direct addition of molecular wires and control molecules to gold nanostars

2 mg of the appropriate molecular wire or control molecule was added to a solution of AuNS in DMF as prepared in section 6.2 (20 ml) and stirred 16 h. The mixture was then centrifuged twice for 20 mins at 4.4 x10^3 rpm to remove excess reagent before resuspending in water (20 ml).

General method for the stepwise synthesis of OTP molecular wires on gold nanostars

1,4-azido(methylthio)phenol (20 mg, 0.12 mmol) was added to a solution of AuNS in DMF as prepared in section 6.2 (10 ml) and stirred 16 h. The mixture was centrifuged twice for 20 mins at 4.4 x10^3 rpm and resuspended in DMF. Tetrakis(acetonitrile)copper(I) hexafluorophosphate (8 mg, 0.02 mmol, 0.5 eq), tetrabutylammonium difluorotriphenylsilicate (11 mg, 0.02 mmol, 0.5 eq.), and diisopropylamine (24 µl, 0.17 mmol, 4 eq.) were dissolved in the suspension. The appropriate alkyne (0.04 mmol) was then added, and the mixture was stirred 16 h at RT before centrifuging twice for 20 mins at 4.4 x10^3 rpm and resuspending in water.

6.4 Biological sample preparation

Cell culture

Cell lines used were NIH-3T3 (mouse skin fibroblasts), MCF7 (human breast cancer cells), and A375 (human melanoma cells) grown in Dulbecco's Modified Eagle Medium with 10% foetal bovine serum. MCF7s were also supplemented with sodium pyruvate (1 %) and non-essential amino acids (1 %). Cell were incubated at 37°C and 5% CO_2 in average humidity. Cell harvesting was carried out by addition of trypsin solution (0.25 %) for 5 minutes at 37°C, before resuspending in fresh media.

Cell samples for microscopy

Cells were prepared by seeding into 24-well plates on glass coverslips and incubated at 37°C and 5% CO_2 until 60-70 % confluent. The cell culture medium was then changed to Leydig Cell Medium, before adding 50 µl of a 0.5 mg cm^{-3} solution of the appropriate gold nanostar probe. These were incubated for the required time period at 37°C and 5% CO_2. After washing with phosphate buffer solution, cover slips were mounted onto glass slides which were sealed with clear nail polish.[10]

Cell samples for Raman spectroscopy

Samples of cells at 10^7 cells ml^{-1} were centrifuged at 1000 rpm for 30 minutes to acquire cell pellets, which were then transferred onto glass slides. The cell pellets were soaked in an excess of a 0.5 mg cm^{-3} solution of the appropriate gold nanostar probe and allowed to air dry. After Raman spectra were acquired, the slides were washed with deionised water to remove unbound probe from the adhered cells before obtaining further Raman spectra.

Toxicity Measurements

Cells were seeded into 24-well plates and incubated in 5 % CO_2 at 37 ^oC until 80-90 % confluence was reached. The cells were then given fresh media and dosed with the desired gold nanostar probe, suspended in cell media, from a concentration of 0 mg cm^{-3} to 0.9 mg cm^{-3} with intervals of 0.1 mg cm^{-3}. After incubating for 24 h at 5 % CO_2 and 37 ^oC, the cells were harvested with trypsin and loaded into Via1-casette cell viability cartridges, containing DAPI and acridine orange for the detection of non-viable cells and live cells respectively. A ChemoMetec A/S Nucleocounter3000-Flexicyte was used to count live cells and measure cell viability of the samples using the Via-1 cassettes preloaded with DAPI and Acridine orange.[11]

6.5 References

1 J. Turkevich, P. C. Stevenson and J. Hillier, *Discuss. Faraday Soc.*, 1951, **11**, 55–75.

2 X.-D. Tian, B.-J. Liu, J.-F. Li, Z.-L. Yang, B. Ren and Z.-Q. Tian, *J. Raman Spectrosc.*, 2013, **44**, 994–998.

3 M. Montalti, L. Prodi, N. Zaccheroni and G. Falini, *J. Am. Chem. Soc.*, 2002, **124**, 13540–13546.

4 A. Kedia, H. Kumar and P. S. Kumar, *RSC Adv.*, 2015, **5**, 5205–5212.

5 S. Atta, M. Beetz and L. Fabris, *Nanoscale*, 2019, **11**, 2946–2958.

6 K. D. Grimes, A. Gupte and C. C. Aldrich, *Synthesis (Stuttg).*, 2010, **2010**, 1441–1448.

7 Z. Jia and Q. Zhu, *Bioorg. Med. Chem. Lett.*, 2010, **20**, 6222–6225.

8 S. Lal and S. Díez-González, *J. Org. Chem.*, 2011, **76**, 2367–2373.

9 C. Kluger and W. H. Binder, *J. Polym. Sci. Part A Polym. Chem.*, 2007, **45**, 485–499.

10 R. Pal, *Faraday Discuss.*, 2015, **177**, 507–515.

11 A. T. Frawley, H. V. Linford, M. Starck, R. Pal and D. Parker, *Chem. Sci.*, 2018, **9**, 1042–1049.